METATHESIS CATALYSTS: AN INTEGRATED COMPUTATIONAL, MECHANISTIC AND SYNTHETIC STUDY

A thesis submitted in fulfilment of the
requirements for the degree of

DOCTOR OF PHILOSOPHY
of
RHODES UNIVERSITY

by

INGRID THERESA SABBAGH

July 2005

ABSTRACT

An integrated approach to the design of potential ruthenium-based metathesis catalysts is described, in which closely defined synthetic forays provide the focus and rationale for detailed computational and mechanistic studies.

The ground-state geometry of a 1st-generation Grubbs catalyst has been explored at the molecular mechanics, semi-empirical and DFT levels, and the resulting structures have been shown to compare favourably with literature data and with the structure of a known crystalline analogue. The DMol^3 DFT code has also been shown to represent accurately both the geometry of the corresponding co-ordinatively unsaturated monophosphine derivative, and the ligand dissociation energy associated with its formation. A DFT free-energy profile of the degenerate metathesis of ethylene has been generated, using a truncated model of the 1st-generation Grubbs catalyst, permitting location, for the first time, of the three expected transition states and providing new information regarding the rate-determining step.

DFT methods have been used to facilitate the design of a tridentate camphor-derived ligand for use in the construction of a novel Grubbs-type catalyst. The phosphine ligand dissociation energy of the putative catalyst and the ethylene metathesis energy profile of a truncated model have also been studies at the DFT level. The attempted synthesis of the proposed ligand proceeded *via* a novel 8-bromocamphoric anhydride intermediate and afforded several unexpected and novel products, including a *cis*-fused γ-lactone, and a bromocamphoric acid derivative. Single crystal X-ray analysis of the latter reveals a chiral, polymeric H-bonded packing arrangement, rendering it suitable for chiral inclusion studies. Computational methods, including the GAUSSIAN-based GIAO NMR prediction technique, were used to support the structural characterisation of the novel camphor derivatives.

DFT-level computational analysis of the C-8- and C-9 bromination of camphor has afforded theoretical insights which permit the reconciliation of two earlier empirical explanations regarding the regioselectivity of these transformations; moreover, the theoretical results suggest that a third, previously disregarded factor, plays a significant role. A coset analysis, in conjunction with DFT-level energy profiling, has also been used to resolve conflicting opinions regarding the origin of the major by-product.

Computed electronic parameters (CEP's) have been calculated for the anionic ligands involved in a series of 2nd-generation Grubbs-Hoveyda-type catalysts, and used to explain some apparently anomalous trends in catalyst activity. A linear relationship between ligand CEP's and selected ^{1}H NMR chemical shifts has also been demonstrated and used to identify a transient ruthenium complex in solution.

The ability of the malonate di-anion to bind to ruthenium in a bidentate manner has been explored and demonstrated, under suitable conditions. DFT methods have been used to design and assess the ruthenium-chelating potential of a novel tridentate malonate derivative. A synthetic pathway to this ligand has been designed and several novel heterocyclic intermediates have been isolated and characterised.

An NMR-based kinetic study of the Grubbs-catalysed self-metathesis of 1-octene has been completed, and the effects of temperature, concentration and solvent variations on the kinetic parameters have been studied. Application of the Guggenheim method and a simplified mechanistic model has permitted the accurate calculation of pseudo-rate constants for the initiation and, for the first time, the propagation phase of the reaction. Theoretical studies of this reaction at the DFT and molecular mechanics levels have been shown to support previous assumptions regarding the selectivity and temperature-dependence of metallacycle formation.

CONTENTS

ACKNOWLEDGEMENTS

I would like to express my gratitude to my supervisor, Professor P.T. Kaye, who has, in every respect, set the standards to which I shall aspire throughout my career. It has indeed been a privilege to have worked under his guidance.

I would also like to thank Mr K. Lobb for many fruitful discussions regarding the computational work, Mr A. Sonneman for technical support and low-resolution MS analysis, and Dr G.M. Watkins for his input on the organometallic work. Thanks to Professor Mino Caira from the University of Cape Town and Mr Manuel Fernandes from the University of the Witwatersrand for X-ray crystallography, and Mr Tommie van der Merwe from the University of the Witwatersrand for high-resolution mass spectroscopy.

Many thanks to Sasol, and to Rhodes University, whose generous financial support have made this project possible.

1. INTRODUCTION

The introduction will provide a brief outline of the role of catalysis in the chemical industry in general, and in the refining and petrochemical industries in particular. This will be followed by a more detailed review of metathesis reactions and their catalysis.

1.1 INDUSTRIAL CATALYSIS

Since the mid-20th century the use of catalysts has expanded into every sector of the chemical industry. Not surprisingly, it is a field that has seen considerable development, from the petrochemical revolution of catalytic cracking in the 1930's, to the recent and explosive development of enzymatic catalysis. Today, it is estimated that 85 percent of all chemical processes are operated catalytically.[1]

1.1.1 Properties of an industrial catalyst

Six primary factors are generally considered when determining the viability of a catalyst for an industrial process.[2]

i. *Activity,* expressed in terms of rate, turnover number or conversion. High catalyst activity allows for lower reaction volumes and milder conditions, while increasing general productivity.

ii. *Selectivity,* which decreases the amount of reagent required and minimizes costs of separation, purification and waste treatment.

iii. *Lifetime,* which must be long enough to balance the cost of down-time and catalyst replacement.

iv. Ease of regenerating spent catalyst.

v. *Toxicity,* both in terms of handling safety and disposal.

vi. Price.

1.1.2 Heterogeneous *vs.* homogeneous catalysts

Heterogeneous catalysis was the first to be applied commercially, and still constitutes some 75% of modern catalytic processes.[1] It has several obvious advantages, including ease of catalyst separation and minimization of liquid waste. However, a survey of the recent literature reveals a distinct shift in focus amongst both the academic and industrial communities.[1] Homogeneous processes are now receiving a great deal of attention, particularly in the production of fine chemicals and in green chemistry applications. This shift can be attributed, largely, to a growing understanding of the kinetic and mechanistic aspects of homogeneously catalyzed processes,[3] and the characterization of various catalytic species. These developments have helped to solve the problem of catalyst separation and streamline rational catalyst design.

A further factor contributing to the growing interest in homogeneous catalysis has been the advent of combinatorial screening methods,[4] which are now routinely used to fine-tune homogeneous catalysts in industry. Apart from their most obvious role in accelerating the rate of catalyst discovery and development, combinatorial techniques provide the opportunity to assay even unlikely catalyst candidates. It is hoped that this will lead to the discovery of new classes of catalysts that have been overlooked by false or oversimplified mechanistic arguments. This type of high-throughput screening is not readily applicable to heterogeneous catalysts, where the performance of the catalyst is greatly influenced by the plant-scale reproducibility of laboratory results.

Many researchers have attempted to combine the advantages of homo- and heterogeneous methods by immobilizing or anchoring homogeneous catalysts on to heterogeneous supports. Thus far, however, only limited success has been achieved due to leaching of the catalytic moieties or decreased activity.[1,5] New variants of biphasic homogeneous processes, including the use of non-aqueous ionic liquids,[6] supercritical fluids[7] and the application of fluorous phases[8] are also receiving attention. Although promising, these technologies have yet to prove their usefulness and economic viability.

1.2 CATALYSIS IN THE REFINING AND PETROCHEMICAL INDUSTRIES

Many of the accomplishments in catalysis research over the past century can be attributed directly or indirectly to the refining and petrochemical industries. At the same time, these industries have been transformed by the move from purely thermal processes to catalytic processes. On the refining side, catalysis is used in processes such as catalytic cracking, hydrotreating, olefin oligomerisation and the aromatisation of alkanes. Catalytic petrochemical processes, on the other hand, mainly involve the transformation of olefins, notably *via* hydrogenation and metathesis.[9]

Although these are all relatively mature fields, predictions for the long-term future of the refining and petrochemical industry have highlighted several important implications for catalyst research.[9]

i. Increasing environmental concerns over the coming decades will force the industry to tighten regulations regarding the production of greenhouse gases and other industrial wastes, including spent catalysts. This may render some catalysts unusable in the future. The problem of rising CO_2 levels may be countered by the catalytic sequestration of CO_2 at source.[10]

ii. Dwindling hydrocarbon reserves will lead to an increased emphasis on energy conservation, which will demand increased efficiency in refining and petrochemical processes.[11] In light of this, catalyst activity and selectivity will become increasingly important.

iii. The search for new, renewable energy sources will create even further scope for the use of catalysis, particularly in the task of harnessing energy from biomass.[12]

1.3. METATHESIS

Double-bond scrambling reactions were already known in the 1950's, in the form of Ziegler's olefin polymerisation reactions. It had also been noted that Ziegler-type catalysts could effect the disproportionation of acyclic olefins. However, it was not until a decade later that Calderon and co-workers realized that these involved the same reaction.[13] The term 'olefin metathesis' was coined in 1967 and, as we now understand it, refers to the metal-catalysed redistribution of carbon-carbon double bonds (Figure 1).

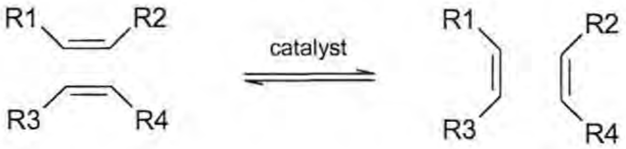

Figure 1. Olefin metathesis.

Although there are thought to be some variations with different catalyst systems, the generally accepted mechanism for metathesis is that proposed by Chauvin in 1970 (Figure 2).[13] This involves a series of alternating [2 + 2] cycloadditions and cyclo-reversions. The mechanistic proposal provided the impetus for innovative catalyst design during the following decades and this, in turn, prompted chemists to find new uses for the reaction. As a result, metathesis is now an invaluable tool in both organic and polymer chemistry.

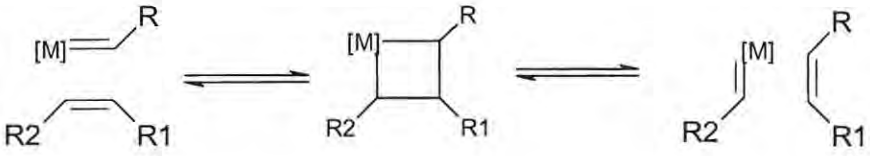

Figure 2. Chauvin's mechanism for olefin metathesis.

1.3.1 Types of metathesis and their applications

There are several variations of the metathesis reaction, as illustrated in Figure 3.[13] These include ring-closing metathesis (RCM), acyclic diene metathesis (ADMET), ring-opening metathesis polymerisation (ROMP), ring-opening metathesis (ROM) and cross-metathesis (CM). In addition to these, several tandem or domino processes have also been reported.

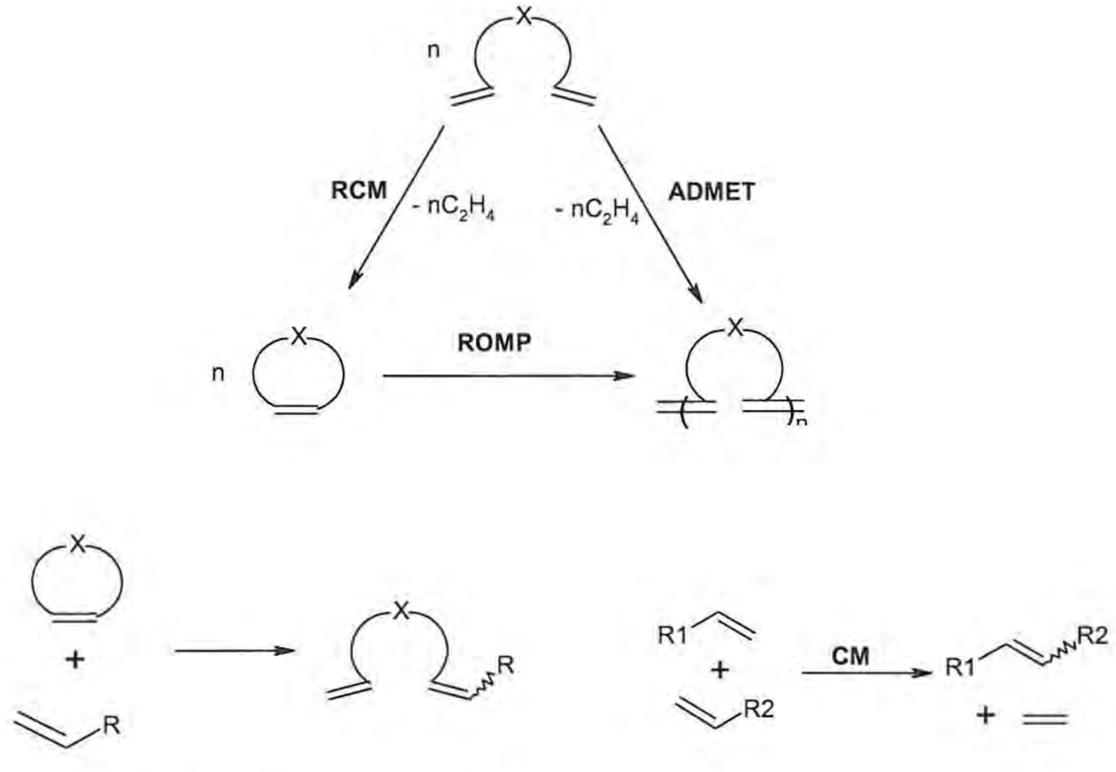

Figure 3. Olefin metathesis reactions.

1.3.1.1 Ring-closing metathesis (RCM)

RCM is perhaps the most versatile and widely used form of metathesis. Its applications have been extensively reviewed by Armstrong,[14] and by Grubbs and Chang.[15] RCM finds its simplest and most obvious use in the synthesis of medium sized (5-8 membered) monocyclic products, including highly substituted and heterocyclic systems. A wide variety of functional groups and substitution patterns can be accommodated using this technique as illustrated in Scheme 1,[15] where [M]=CHR refers to a Grubbs or Schrock-type metal alkylidene catalyst.

Although limitations do exist in applications of RCM, these continue to be overcome by improved catalyst systems and innovative synthetic methods. A recent example of such progress is the use of microwave irradiation to accelerate the RCM of sterically encumbered dienes.[16]

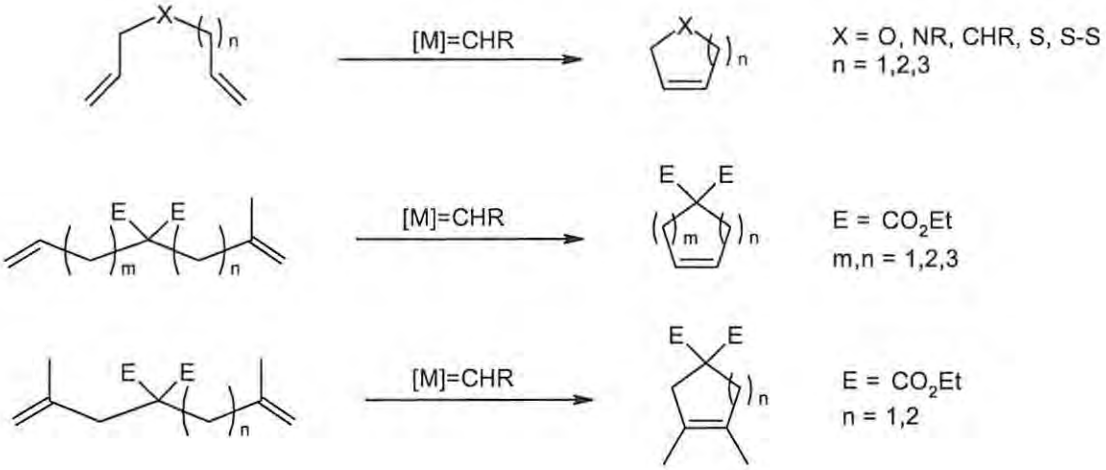

Scheme 1

Some work has been done on achieving diastereoselectivity in these types of reactions, by making use of the substitution pattern of the substrate to direct metathesis towards the less sterically hindered of two alkenes. This is well illustrated by the work of Blechert (Scheme 2)[14] and, more recently, by the stereoselective synthesis of 9-membered lactams by Banfi and co-workers.[17]

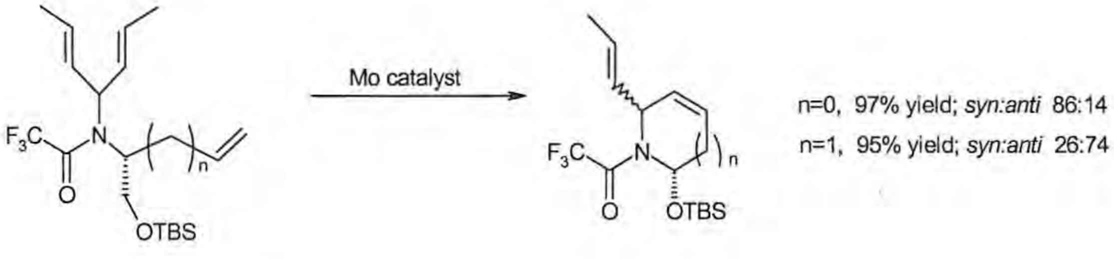

Scheme 2

Asymmetric RCM can also be achieved by the use of chiral catalysts, an example of which is the chiral molybdenum alkylidene complex **1** developed by Grubbs.[18]

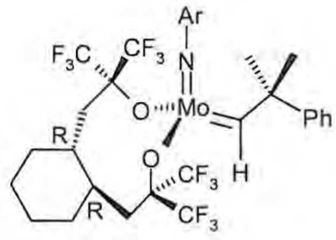

1

RCM is one of the most widely used methods for the formation of macrocyclic systems, particularly in the area of natural product synthesis. Figure 4 illustrates several macrocyclic natural products synthesized by such reactions.[19] Some degree of stereoselectivity can be introduced into the macrocyclisation reactions by employing a metal ion template that forms a suitably oriented complex with the olefin substrate. This technique has been successfully employed in the stereoselective synthesis of catenanes (Scheme 3).[15]

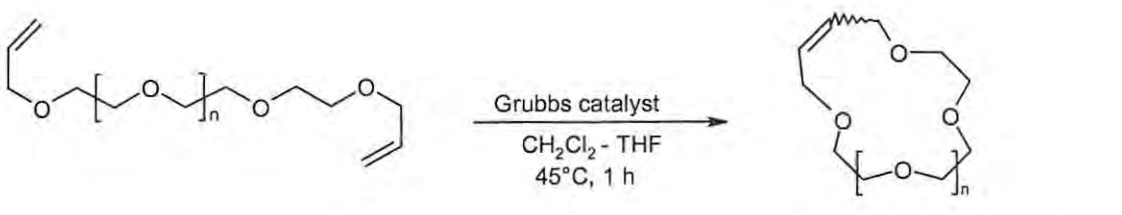

n = 1, no template; 39% (38:62 Z/E)
n = 1, $LiClO_4$ (5 equiv); >95% (100:0 Z/E)

Scheme 3

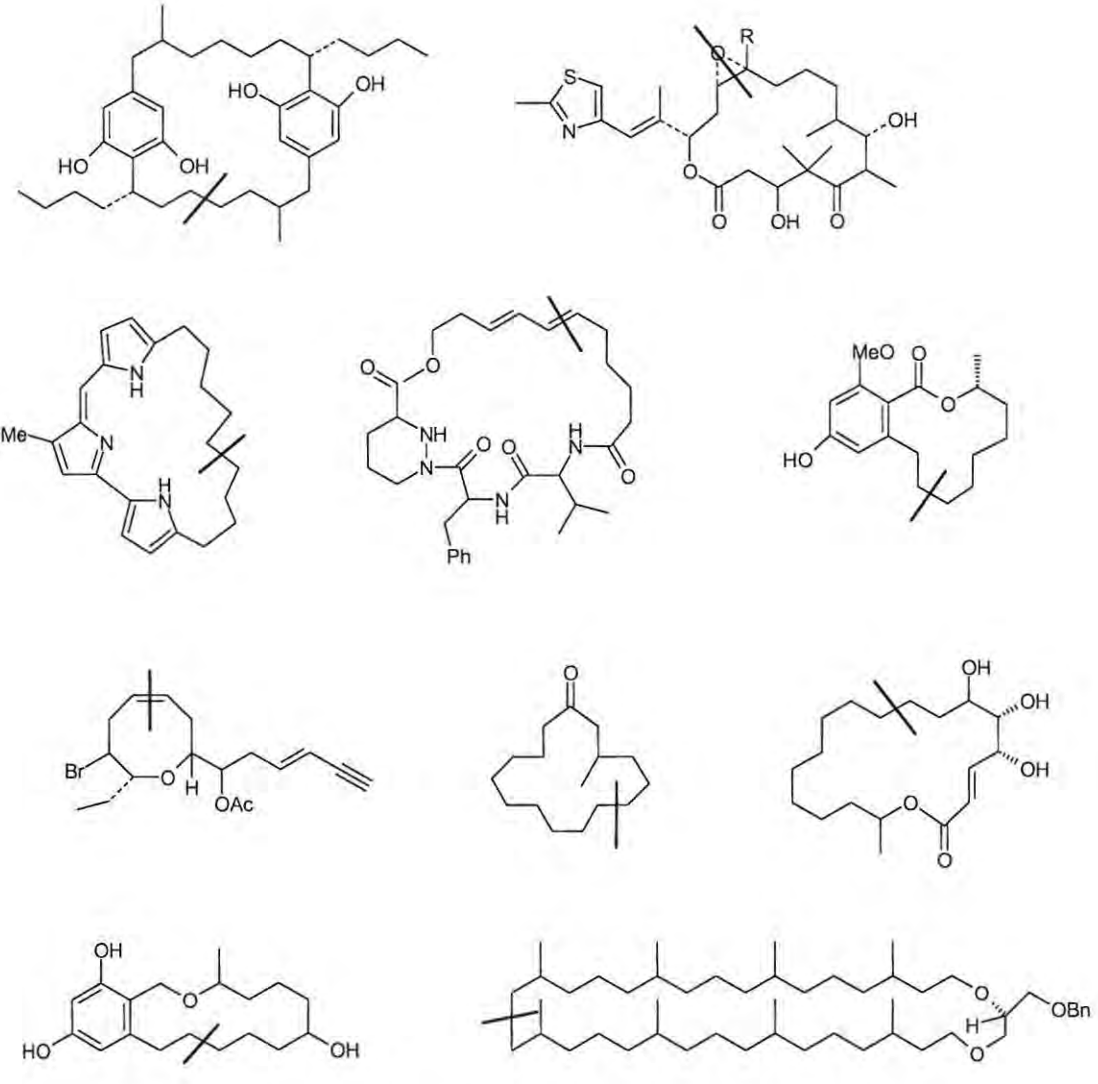

Figure 4. Macrocyclic natural products prepared by RCM (dashed lines indicate sites of ring closure).

Multiple RCM reactions have also begun to appear in the literature. A recent paper by Wallace[20] describes the first reported quadruple ring closure by this technique (Scheme 4).

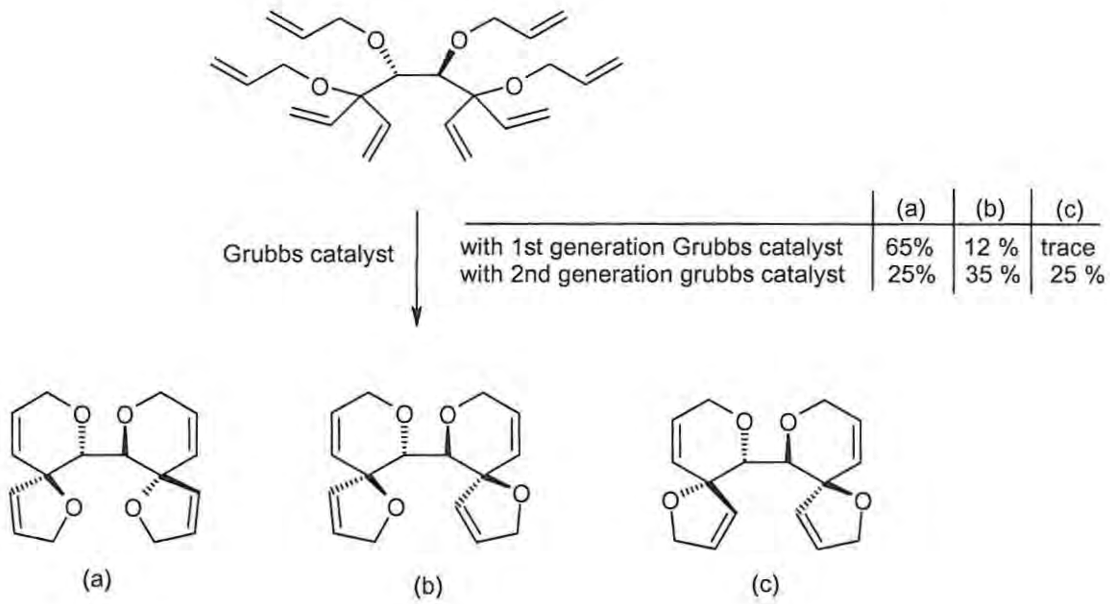

	(a)	(b)	(c)
with 1st generation Grubbs catalyst	65%	12 %	trace
with 2nd generation grubbs catalyst	25%	35 %	25 %

Scheme 4

The scope of RCM reactions is not limited to the synthesis of cyclic products. It can be extended to the production of acyclic alkenes by the reaction of dienes connected by a temporary tethering species (usually silicon-based). This is well illustrated by the recent synthesis of the natural product attenol A **2**, outlined in Scheme 5.[21]

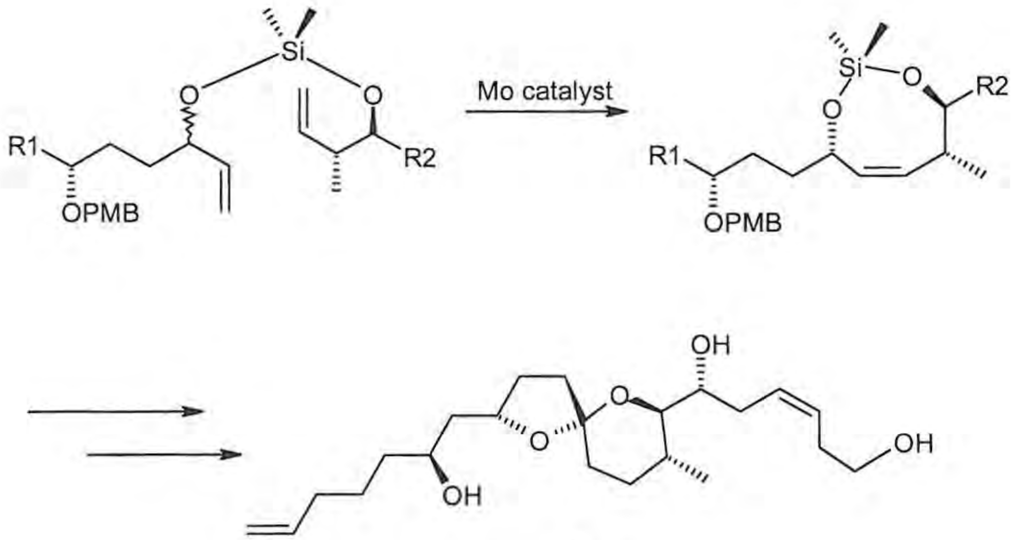

2

Scheme 5

1.3.1.2 Cross-metathesis (CM)

Unlike RCM, the synthetic utility of cross metathesis has been largely ignored until recently. This was due, mainly, to the difficulty of controlling or predicting product selectivity and *cis/trans* ratios in these reactions (Scheme 6).[22] However, the advent of well-defined catalyst systems and innovative synthetic strategies has brought about renewed interest in CM.

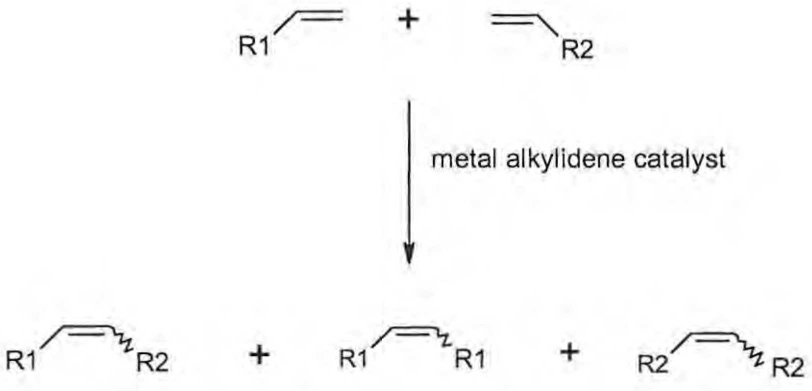

Scheme 6

Cross-metathesis is typically carried out on terminal olefins, as the use of internal olefins adds unwanted complexity to the product mixture. Even so, cross-metathesis generally competes with self-metathesis to generate a mixture of homo- and heterodimeric products.[22] Chemo- and stereoselective CM was first achieved by Crowe *et al.* with small alkyl-substituted olefins and π-substituted olefins, such as styrene[23] and acrylonitrile[24] (Scheme 7).

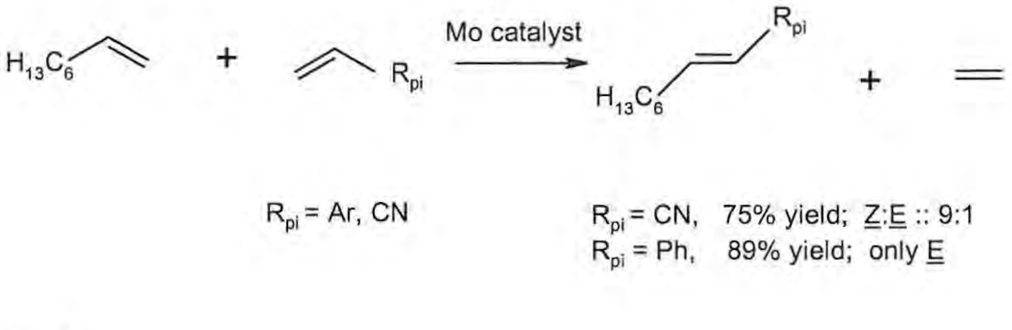

Scheme 7

The synthetic utility of CM is well illustrated by the synthesis of the plant pheromone, jasmonic acid **3** by Blechert and co-workers (Scheme 8).[15]

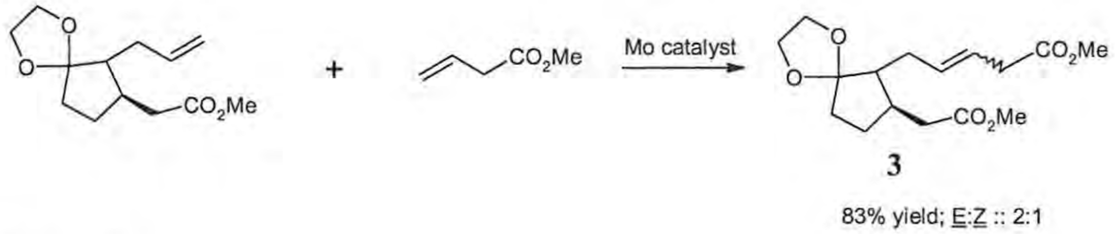

Scheme 8

Recently, a small but expanding body of literature has begun to emerge regarding selective CM reactions. This has culminated in the proposal by Grubbs and co-workers of an empirical model to predict the selectivity and stereoselectivity of CM reactions.[25] The model involves the ranking of olefin substrates according to their relative abilities to undergo homodimerisation, and the susceptibility of the homodimers to secondary metathesis reactions. It is hoped that this model will provide a starting point for the design of new CM methodologies. Already, it has been applied to achieve unprecedented selectivity in multicomponent reactions (Scheme 9).[25]

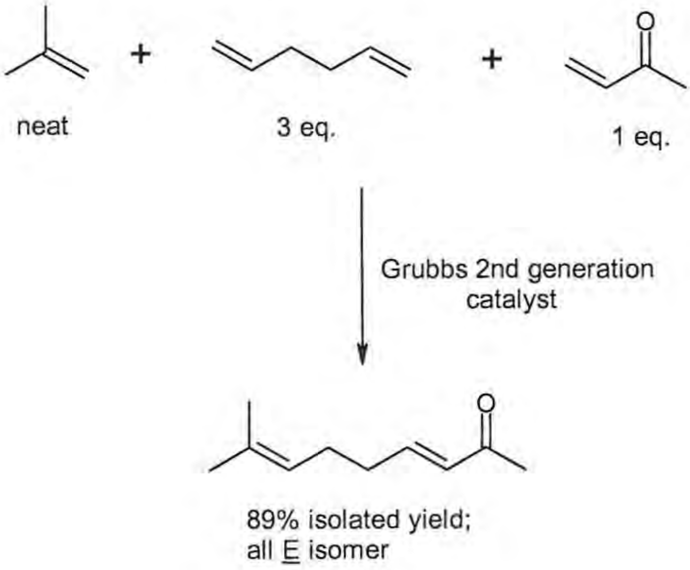

Scheme 9

1.3.1.3 Ring-opening metathesis (ROM)

As with CM, progress in the field of ROM has been hampered by poor chemo-, stereo- and regioselectivity. In a problem analogous to that of homodimerisation in CM reactions, ROMP can compete with ROM if the acyclic olefin partner does not effectively intercept the oligomerisation process. To avoid this, ROM reactions are generally performed with very dilute concentrations of the cyclic olefin and an excess of the acyclic olefin. Some attention has also been given to immobilizing the cyclic component on solid supports.[15]

Perhaps the most notable ROM results, thus far, have been reported by Blechert *et al.*[15] on reactions of strained norbornene derivatives (Scheme 10), and by Snapper and co-workers[26] on unsymmetrical cyclobutenes (Scheme 11). More recently, the advent of new phosphine-free catalysts has extended the scope of ROM to unstrained cycloolefins.[27]

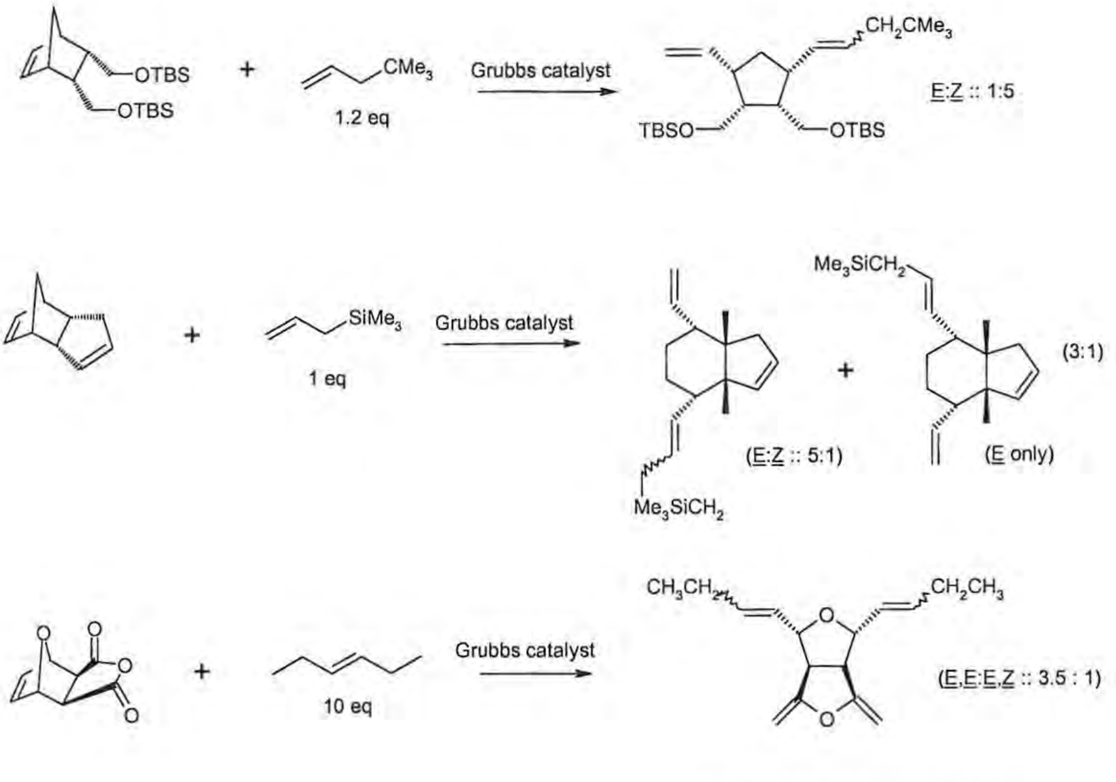

TBS = *t*-butyldimethylsilyl

Scheme 10

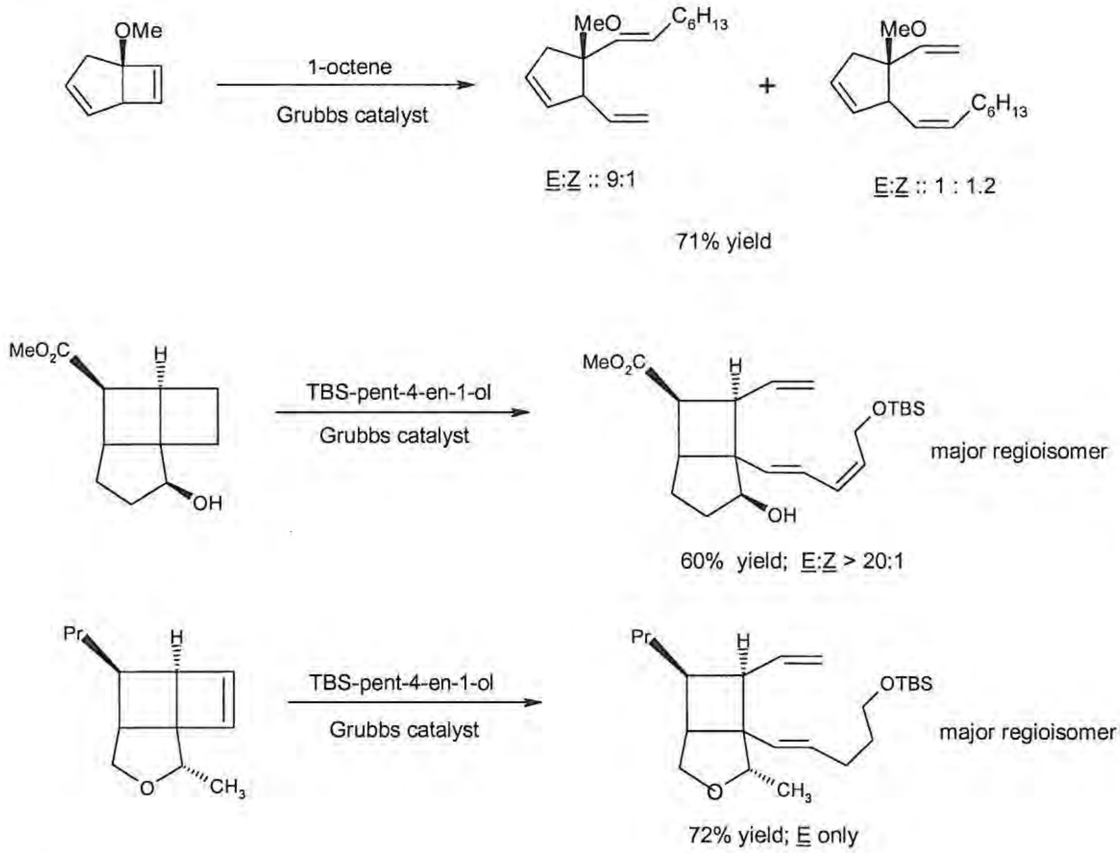

E:Z :: 9:1

E:Z :: 1 : 1.2

71% yield

major regioisomer

60% yield; E:Z > 20:1

major regioisomer

72% yield; E only

Scheme 11

ROM methodology has also been applied to natural product synthesis, most notably in the synthesis of the brown algae pheromones, multifidene **4** and viridiene **5** (Scheme 12).[26]

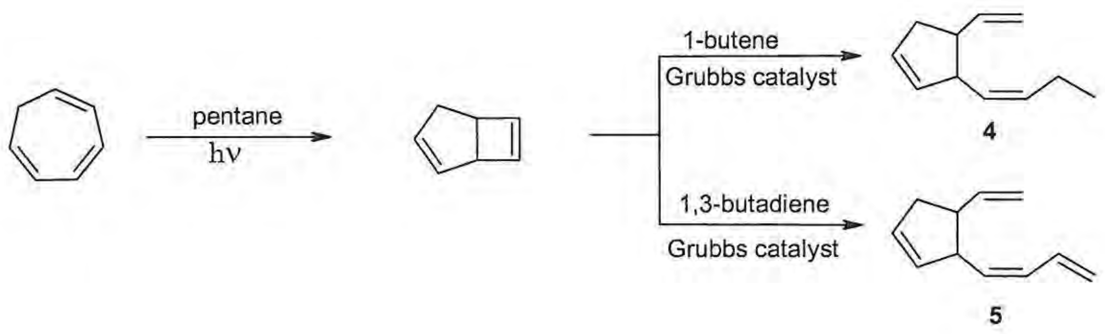

Scheme 12

1.3.1.4 Ring-opening metathesis polymerisation (ROMP)

ROMP is, historically, the most widely used metathesis technique, dating back to the polymerisation of norbornene **6** by Anderson and Merckling in 1955 (Scheme 13).[28] The technique is attractive for polymer synthesis due to the retention of backbone unsaturation and the ability to incorporate monomer functionality directly.

Scheme 13

Early work in this field was limited to the ROMP of hydrocarbon monomers, cycloalkenes and bicycloalkenes. However, new and improved catalyst systems have extended the scope of ROMP to include highly functionalised substrates, for example the fluorinated systems investigated by Feast and Khosravi.[28] The development of water-tolerant catalysts has also enabled ROMP reactions to be carried out in aqueous media – an obvious benefit for industrial processes.[29]

ROMP has recently found several interesting new applications. For example, Bolm and co-workers[30] have used ROMP methods to synthesize polymeric multivalent chiral catalysts (Figure 5). Polymer-supported catalysts are widely used in industry, offering the advantages of durable catalytic activity and easy catalyst separation. However, the randomness of the catalyst distribution along the polymer chain makes this a difficult protocol to apply to the synthesis of optically active products, which demands a high degree of enantioselectivity. This problem has been elegantly overcome by the development of highly organized systems such as that in Figure 5, which has been used to catalyse the enantioselective addition of diethylzinc to benzaldehyde.

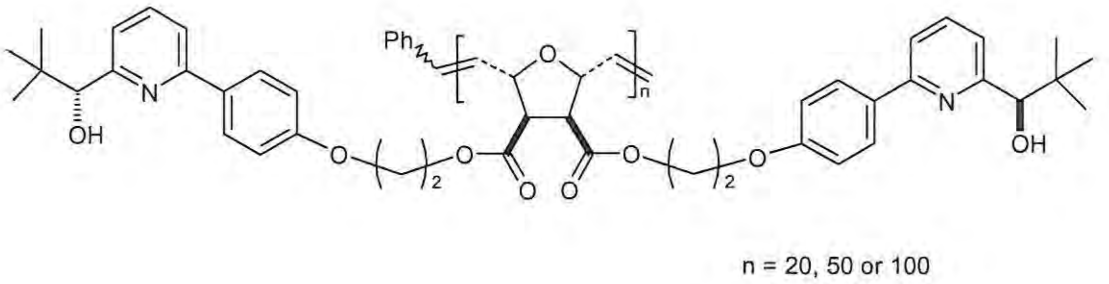

Figure 5. Polymeric chiral catalyst of Bolm and co-workers.

A recently reported capture-ROMP-release strategy makes use of norbornenyl tags to capture a reagent (usually in a Mitsunobu reaction), followed by *in-situ* ROMP.[31] The polymers can then be filtered off and treated with an appropriate reagent to release the captured species as a new product. This strategy successfully integrates synthesis and purification, making it an ideal tool for combinatorial chemistry. Scheme 14 illustrates the application of this protocol to the synthesis of alkylhydrazines. A series of alcohols are captured on reagent **7** *via* a Mitsonobu reaction. The intermediates are phase-switched by applying ROMP conditions, yielding the differentially soluble polymers **8**, which are precipitated from methanol. The hydrazine derivatives are cleaved from the polymers by refluxing in THF, and the polymeric by-products removed by extraction with Et_2O/H_2O to afford the pure hydrazine derivatives **9** in good yields.

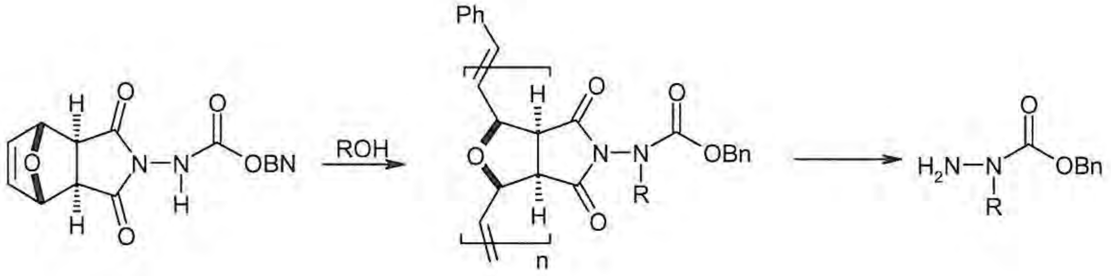

7 **8** **9**

Scheme 14.

ROMP has also recently been applied to adhesive and coating formation, in a process termed contact metathesis polymerisation (CMP). CMP involves applying the catalyst directly to a surface and then exposing it to a suitable monomer. The resultant metathesis product forms an adhesive coating.[32]

1.3.1.5 Acyclic diene metathesis (ADMET)

Polymerisation can also be achieved using acyclic isolated dienes. ADMET methods are generally applied to the polymerisation of aliphatic and aromatic α,ω-dienes, including bis(alkenyl)silanes and dienes containing ether, ester or hydroxyl groups. ADMET has also been used in the synthesis of liquid crystal polymers (LCP's) from α,ω-diene mesogens.[33]

1.3.1.6 Tandem metathesis

Metathesis strategies are frequently combined to effect more complex transformations, or to overcome the limitations of the individual techniques. For instance ROM is often combined with CM or RCM in order to avoid polymerisation. The most commonly combined metathesis techniques are those of RCM and ROM which, when applied to intramolecular reactions, are often termed ring-rearrangement metatheses or RRM's. This combination of techniques has the advantage that stereochemical information in the substrate remains unchanged by metathesis. RRM thus occurs with conservation of stereochemistry, as illustrated in Scheme 15.[34]

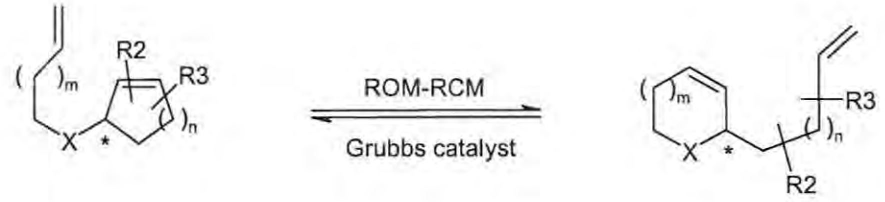

X = O or N
* = stereocentre

Scheme 15

One of the earlier applications of ROM-RCM is the synthesis, by Grubbs, of polycyclic ethers from cyclic olefins containing two alkenyl side chains (Scheme 16).[26]

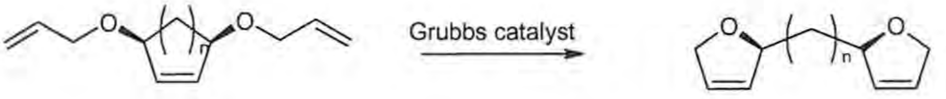

n = 0 to 3

Scheme 16

This protocol has subsequently been extended to the synthesis of fused polycyclic systems, notable examples being Hoveyda's synthesis of chromenes (Scheme 17)[26] and several useful transformations of norbornene derivatives.[35]

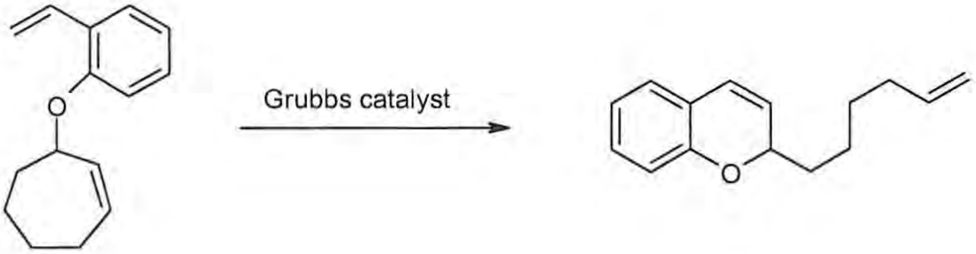

Scheme 17

Numerous other tandem metathesis combinations have been reported. Substrates containing both alkene and alkyne substituents undergo useful tandem RCM-CM or 'enyne' metathesis reactions, in which the alkyne substituent acts as a metathesis relay. This protocol has been successfully applied to the synthesis of polycyclic systems from alkynyl norbornene derivatives.[15,36] Schrock and Hoveyda have applied ROM-CM techniques to the synthesis of a wide range of optically pure, functionalised cyclopentanes.[37]

The versatility and scope of these tandem approaches is elegantly illustrated by a sequence of RCM-ADMET-RCM reactions employed by Harrity and co-workers,[38] to produce the 18-membered spirocyclic ester **10** (Scheme 18).

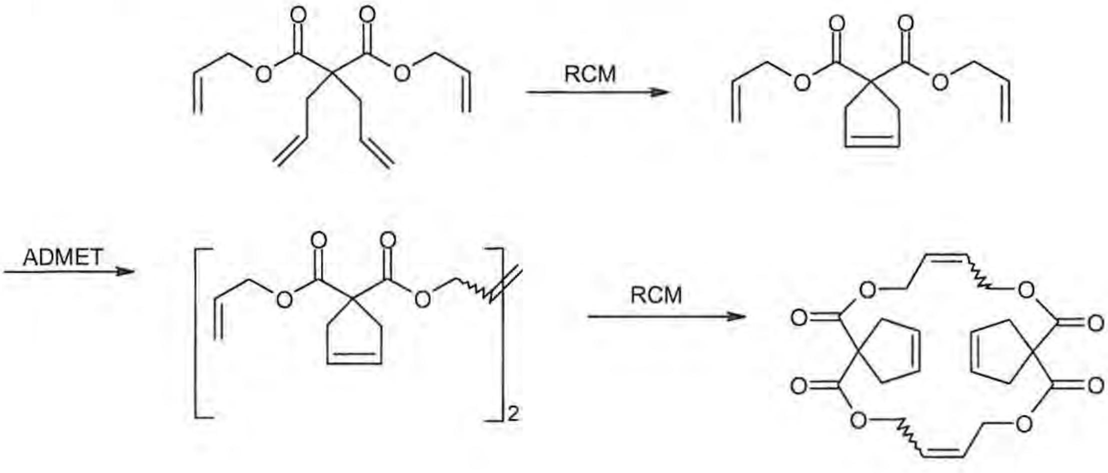

10

Scheme 18

1.3.2 Metathesis catalysts

Although a great many metathesis catalysts are known, the scope of this review is limited to the development of late transition metal catalysts. In order to provide a context for the current work, particular attention is given to the ruthenium alkylidenes.

1.3.2.1 Early Developments

Until the early 1980's all metathesis reactions were carried out using poorly defined mixtures of transition metal salts and main group alkylating agents, common combinations being WCl_6/ $EtAlCl_2$,[39] $WOCl_4/EtAlCl_2$,[40] MoO_3/SiO_2 and Re_2O_7/Al_2O_3.[13] These 'classical' systems are still of interest in large-scale commercial applications of olefin metathesis due to their low cost and ease of preparation.[41] However, the need for harsh conditions and strong Lewis acids renders them incompatible with most functional groups, which severely limits their synthetic utility.[13]

The first single-component homogeneous metathesis catalysts were developed in the late 1970's, following the proposal of Chauvin's mechanism (Figure 2) and the resultant efforts to synthesize alkylidene and metallacyclobutane complexes.[13] Of these, the molybdenum and tungsten alkylidenes were the first to become widely used. Schrock's molybdenum catalyst **11** is now commercially available, and remains the benchmark standard for metathesis activity.[19]

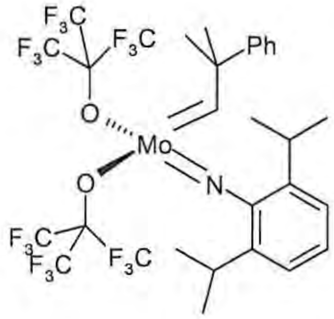

11

However, the high oxophilicity of the metal centre causes this and other early transition metal catalysts to be extremely sensitive to oxygen and moisture, which makes their handling and synthesis problematic. Their usefulness is further limited by relatively poor functional group tolerance.[13]

1.3.2.2 Ruthenium catalysts

Crucial to the development of any catalyst system is the minimization of interference by functional groups in the substrate or solvent molecules. In olefin metathesis, the specific requirement is that the catalyst should react preferentially with olefins in the presence of heteroatomic functionalities. Metathesis catalysts have been observed to react more selectively with olefins as the metal centres are varied from left to right, and bottom to top on the periodic table. This trend, illustrated in Figure 6, suggests that ruthenium is the ideal choice in terms of functional group tolerance.[13]

Increasing Reactivity

↑

Titanium	Tungsten	Molybdenum	Ruthenium
Acids	Acids	Acids	Olefins
Alcohols, Water	Alcohols, Water	Alcohols, Water	Acids
Aldehydes	Aldehydes	Aldehydes	Alcohols, Water
Ketones	Ketones	Olefins	Aldehydes
Esters, Amides	Olefins	Ketones	Ketones
Olefins	Esters, Amides	Esters, Amides	Esters, Amides

Figure 6. Functional group tolerance of olefin metathesis catalysts.[13]

(i) *1st Generation ruthenium catalysts*

The first well-defined ruthenium alkylidene metathesis catalyst **12** (Scheme 19) was synthesized in 1992 by Grubbs and co-workers, using 3,3-disubstituted cyclopropenes as carbene precursors.[42] Subsequent modification of the ligand environment led to the discovery that larger and more basic phosphines enhance metathesis activity. The tricyclohexylphosphine (PCy_3) analogue **13** was developed by the same group a year later,[43] extending the scope of ruthenium catalysts to include the metathesis of acyclic olefins.[44]

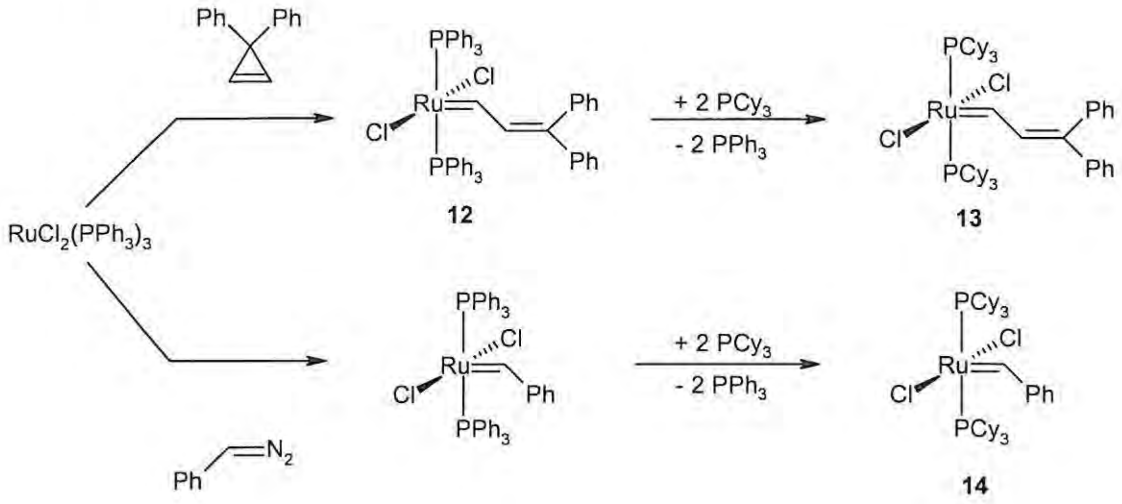

Scheme 19

The difficulty of synthesizing diphenylcyclopropene, needed for the synthesis of catalysts **12** and **13**, prompted Grubbs and co-workers to look for alternative carbene sources. The synthesis of complex **14** *via* alkylidene transfer from phenyldiazomethane was achieved in 1996.[45] Several analogues of these so-called Grubbs 1st-generation catalysts have been prepared by varying the phosphine,[46] halide[46,47] and alkylidene[45] moieties. Common to all of the reported analogues is a distorted square-pyramidal structure with two *trans* halide ligands and two *trans* phosphine ligands at the base of the pyramid, and with the carbene moiety at the apex. In all cases, the active catalytic species is thought to be generated by the liberation of one phosphine ligand, followed by coordination of the olefin substrate.[48] Thus far, the combination of electron-withdrawing chlorides and bulky, electron-donating PCy_3 in complex **14** seems to be optimal for metathesis activity.

(ii) 2nd Generation ruthenium catalysts

The report of complex **15** by Herrmann and co-workers[49] sparked a great deal of interest in the potential of *N*-heterocyclic carbenes (NHC's) as alternatives to the widely used phosphine ligands. However the NHC's, while rendering complex **15** more thermally stable than its phosphine analogues, failed to bring about an improvement in the activity profile. Because the NHC ligands are not as coordinatively labile as the phosphines, the dissociative pathway is less likely, resulting in low concentrations of the active species in solution.[19]

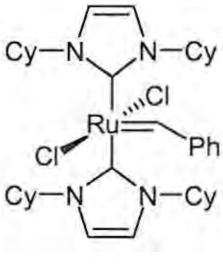

15

This problem was overcome by the development of monosubstituted structures, bearing one phosphine and one NHC ligand.[50] The synthesis of the mixed-ligand structure **16** was reported almost simultaneously by Grubbs'[51] and Nolan's groups.[52] Shortly thereafter, the unsaturated NHC analogue **17** was reported by Grubbs and co-workers to display even greater metathesis activity than that of complex **16**.[53]

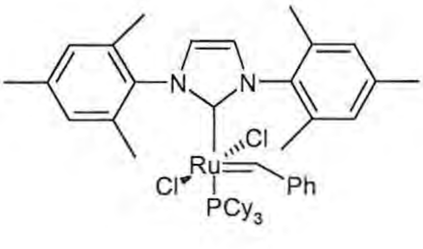

16

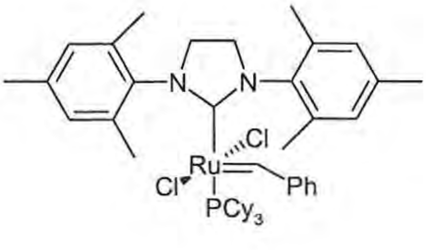

17

Numerous variations of these 2nd-generation ruthenium catalysts have been reported, which differ in the saturation or unsaturation of the NHC ligand, the substituents on the nitrogen atoms, and the nature of the alkylidene fragment.[19] In addition to exhibiting much greater thermal stability than their 1st-generation predecessors, this series of catalysts have expanded the application of ruthenium-based metathesis catalysts to include more highly substituted substrates, rendering their activity comparable to that of the molybdenum-based catalyst **11**.[54]

(iii) Other ruthenium catalysts

The interest in applying metathesis reactions to biological substrates created a need for catalysts that are soluble and active in aqueous media. The water-soluble complexes **18** and **19**, reported by Grubbs and coworkers,[55] have been shown to catalyse both ROMP[56] and RCM[57] in protic solvents such as water and methanol.

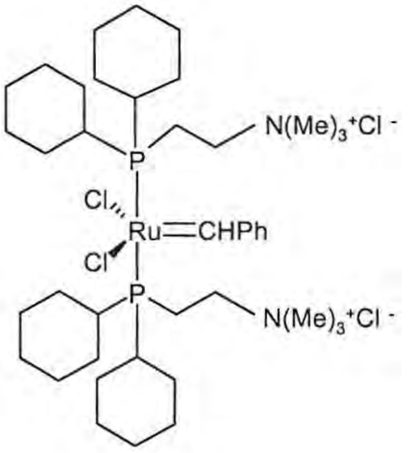

18

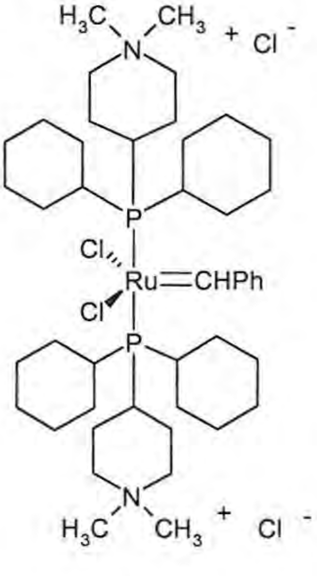

19

In the course of studying the metathesis of styrenyl ethers to form chromenes, Hoveyda and co-workers proposed the *in-situ* formation of the Ru-chelate complex **20**.[58] Further investigation revealed that not only is complex **20** an air-stable, active metathesis catalyst, but is also able to be recycled in high yield by silica gel chromatography. Hoveyda's group has since published several variations of complex **20**, including an enantioselective version with a bidentate chiral imidazolinylidene moiety replacing one chloride ion and the phosphine moiety.[59]

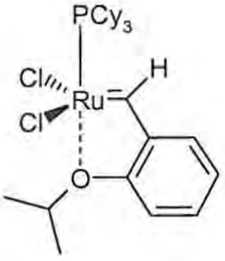

20

Several researchers have focused on the immobilization of ruthenium catalysts on solid supports. This is a particularly attractive option for industry as it allows for catalyst separation and recycling, which has both economic and environmental benefits. There have been several reports of the immobilization of complex **14** on functionalised polystyrene resins, both *via* phosphine[60] and anionic ligands.[61] However, the most successful immobilization strategies have used the carbene as the anchor group. Barrett and co-workers coined the term 'boomerang catalyst' to describe their immobilized precatalyst **21** (Scheme 20)[62] which is cleaved from the resin during the first catalytic cycle, and recaptured once the substrate has been consumed.

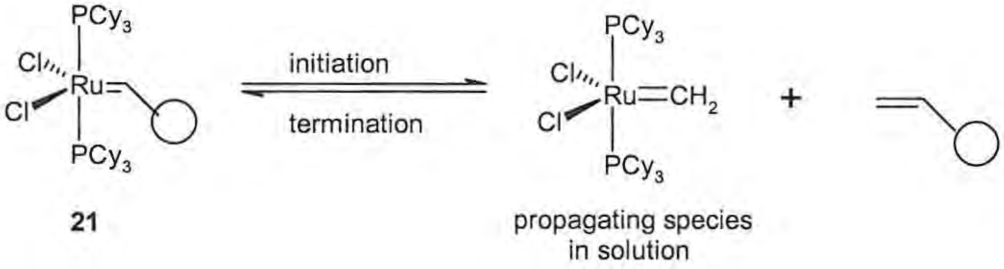

Scheme 20

This strategy has also been successfully applied in the synthesis of polystyrene-supported analogues of the Hoveyda catalyst **20**.[63] In a recent study the useful functionalities of complexes **17** and **20** have been combined on a poly(ethylene glycol) support, to produce the highly reactive and recyclable species **22**.[64]

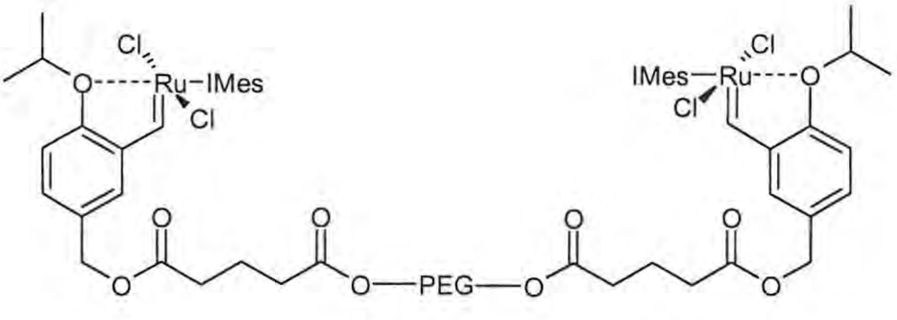

22

IMes = unsaturated NHC (as in **17**)

PEG = poly(ethylene glycol)

The 18-electron complex **23**, although itself exhibiting only moderate metathesis activity, has proven to be a most convenient starting point for the development of several new, highly active catalysts. Reaction of complex **23** with propargyl alcohols in the presence of a chloride trap affords cationic ruthenium allenylidene complexes, such as **24**, which are widely applicable metathesis catalysts.[19] A recent report by Dixneuf and co-workers[65] outlines the intramolecular rearrangement of allenylidenes such as **24**, and subsequent loss of the arene moiety to generate indenylidene ruthenium complexes such as **25**, which exhibit higher metathesis activity than their allenylidene precursors. This series of catalysts and their related analogues are proving to be an attractive alternative to the Grubbs-type carbenes due to their comparative ease of preparation.

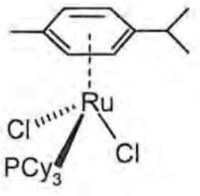

23

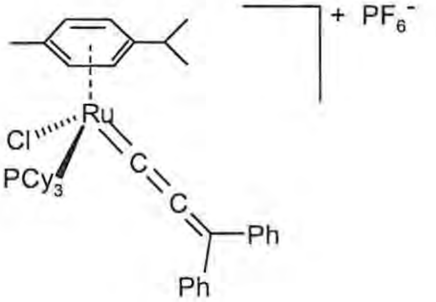

24

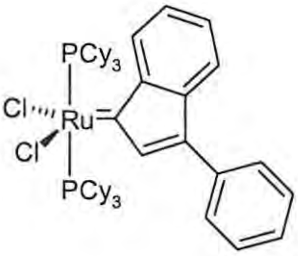

25

Yet another variation on the Grubbs theme is the incorporation of a bidentate Schiff base ligand, one arm of which de-coordinates to generate the active catalytic species. This series of complexes has been explored by Verpoort and co-workers, who have produced alkylidenes **26** and **27**,[66] and vinylidene **28**.[67] The Schiff base ligands, while not improving catalyst activity, do serve to enhance the thermal stability of the complexes. This makes them ideal for inclusion in a mixed-ligand system, together with a rate-enhancing complementary group (e.g. the NHC in **27**).

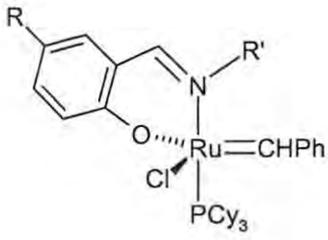

26

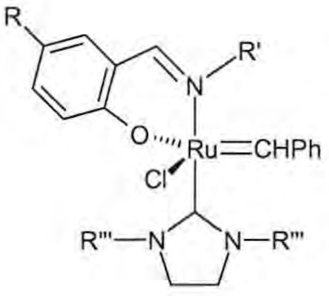

27

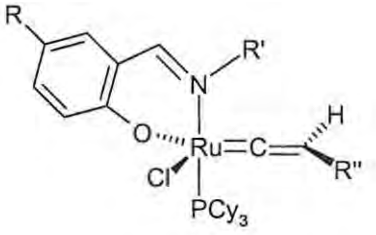

28

R = H, NO_2
R' = substituted aliphatic/aromatic group
R'' = Ph, $SiMe_3$, *t*-Bu
R''' = 2,4,6-trimethylphenyl

1.3.3 Mechanistic studies of metathesis reactions

The Chauvin mechanism (Figure 2, p.4) outlines the general mechanistic features of the metathesis reaction. It involves olefin coordination to the metal carbene complex to form a π-complex, migratory insertion of the olefin into the metal-carbene bond to form a metallacyclobutane, breaking of two bonds in the metallacyclobutane to form another π-complex, and dissociation to form the products.[68] Although there is consensus on this general outline, several more detailed aspects of the mechanism remain subject to debate, and may vary depending on catalyst/substrate combinations. Two basic pathways have been proposed for catalysis by ruthenium carbenes. These are illustrated below for the metathesis of ethene by a generic Grubbs-type carbene.

The associative mechanism (Scheme 21) involves bonding of the olefin to form a hexacoordinate, 18-electron complex **29**.

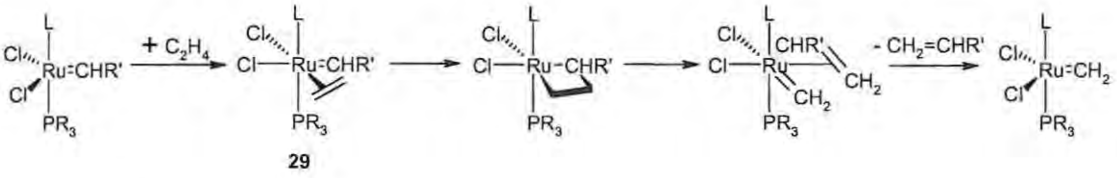

Scheme 21

The dissociative mechanism (Scheme 22) begins with the dissociation of one phosphine ligand to form a highly reactive tetracoordinate 14-electron complex **30**. Addition of the olefin substrate may then occur cis or trans to ligand L, with formation of the metallacycle either in, or at right angles to, the metal-halide plane.[68]

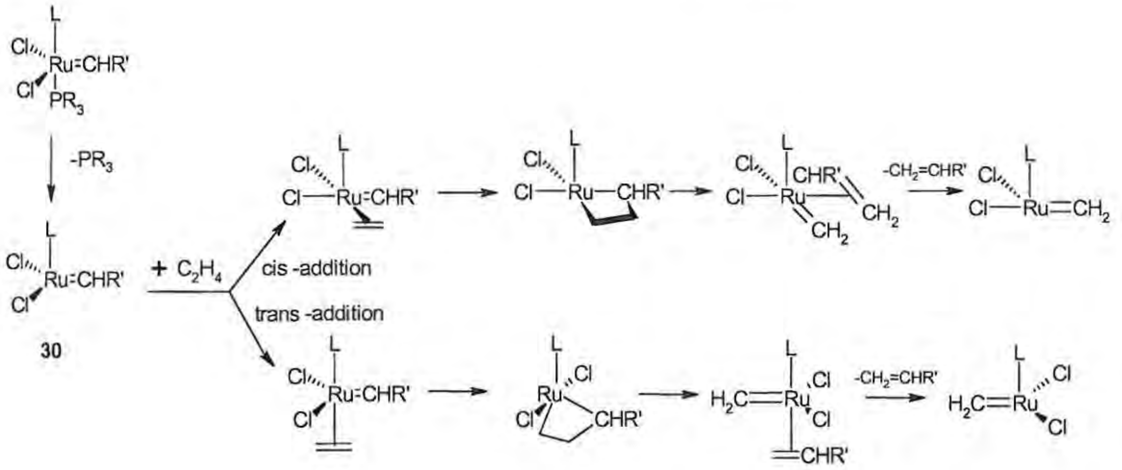

Scheme 22

Debate also exists about whether the metallacycle species is a true intermediate, or a transition state. Clarification of these and other mechanistic issues may help to provide valuable insights into the activity and selectivity of these catalysts, permitting the rational design of new, improved analogues.

1.3.3.1 Experimental studies

As the library of metathesis-active ruthenium complexes began to grow, researchers turned their attention to the mechanism of the reaction in an attempt to explain and/or predict the effect of ligand variations on catalyst activity. Grubbs and co-workers reported several kinetic studies,[45,46] in which several important observations were made. They noted that the greater activity of the alkylidene complex **14**, compared to that of the corresponding vinylalkylidene **13**, fitted a general trend, which suggested an inverse relationship between catalyst activity, and the degree of conjugation of the carbene moiety. This was attributed to a lowering of the ground state energy of the starting species with respect to the metallacycle intermediate, thus retarding the catalyst initiation rate.[45] It was further noted that catalytic activity was promoted by larger and more electron-donating phosphines, on one hand, but by smaller and more electron-withdrawing halogens on the other. This unusual observation prompted a more thorough kinetic investigation, in which an empirical rate equation was formulated for a model RCM reaction. The results of this study provided the first experimental evidence that the dissociative pathway (Scheme 22) is the dominant one.[46] This theory was supported by the subsequent isolation of a monophosphine intermediate in an ROM reaction.[69]

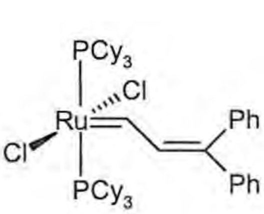

13

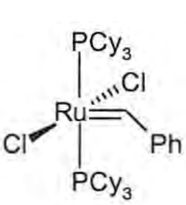

14

Some useful contributions to the understanding of olefin metathesis mechanisms have been made by Chen and co-workers, who have used electron-ionization mass spectrometry (EI-MS) to identify and assay catalytically active species.[70] Perhaps their most important observation to date is the close parallel between metathesis reactions in the gas phase and in solution,[71] which is an important factor when applying computational techniques to such mechanistic studies. The EI-MS technique has also highlighted the role of phosphine dissociation in the metathesis reaction. While a kinetic study using EI-MS data in conjunction with linear free energy analysis suggested that the metallacycle structure is a transition state rather than an intermediate, quantum mechanical calculations by the same group failed to corroborate this theory.[72]

Arguably the most comprehensive mechanistic study was carried out by Grubbs and co-workers shortly after the introduction of the second-generation carbenes.[73,74] The group used phosphine exchange and initiation kinetics to study the effect of ligand variations on the mechanism and activity of metathesis reactions. ^{31}P-NMR magnetization transfer experiments were used to monitor the degenerate exchange of free and bound phosphines (Scheme 23) that, it was argued, can be considered a model system for phosphine-olefin substitution.

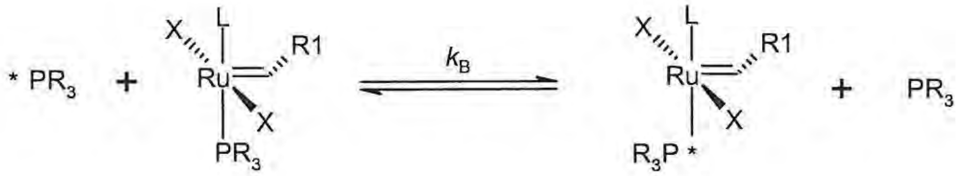

Scheme 23

A parallel study using ^{1}H NMR and UV-Vis spectroscopy was undertaken to plot the initiation kinetics of a model metathesis reaction, by monitoring the disappearance of the initiating catalytic species.[74] On the basis of the results obtained for a range of first- and second-generation ruthenium carbenes, some important observations were made. Firstly, there was no evidence to suggest that an associative mechanism (Scheme 21) contributed significantly to reactions involving any of the catalysts studied. Secondly, and somewhat surprisingly, it was reported that second-generation NHC catalysts do not undergo phosphine dissociation more readily than first-generation catalysts and, hence, more effective labilisation of the leaving phosphine could not be the reason for their higher metathesis activity. Once in the monophosphine state, however, it seems that the NHC complexes show a stronger tendency to bind the olefin substrate than to rebind the phosphine species, thus performing multiple metathesis events before returning to the resting state. It is this selectivity for binding olefinic substrates that appears to be responsible for their higher activity. The effects of the ancillary ligands were also investigated, the results agreeing largely with those obtained in previous studies.

1.3.3.2 Computational studies

Theoretical studies of olefin metathesis have begun to cast some light on mechanistic aspects that are difficult to resolve experimentally, notably the characterization and conformational analysis of transition states and intermediates. The first full computational paper dealing with this topic involved a Car-Parinello quantum molecular dynamics study of the behaviour of the model complex $[(PH_3)_2Cl_2Ru{=}CH_2]$ **31** and its reaction with ethene at various temperatures.[75] Ambient temperature dynamics of complex **31** showed a rotation of the carbene around the $Ru{=}CH_2$ bond, while high temperature dynamics showed dissociation of one phosphine ligand, and cis-trans isomerisation of the Cl ligands. Ethene insertion to form a metallacycle was demonstrated for the monophosphine species and, under forcing conditions, also for the biphosphine parent species **31**.[76] These theoretical findings all serve to corroborate the mechanistic evidence presented by Grubbs in earlier papers,[45,46] particularly the negligible contribution of the associative pathway to the overall mechanism, and the feasibility of carbene rotation and halide isomerisation (to facilitate the two proposed orientations of the metallacycle in Scheme 22).

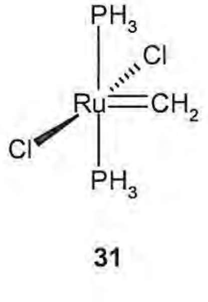

31

Recently, several groups have published results of DFT studies on metathesis reactions catalysed by model ruthenium carbenes such as **31**. Bottoni and co-workers suggested the existence of three pathways for the reaction.[77] The first is similar to the standard dissociative pathway (Scheme 22), but involves recoordination of the expelled phosphine ligand after olefin coordination, leading to a bis-phosphine metallacycle intermediate **32**. The second involves the migration of a chlorine atom from the metal to the methylidene carbon after olefin insertion (trans to the carbene moiety), forming a carbenoid-type intermediate **33**. The third and least energetically viable pathway involves both carbenic and carbenoid species.

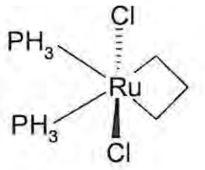

32

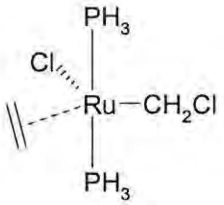

33

Fomine and co-workers concluded that a dissociative mechanism was preferred, while illustrating the importance of considering entropy contributions to reaction energetics.[78] Thiel and co-workers favoured a dissociative mechanism, with coordination of the olefin trans to the remaining phosphine. Their study emphasized the electronic effects of the ligands, concluding that the most effective catalysts should contain one weak and one strong σ-donating ancillary ligand to promote dissociation and insertion respectively.[68] Cavallo[79] reported a satisfactory correlation between DFT-calculated ligand binding energies and Grubbs' experimental activation energies for phosphine exchange (Scheme 23).[74] Comparison of ligand binding energies also cast some light on the role of the bulky mesityl groups in the NHC systems. Cavallo proposed that the influence of these groups is predominantly steric in nature. Their steric bulk destabilizes the phosphine- and olefin-free intermediates, which does not promote phosphine dissociation, but does promote olefin coordination and stabilizes the metallacycle intermediate, thus accelerating overall activity.

Recent quantum mechanical/molecular mechanical (QM/MM) studies by Chen and Adlhart[80] involved explicit treatment of the large phosphine ligands that are typically approximated by PH_3 or PMe_3 in other DFT studies. They propose that if the non-leaving phosphine displays threefold symmetry (as is typically the case), the rate-determining step is ligand rotation at the metallacycle structure. With ligands displaying twofold symmetry (e.g. the NHC's), no such rotation is necessary, thus lowering the overall potential barrier (figure 7).

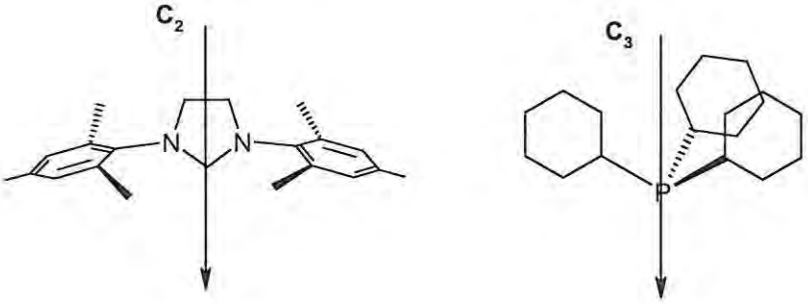

Figure 7. Ligands displaying twofold and threefold symmetry.[80]

A recent, exhaustive study by Chen and Adlhart[81] concluded that the trans dissociative pathway (Scheme 22) is the most favourable for both first- and second-generation systems, on the basis of the translational entropy gain in the phosphine dissociation step. They also note that the reaction energetics are profoundly substrate-dependant. Thermoneutral reactions (as in the case of the degenerate metathesis of ethylene) are highly reversible, whereas for the exergonic reactions with ethyl vinyl ether and norbornene, release of excess energy occurs after metallacycle formation, rendering the reaction irreversible. Rate-limiting steps are identified as metallacycle formation for first-generation systems, and phosphine dissociation for second-generation systems. In contrast to the findings of Cavallo,[79] the greater activity of the second-generation catalysts is ascribed to electronic rather than steric effects.

1.4 PREVIOUS WORK IN THE GROUP AND AIMS OF THE PRESENT INVESTIGATION

In past years, members of the group have studied, designed and synthesised numerous ligands for the selective chelation of various metals. These projects have almost always employed computational techniques to some extent, whether in a design capacity, or simply as a visualisation tool.

The earliest example of such work in the group arose from a study of the biocatalytic effect of mushroom polyphenol oxidases in the synthesis of *o*-quinones. Computer modelling was employed to explore the potential of novel copper complexes to act as biomimetic models of the active site of the tyrosinase enzyme.[82] This work yielded several novel diamido, diamino and diimino ligands that were succesfully complexed to copper, cobalt, nickel and platinum.[83]

The group has also worked on the development of metal-selective ligands for use in the mining industry. A range of bidentate, tridentate and tetradentate sulfur-containing amide ligands were designed to selectively chelate platinum and palladium in the presence of base metals.[84] For these multidentate systems, computer modelling and ^{1}H NMR chemical shift data were used to explore the comformational preferences and resultant chelating potential. Silver(I)-specific malonamide ligands were designed using the same computational approach, and were prepared using conventional thermal, as well as microwave-assisted techniques. In solvent extraction studies, one such ligand displayed silver(I) selectivity in excess of 96%.[85]

A further area of interest has been the development of metal-selective molecularly-imprinted polymers (MIP's). Novel bidentate, nickel-selective ligands were designed that contained amine and pyridyl nitrogen donors and allyl groups for co-polymerisation to form the MIP's. These MIP's were shown, using IPC-MS analysis, to exhibit high selectivity for nickel over iron.[86, 87]

With this background in ligand design and synthesis, and with an interest in expanding the scope and utility of the computational tools available to us, the present investigation has focussed on:-

i) establishing reliable and readily accessible computational methods for the analysis of ruthenium-based metathesis catalysts, and benchmarking these methods against existing computational techniques and available experimental data;

ii) applying these techniques to the design of novel multidentate ligands for ruthenium-based metathesis catalysts;

iii) exploring the synthesis of target ligands, with an emphasis on the use of computational methods in facilitating the structural characterisation of synthetic intermediates, and elucidating the mechanistic details of complex rearrangements occurring in the syntheses;

iv) employing computational techniques to probe ligand electronic and steric effects in various ruthenium complexes; and

v) undertaking detailed kinetic and computational studies of the self-metathesis of 1-octene with the 1st-generation Grubbs catalyst **14**.

2. DISCUSSION

Throughout this project we have attempted to combine computational and experimental techniques, employing computational methods both as a design tool and as an aid in structural and mechanistic elucidation. The discussion will begin by outlining the benchmarking process by means of which we developed the standard computational techniques employed in the main body of the work. This is followed by two sections detailing our efforts at designing novel camphor- and malonate-derived multidentate ligands for the construction of novel Grubbs- and Hoveyda-type catalysts. Finally, we investigate some kinetic aspects of the self-metathesis of linear alkenes - a branch of metathesis chemistry that has been largely ignored in the academic literature.

2.1 BENCHMARKING OF COMPUTATIONAL TECHNIQUES

Preliminary modelling studies were carried out using three computational techniques, employing three different software packages. Molecular mechanics (MM) calculations were performed using Cerius$^{2®}$ (Version 4.0, Molecular Simulations Inc), semi-empirical calculations using PC Spartan Pro (Wavefunction Inc),[88] and density functional calculations using the DMol^3 density functional theory (DFT) code[89] as implemented in the MaterialsStudio (version 2.2) package from Accelrys Inc. (for further computational details, see Section 3.1.1).

2.1.1 Structural data

As a starting point, all three techniques were applied to reproduce the ground-state geometry of the Grubbs 1st-generation catalyst **14**. While the X-ray structure of complex **14** has not been reported, crystallographic data is available for the close structural analogue **34**,[90] which was used as a reference model. The X-ray data for complex **34** reveal a distorted square pyramidal coordination geometry about the metal centre, with the carbene moiety perpendicular to the P-Ru-P axis and an almost linear Cl-Ru-Cl angle.

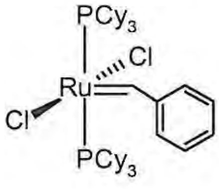

14

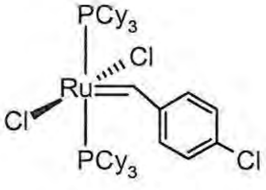

34

At the molecular mechanics level, preliminary energy minimisations were performed both on structure **14**, drawn using the programme's drawing tools, and on the crystal structure data extracted for complex **34** from the Cambridge Crystallographic Database and modified to give structure **14**. On minimisation, both models converged to the same structure. A molecular dynamics routine was performed on this structure to explore conformational space, and the global energy minimum located (Figure 8). The ten highest- and ten lowest-energy conformers generated by the molecular dynamics simulation were then imported into Spartan Pro, and semi-empirical geometry optimisations were performed on these structures, as well as a structure generated by the software's own drawing tools. All structures converged to a single, minimum-energy conformer, which was subjected to DFT calculations at the GGA/PW91/DNP level (see section 3.1.1.3) using DMol^3.

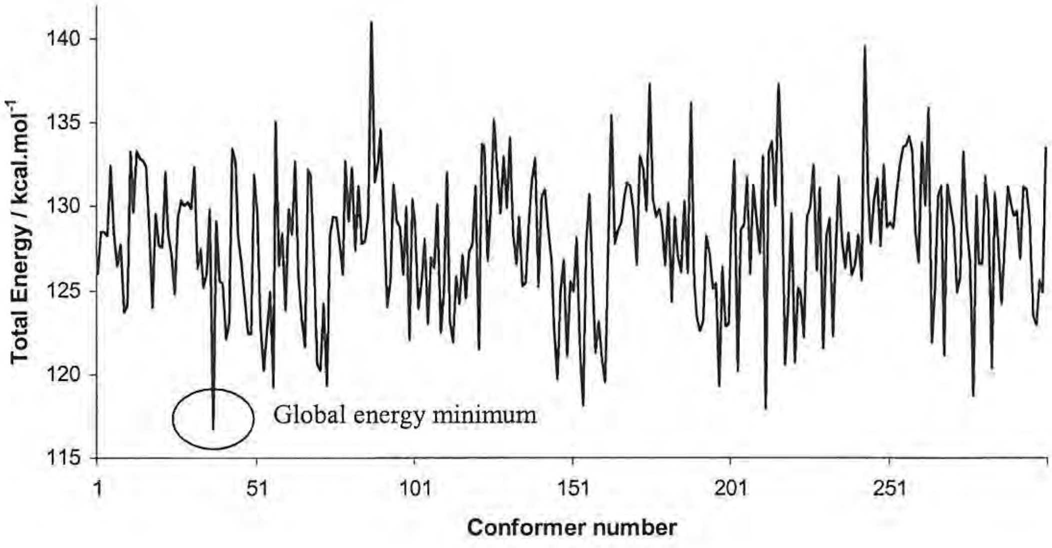

Figure 8. Conformational trajectory for the molecular dynamics simulation performed on structure **14**.

In general, all three computational methods afforded structures that correspond remarkably well with each other and with the X-ray data for the analogue **34**. The semi-empirical and DFT methods performed equally well for bond length calculations (Table 1) with mean errors (0.057 ±0.002Å) approximately half the MM value (0.118 Å). The DFT structure of complex **14** correlates most closely with previously computed bond angles[79] and the X-ray geometry[90] of the structural analogue **34**. The mean absolute errors for calculated bond angles were 6.5, 4.7 and 3.7 degrees for the MM, semi-empirical and DFT methods respectively (Table 2).

Table 1 : Calculated bond lengths (in Å) for structure **14** and the corresponding X-ray data[90] for the structural analogue **34**.

Bond	Molecular Mechanics	Semi-Empirical	DFT	X-ray data for 34
Ru=C	2.022	1.851	1.879	1.839
Ru-Cl1	2.414	2.357	2.455	2.401
Ru-Cl2	2.412	2.357	2.453	2.395
Ru-P1	2.608	2.313	2.472	2.397
Ru-P2	2.603	2.315	2.490	2.435
Mean error*	0.118	0.059	0.056	

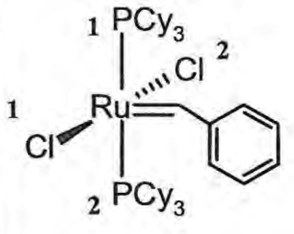

14

*Mean errors are mean absolute errors compared to crystal structure data for RuCl$_2$(=CHp-C$_6$H$_5$Cl) (PCy$_3$)$_2$ **34**.

Table 2 : Calculated bond angles (in degrees) for structure **14** and the corresponding X-ray data[90] for the structural analogue **34**.

Angle	Molecular Mechanics	Semi-Empirical	DFT	X-ray data for 34
Cl1-Ru-P1	89.9	88.0	91.2	87.2
P1-Ru-C	95.4	95.6	94.5	97.5
P1-Ru-Cl2	88.8	90.9	89.7	91.5
Cl1-Ru-P2	91.1	91.4	83.6	90.8
C-Ru-P2	90.6	97.7	103.0	101.2
Cl1-Ru-C	96.6	97.9	93.6	88.7
Cl1-Ru-Cl2	175.1	174.7	159.6	167.6
C-Ru-Cl2	88.2	87.4	106.6	103.7
P1-Ru-P2	173.8	166.7	162.0	161.1
Cl2-Ru-P2	89.7	88.4	83.6	86.5
Mean error*	6.5	4.7	3.7	

*Mean errors are mean absolute errors compared to crystal structure data for RuCl$_2$(=CHp-C$_6$H$_5$Cl) (PCy$_3$)$_2$ **34**.

In light of the abovementioned results, DFT methods were employed for the majority of the subsequent computational work. However, given that the MM approach appeared to offer a convenient and surprisingly good analysis of the overall geometry of complex **14**, its application was revisited at a later stage (see Section 2.6), for systems that proved to be prohibitively large for the application of DFT methods.

In order to assess the capacity of the DFT method to reproduce a co-ordinatively unsaturated ruthenium system, the active monophosphine derivative **35** of complex **14** (the 'precatalyst') was modelled at the DFT level (Figure 9). The observed geometry on formation of the monophosphine complex **35** is, in fact, consistent with reported computational data for several Grubbs-type catalysts,[79] as well as the X-ray data for an isolated ruthenium monophosphine complex.[90] This observation confirms the ability of the DFT method to provide credible geometries for ruthenium complexes in two of the coordination modes relevant to the metathesis catalytic cycle (*i.e.* complexes **14** and **35**).

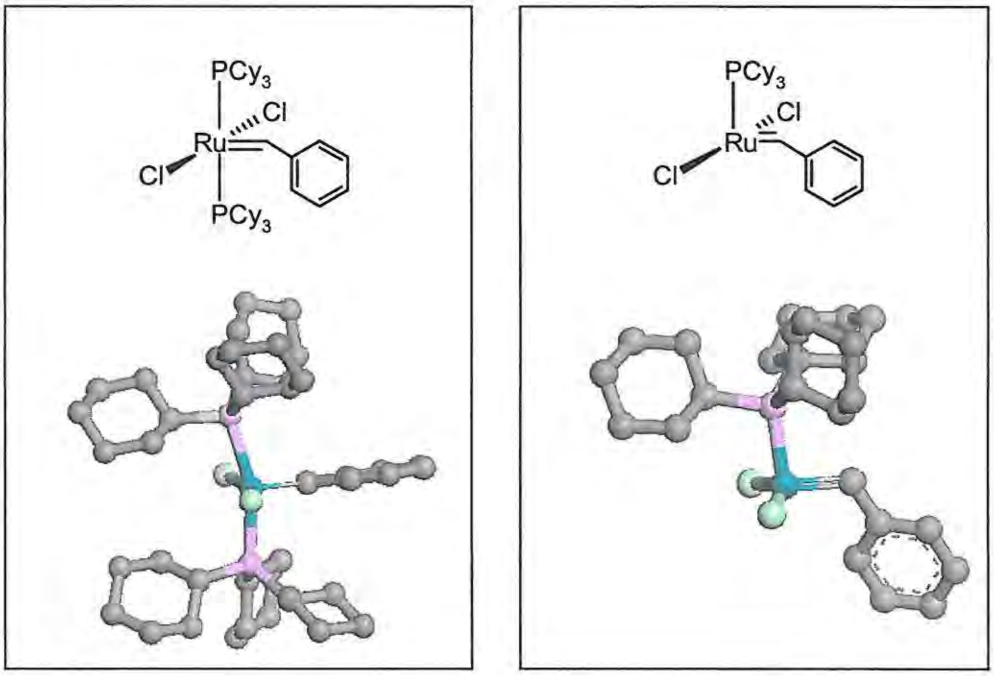

14 **35**

Figure 9. DMol^3/GGA/PW91/DNP optimised structures of precatalyst **14** and its active monophosphine derivative **35**. (H's omitted for clarity)

2.1.2 Energy data

In order to assess the validity of the energy data calculated using the DFT protocol, we performed benchmarking calculations both on full Grubbs-type catalyst systems, and on the simplified analogues typically used to represent them in more fundamental mechanistic studies. As a sample study on the full systems, the electronic ligand dissociation energies (ΔE) for the dissociation of tricyclohexylphosphine (PCy_3) from the Grubbs 1st- and 2nd-generation precatalysts **14** and **17** were calculated. The calculated value for the dissociation of precatalyst **14** (34.8 $kcal.mol^{-1}$) was found to be 79.6% of ΔE for the 2nd-generation system **17** (43.7 $kcal.mol^{-1}$). This value compares very favourably with the 80.8% calculated by Adlhart and Chen[81] and reasonably well with the 70.4% calculated by Cavallo,[79] and closely parallels the experimental trends observed by Grubbs.[73]

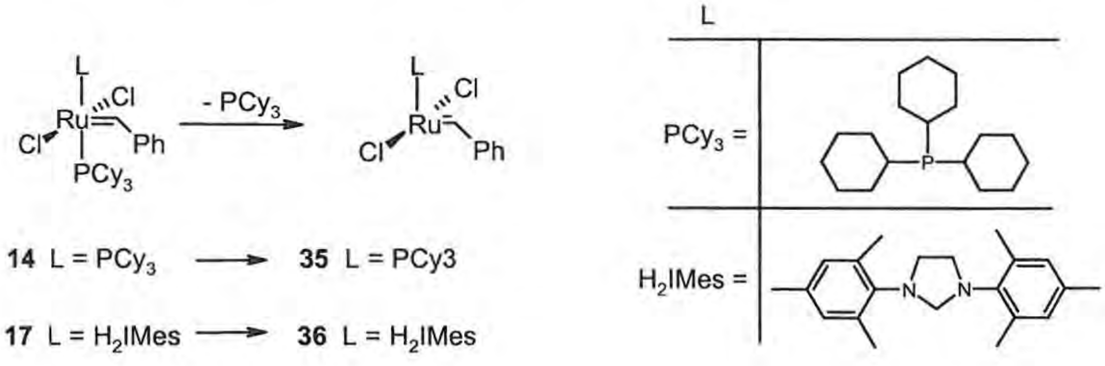

14 → **35** ΔE = 34.8 $kcal.mol^{-1}$
17 → **36** ΔE = 43.7 $kcal.mol^{-1}$

Figure 10. Calculated ligand dissociation energies (ΔE) for precatalysts **14** and **17** (mass balanced for leaving group L).

For detailed mechanistic studies, calculations involving the full catalyst systems are rendered impractical by the extended computational time required. For this reason, truncated analogues, such as complex **31** (Scheme 24), and model substrates, such as ethylene, are typically used. While these smaller systems allow for calculation at higher levels of theory and the inclusion of vibrational energy data, they do not accommodate the steric or substrate effects that may well be significant in the actual reactions.

The DFT method was applied to explore the degenerate metathesis of ethylene with the truncated Grubbs catalyst analogue **31** *via* the widely accepted[68,78,81] trans-dissociative pathway detailed in Scheme 24. The calculated Gibbs free energy (ΔG_{298}) profile is illustrated in Figure 11, and the corresponding reaction energies are summarised in Table 3 (mass balanced for PH_3 and ethylene). The ground state and transition state structures were verified by vibrational analysis, and transition state structures linked to the relevant intermediates by mapping the respective intrinsic reaction paths (for further computational details, see Section 3.1.1.3).

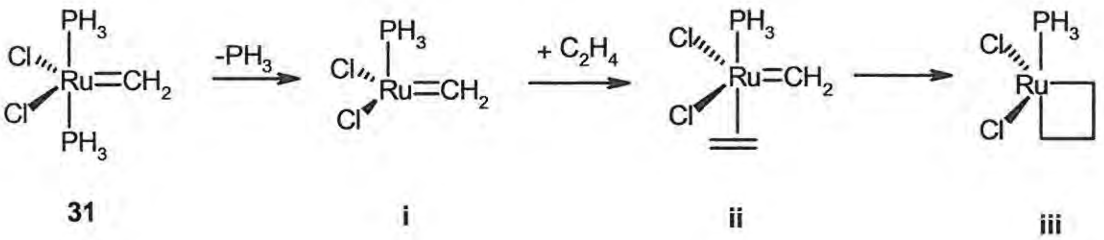

Scheme 24

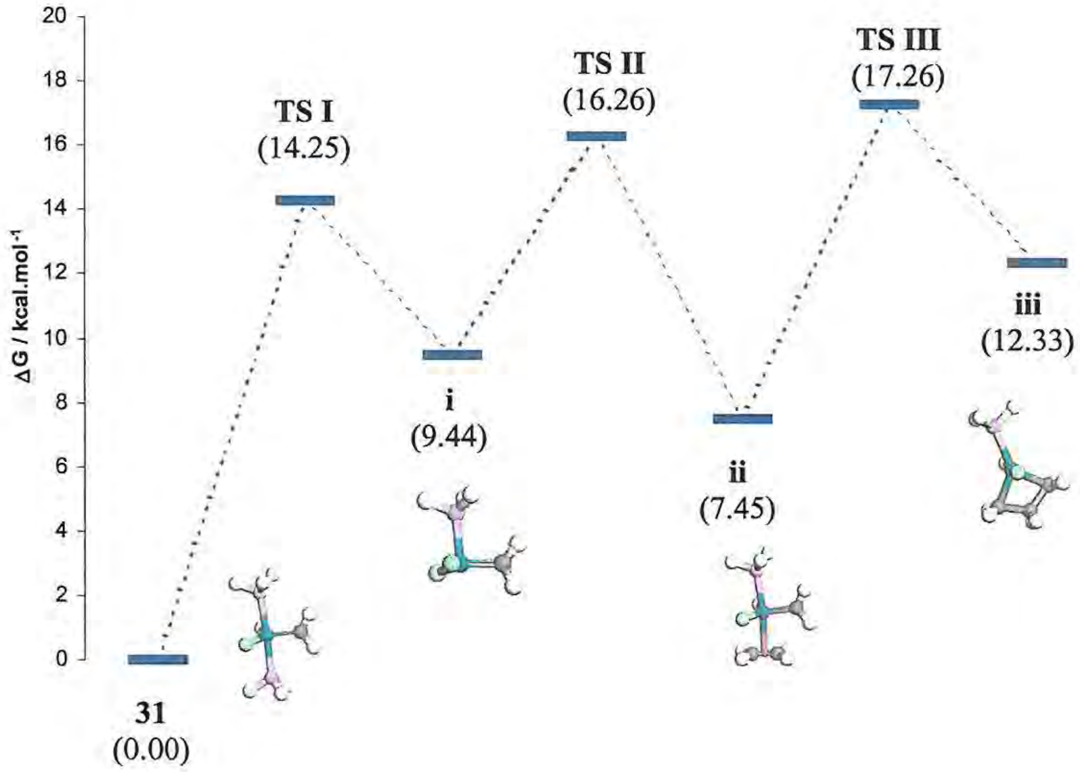

Figure 11. DMol^3/GGA/PW91/DNP ΔG_{298} profile for the degenerate metathesis of ethylene with the model catalyst **31**.

It must be emphasised that it is the free energies (G), obtained by thermodynamic corrections to the electronic energies (E), which are of interest in fundamental studies of this type since enthalpic and entropic effects are not reflected by E values. This discrepancy is particularly evident in steps involving a change in molecularity (e.g. **31**→**i** and **i**→**ii**; Table 3) where entropic affects render E values meaningless.

Table 3. DMol^3/GGA/PW91/DNP reaction energies for the degenerate metathesis of ethylene with the model catalyst **31** (Scheme 24, Figure 11).

Reaction	ΔE (kcal/mol)	E_a (kcal/mol)	ΔG_{298} (kcal/mol)	$\Delta G^{\ddagger}_{298}$ (kcal/mol)
31→i	22.07	19.96	9.44	14.25
i→ii	-14.81	-2.71	-1.99	6.28
ii→iii	3.31	10.39	4.88	9.81

The geometries of the calculated transition state complexes **I-III** are depicted in Figure 12. The geometry of the ruthenium complex in the late transition state **I**, corresponds closely to that of the intermediate **i**, the distance between the metal centre and the departing phosphine (5.597Å) being greater than twice the Ru-P bond length in the precursor **31**. The relative orientation of the interacting species in the transition state **II** is clearly supported by the vibrational analysis; there is little perturbation in the geometry of the ruthenium complex (compared to the intermediate **i**) and the distance (4.507Å) between the proximal ethylene carbon and the metal centre is consistent with formation of an early transition state complex.

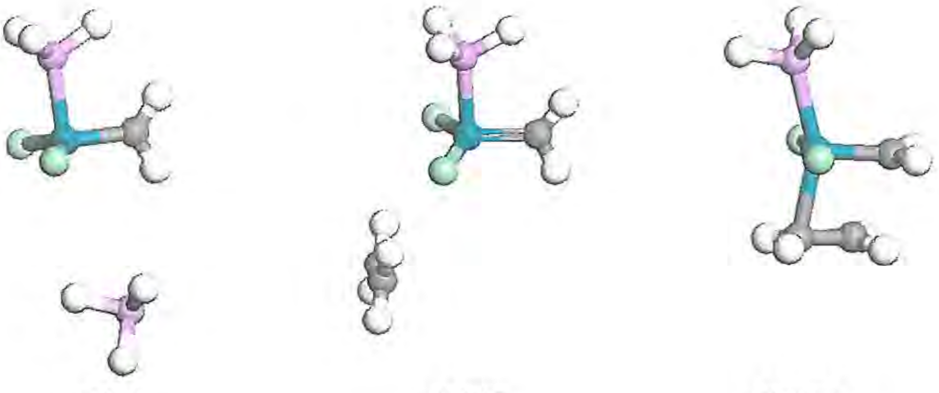

Figure 12. Geometry-optimised structures of the transition states **I-III** depicted in Figure 11 (Table 3).

Transformation of the π-complex **ii** to the metallacycle **iii**, however, proceeds *via* a late transition state **III**, in which:- the ethylene moiety is linked as a σ-complex to the metal centre; the Cl-Ru-Cl bond angles approaches 180°; the carbene methylene group is rotated through 90°; and there is evidence of a developing σ-bond between the eclipsed, methylene termini of the acyclic precursor (C-C distance = 2.333Å).

Table 4. Reaction energies for the degenerate metathesis of ethylene with the model catalyst **31**, as calculated by Chen and Adlhart[81] and by Cavallo[79] (in parentheses).

Reaction	**ΔE (kcal/mol)**	**E_a (kcal/mol)**	**ΔG_{298} (kcal/mol)**	**$\Delta G^{\ddagger}_{298}$ (kcal/mol)**
31→i	21.5	-	8.2	-
i→ii	-14.8 (-11.5)	-	-0.2	-
ii→iii	7.6 (5.6)	14.8 (12.0)	9.1	13.7

Results of calculations performed on the same model system by Chen and Adlhart,[81] and by Cavallo[79] are tabulated above (Table 4). In both cases, the calculations were performed at the DFT/BP86 level, without correction for solvent effects. Comparison of these data with our results reveal a good general correlation, with our calculation of all three relevant transition states – reported presumably for the first time – appearing to suggest that phosphine dissociation is the rate-limiting step for this truncated system.

Furthermore, no significant differences were apparent between the geometries of the reported structures, and those obtained in this study. In the study by Cavallo,[79] these calculations were repeated with the inclusion of solvent effects, which proved to have a negligible effect on the reaction profile. On the basis of this comparative study, the computational approach outlined above was deemed to be sufficiently reliable for the proposed ligand-design purposes.

2.2 TRIDENTATE CAMPHOR-DERIVED SYSTEM

Ongoing work in the group on the use of camphor derivatives in asymmetric synthesis prompted us to explore the use of camphor-derived systems as ligand precursors for metathesis catalysts. Naturally occurring (+)-camphor **37** is a widely used chiral starting material for natural product synthesis.[91] Its conformationally rigid backbone and its potential to undergo regiospecific functionalization at various positions renders it an ideal building block for multidentate ligand systems.

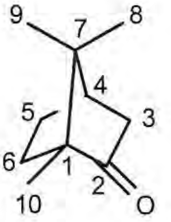

37

2.2.1 Design Rationale

Initially, we chose to work from the basic conformational framework of the Grubbs 1st-generation system, using complex **14** as a model catalyst system. The design rationale was to retain the carbene and at least one of the phosphine moieties, but to replace the two chloride ligands, and possibly one phosphine ligand, with a bi- or tridentate chelating system. The reasons for this approach were threefold. Firstly, there has been some evidence to suggest formation of chloride-bridged dimers as a decomposition pathway for Grubbs-type complexes;[92] removal of the chloride ligands effectively eliminates this pathway. Secondly, chelation could serve to stabilise the complex thus increasing catalyst lifetime and, thirdly, an appropriate chelating ligand could provide a suitable anchor point for immobilising the catalyst onto a solid support. Relatively few attempts have been reported at replacing the halide ligands in Grubbs-type systems, notable examples being the dimeric Ruthenium carboxylates of Mol and coworkers,[93] and Grubbs' four-coordinate *tert*-butoxy catalyst.[94] Preliminary modelling studies of several hypothetical camphor-derived ligand systems led us to structure **38** as a promising tridentate ligand, with the potential for replacing both chloride ions and one phosphine group from the original Grubbs system **14**.

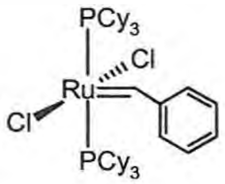

14

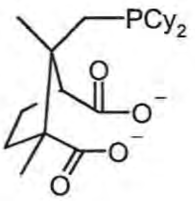

38

DFT geometry optimisation of the putative precatalyst **39** (Figure 13), which could be formed using ligand **38**, showed coordination geometry very similar to that of the 1st-generation precatalyst **14**. The calculated phosphine dissociation energy for the formation of monophosphine **40** from complex **39** (ΔE = 39.3 kcal.mol^{-1}) compares favourably with those of known catalyst systems **14** (ΔE = 34.8 kcal.mol^{-1}) and **17** (ΔE = 43.7 kcal.mol^{-1}), indicating a strong likelihood that formation of the active monophosphine **40** and, thus, metathesis initiation should take place. Retention of the square pyramidal geometry on formation of monophosphine **40**, which is consistent with the behaviour of known catalysts (see Section 2.1.1), is likely to promote substrate coordination at the vacant site.

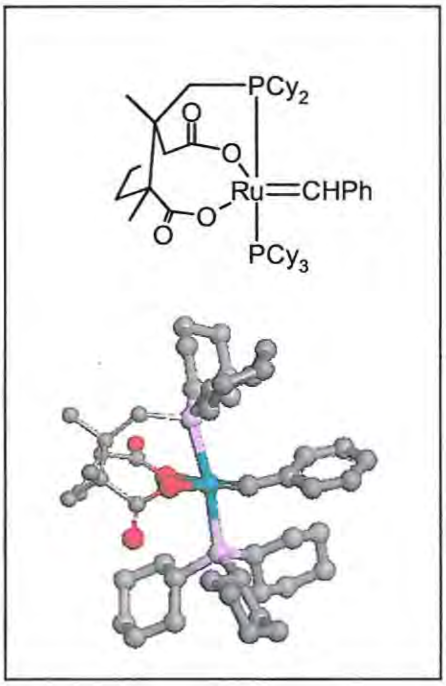

39

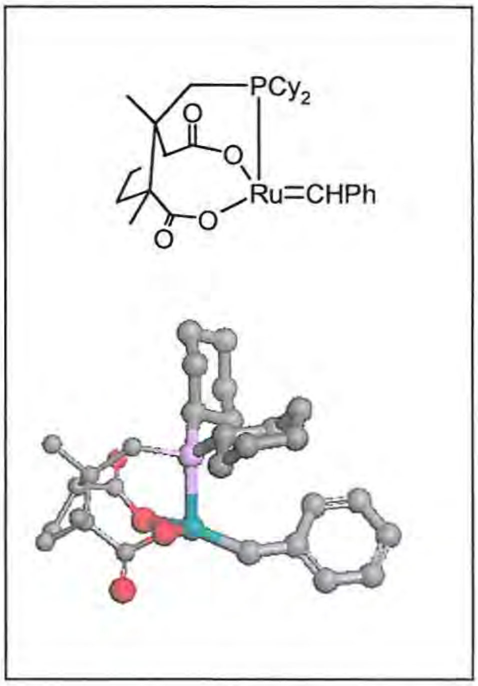

40

Figure 13. DMol^3/GGA/PW91/DNP optimised structure of the putative catalyst **39** and its active monophosphine derivative **40** (H's omitted for clarity).

In order to assess the potential metathesis activity of complex **39**, a Gibbs free energy (ΔG_{298}) profile was generated for the degenerate metathesis of ethylene with the structurally simpler model complex **41** (Scheme 25), and the results (Table 5; Figure 14) were compared to those obtained for the Grubbs analogue **31** (Table 3; Figure 11).

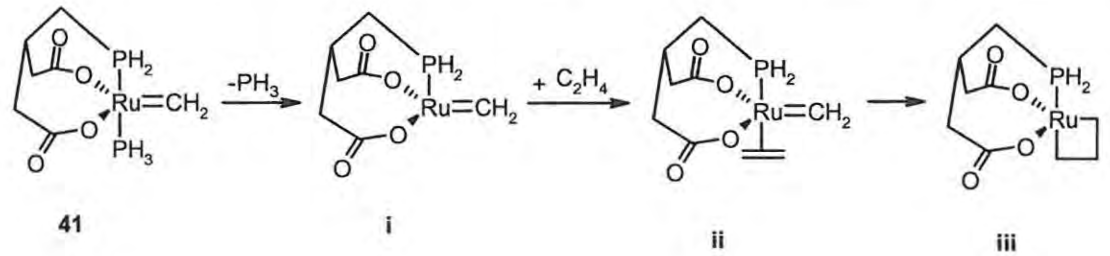

Scheme 25.

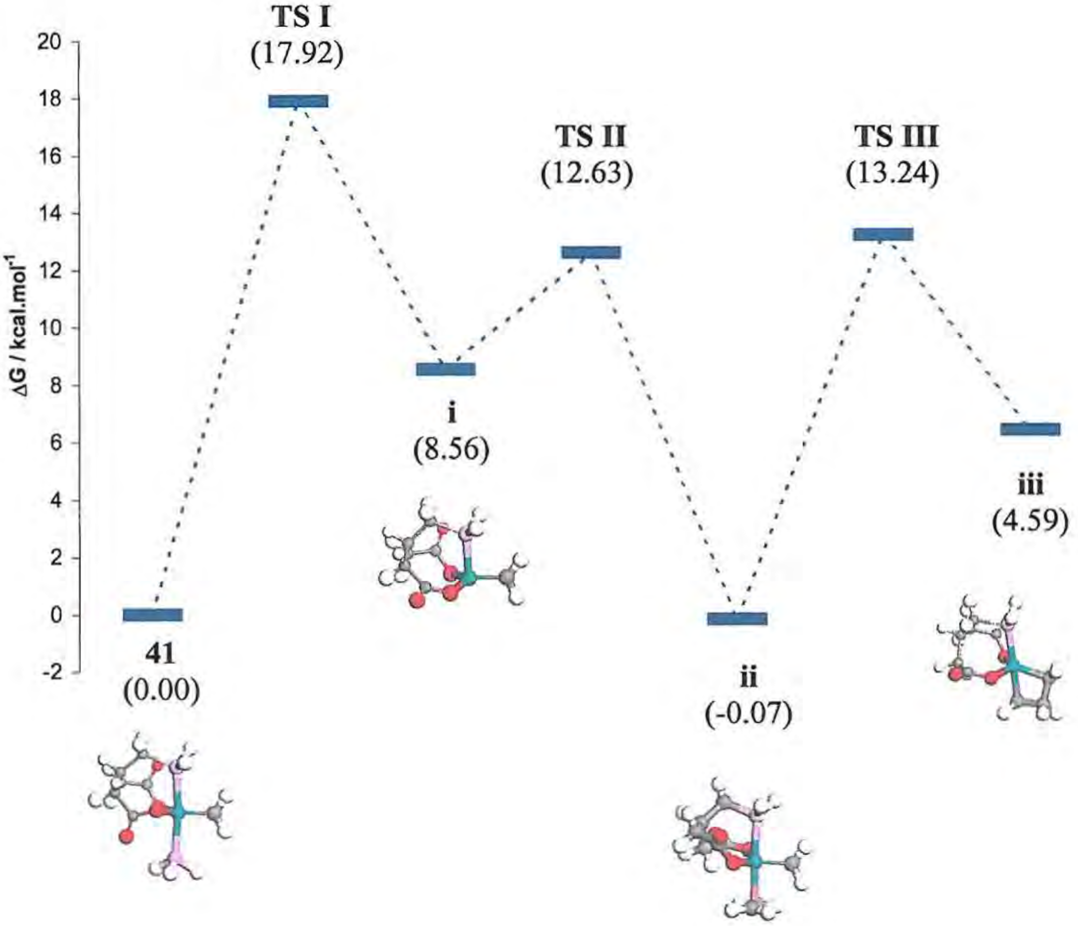

Figure 14. ΔG_{298} profile for the degenerate metathesis of ethylene with the model catalyst **41**.

Table 5. DMol^3/GGA/PW91/DNP reaction energies for the degenerate metathesis of ethylene with the model catalyst **41**.

Reaction	ΔE (kcal/mol)	E_a (kcal/mol)	ΔG_{298} (kcal/mol)	$\Delta G^{\ddagger}_{298}$ (kcal/mol)
41→i	22.41	21.62	8.56	17.92
i→ii	-23.06	-5.88	-8.72	4.07
ii→iii	7.39	13.39	6.61	13.40

A comparison of Figures 11 and 14 reveal some interesting differences between pathways involving model catalysts **31** and **41**.

i) Phosphine dissociation (**41→i**) in the camphor-derived system has a slightly higher activation energy than in the Grubbs-type system. This can be explained by the greater electron-withdrawing ability of the carboxylate moieties in species **41** than that of the chloride ligands in species **31**, resulting in stronger binding of the phosphine leaving group.

ii) Substrate coordination (**i→ii**) is considerably more favourable in the camphor-derived system, both kinetically (smaller $\Delta G^{\ddagger}$) and thermodynamically (more negative ΔG), due to the greater electron-deficiency of the monophosphine intermediate **i** (see note i above).

iii) The activation energy for metallacycle formation is higher for the camphor-derived species **41** than for the Grubbs-type system **31**. If Chen and Adlhart's proposal of phosphine ligand rotation during metallacycle formation[80] is accepted (see Section 1.3.3.2), then the higher activation energy may reflect the consequence of employing a rotationally hindered tridentate system.

Because energy profiles for real systems are highly substrate-dependent and influenced by the size, electronic properties and conformational flexibility of the bulky phosphine ligands,[81] the data derived for truncated systems, such as those shown above, should be interpreted with some degree of caution. However, we feel that the data obtained are sufficient to provide a qualitative idea of the likely metathesis activity of the putative catalyst **39**, which would appear to compare favourably with existing systems. On the basis of this computational evidence, the synthesis of the ligand **38** and the ruthenium complex **39** was considered to be justified.

2.2.2 Synthesis and mechanistic aspects

The intention was to approach the diacid **38** *via* selective bromination of camphor at the C-8 position, subsequent oxidation to 8-bromocamphoric acid **43** and, finally, substitution of the C-8 bromine by a dicyclohexylphosphine group (Scheme 26).

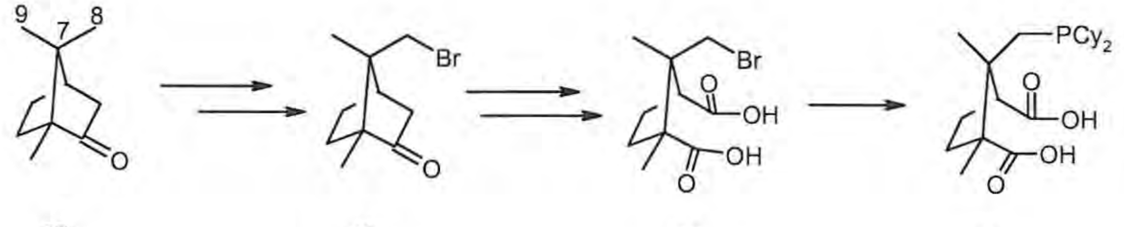

37 **42** **43** **38**

Scheme 26

2.2.2.1 C-8 functionalisation of camphor

(+)-8-Bromocamphor **42** was synthesised from commercial (+)-3-bromocamphor **44a**, following the literature procedures of Money and co-workers,[95,96] as outlined in Scheme 27. Thus, 3-*endo*-bromocamphor **44a** was brominated under solvent-free conditions to afford 3,3-dibromocamphor **44b** in 78% yield. This was followed by a two-step, one-pot procedure involving bromination of 3,3-dibromocamphor **44b** in chlorosulphonic acid to yield 3,3,8-tribromocamphor **45**, and subsequent debromination by treatment with zinc in glacial acetic acid. This afforded the final product, 8-bromocamphor **42**, in 33% overall yield from 3-bromocamphor **44a**, which is consistent with Money's optimised yield of between 30 and 40%.[97]

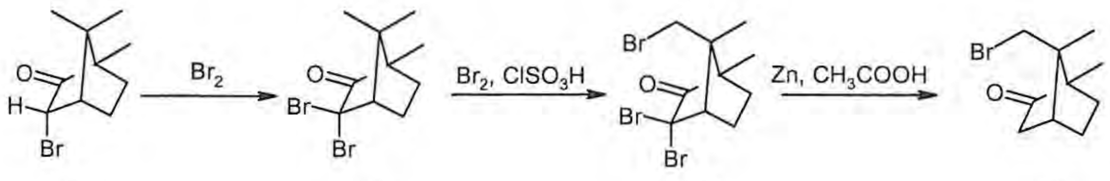

44a **44b** **45** **42**

Scheme 27

Direct bromination of camphor at C-8 was first achieved by Money and co-workers in the mid-1970's.[95] The accepted mechanism for the formation of the isomeric 9-bromocamphor **51** (Scheme 28) involves, as the key step, a 2,3-*exo*-methyl shift (**48a**→**49a**).[96] Money postulated that, in order to facilitate direct bromination of camphor at the C-8 position, it is necessary to force an energetically unfavourable 2,3-*endo*-methyl shift (**48b**→**52**) by introducing a bulky substituent X at the 7-*syn* position of the intermediate **48**. By starting with a 3-*exo*-substituted camphor species, *i.e.* 3,3-dibromocamphor **44b**, Money was indeed able to achieve the 8-bromo-product **42**. His proposed mechanism for C-8 bromination has been experimentally verified by the use of deuterium-labelled precursors and subsequent monitoring by ^{1}H NMR analysis.[98] However, while Money's method for promoting the 2,3-*endo*-methyl shift (**48b**→**52**) does, in fact, afford 8-bromocamphor **42**, his assumption that this was due to steric inhibition of the corresponding *exo*-shift by the bulky bromine substituent in intermediate **48b** (X=Br) has never been fully validated. Antkowiak and Antkowiak,[99] in response to Money's proposal, preferred to ascribe the observed *endo*-methyl shift in intermediate **48b** to anchimeric assistance by the C(7)-*syn* bromine, as illustrated in Scheme 29.

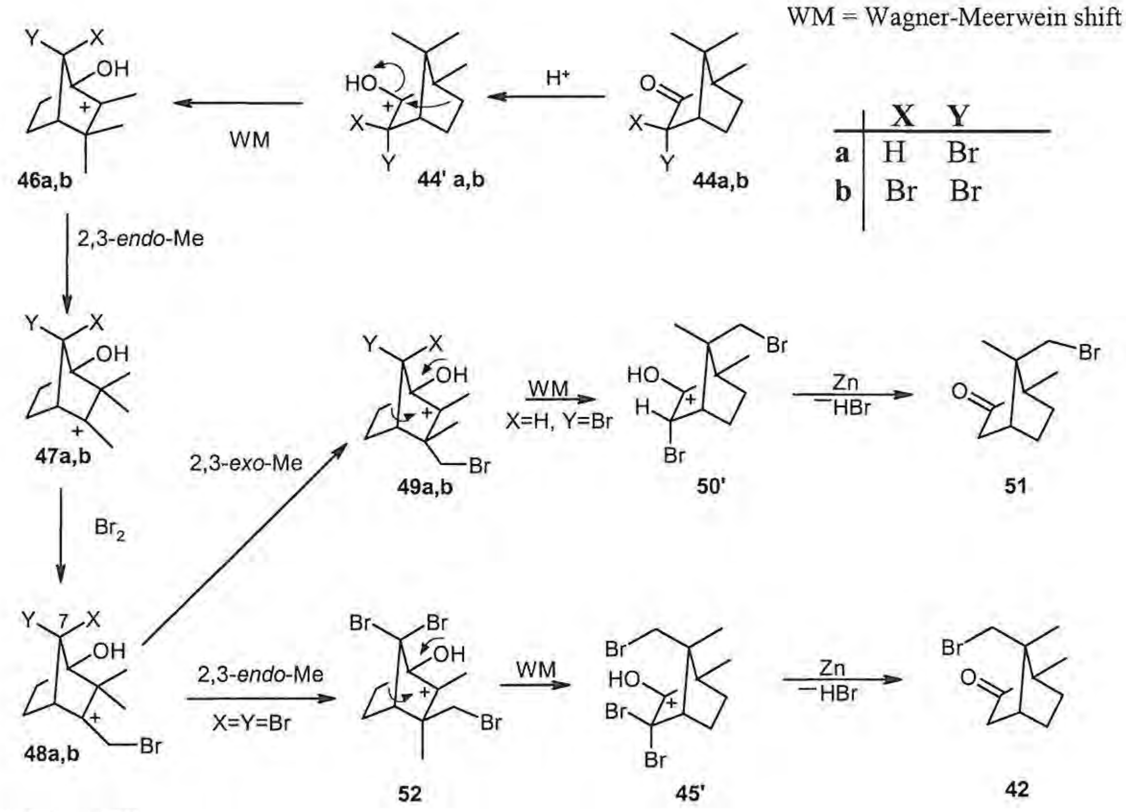

	X	Y
a	H	Br
b	Br	Br

Scheme 28

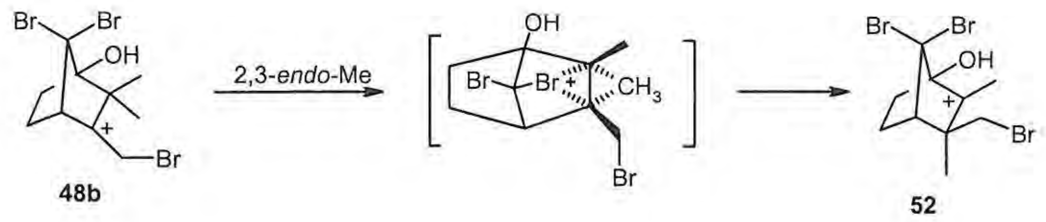

Scheme 29

Given the relatively low yield of the 8-brominated product **42** obtained in this reaction (typically 30-40%),[97] and the importance of C-8 functionalisation to our work, a modelling study was undertaken in order to clarify the mechanistic details of the transformations outlined in Scheme 28. All relevant intermediates and associated transition states in Scheme 28 were optimised at the DFT level for both C-8 and C-9 bromination, and the results are summarised in Tables 6 and 7 and in Figures 15 and 17. Since the reaction is conducted in acidic medium, the carbonyl group was treated in its protonated form.

Table 6. Reaction energies for the rearrangement **48a→50'** (X=H, Y=Br; Scheme 26) calculated at the DFT level.

Reaction	ΔE (kcal/mol)	E_a(kcal/mol)	ΔG_{298} (kcal/mol)	$\Delta G^{\ddagger}_{298}$ (kcal/mol)
48a → 50'	-19.12	2.73	-17.40	4.15

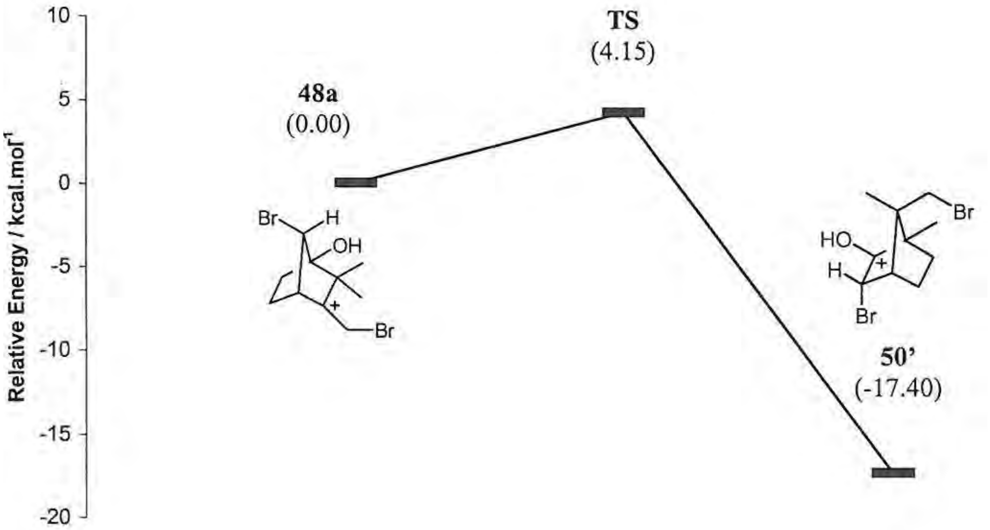

Figure 15. Free energy diagram for pathway **48a → 50'** (X=H, Y=Br; Scheme 28).

Figure 15 depicts a portion of the free energy diagram for C-9 bromination (**48a→50'**, X=H, Y=Br). The modelling data suggests that the 2,3-*exo*-methyl (**48a→49a**) and Wagner-Meerwein (**49a→50'**) shifts are concerted and involve a single transition state. This is clearly illustrated by the results of the transition state search depicted in Figure 16. The green line depicts the linear synchronous transit (LST) path from reactant **48a** to product **50'**, obtained by a series of LST maximizations along the projected reaction pathway. Each LST maximization is followed by a conjugate gradient (CG) minimization, i.e. a minimization in a direction conjugate to the reaction pathway. The orange line indicates the unique CG path terminating in a stationary point, *i.e.* the transition state, denoted by the blue asterisk. This transition state was characterised by a single negative eigenfunction corresponding to a vibration along the reaction coordinate, and confirmed by intrinsic reaction path calculations (see Section 3.1.1.3 for further computational details).

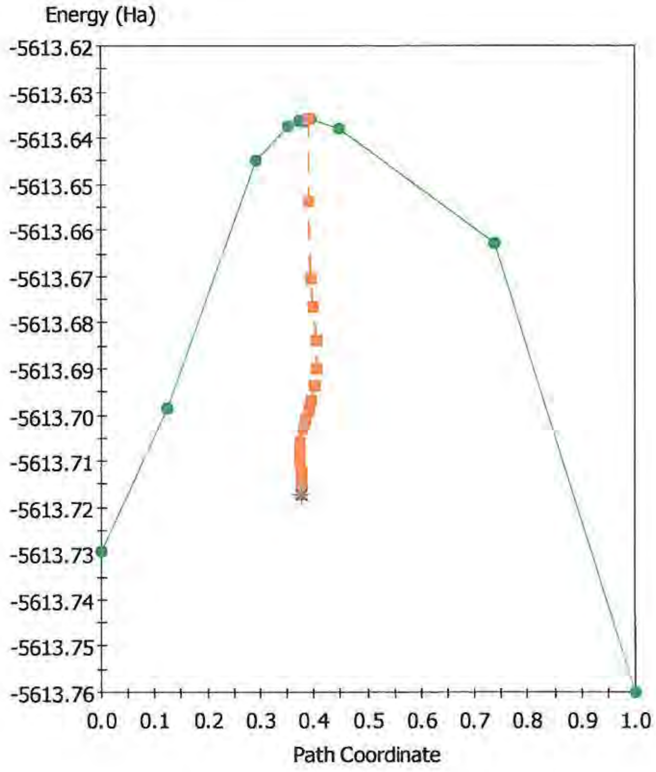

Figure 16. Transition state search results for the pathway **48a → 50'** (X=H, Y=Br; Scheme 28).

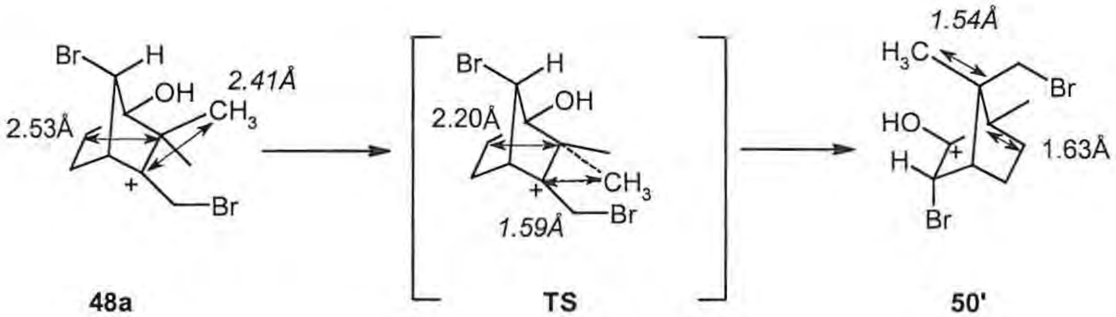

48a **TS** **50'**

Scheme 30

The geometry of the transition state between structures **48a** and **50'** is illustrated in Scheme 30, which highlights the distances (in Å) between the carbon atoms involved in the 2,3-*exo*-methyl shift (italicised) and the Wagner-Meerwein shift. The relatively low free energy of activation ($\Delta G^{\ddagger}$= 4.15 kcal.mol^{-1}) for the transformation is consistent with the dominance of this pathway over competing bromination pathways and the resulting isolation of C-9-brominated products in good yields.[97]

The formation of the C-8-brominated product **42** (*i.e.* **48b→42**; Scheme 28), however, is somewhat more complicated due to:- i) the fact that the 2,3-*endo*-methyl (**48b→52**) and Wagner-Meerwein (**52→45'**) shifts are no longer concerted; and ii) competition between two rotational isomers of the intermediate **52**. The computational data indicates the existence of these rotamers as two geometrically distinct equilibrium structures, separated by a transition state situated along the relevant rotational coordinate (Scheme 31).

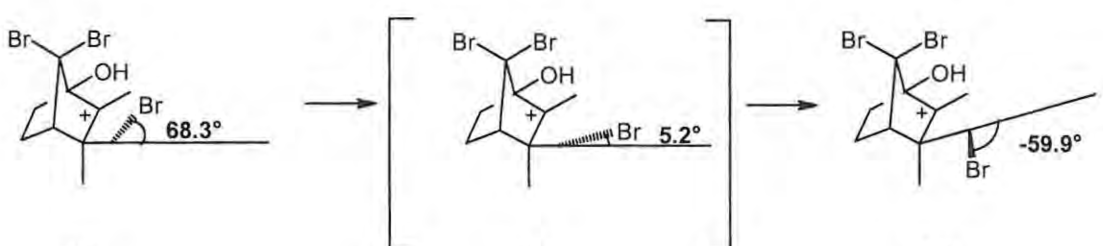

52ii **TS** **52i**

Scheme 31. Equilibrium structures and transition state for rotamers of intermediate **52** (Scheme 28). The depicted angles are dihedral angles CH_2-Br/C-CH_3.

The activation energies for the *endo*-methyl shift associated with either rotamer (Figure 17, Table 7) are significantly larger (>11 kcal.mol^{-1}) than for the *exo*-methyl shift leading to C-9 bromination (Figure 15, Table 6). This allows further bromination reactions to compete more effectively with the desired formation of the intermediate **52**, thus lowering the overall yield. An example of such competition is the addition of a second bromine to the bromomethyl group in **48b** to afford the tetrabrominated compound **60** (see Scheme 34, page 60) with a concomitant reduction in overall free energy of 3.2 kcal.mol^{-1}.

Table 7. Reaction energies for rearrangements of intermediate **48b** (X=Y=Br) depicted in Scheme 28, calculated at the DFT level.

Reaction	ΔE (kcal/mol)	E_a (kcal/mol)	ΔG_{298} (kcal/mol)	$\Delta G^{\ddagger}_{298}$ (kcal/mol)
48b → 52ii	-2.67	11.33	-3.41	11.54
52ii → 52i	0.97	4.84	-0.16	4.58
52i → 45'	-11.34	4.28	-9.26	5.43
48b → 52i	-1.70	13.93	-3.57	13.42

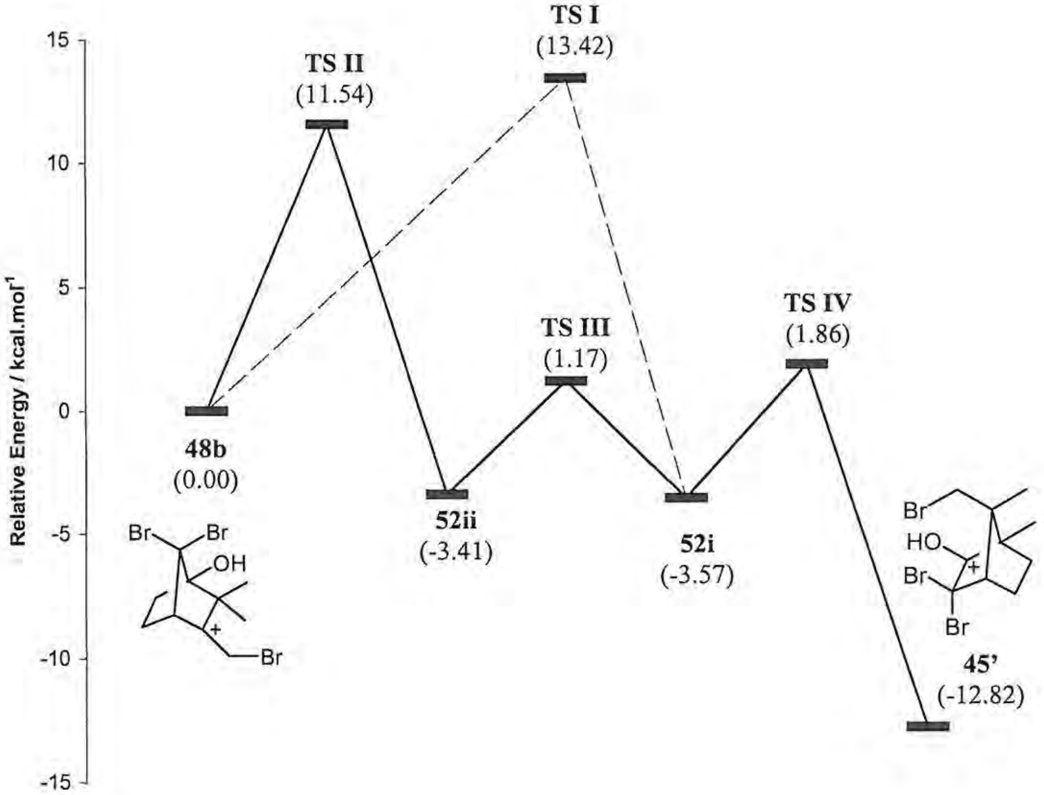

Figure 17. Free energy diagram for pathway **48b→45'** (X=Y=Br; Scheme 26).

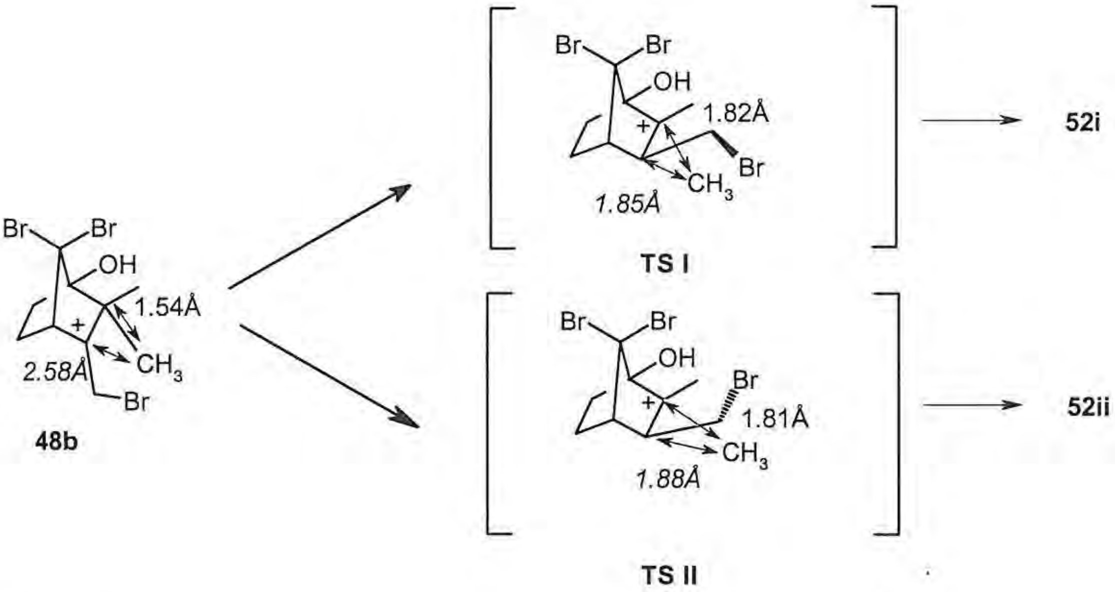

Scheme 32

The geometries of the transition states leading to both rotamers of the intermediate **52** are illustrated in Scheme 32, which highlights the lengths of the bonds being formed (italicised) and broken in the 2,3-*endo*-methyl shift. The lower activation energy calculated for the formation of rotamer **52ii** (**TS II**) is perhaps due to an electrostratic stabilising effect of the bromine moiety on the carbocation, to which it is in closer proximity than in **TS I**. Several other features of the transformation outlined in Figure 17 are worth mentioning. Firstly, no single transition state could be located that linked structures **48b** and **45'** (*i.e.* computational evidence does not support a concerted rearrangement). Moreover, only one of the rotamers of intermediate **52** could be linked directly to compound **45'**, thereby suggesting that that the pathway must necessarily proceed *via* rotamer **52i**. This pathway, which involves either two or three energy maxima, is notably more complex than that leading to bromination at position nine (Figure 15, Table 6), which may be a further factor leading to the existence of numerous competing side-reactions.

Table 8 and Figure 18 show the calculated comparative free energy profiles for the observed *endo*-methyl shift (**48b→52i**), and the unobserved *exo*-methyl shift leading to the hypothetical intermediate **49b** (Scheme 28).

Table 8. Reaction energies for rearrangements of intermediate **48b** (X=Y=Br) depicted in Scheme 28, calculated at the DFT level.

Reaction	**ΔE (kcal/mol)**	**E_a (kcal/mol)**	**ΔG_{298} (kcal/mol)**	**$\Delta G^{\ddagger}_{298}$ (kcal/mol)**
48b → 49b	-0.99	15.32	-1.36	15.29
48b → 52i	-1.70	13.93	-3.57	13.42

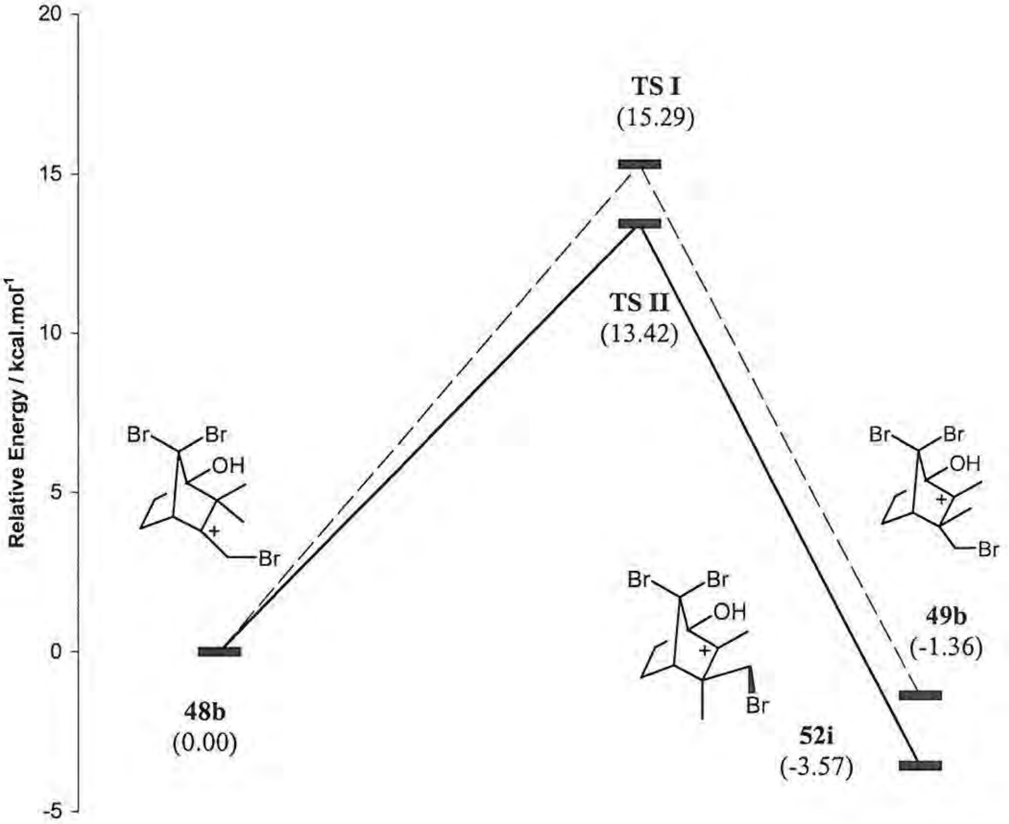

Figure 18. Free energy diagram for pathways **48b** → **52i** and **48b** → **49b** (X=Y=Br; Scheme 26).

A comparison of the free energy data (Table 8, Figure 18) shows the *endo*-migration product **52i** to be both kinetically and thermodynamically favoured, as is evident from the lower activation energy and the lower energy of the resultant intermediate (**52i** *vs.* **49b**) respectively. Some possible reasons for the lower activation energy of the *endo*-shift become apparent upon comparing the geometries of the respective transition states (Figure 19).

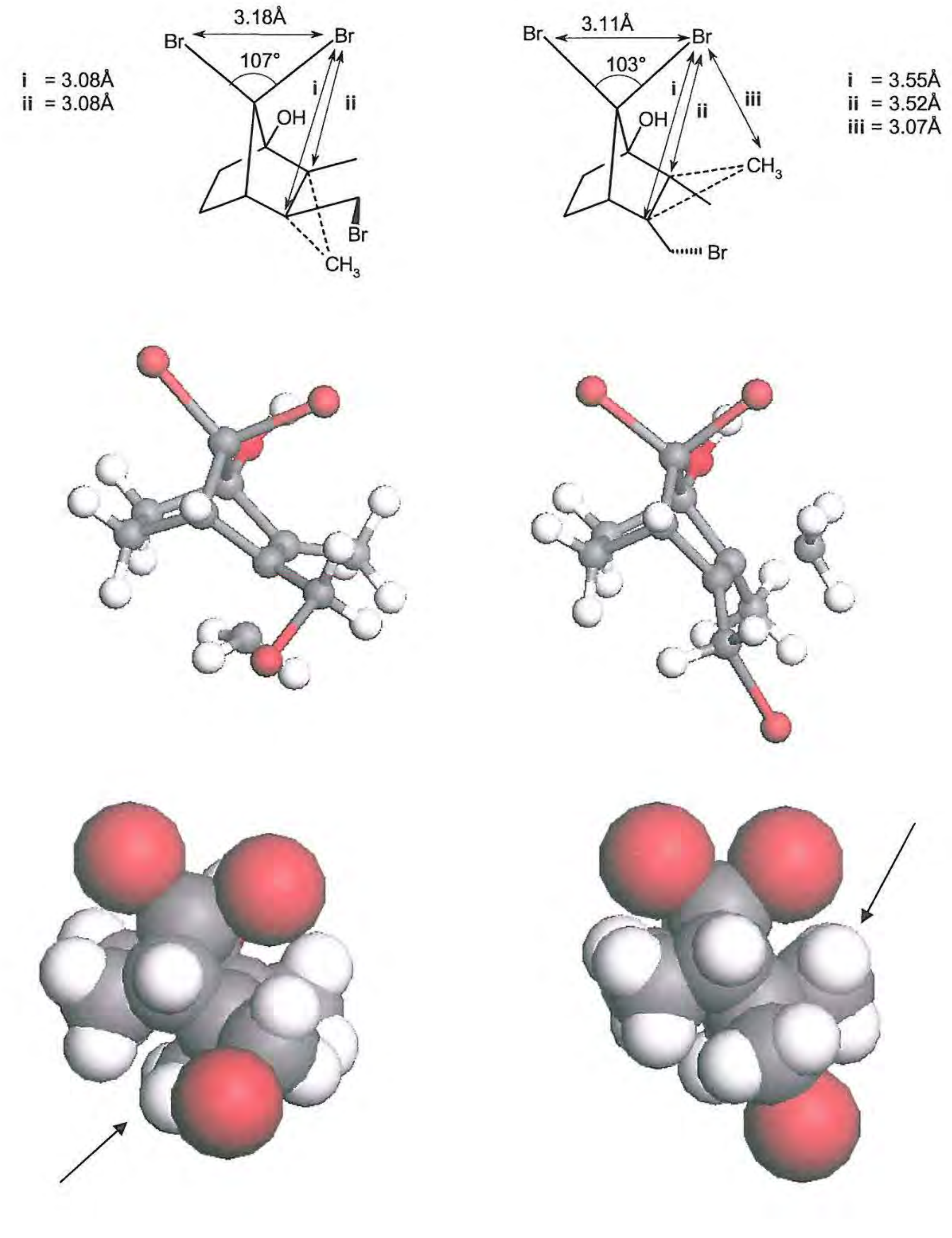

Figure 19. Line-bond structures (top), ball and stick (middle) and space-filling models (bottom, represented volumes are 70% of the Van der Waals radii, migrating methyl groups indicated by arrows) of transition state structure for the *endo*- (left; **TS II**) and *exo*- (right;**TS I**) methyl shifts depicted in Figure 18.

Analysis of the *exo*- transition state in Figure 19 (right) shows evidence of unfavourable steric interaction between the migrating methyl group and the C-7-*syn* bromine atom in that:- 1) the bromine and carbon atoms, at a separation of 3.07Å, are significantly closer together than the sum of their Van der Waals radii (3.55Å);[100] and 2) the Br-C-Br angle at C-7 is smaller than for the *endo*-shift, indicating that the bromine atoms have been pushed closer together by the migrating methyl group. This evidence would appear to support Money's assumption of steric inhibition of the *exo*-methyl shift.[96] However, in the *endo*-transition state (left, Figure 19), the distances between the C-7-*syn* bromine atom and carbons two and three (marked i and ii) are also significantly less than the sum of their Van der Waals radii indicating, perhaps, an electrostatic attraction between the electronegative bromine atom and the electron-deficient carbon atoms. This observation lends credence to the Antkowiaks' claim that the *endo*-methyl shift is facilitated by anchimeric assistance (Scheme 29).[99]

A further factor that warrants consideration became evident upon comparing the geometries of intermediates **48b** and **52i** (Figure 20). In both cases, there is a distinct shortening of the distance between the C-7-*syn* bromine and the carbon bearing the positive charge. This can be ascribed to an electrostatic attraction between the electron-rich bromine atom and the positively-charged carbocation. This electrostatic interaction causes a twisting of the camphor skeleton, which brings about an as-yet unconsidered torsional effect.

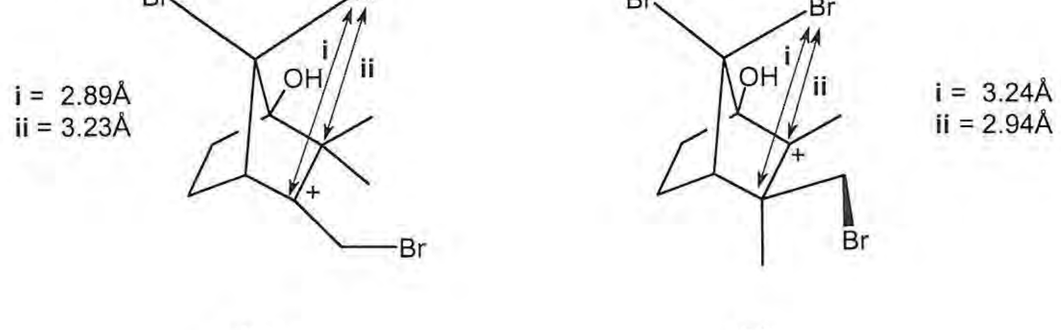

48b **52i**

Figure 20. DFT-optimised geometries of the intermediates **48b** and **52i**.

The abovementioned torsional effect is best illustrated by comparing the relevant dihedral angles in the intermediates **48b** with those of the dibrominated analogue **48a** (Figure 21), in which the C-7-*syn* substituent is a proton, and unlikely to exert an electrostatic influence on the carbocation centre. The 'ideal', undistorted values of the dihedral angles α [(C-3)-(C-8)/(C-2)-(C-10)] and β [(C-3)-(C-9)/(C-2)-(C-10)] in intermediates **48a** and **48b** are expected to be *ca* 60°, which (barring all other factors) would result in comparable intrinsic barriers to *exo*- and *endo*-methyl shifts. However, the fact that β is significantly larger than α in intermediate **48b** means that:- 1) the *endo*-methyl group (C-9) is much closer to co-planarity with the empty *p*-orbital at C-2 than the *exo*-methyl group (C-8), and is therefore likely to migrate preferentially; and 2) the smaller α angle positions C-8 close to the final position it will assume in an *endo* migration, *i.e.* if C-9 is the migrating group. These factors should render the *endo* migration the more favourable of the two possibilities in the case of the 7,7-dibromo system **48b**. In the case of the 7-bromo derivative **48a**, however, the dihedral angles are sufficiently close to the normal value of 60° to render any torsional contribution insignificant.

While clearly not the only factors involved, it is our opinion that torsional effects should not be overlooked as contributing factors in the rearrangements described here. This observation is not unprecedented, as torsional factors are considered to exert a strong influence over a similar migration process in the racemization of camphene *via* the Nametkin rearrangement.[101]

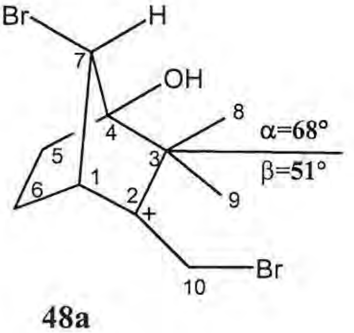

48a

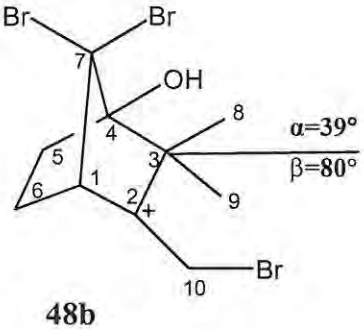

48b

Figure 21. Dihedral angles for the DFT geometry-optimised intermediates **48a** (X=Br, Y=H) and **48b** (X=Y=Br).

Interestingly, Money himself considered this explanation[102] but, in the absence of experimental or computational evidence, considered the steric hindrance of the C-7-*syn* bromine to be the more compelling explanation. This study demonstrates that the selectivity of these rearrangements is, in fact, controlled by several factors. This new mechanistic insight may prove useful in optimising conditions for selective rearrangements of camphor-derived systems in general, and C-8 functionalisation of camphor in particular.

Our synthesis of (+)-8-bromocamphor **42** (Scheme 27) gave rise to an additional side-product that was isolated in 10% overall yield and, on the basis of one-and two-dimensional NMR spectroscopy, identified as (1*S*,4*S*,7*R*)-3,3,4-trimethyl-7,7-dibromonorbornan-2-one **53**. Using a computational technique developed by Johnson and Collins,[103] and refined within our group,[104] we performed a coset analysis to determine all possible pathways for the rearrangement of 3,3-dibromocamphor **44b** to form compound **53**. This procedure involves enumerating all the possible intermediates that can be arrived at through common rearrangements of substituted bicyclo[2.2.1]heptyl cations. The programme then maps out all feasible pathways from a designated starting material to a designated product, *via* the allowed intermediates, and within a predetermined number of steps. Searching within the limit of 13 rearrangement steps, and the operations of Wagner-Meerwein rearrangements (WM), 2,3-*exo*- (23x), 2,3-*endo*- (23e) and 6,2- (62) shifts, the analysis generated only four potential pathways for formation of compound **53** (in its protonated form as compound **53'**) from the protonated dibromocamphor starting material **44'b** (Figure 22). The shortest of these - a 7-step pathway - is outlined in Scheme 33.

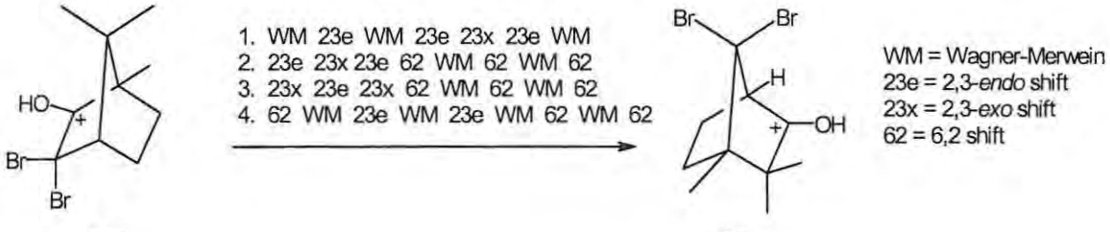

44'b **53'**

Figure 22. Potential, shortest-path rearrangement pathways for formation of compound **53'** from protonated 3,3-dibromocamphor **44'b**.

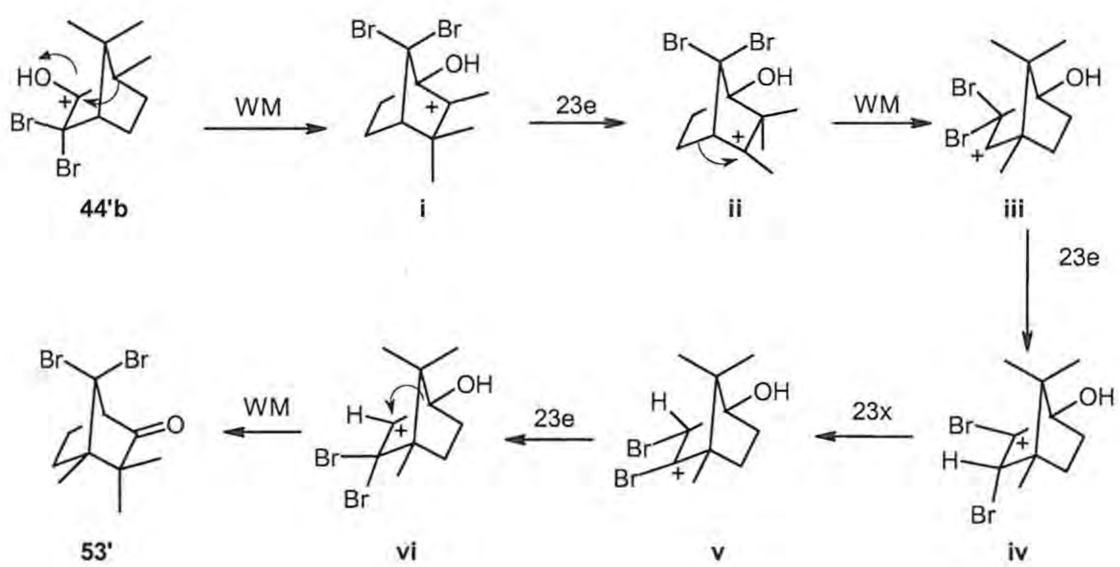

Scheme 33

Thus, Wagner-Meerwein rearrangement of the protonated dibromocamphor **44'b** is followed by a 2,3-*endo*-methyl shift to intermediate **ii**, a second Wagner-Meerwein rearrangement to intermediate **iii**, and a 2,3-*endo*-bromide shift to intermediate **iv**. At this stage, two unlikely steps occur, namely a 2,3-*exo*-hydride shift to intermediate **v**, followed by a 2,3-*endo*-bromide shift back to a gem-dibromide species **vi**. The hydride shift to species **v**, while not a impossible transformation, does not lead to any further stabilisation of the system (neither by release of steric strain, nor generation of a more highly substituted carbocation). The subsequent bromide shift to species **vi** is in fact generating a more sterically hindered system, which is likely to be much higher in energy. An examination of the alternative routes to compound **53'** (Figure 22) revealed the same energetically unfeasible bromide and hydride shifts in every pathway – an observation that called into question the structural assignment of the product **53**. This prompted single crystal X-ray analysis of the compound, the results of which proved the initial assignment to be false and permitted its positive identification as 3,3,4-trimethyl-1,7-dibromonorbornan-2-one **54** (Figure 23).

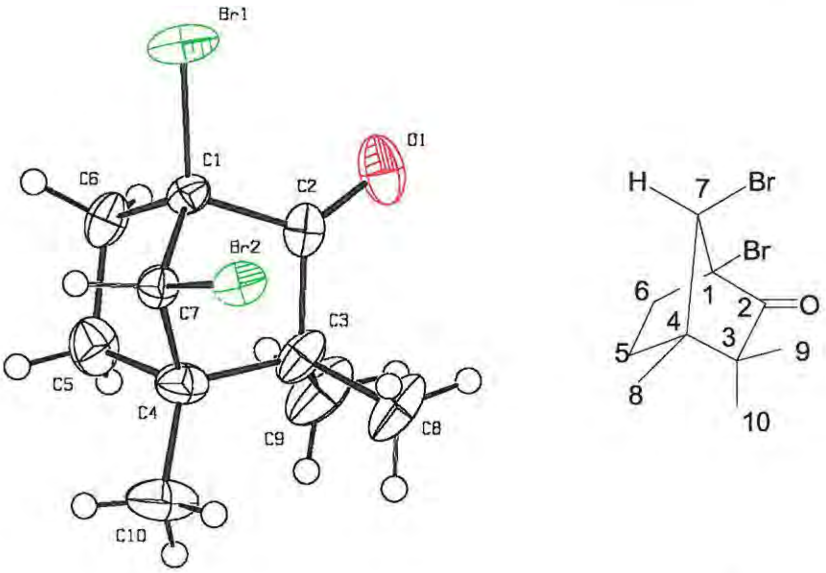

a **b**

Figure 23 **a)** X-ray crystal structure of 3,3,4-trimethyl-1,7-dibromonorbornan-2-one **54**, showing the crystallographic numbering and **b)** the corresponding wire-frame structure showing the systematic numbering.

Figures 24 through 27 show selected NMR data for compound **54**. Integration of the ^{1}H spectrum (Figure 24) clearly indicates:-

i) the presence of three methyl singlets at 1.08, 1.23 and 1.39 ppm;

ii) the characteristic multiplets due to the two methylene groups at carbons 5 and 6; and

ii) a relatively deshielded methine proton resonating at 4.22 ppm.

The ^{13}C spectrum (Figure 25) shows 10 carbon signals, *i.e.* the methine, methylene and methyl groups detected in the ^{1}H spectrum, as well as three quaternary carbon signals, and that of the carbonyl carbon signal at 210 ppm. Proton-carbon connectivity was established by HMQC correlations (Figure 26). This NMR data, as well as the HMBC correlations (Figure 27) appears to be consistent with both the correct structure **54** and the wrongly assigned structure **53**! Mass spectrometric analysis of compound **54** did not reveal a molecular ion, but fragmentation patterns were detected that were consistent with the isotopic distribution characteristic of a dibrominated species. Here again, no data was available that could unambiguously discriminate between compound **54** and its constitutional isomer **53**.

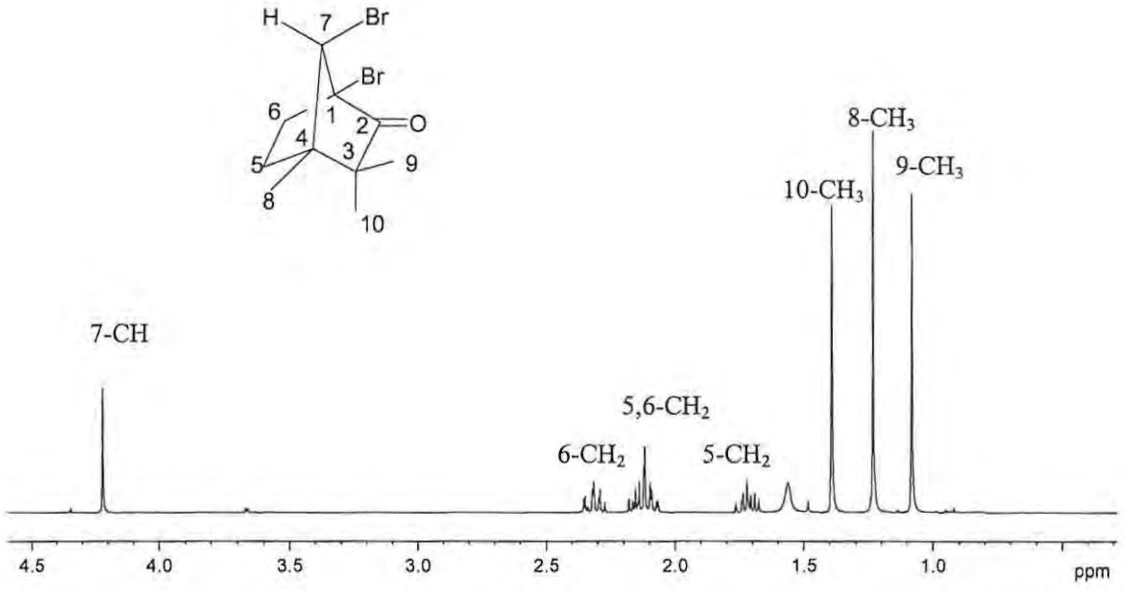

Figure 24. 400MHz ^{1}H NMR spectrum of 3,3,4-trimethyl-1,7-dibromonorbornan-2-one **54** in $CDCl_3$.

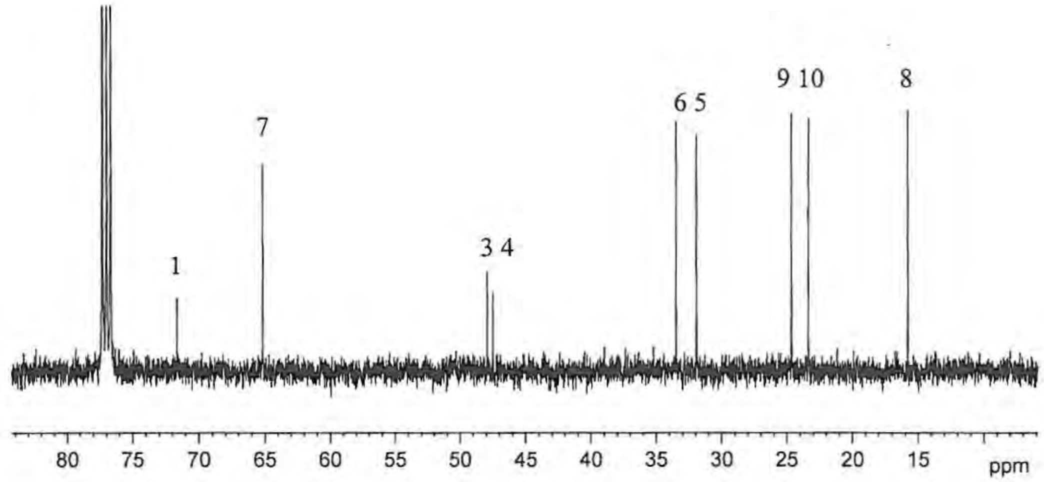

Figure 25. Partial 100 MHz ^{13}C NMR spectrum of 3,3,4-trimethyl-1,7-dibromonorbornan-2-one **54** in $CDCl_3$ (carbonyl signal at $\delta = 210$ppm not shown).

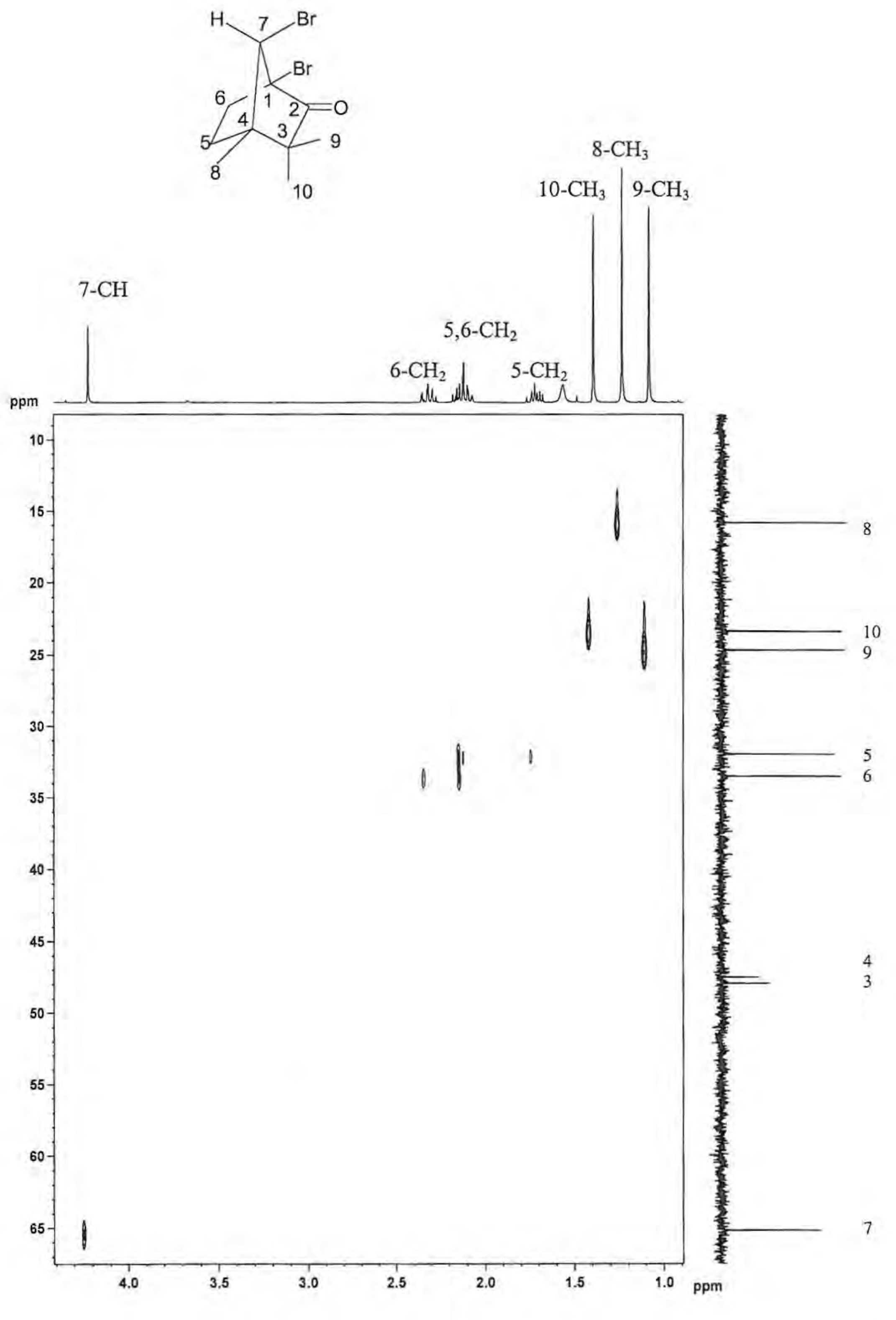

Figure 26. 400MHZ HMQC spectrum of 3,3,4-trimethyl-1,7-dibromonorbornan-2- one **54** in $CDCl_3$.

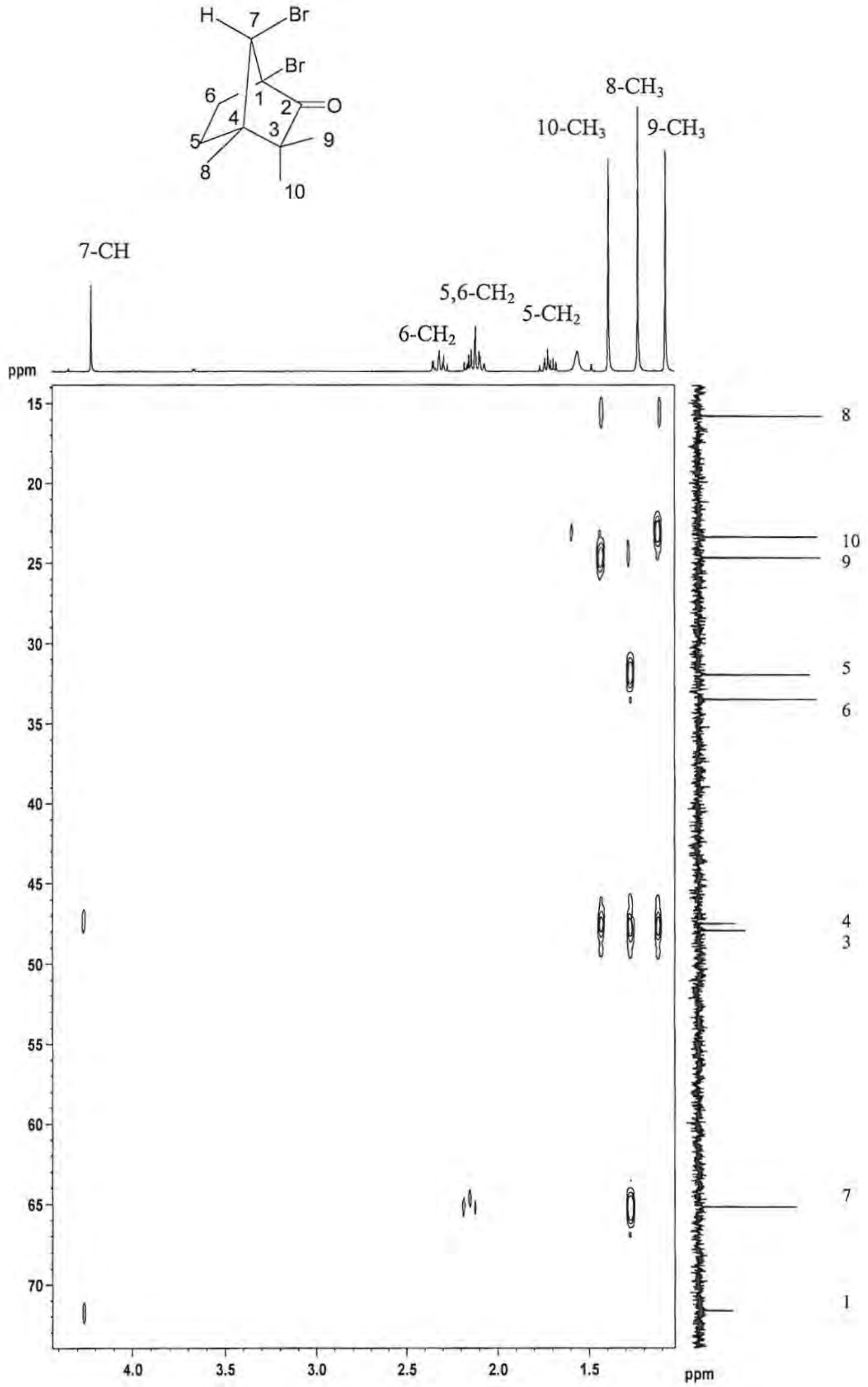

Figure 27. 400MHZ HMBC spectrum of 3,3,4-trimethyl-1,7-dibromonorbornan-2- one **54** in $CDCl_3$.

Compound **54** had, in fact, been isolated by Money during his own synthesis of 8-bromocamphor, and identified by single-crystal X-ray analysis.[105] He proposed pathway I (Scheme 34) for its formation,[96] which involves the Wagner-Meerwein rearrangement of intermediate **47b**, followed by a 2,3-*exo*-bromide shift and another Wagner-Meerwein rearrangement. However, Antkowiak and Antkowiak[99] claimed that the Wagner-Meerwein shift from intermediate **47b** to intermediate **55** was not feasible unless the methyl group attached to the cationic carbon is additionally substituted by a second bromine atom, as in structure **57**. They reasoned that the steric hindrance caused by the dibromomethyl group in structure **57** is necessary in order to render the Wagner-Meerwein rearrangement **57** → **58** energetically preferable to the competing 2,3-methyl shift (as in the bromomethyl case **48b** → **52**). They thus attributed the formation of compound **54** to pathway II (Scheme 34), with the reduction of compound **60** (to form product **54**) only taking place upon addition of Zn during the final reduction step to form the desired 8-bromocamphor product **42**.

In our modelling study, a stable ground state structure could not be generated for either of the intermediates **55** or **56**. However, computational analysis of pathway II is characterised by stable structures for the intermediates **57** and **59**, joined by a single transition state with a relatively low activation energy (7.59 kcal.mol^{-1}). This transformation is depicted in Scheme 35, which highlights the carbon-carbon distance of the bond formed in the Wagner-Meerwein rearrangement (italicised), and the carbon-bromine distance of the bond formed in the bromide shift. An energetically favourable conversion of intermediate **59** affords the tetrabrominated side-product **60** *via* a second transition state, depicted in Scheme 36 [showing carbon-carbon distances of bonds broken (italicised) and formed in the Wagner-Meerwein rearrangement]. Energy data for the transformations in pathway II are summarised in Table 9, and Figure 28. The computational evidence thus points to pathway II as a more likely route to compound **54** than that suggested by Money.[96] This pathway is further supported by our experimental results, which showed no spectroscopic evidence for the presence of compound **54** in the reaction mixture until after the final reduction step.

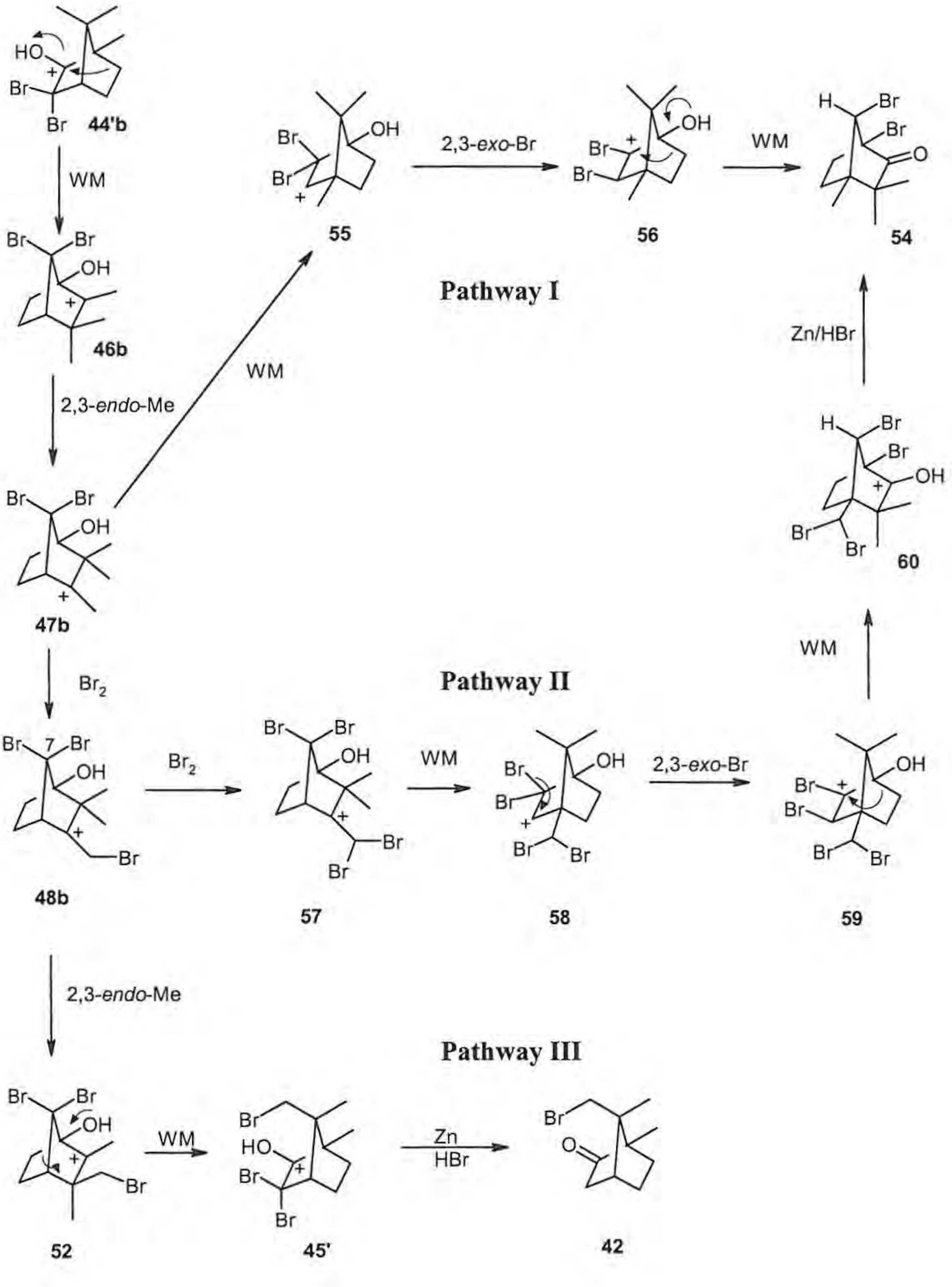
44'b
WM
46b
2,3-*endo*-Me
47b
WM
55
2,3-*exo*-Br
56
WM
54
Pathway I
Zn/HBr
60
WM
Pathway II
Br2
48b
Br2
57
WM
58
2,3-*exo*-Br
59
2,3-*endo*-Me
Pathway III
52
WM
45'
Zn
HBr
42

Scheme 34

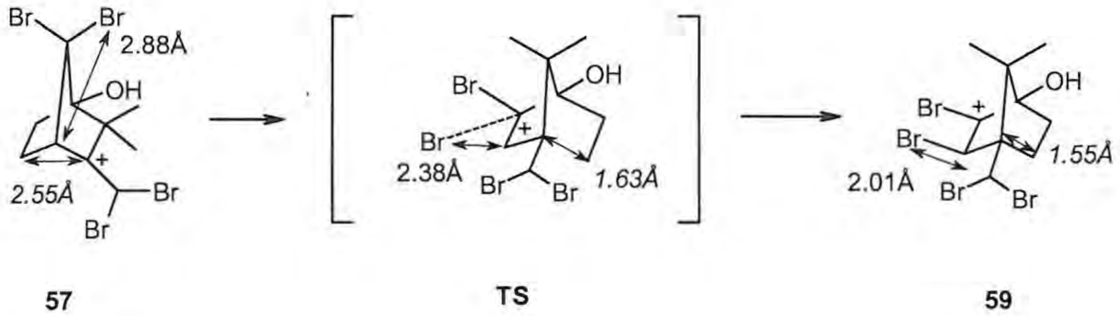

Scheme 35

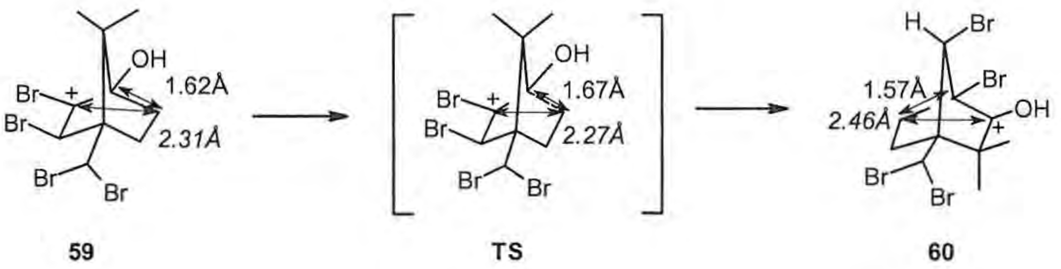

Scheme 36

Table 9. Reaction energies for the rearrangements depicted in Pathway II, Scheme 34, calculated at the DFT level.

Reaction	ΔE (kcal/mol)	E_a (kcal/mol)	ΔG_{298} (kcal/mol)	$\Delta G^{\ddagger}_{298}$ (kcal/mol)
57 → 59	-4.02	8.39	-5.06	7.59
59 → 60	-25.75	2.78	-24.75	2.45

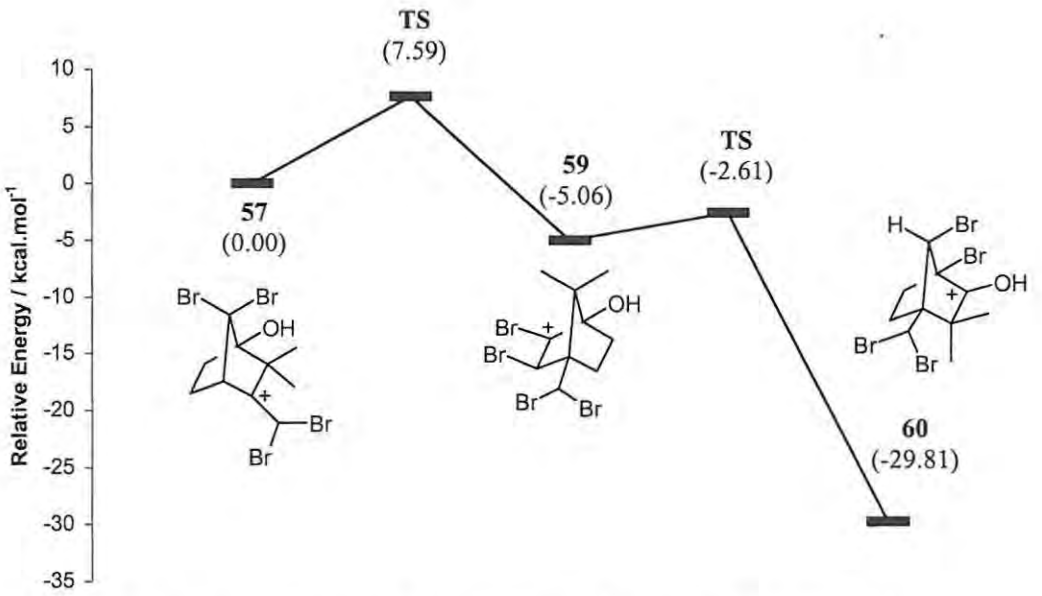

Figure 28. Free energy diagram for pathway II (**57** → **60**), Scheme 34.

2.2.2.2 Approach to the ring-opening of (+)-8-bromocamphor (42)

(+)-8-bromocamphorquinone **61** was produced in 75% yield by oxidation of (+)-8-bromocamphor **42** with selenium dioxide (Scheme 37), following a procedure developed for the analogous reaction of 9-bromocamphor **51**.[106] The camphorquinone **61** had been previously isolated by Antkowiak and Antkowiak as a trace product in the preparation of (+)-8-bromocamphor, and its formation ascribed to the hydrolytic debromination of 3,3,8-tribromocamphor.[99] In the same report, the synthesis of compound **61** was mentioned briefly (in poor yield), but no experimental details given. Thus, our yield of 75% marked a pleasing improvement on existing methods for this reaction.

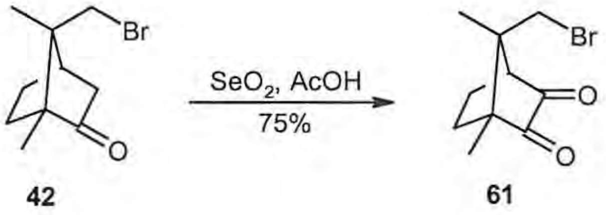

Scheme 37

Further oxidation of compound **61** with hydrogen peroxide, following the same literature reference,[106] afforded the novel (+)-8-bromocamphoric anhydride **62** in 61% yield (Scheme 38). The structure of the anhydride **62** was confirmed by one-and two-dimensional NMR, and MS analysis, while infrared analysis clearly revealed two strong carbonyl stretching bands at 1810 and 1764 cm^{-1} characteristic of cyclic anhydrides.

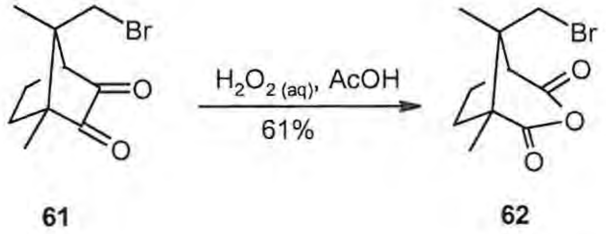

Scheme 38

The NMR data for compound **62** is shown in Figures 29 through 32. In the ^{1}H spectrum (Figure 29), the two (overlapping) doublets at *ca.* 3.3ppm are characteristic of the diastereotopic methylene protons on carbon 8. This, together with the presence of only two methyl group signals, indicates retention of the C-8 bromine in product **62** as confirmed by MS analysis. The methine proton attached to carbon 4 was identified by its downfield appearance, and characteristic coupling to the equatorial proton on carbon 5. In the ^{13}C spectrum (Figure 30), the two signals in the carbonyl region at 171.6 and 168.2 ppm are an immediate indicator of the presence of the anhydride functionality. HMQC correlations (Figure 31) were used to assign carbons 4 and 8. An HMBC correlation to the C4 proton (Figure 32) was then used to distinguish between:- i) the carbonyl carbon signals, due to correlation to carbon 3; and ii) the quaternary carbon signals, due to correlation to carbon 7. The methyl groups were distinguished by HMBC correlation between carbon 2 and the methyl protons attached to carbon 10. High-resolution chemical ionisation (CI) MS analysis of compound **62** revealed the isotopic [M+H] peaks at m/z = 261 and 263 as the parent peaks.

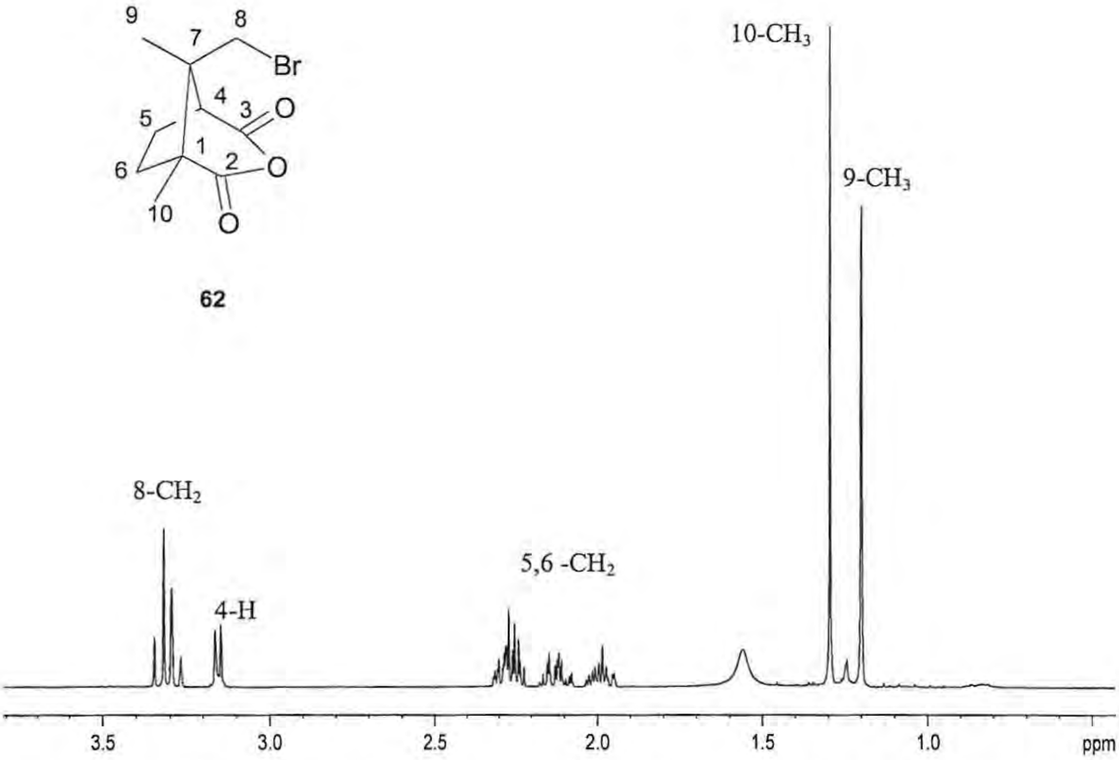

Figure 29. 400MHz ^{1}H NMR spectrum of (+)-8-bromocamphoric anhydride **62** in CDCl$_3$.

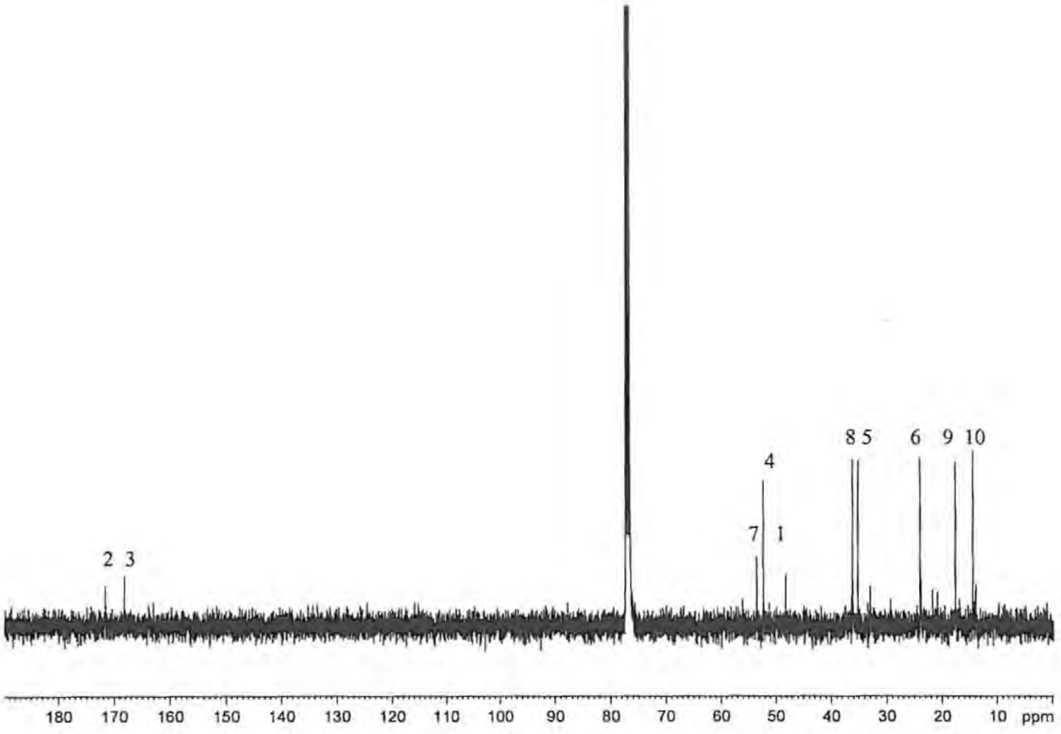

Figure 30. 100 MHz ^{13}C NMR spectrum of (+)-8-bromocamphoric anhydride **62** in CDCl$_3$.

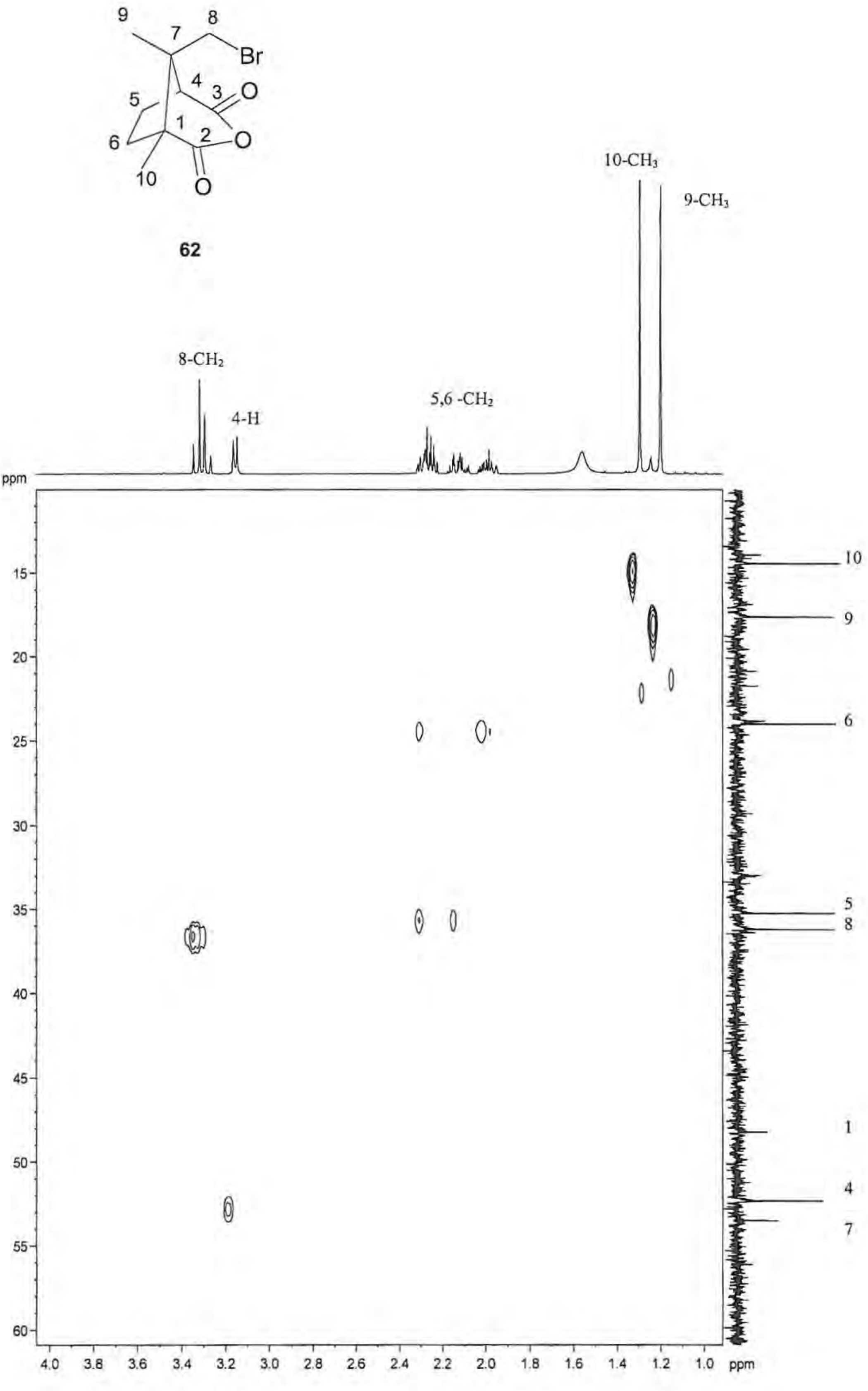

Figure 31. 400 MHz HMQC NMR spectrum of (+)-8-bromocamphoric anhydride **52** in $CDCl_3$.

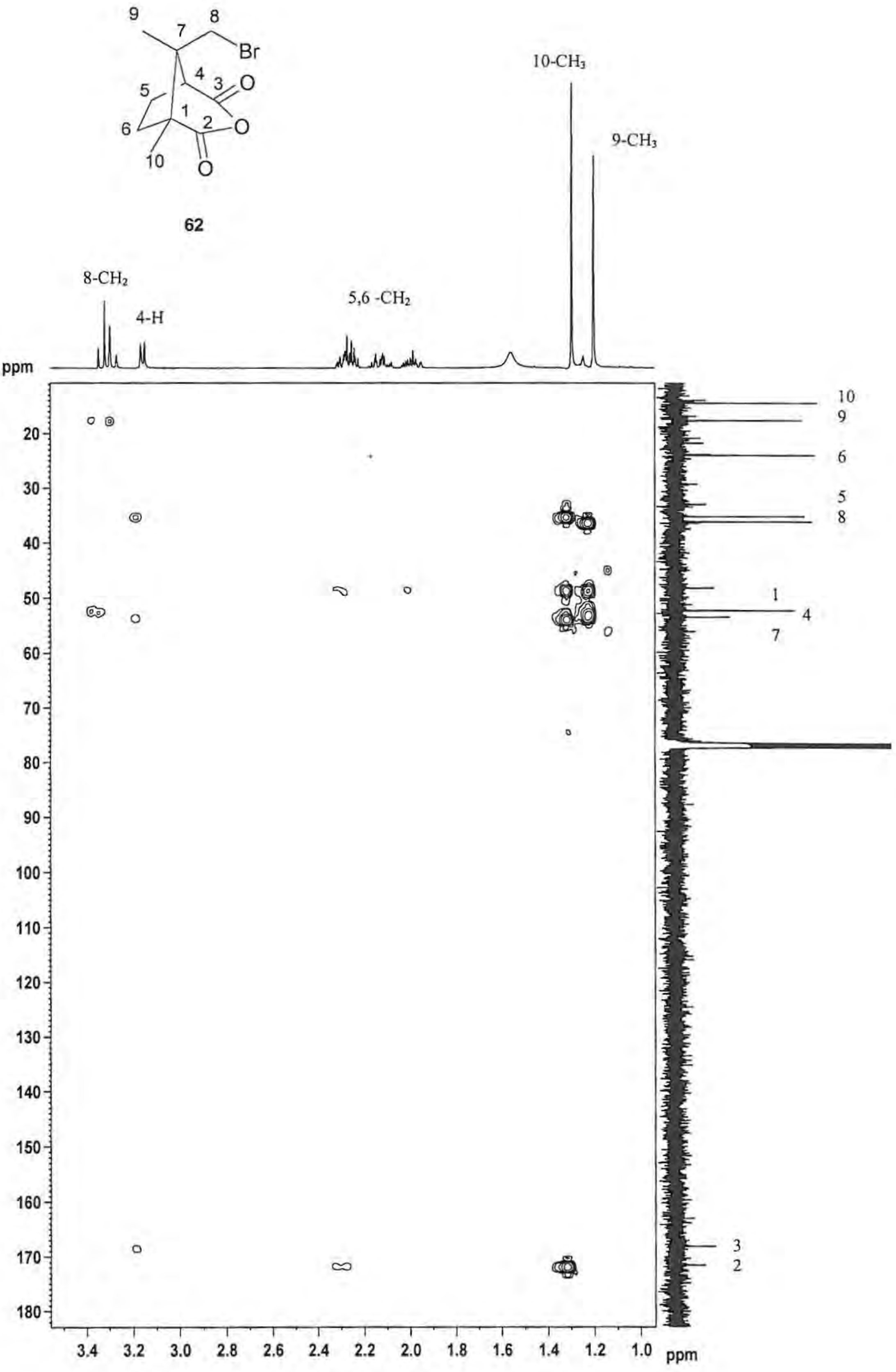

Figure 32. 400 MHz HMBC NMR spectrum of (+)-8-bromocamphoric anhydride **62** in $CDCl_3$.

The next step required opening of the cyclic anhydride **62**. Attempted acid hydrolysis of anhydride **62**, however, failed to produce the desired 8-bromocamphoric acid **43** (Scheme 39). Instead, a crystalline compound was isolated as the major product in roughly 30% yield, IR analysis of which revealed a broad CO_2H stretching band at 3276 cm^{-1}, two strong C=O stretching bands at 1743 cm^{-1} and 1728 cm^{-1} characteristic of a 5-membered lactone ring, and two C-O stretching bands at 1182 and 1163 cm^{-1}, characteristic of γ-lactones.[107] High-resolution MS analysis confirmed a molecular formula of $C_{10}H_{14}O_4$. This information was consistent with formation of either of the constitutional isomers **63** or **64** (Scheme 39).

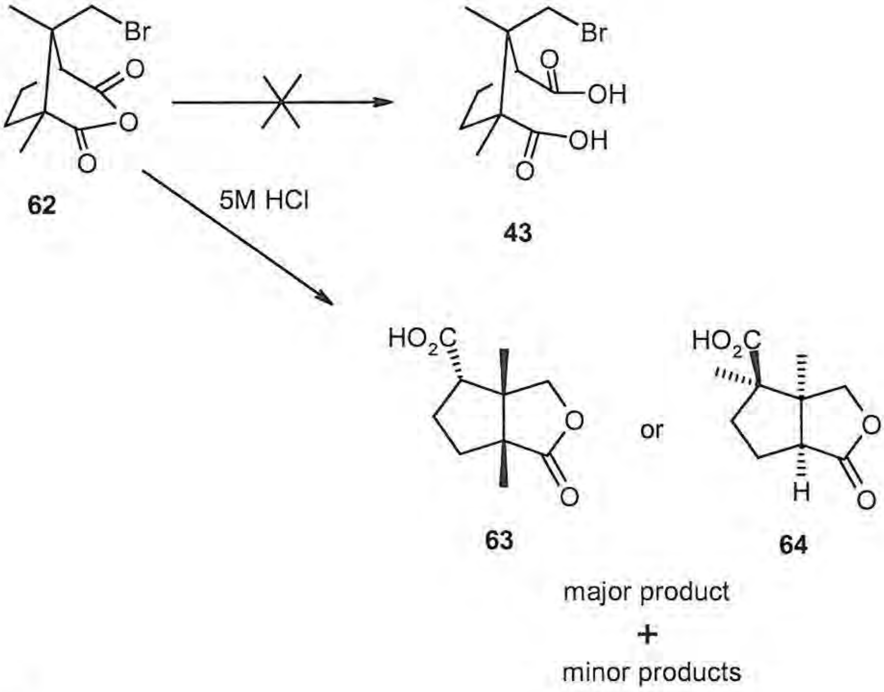

Scheme 39

Access to either of these products could be rationalised mechanistically as indicated in Scheme 40. Thus, acid-catalysed hydrolysis at either carbonyl centre, followed by intramolecular nucleophilic displacement of bromide by the released carboxylate moiety, could account for the formation of either of the isomeric lactones **63** or **64**. However, using the available spectroscopic data, structure **63** or **64** could not be assigned unambiguously to the isolated product.

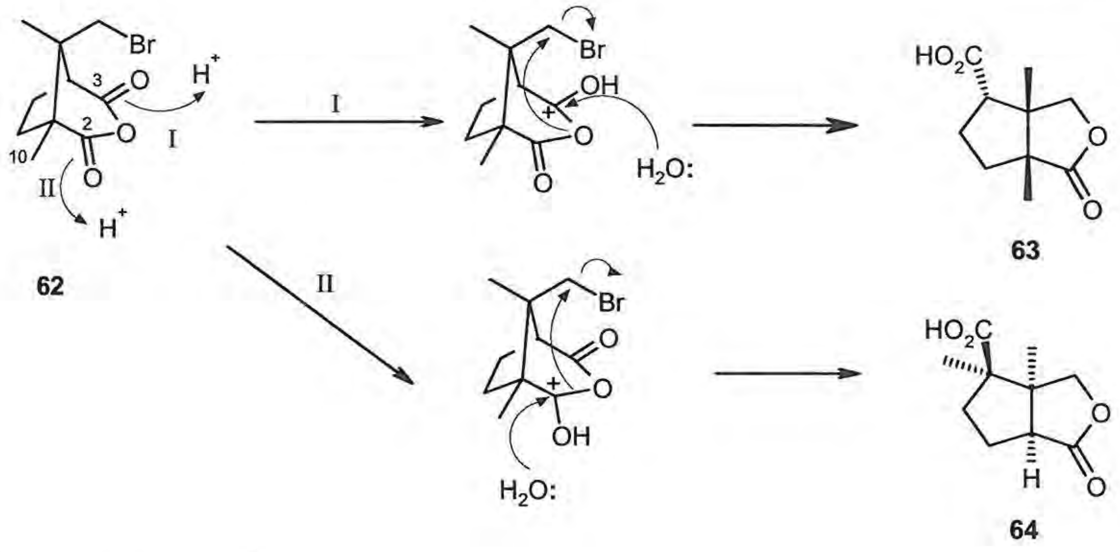

Scheme 40

Geometry optimisations were consequently performed on both structures at the DFT level. While a stable, minimum-energy structure was obtained for lactone **63** (Figure 33), no minimum-energy conformation could be located for the isomer **64**. We thus tentatively assumed lactone **63** to be the isomer in hand. Moreover, from a consideration of steric effects, the 10-methyl group could be expected to inhibit attack by H_2O at C-2 and thus favour attack at C-3 to give lactone **63** rather than the isomeric system **64**. Such regioselectivity is common in camphor derivatives.[108]

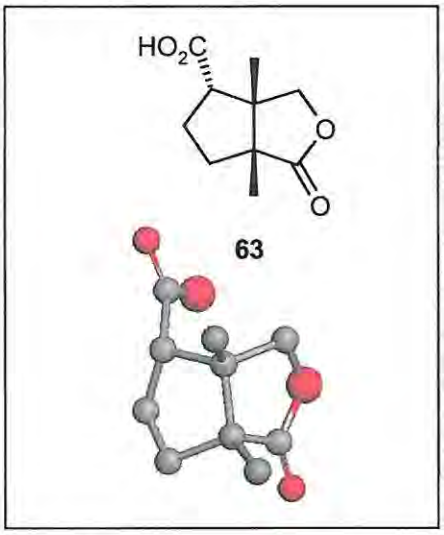

Figure 33. DMol^3/GGA/PW91/DNP optimised structure **63**, protons omitted for clarity.

Although lactonisation of anhydride **62** marked a departure from the desired synthetic sequence, it presented an opportunity to address one of the broader aims of the project, being integration of computational techniques with traditional physical organic methods. Studies by other researchers[109] and within our own group[110] have clearly demonstrated that rearrangements involving camphor derivatives are seldom trivial, and an understanding of the underlying chemistry warrants very careful consideration. The revisiting of some of these rearrangements armed with new computational methods continues to provide new mechanistic insight,[111] and is one of the main points of focus within our group. For this reason, the transformation outlined in Scheme 39 was afforded a more thorough investigation.

In order to support the structure and stereochemistry assigned to the lactone **63**, it was decided to prepare the *trans*-fused isomer **67** originally synthesised by Brienne and Jacques,[112] for comparative purposes. The 3,9-dibromocamphor starting material **65**, which had been synthesised within the group, was hydrolysed under acidic conditions to afford 9-bromocamphoric acid **66** in 39% yield. The carboxylate anion of species **66** was then generated by treatment with $NaHCO_3$, and a spontaneous intramolecular S_N2 reaction afforded, after neutralisation, the lactone **67** in approximately 40% yield.

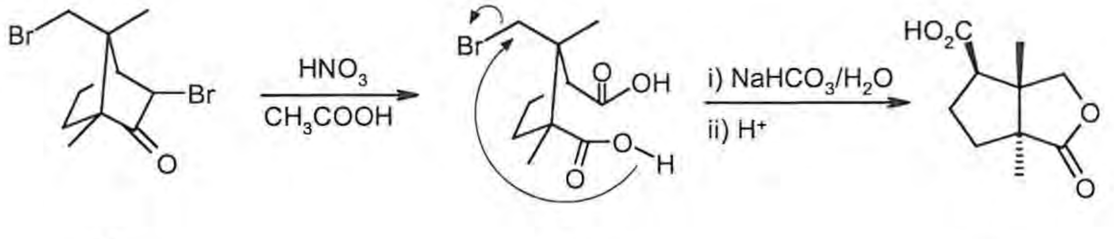

65 **66** **67**

Scheme 41

A comparison of the ^1H NMR spectra of the putative lactone **63** and the known compound **67** (Figures 34 and 35 respectively) suggests that the two methyl groups are similarly positioned with respect to the free carboxylic acid group in both compounds, *i.e.* no significant downfield shift is evident as one might expect for a methyl group on the carbon bearing the carboxylic acid as in structure **64**.

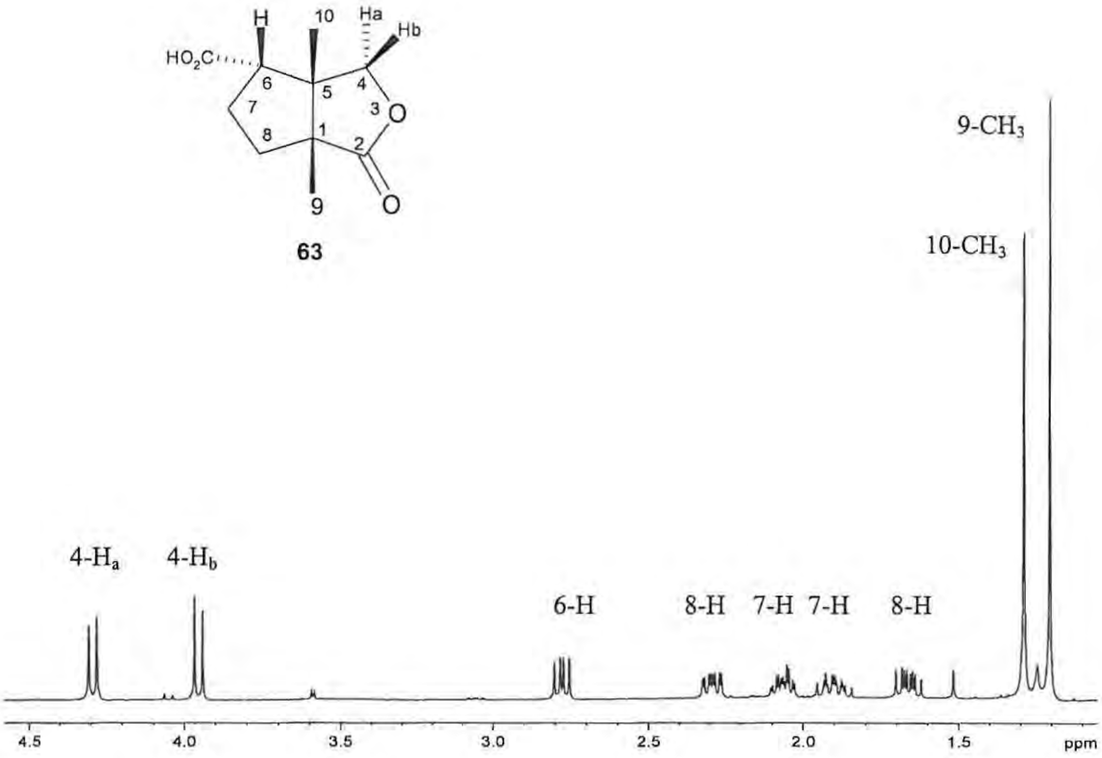

Figure 34. 400MHz ^{1}H NMR spectrum of lactone **63** in CDCl$_3$.

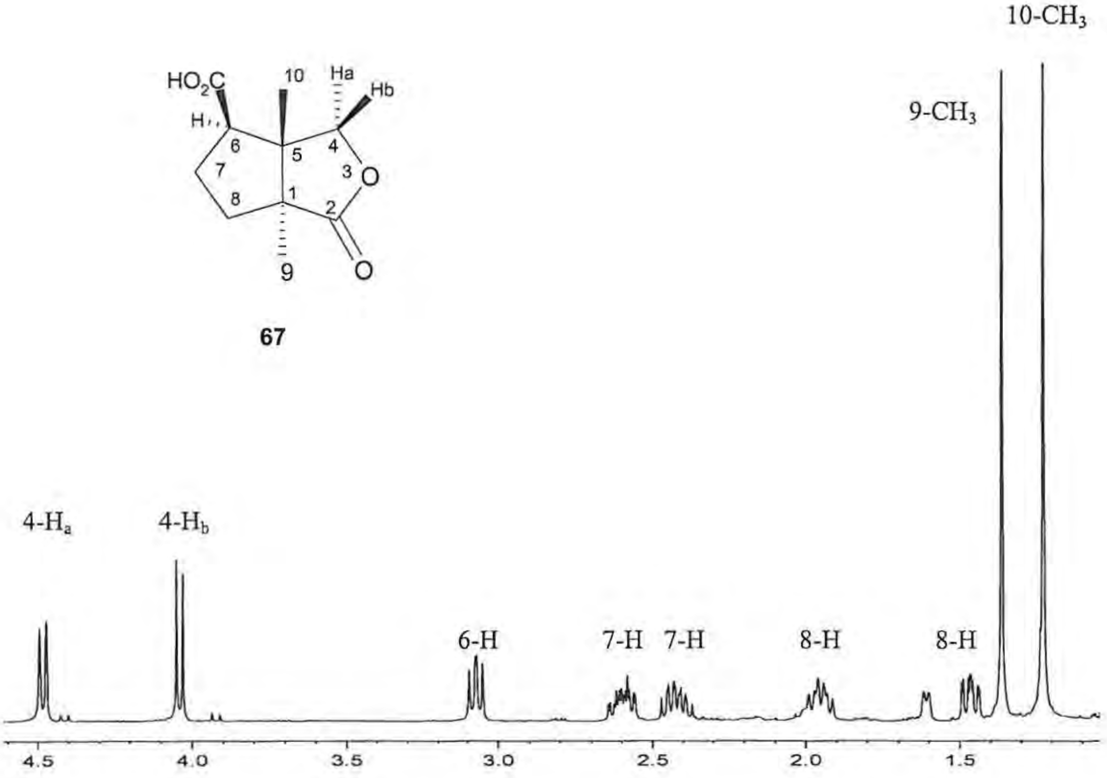

Figure 35. 400MHz ^{1}H NMR spectrum of lactone **67** in CDCl$_3$.

The assigned stereochemistry at C-6 in structure **63** is supported by the fact that the 6-H nucleus resonates slightly upfield (*ca.* 0.3ppm) of the corresponding nucleus in the isomeric system **67** – an observation consistent with greater van der Waals' shielding of the axial proton. Further spectroscopic support for the assigned structure **63** is provided by the DEPT-135 (Figure 36) and HMQC data (Figure 37), which was used to assign:- i) the ^{13}C signal coupled to the distinctive diastereotopic protons at position 4; and ii) the ^{13}C and ^{1}H signals corresponding to C-6 (being the only methine carbon in the molecule and its attached proton). The remaining signals were assigned using the HMBC correlations (Figure 38). Thus:-

i) the carbonyl carbons were distinguished by coupling of C-11 to the C-6 methine proton.

ii) the methyl groups were distinguished by coupling of C-2 to the C-9 methyl protons;

iii) quaternary carbons 1 and 5 were distinguished by coupling of the diastereotopic protons on C-4 to C-5; and

iv) C-7 and C-8 were distinguished by the coupling of the C-8 protons to C-2.

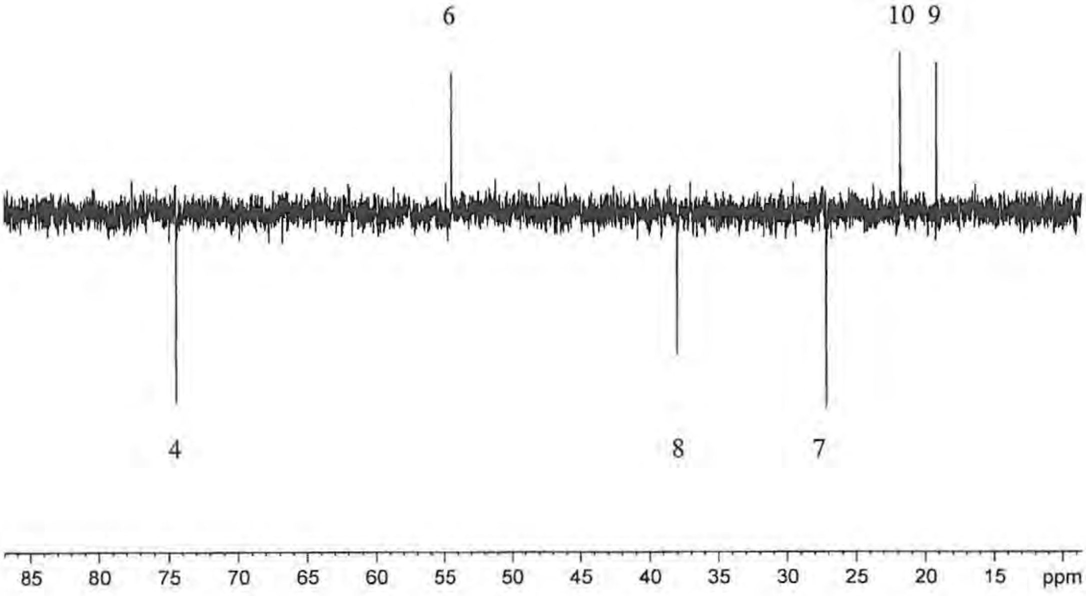

Figure 36. 100 MHz DEPT-135 NMR spectrum of lactone **63** in $CDCl_3$.

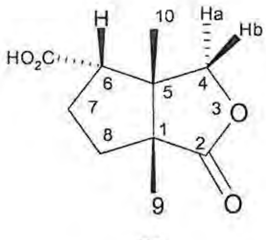

63

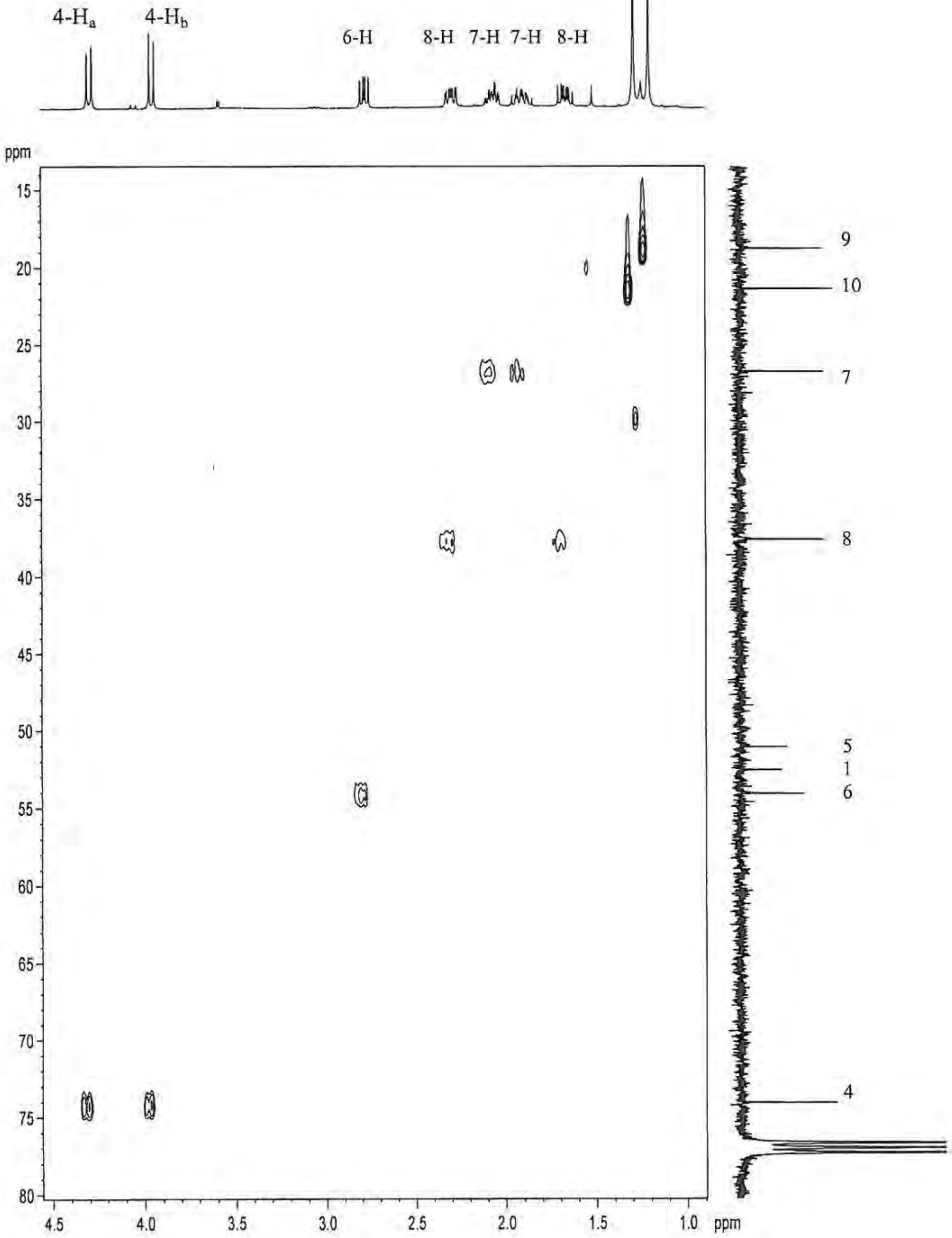

Figure 37. 400 MHz HMQC NMR spectrum of lactone **63** in $CDCl_3$.

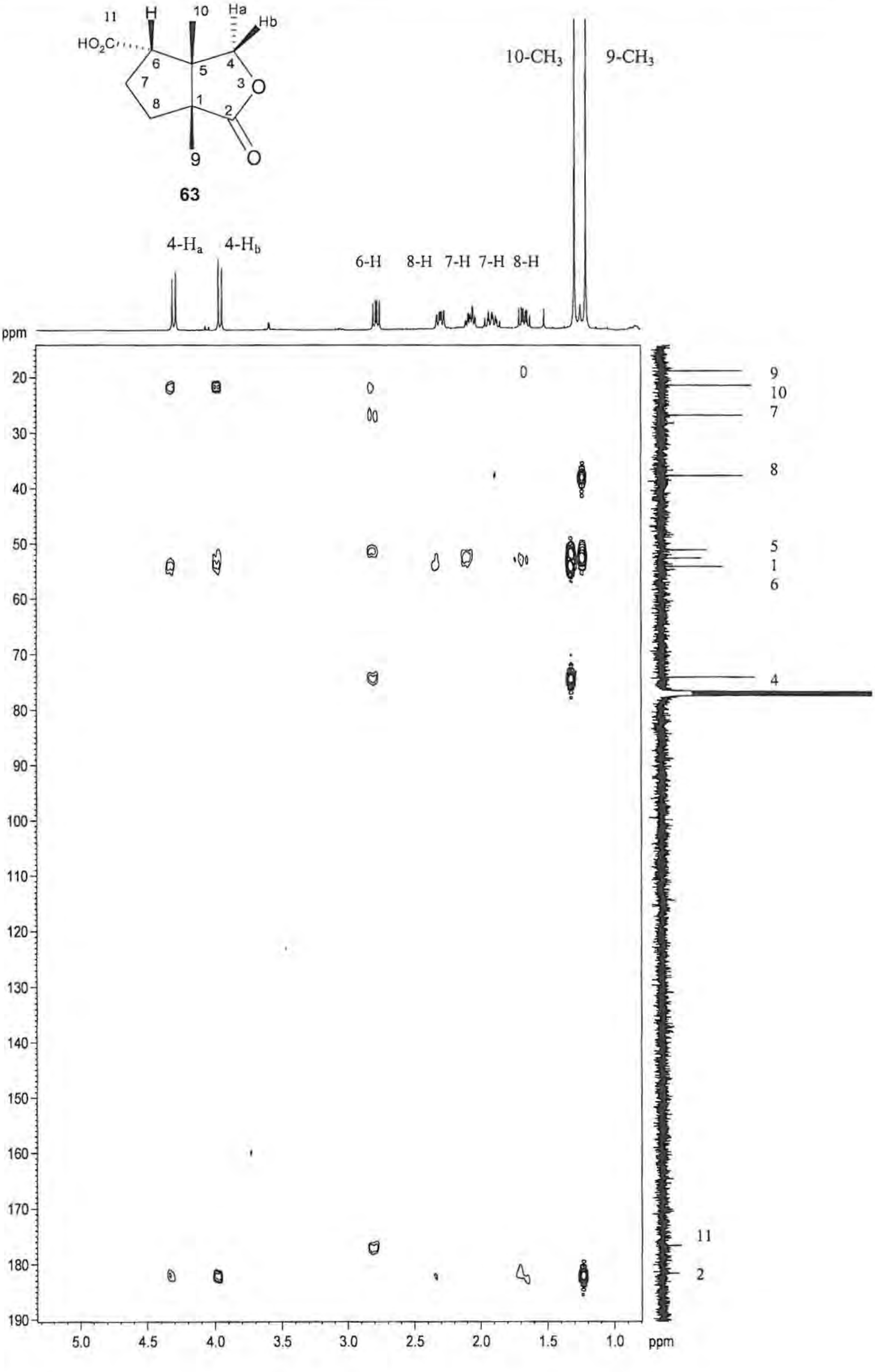

Figure 38. 400 MHz HMBC NMR spectrum of lactone **63** in $CDCl_3$.

The assignment of the lactone structure **63** to the major product isolated from the hydrolysis of the anhydride **62** (Scheme 39) was finally confirmed by single crystal X-ray analysis (Figure 39), and the geometry of the structure compared to that obtained by the DFT calculations (Tables 10 and 11).

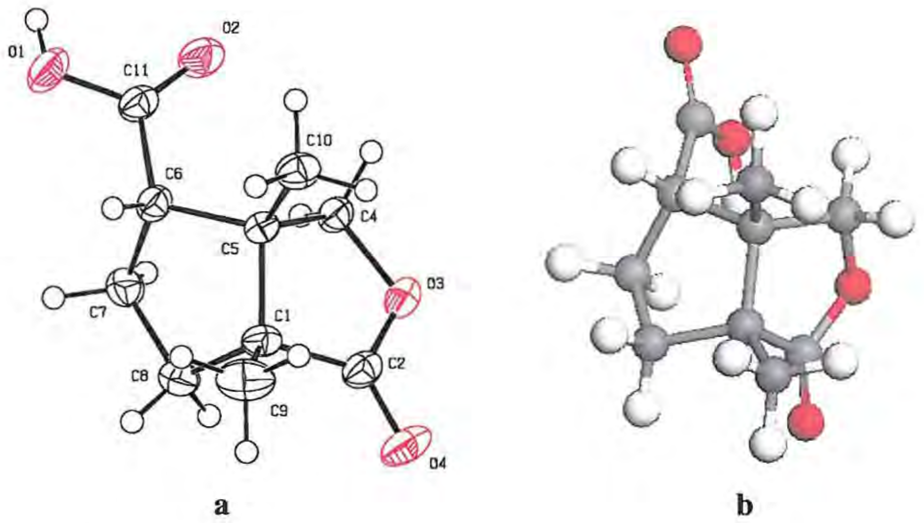

Figure 39. a) X-ray crystal structure of lactone **63**, showing the crystallographic numbering. b) DFT geometry-optimised structure **63**.

Table 10. Selected Bond lengths (in Å) for lactone **63** as determined by single crystal X-ray analysis, and as calculated from the DFT geometry-optimised structure, showing the error in the calculated values.

Bond	X-Ray	DFT	Error
C1-C2	1.514	1.538	0.024
C1-C9	1.522	1.531	0.009
C1-C5	1.556	1.568	0.012
C1-C8	1.564	1.537	-0.027
C2-04	1.216	1.209	-0.007
C2-03	1.331	1.372	0.041
C4-O3	1.466	1.453	-0.013
C4-C5	1.543	1.535	-0.008
C5-C10	1.532	1.529	-0.003
C5-C6	1.534	1.589	0.055
C6-C11	1.510	1.522	0.012
C6-C7	1.545	1.541	-0.004
C7-C8	1.534	1.529	-0.005
C11-O2	1.211	1.213	0.002
C11-O1	1.331	1.367	0.036

Mean absolute error of calculated bond lengths = 0.017 Å

Table 11. Selected Bond angles (in degrees) for lactone **63** as determined by single crystal X-ray analysis, and as calculated from the DFT geometry-optimised structure, showing the error in the calculated values.

Angle	X-Ray	DFT	Error
C2-C1-C9	110.76	109.04	-1.72
C2-C1-C5	102.49	102.78	0.29
C9-C1-C5	116.55	116.82	0.27
C2-C1-C8	110.30	107.86	-2.44
C9-C1-C8	111.39	113.61	2.22
C5-C1-C8	104.84	105.90	1.06
O4-C2-O3	120.42	121.98	1.56
O4-C2-C1	127.83	127.38	-0.45
O3-C2-C1	111.74	110.61	-1.13
O3-C4-C5	105.45	106.61	1.16
C10-C5-C6	113.56	109.58	-3.98
C10-C5-C4	110.04	110.69	0.65
C6-C5-C4	113.20	114.83	1.63
C10-C5-C1	114.38	116.44	2.06
C6-C5-C1	103.63	103.45	-0.18
C4-C5-C1	101.34	101.67	0.33
C11-C6-C5	115.27	114.21	-1.06
C11-C6-C7	112.33	117.58	5.25
C5-C6-C7	104.19	106.69	2.50
C8-C7-C6	104.73	103.22	-1.51
C7-C8-C1	107.34	103.35	-3.99
O2-C11-O1	123.07	119.49	-3.58
O2-C11-C6	124.65	123.19	-1.46
O1-C11-C6	112.27	117.29	5.02
C2-O3-C4	110.11	109.39	-0.72

Mean absolute error of calculated bond angles = 1.85°

Tables 10 and 11 indicate a good correlation between experimental and calculated bond lengths and angles. The largest single discrepancy between calculated and experimental geometries appears to be in the position of the carboxylic acid moiety attached to C6. This can be ascribed to the intermolecular hydrogen bonding in the crystalline material (Figure 40), which occurs between the carbonyl oxygen O-4, and the acidic proton attached to the carboxylic acid oxygen O-1; such intermolecular interactions are, of course, not taken into account in the gas-phase DFT calculations. The distortion in the crystal structure due to this hydrogen bonding is most evident in the widening of the O2-C11-O1 angle and the resultant decrease in the C11-C6-C7 angle, which are respectively under- and over-estimated in the gas-phase calculations.

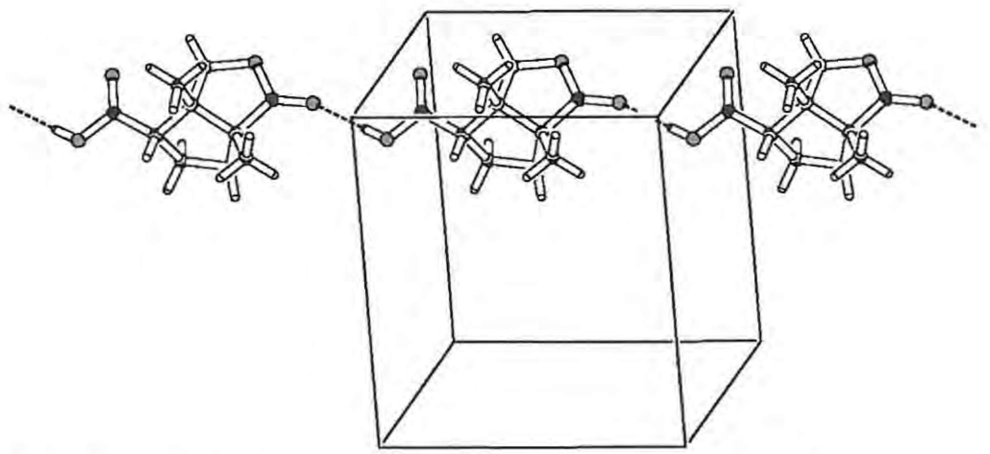

Figure 40. Ball-and-stick model illustrating the intramolecular hydrogen bonding in lactone **63**, as determined by single crystal X-ray analysis.

Three further products were isolated, by HPLC, from the reaction mixture which yielded the lactone **63** (Scheme 42). One of these products was shown by NMR and MS analysis to be camphoric acid **68**. FAB-MS analysis indicated the molecular formula to be $C_{10}H_{15}O_4Br$ for both of the remaining products. A comparison of the ^1H NMR spectra of the two unknown products with that of camphoric acid **68** (Figure 41) revealed common signals at *ca.* 12 ppm each integrating for two protons corresponding to two carboxylic acid groups in each molecule. However, the spectra of the two unknown compounds differ from that of camphoric acid **68** in that they both contain only two methyl groups instead of three, and exhibit signals between 3.5 and 4 ppm, which are characteristic of diastereotopic methylene protons adjacent to a bromine atom. Given the NMR evidence, and the expectation that these two products were formed by the hydrolysis of 8-bromocamphoric anhydride **62** followed, presumably, by one or more rearrangement steps, it seemed reasonable to assume that they were both brominated camphoric acid derivatives with the carboxylic acid groups located *cis* to each other.

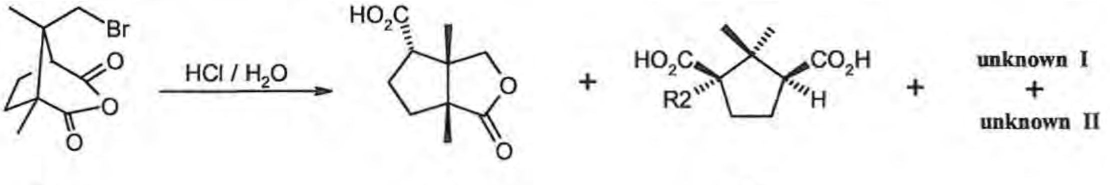

62 **63** **68**

Scheme 42.

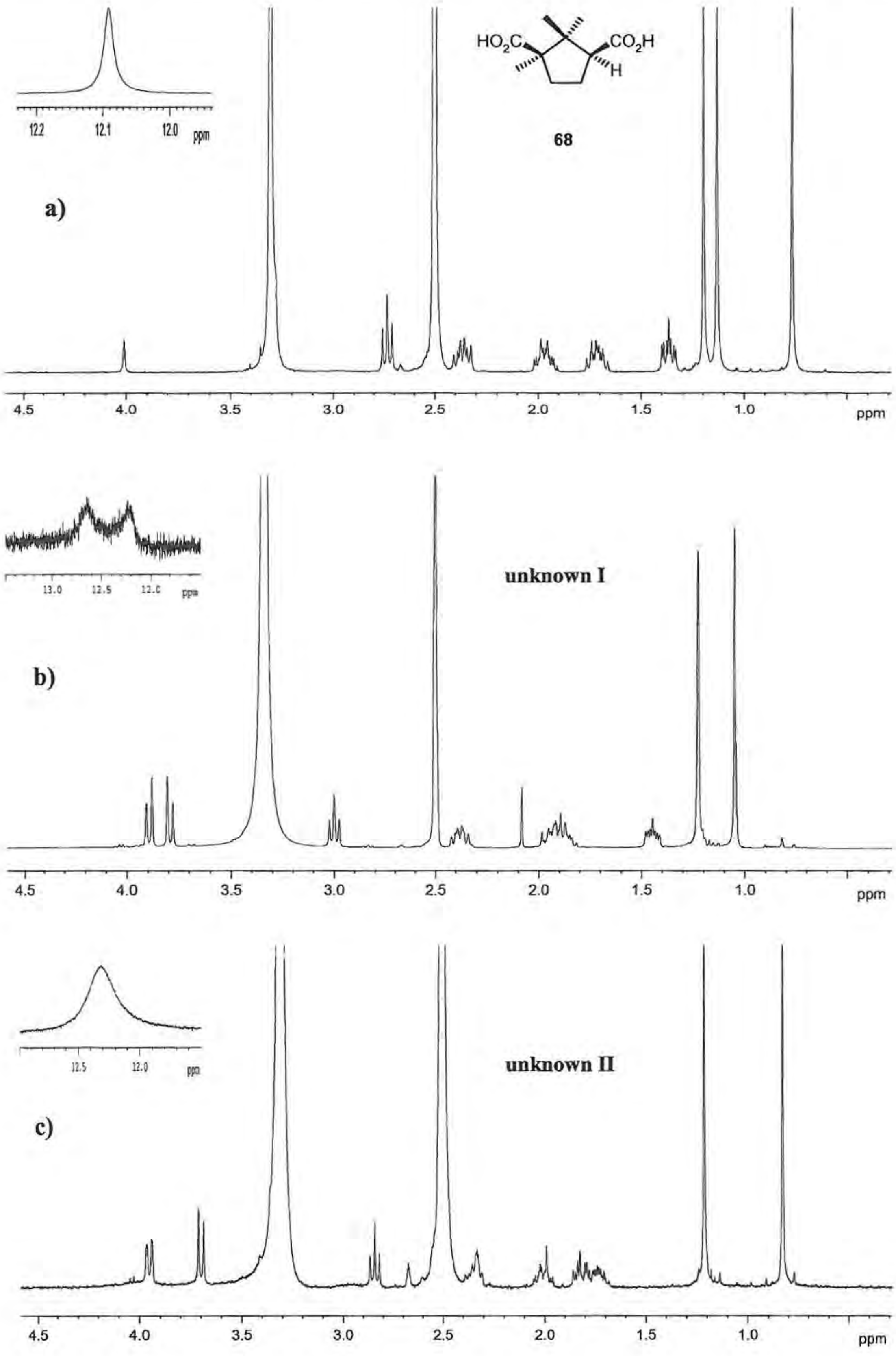

Figure 41. 400MHz ^{1}H NMR spectra of a) camphoric acid **68** and the two unknown compounds **I** (b) and **II** (c) in DMSO-d_6.

On the basis of the abovementioned assumptions, three possible structures seemed likely, *viz.*, the desired 8-bromocamphoric acid **43**, the previously synthesized 9-bromocamphoric acid **66** (Scheme 41), and the diastereomeric system **69** which, although not an anticipated product, would also fit the acquired data. These three potential products were geometry-optimised at the DFT level (figure 42), and their relative energies calculated (Table 12). On the basis of these calculations, structure **69** would appear to be the most energetically favourable, and the sterically crowded 8-bromocamphoric acid **43** least favourable. However, because there is no obvious mechanism at hand for the formation of these species, and the calculated energy differences are relatively small, this data cannot be used to assign structures to the reaction products with any degree of certainty.

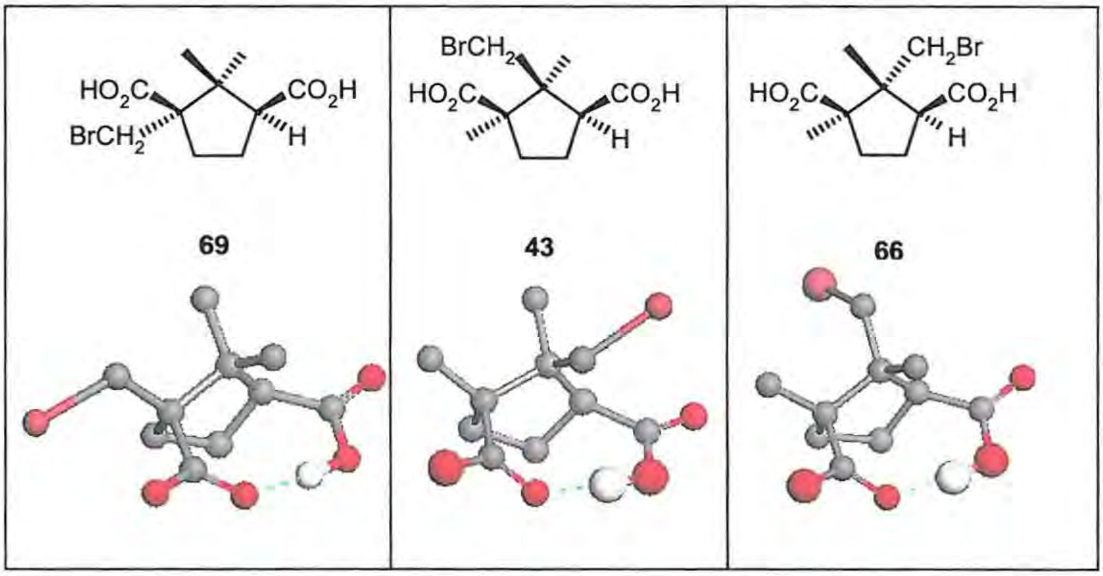

Figure 42. DFT geometry-optimised structures of possible minor products of the hydrolysis of 8-bromocamphoric anhydride **62** (Scheme 42). Protons are omitted unless involved in hydrogen-bonding interactions.

Table 12. Electronic (E) and Gibbs free energies (G) for possible minor products of the hydrolysis of 8-bromocamphoric anhydride **62** (Scheme 42).

Molecule	**E (Hartrees)**	**G (Hartrees)**	**ΔG_{rel} (kcal/mol)**
69	-3265.4343748	-3265.2355534	0
66	-3265.4329019	-3265.2335355	1.27
43	-3265.4285282	-3265.2295331	3.78

Suitable crystals of unknown I (Scheme 42; Figure 41) were obtained by recrystallisation from ethanol. Single crystal X-ray analysis revealed the structure to be, somewhat surprisingly, (1*S*,3*S*)-1-bromomethyl-2,2-dimethylcyclo-pentane-1,3-dicarboxylic acid **69** (Figure 43).

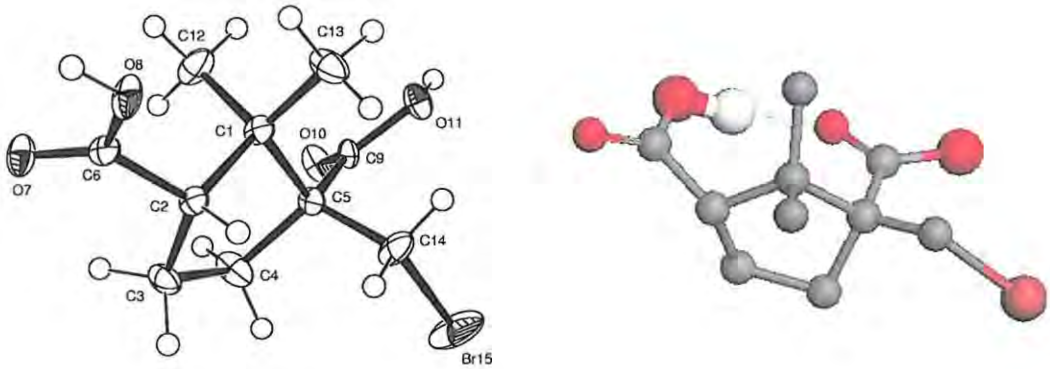

Figure 43. a) X-ray crystal structure of (1*S*, 3*S*)-1-bromomethyl-2,2-dimethylcyclopentane-1,3-dicarboxylic acid **69**, showing the crystallographic numbering.
b) DFT geometry-optimised structure **69** (protons omitted for clarity, except where hydrogen bonding is indicated).

A comparison of Figures 43 (a) and (b) shows a reasonable reproduction of the crystal structure of compound **69** by DFT geometry-optimisation techniques. However, these structures also highlight a potential pitfall in using gas-phase calculations to compare the geometries and energies of condensed-phase compounds. The DFT-optimised structure displays intramolecular hydrogen bonding between the free carboxylic acid functionalities. However, in the crystal lattice, this compound is packed in an *inter*molecularly H-bonded polymeric array (Figure 44). This highly ordered crystalline arrangement clearly affects the conformational arrangement of the individual molecules and highlights the need to treat the gas-phase computational data for these compounds with some caution.

Despite the above-mentioned conformational discrepancies, the calculated bond lengths (Table 13) compare reasonably well with those determined by X-ray crystal structure analysis. As expected, the largest discrepancies arise in the carbon-oxygen bonding distances to oxygen atoms that are involved in hydrogen bonding (see Figure 44). The over-estimation of the calculated C14-Br15 bonding distance can be ascribed to an absence, in the calculated structure, of the steric crowding present in the crystal packing arrangement. Corresponding discrepancies are also evident in the bond angle calculations (Table 14).

Table 13. Selected Bond lengths (in Å) for species **69** as determined by single crystal X-ray analysis, and as calculated from the DFT geometry-optimised structure, showing the error in the calculated values.

Bond	X-Ray	DFT	Error
C1-C2	1.557	1.590	0.033
C1-C12	1.543	1.537	-0.006
C1-C13	1.540	1.546	0.006
C1-C5	1.583	1.613	0.030
C2-C3	1.541	1.547	0.006
C2-C6	1.515	1.533	0.018
C3-C4	1.536	1.530	-0.006
C4-C5	1.538	1.553	0.015
C5-C14	1.532	1.524	-0.008
C5-C9	1.524	1.544	0.020
C6-O7	1.222	1.217	-0.005
C6-O8	1.311	1.348	0.037
C9-O10	1.215	1.224	0.009
C9-O11	1.320	1.344	0.024
C14-Br15	1.947	2.026	0.079

Mean absolute error of calculated bond lengths = 0.020 Å

Table 14. Selected Bond angles (in degrees) for species **69** as determined by single crystal X-ray analysis, and as calculated from the DFT geometry-optimised structure, showing the error in the calculated values.

Angle	X-Ray	DFT	Error
C1-C5-C9	111.6	110.5	-1.1
C1-C5-C14	110.1	109.3	-0.8
C1-C2-C6	112.9	116.4	3.5
C1-C2-C3	105.9	107.2	1.3
C2-C1-C12	111.1	115.7	4.6
C2-C1-C13	111.9	105.7	-6.2
C2-C6-O7	123.4	121.5	-1.9
C2-C6-O8	113.2	117.3	4.1
C2-C3-C4	106.5	105.5	-1.0
C3-C4-C5	106.2	105.2	-1.0
C4-C5-C1	103.4	102.5	-0.9
C4-C5-C14	112.2	113.1	0.9
C4-C5-C9	112.0	107.1	-4.9
C5-C14-Br15	111.6	115.6	4.0
C5-C9-O10	123.7	123.0	-0.7
C5-C9-O11	112.4	119.5	7.1
C5-C1-C13	114.3	111.3	-3.0
C5-C1-C12	109.6	113.4	3.8
C5-C1-C2	100.5	104.1	3.6
C1-C5-C9	111.6	110.6	-1.0
C1-C5-C14	110.1	109.3	-0.8
C1-C2-C6	112.9	116.4	3.5
C1-C2-C3	105.9	107.2	1.3
C12-C1-C13	109.3	106.4	-2.9

Mean absolute error of calculated bond angles = 2.7°

The polymeric H-bonded array formed by this novel compound **69** in its crystalline state (Figure 44) warrants further mention. While camphor derivatives have been commonly employed as chiral reagents and catalysts, their application as crystalline chiral host compounds (clathrates) has not been exploited. There are very few reports of camphor-derived clathrates in the literature,[113] but in one such report, Korkas *et al.* achieved enantiomeric separation of racemic mixtures of numerous chiral compounds *via* co-crystallisation with a terpenoid diol system.[113]

The highly ordered chiral array formed by compound **69** would appear to render it an ideal candidate for chiral molecular recognition studies of crystalline compounds. The H-bonded system provides an ordered crystalline backbone, while the bromine atoms provide a means of generating a series of substituted derivatives that could be used to tailor the system to the geometry of a potential guest complex. Possible applications of this compound will be explored further within the group.

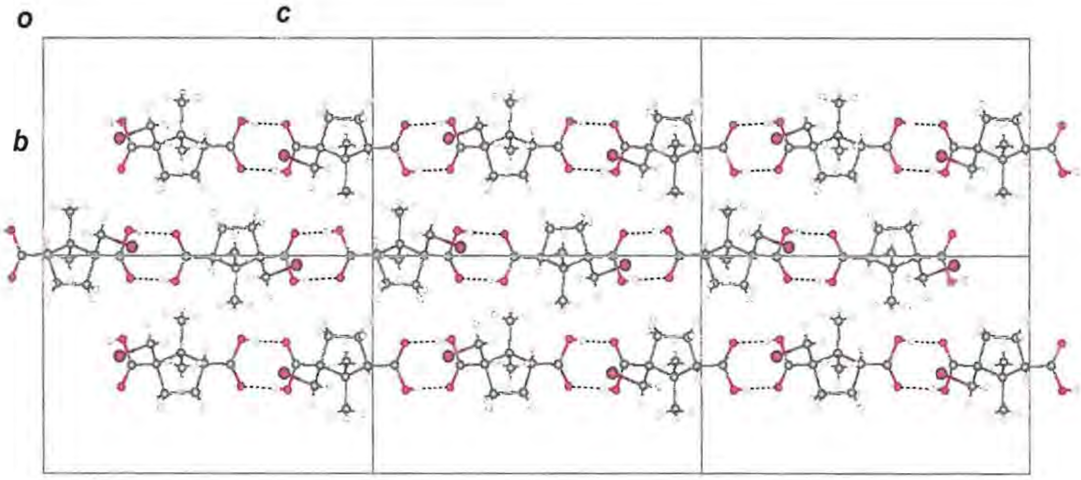

Figure 44. Polymeric H-bonded arrays of the crystalline diacid **69**.

The ^{1}H and ^{13}C NMR assignments for the novel compound **69** are shown in Figures 45 and 46. The 6-methylene protons and the 3-methine proton were identified by their characteristic splitting patterns, while the 7- and 8-methyl signals were distinguished by the relative strength of the *syn*- and *anti*- deshielding effects of the carboxylic acid groups (Figure 45). The remainder of the assignments were made on the basis of two-dimensional HMQC and HMBC correlations.

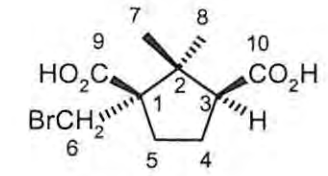

69

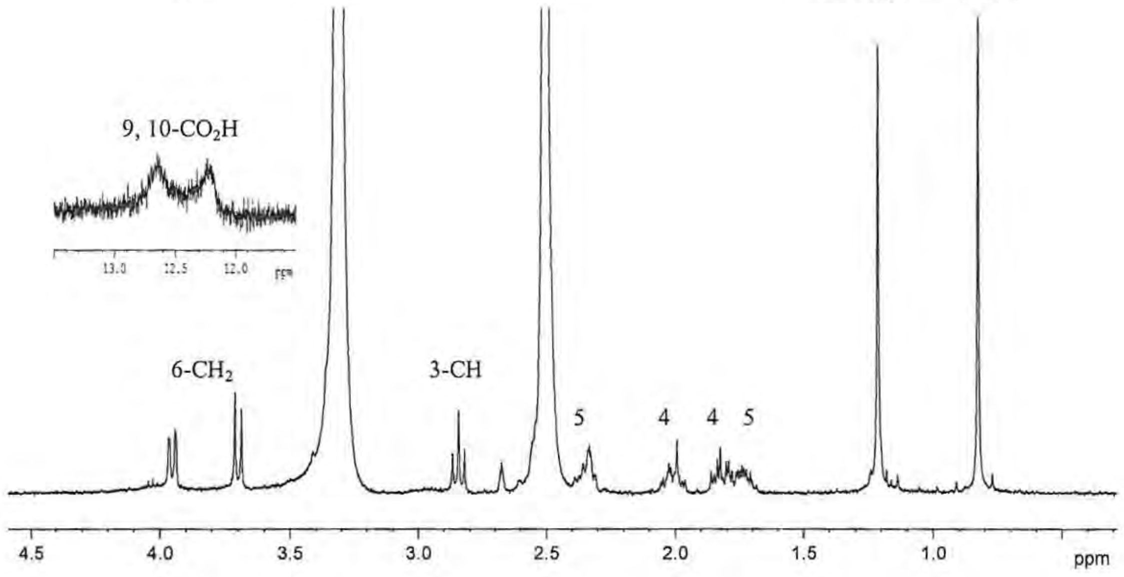

Figure 45. 400MHz ^{1}H NMR spectrum of diacid **69** in DMSO-d_6.

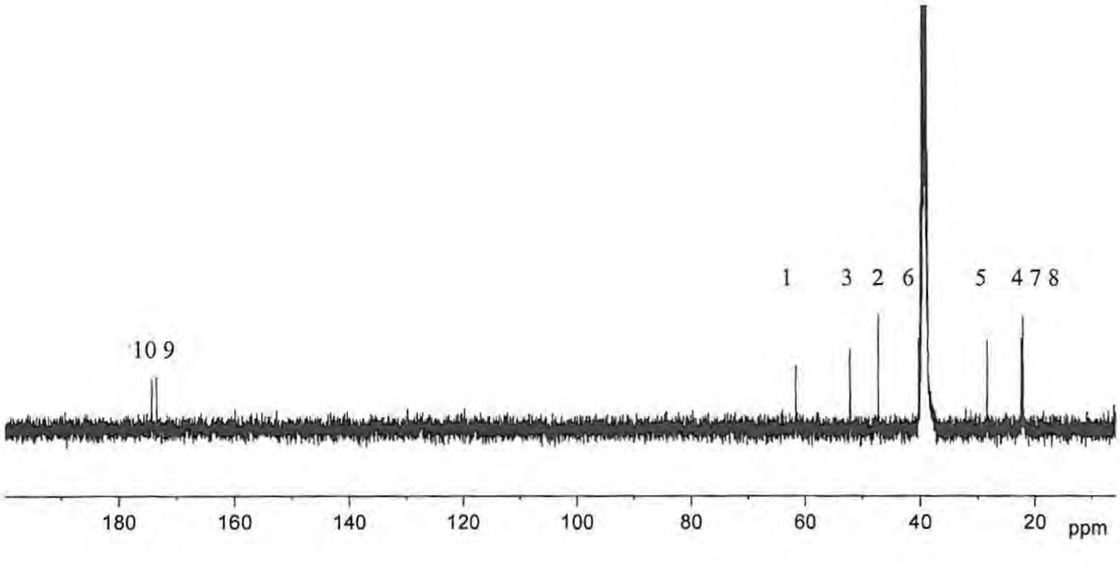

Figure 46. 100MHz ^{13}C NMR spectrum of diacid **69** in DMSO-d_6.

The remaining diacid product (unknown II; Scheme 42) was subsequently identified as 9-bromocamphoric acid **66** by matching of the ^{1}H and ^{13}C NMR spectra to those of a sample of compound **66** synthesised previously (Scheme 41).

The structural similarity of the bromocamphoric acids **43**, **66** and **69**, and of the lactones **63** and **67**, and the resultant difficulties in characterising them by NMR spectroscopy, are fairly typical problems encountered in the chemistry of camphor derivatives. For this reason it was decided to assess the reliability of the GIAO NMR prediction tool, available as part of the GAUSSIAN software package,[114] in predicting the ^{13}C NMR spectra of a number of our camphoric acid derivatives, and to determine whether the method is accurate enough to distinguish between compounds as structurally similar as the bromocamphoric acids **43** and **66**. The prediction method was tested by comparing the ^{13}C NMR data for four of the synthesised compounds (**63**, **68**, **62** and **69**) with predicted data from GIAO calculations at the HF/6-311+G(2d,p) level of structures optimised at the DMol^3/GGA/PW91/DNP level. The calculated ^{13}C shifts are referenced to TMS, optimised at the same level of theory. The data depicted in Figures 47 and 48 (see Section 3.1.3, Tables 25 through 28) shows reasonable correlations between calculated and experimental chemical shifts, but in all cases, the computational technique tends to exaggerate the deshielding of the carbonyl carbons. This trend is also evident, although to a lesser extent, for the carbons adjacent to the bromine atoms in compounds **62** and **69**.

Figure 49 shows the chemical shift comparisons between the experimental data for 9-bromocamphoric acid **66**, and the calculated shifts for compounds **66** and **43** (see Section 3.1.3, Table 29). The correlation between calculated and experimental chemical shifts was slightly better for compound **66** ($r^2 = 0.998$) than for compound **43** ($r^2 = 0.995$). However, of greater significance than the total correlation (given that both r^2 values fall within the range obtained for the model compounds), are the specific correlations for the bromomethyl side-chain. Closer inspection of Figure 49 reveals that fitting of the computed data with the experimental chemical shifts for compound **66** is consistent with the observed tendency to exaggerate the deshielding effect of the bromine atom, while the computed chemical shift for carbon 8 in compound **43** is lower than the corresponding observed signal, and significantly lower (by 11.2 ppm) than the corresponding calculated signal for carbon 9 in compound **66**.

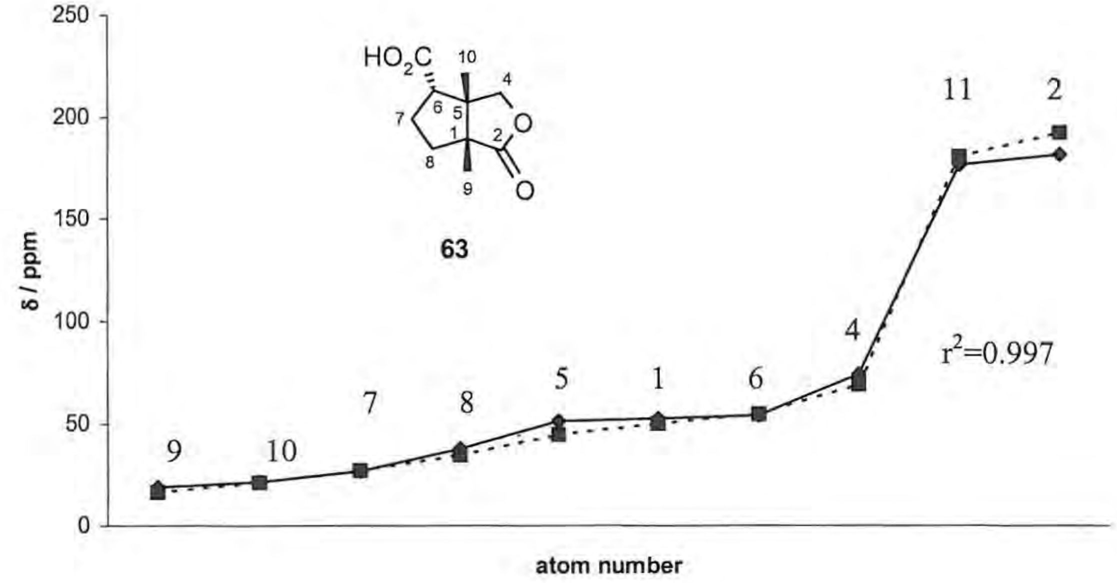

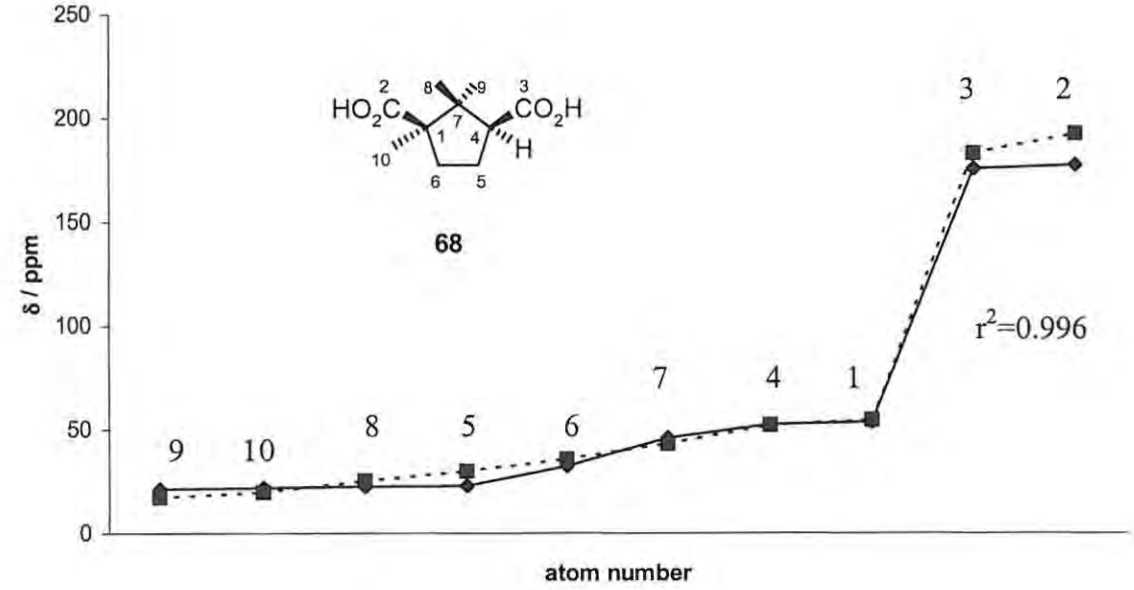

Figure 47. ^{13}C NMR chemical shift comparisons between experimental (solid lines) and GIAO[HF/6-311+G(2d,p)] calculated values (dashed lines) for compounds **63** (top) and **68** (bottom).

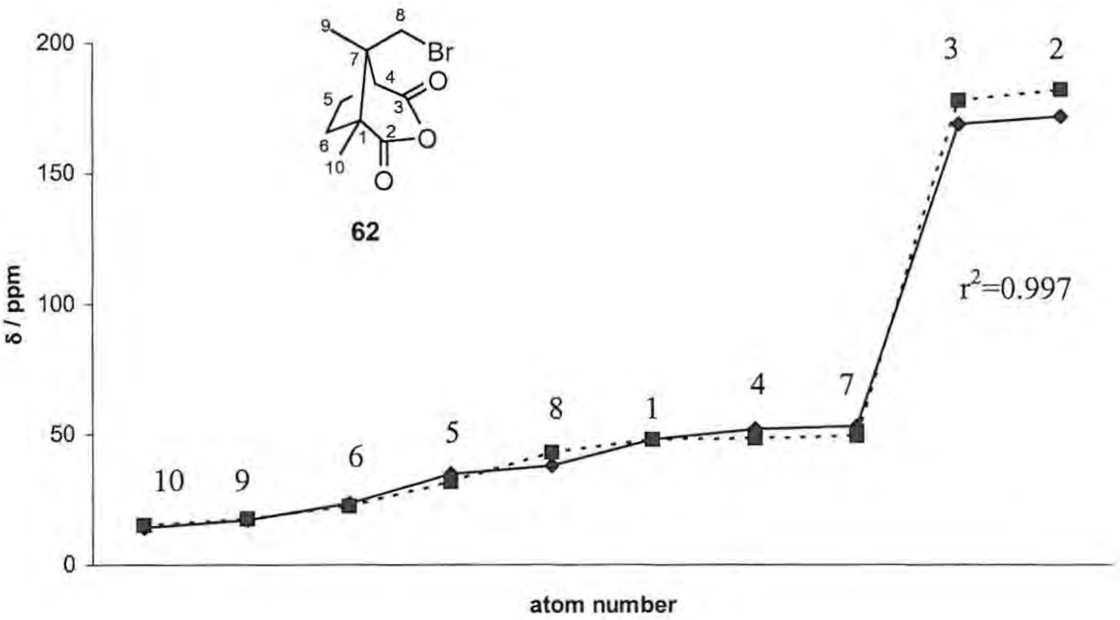

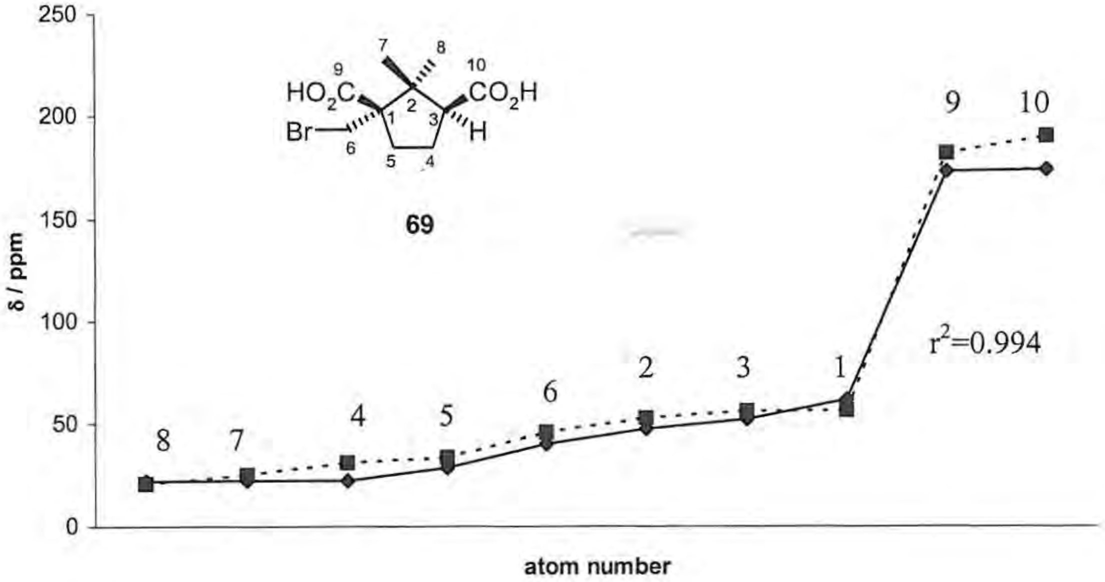

Figure 48. ^{13}C NMR chemical shift comparisons between experimental (solid lines) and GIAO[HF/6-311+G(2d,p)] calculated values (dashed lines) for compounds **62** (top) and **69** (bottom).

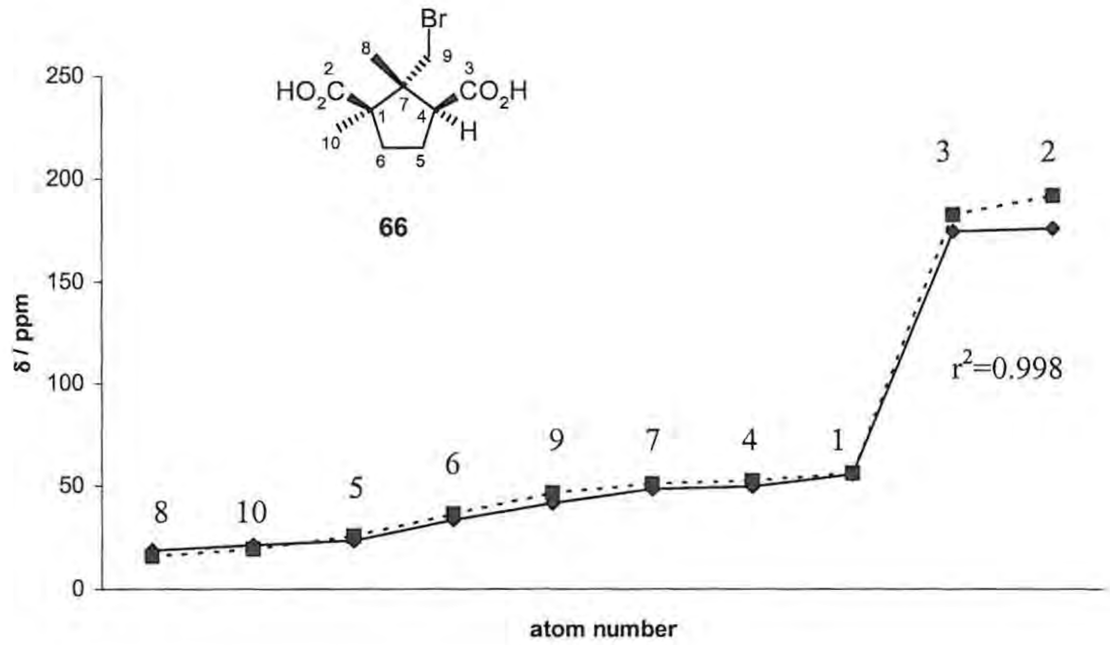

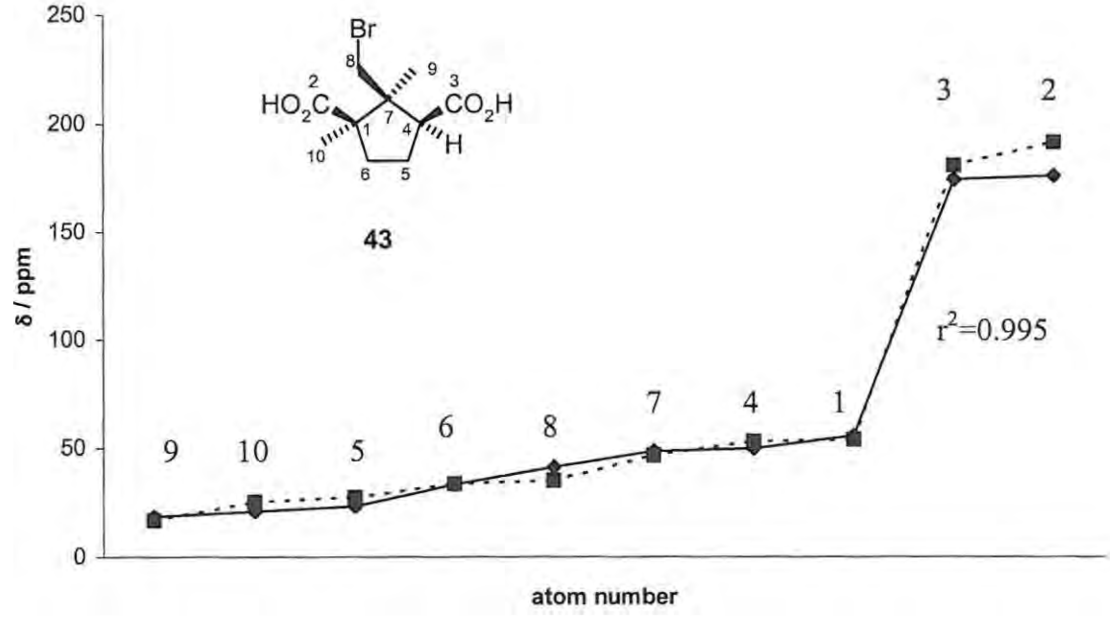

Figure 49. ^{13}C NMR chemical shift comparisons between experimental values (solid lines) determined for compound **66**, and GIAO[HF/6-311+G(2d,p)] calculated values (dashed lines) for compounds **66** (top) and **43** (bottom).

The computational data is thus consistent with the assignment of structure **66** to unknown II, in that i) it suggests that the ^{13}C NMR spectrum for 8-bromocamphoric acid **43** is appreciably different to that of 9-bromocamphoric acid **66**, and ii) a marginally better fit is obtained for experimental shift data with that of computed data for compound **66** than for compound **43** (Figure 49). This methodology thus shows some potential as a tool for the identification of compounds that cannot be unambiguously characterised by NMR analysis. It is not, however, a sufficiently reliable technique to be applied in isolation, and examination of several structurally similar model compounds is clearly useful in assessing trends in the over- or underestimation of experimental chemical shift data.

The complete set of products obtained from the hydrolysis of 8-bromocamphoric anhydride **62** (Scheme 42) thus comprises the lactone **63**, camphoric acid **68**, and the bromocamphoric acids **66** and **69** (Scheme 43). The reaction was repeated several times, affording varying ratios of lactone to acid products. While no yield optimisation studies were performed, it is suspected that the lactone : acid ratio is a function of pH. The ratio of acid products **68**:**66**:**69** remained roughly constant at 1:2:2. The anhydride **62** was also observed to undergo spontaneous transformation to the lactone **63** upon standing for several weeks under atmospheric conditions. The apparent absence of 8-bromocamphoric acid **43** from the product mix would seem to suggest that, if formed at all during the reaction, it readily undergoes cyclisation to form the corresponding lactone **63**. As yet, we have no mechanistic explanation for the formation of the bromocamphoric acids **66** and **69**, but suspect that it involves rearrangement of the camphor skeleton prior to hydrolysis of the anhydride. While there are, to the best of our knowledge, no literature reports involving rearrangements of 8-substituted camphoric anhydrides, α-bromocamphoric anhydrides haves been known to undergo numerous complex rearrangements.[114]

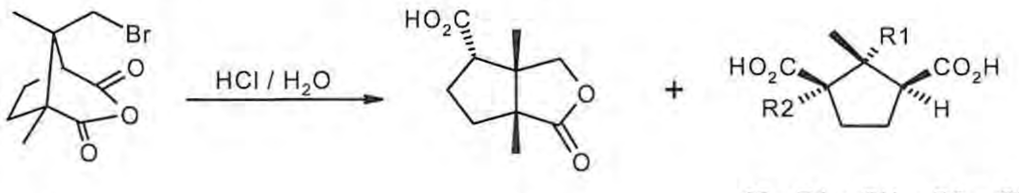

62

63

68: R1 = CH_3 ; R2 = CH_3
66: R1 = CH_2Br ; R2 = CH_3
69: R1 = CH_3 ; R2 = CH_2Br

Scheme 43

A second approach to the ring-opening of the anhydride **62** involved treatment with lithium aluminium hydride, with the expectation that reduction of the carbonyl groups would yield the corresponding diol **70** (Scheme 44) - a method that has been successfully applied to 9-bromocamphoric anhydride.[106] However, ^{1}H NMR analysis showed no signals characteristic of camphor derivatives. Although the starting material was consumed, no identifiable products were isolated from this reaction.

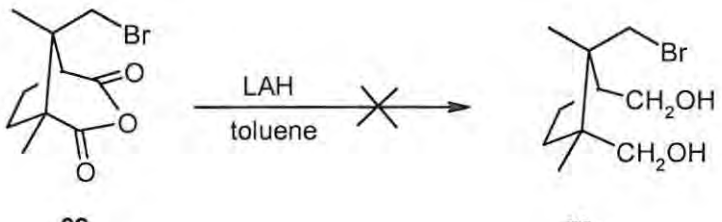

62 **70**

Scheme 44

Given the difficulties encountered in ring-opening of the 8-brominated camphor derivatives, it was decided to attempt the displacement of the bromine at position 8 by a phosphine group at an earlier stage of the synthesis, in the anticipation that the bulky phosphine group could result in a more robust system - one less prone to undergo skeletal rearrangements. It was therefore decided to return to 8-bromocamphorquinone **61** as a potential substrate. This approach would, however, require protection of the ketone moieties, as they would be vulnerable to attack by the incoming phosphine. Ethylene glycol was selected as the protecting group, and attached using a literature procedure (Scheme 45).[116]

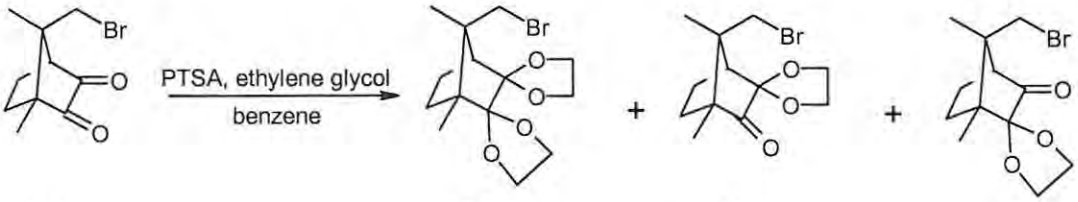

61 **71** **72** **73**

Scheme 45

Unfortunately, this reaction afforded the novel diprotected camphorquinone **71** as a yellow crystalline solid in only 5% yield, with the monoprotected compounds **72** and **73** in combined 50% yield as an inseparable mixture. The structure of the camphorquinone **71** was confirmed by NMR spectroscopy and high-resolution MS analysis. The HMQC spectrum (Figure 50) clearly indicates the presence of the ethylene glycol protecting groups, and the retention of all other functionalities with the exception of the carbonyl moieties. Attempts to improve the yield of the protected 8-bromocamphorquinone **71** by refluxing in toluene for 5 days proved unsuccessful.

In a final attempt to introduce a phosphine group, unprotected 8-bromocamphoric anhydride **62** was treated with lithium diphenylphosphide (Scheme 46), following a literature procedure developed for protected and unprotected 8-brominated camphor derivatives.[117] This procedure returned approximately 50% unreacted starting material, and 40% camphoric anhydride **74**. NMR analysis of a third product, isolated in trace amounts, showed retention of the signals characteristic of the diastereotopic 8-methylene protons, but the absence of carbonyl signals in the ^{13}C spectrum indicated the expected loss of carbonyl functionality in the absence of protecting groups.

Although the foregoing syntheses provided opportunities for several interesting structural and theoretical studies, viable access to camphor-derived ligand species remained elusive, and it was decided to pursue alternative approaches to multidentate ligands.

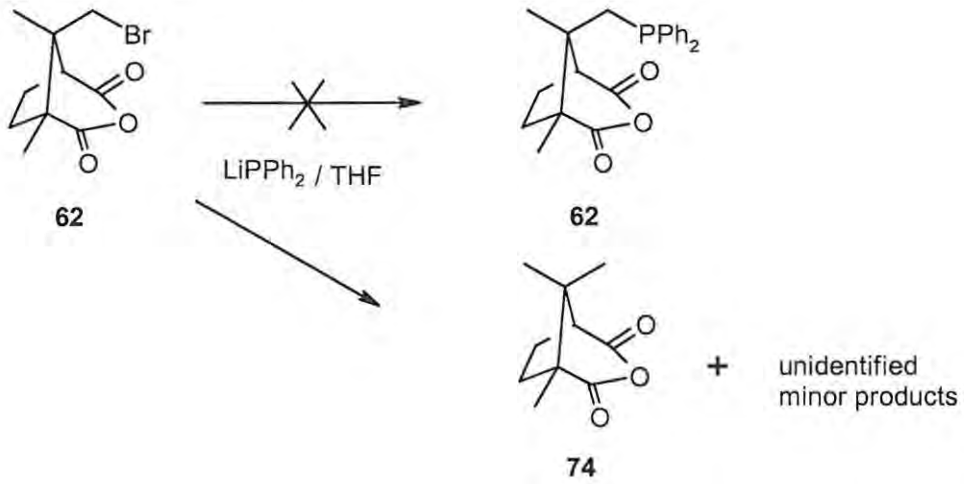

Scheme 46

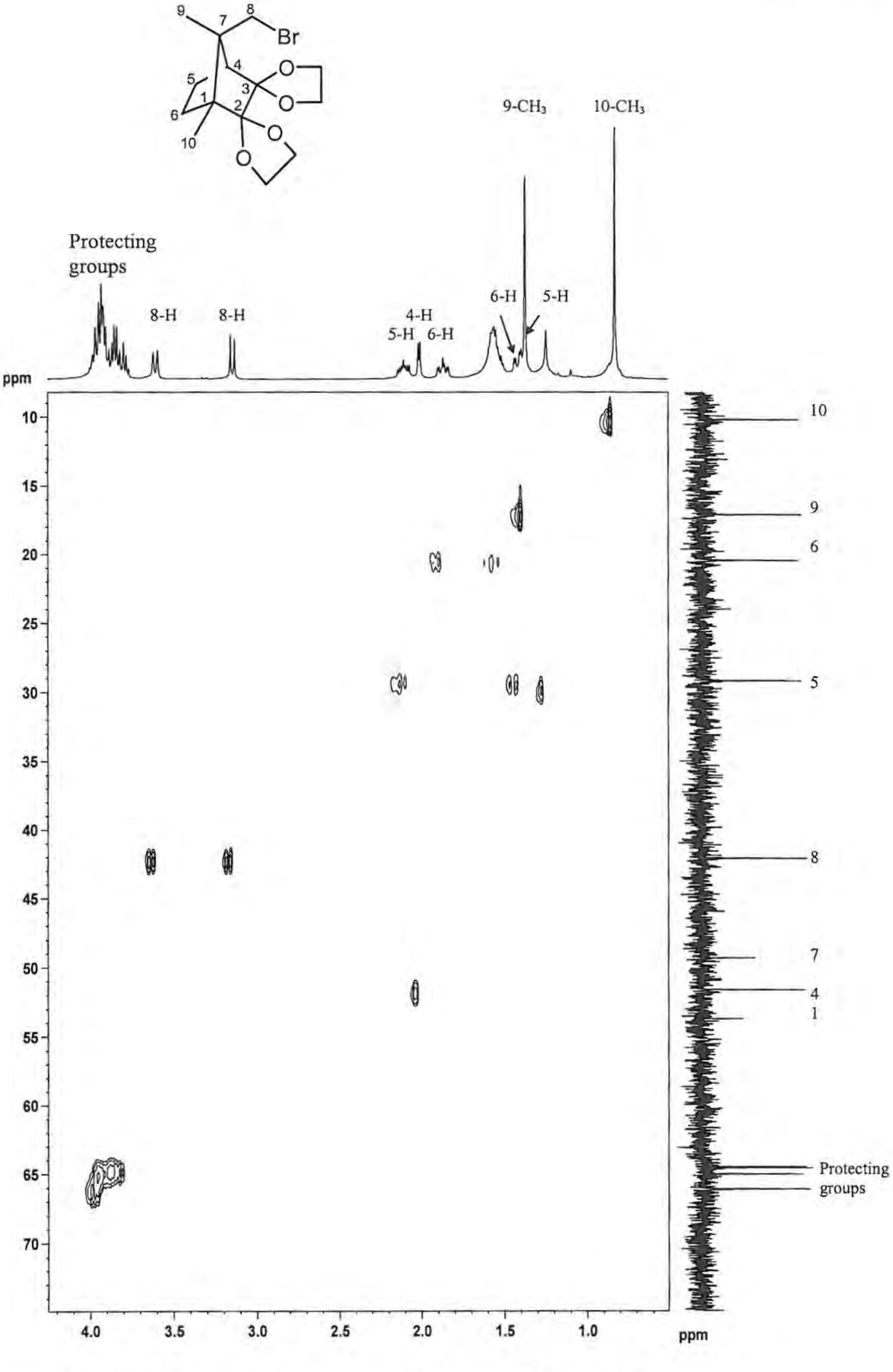

Figure 50. 400MHz HMQC spectrum of compound **71** in $CDCl_3$.

2.3 RUTHENIUM COMPLEXATION STUDIES

2.3.1 Chloride substitution in the Grubbs 1st-generation catalyst $RuCl_2(PCy_3)_2CHPh$ (14)

Several preliminary syntheses were undertaken in order to establish the methodology for chloride substitution in Grubbs-type ruthenium complexes. The first of these was a repeated synthesis of the ruthenium carboxylate dimer **75** reported by Mol and co-workers (Scheme 47).[93] Numerous unsuccessful attempts were made to carry out this transformation, but the only product isolated was $AgClPCy_3$ **76**, which was obtained in an average yield of 65%, and identified by ^1H, ^{13}C and ^{31}P NMR spectroscopy.

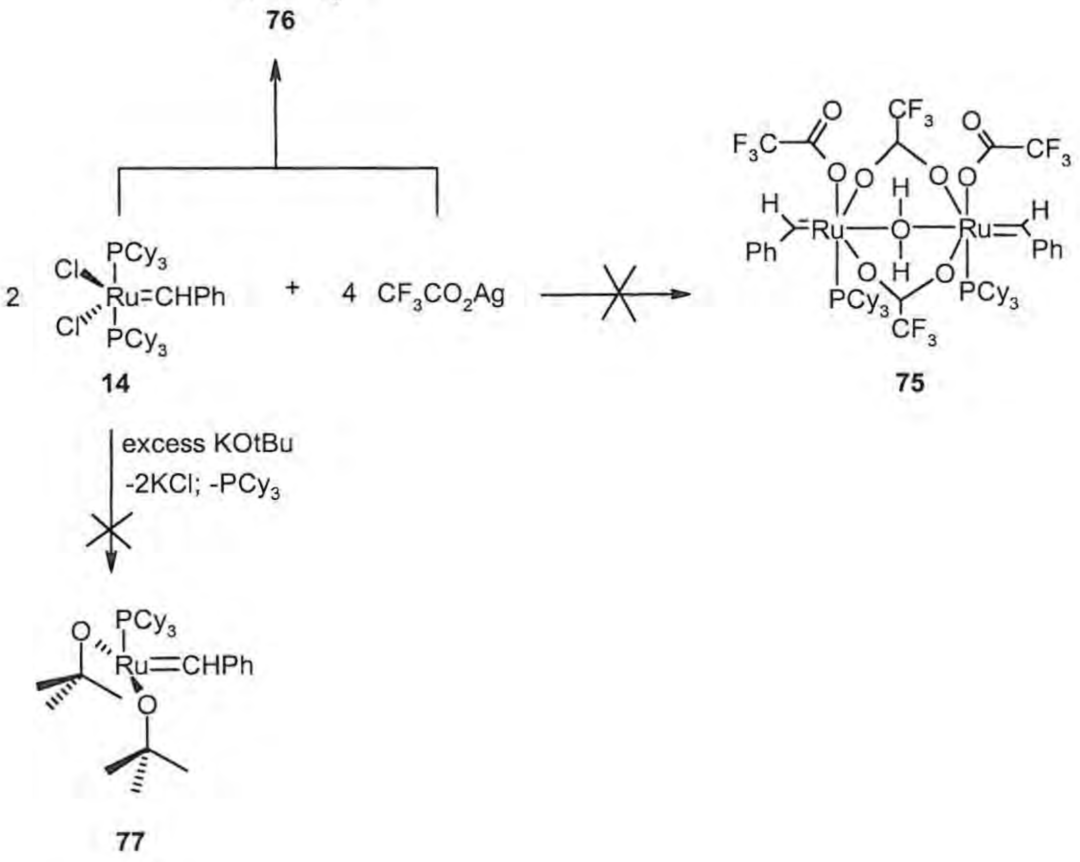

Scheme 47

Subsequent correspondence with the authors[118] suggested the source of the difficulties to be the reaction solvent which, in their case, contained 40 ppm of H_2O, and provided the bridging H_2O molecule present in the dimeric product **75**. Moreover, they confirmed the limited stability of the dimer **75** in the presence of trace contaminants. Other workers have also reported a lack of stability of phosphine-containing species in syntheses involving silver salts, due to the formation of AgCl and $AgClPCy_3$.[119]

An attempt was also made to synthesise the 4-coordinate *tert*-butoxy complex **77** reported by Grubbs and co-workers (Scheme 47).[94] While this reaction appeared to proceed as reported (*i.e.* the relevant reported colour changes were observed), separation of the released phosphine ligand from the product by the addition of a CuCl phosphine scavenger proved to be problematic, resulting in the decomposition of any carbenes present in the reaction mixture.

2.3.2 Chloride substitution in the Grubbs-Hoveyda catalyst (78)

2.3.2.1 Sulfonate, carboxylate and tert-butoxide ligands

Given that the difficulties encountered thus far seemed to arise from the phosphine moiety, we turned our attention to the new-generation, phosphine-free catalysts, which are reported to exhibit vastly increased stability in the presence of oxygen and trace contaminants.[120] The styrenyl ether complex **78** (Scheme 48) developed by Hoveyda and co-workers is of particular interest due to its reported utility in the context of cross-metathesis,[120] and its potential for the development of supported[121] and chiral, optically pure variants.[59] As a benchmark reaction, the chloride exchange reaction reported by Krause *et al.* (Scheme 48)[119] was repeated. The reaction proceeded smoothly, affording complex **79** in 75% yield within 20 minutes. The synthesis and metathesis activity of complex **79** was reported as part of a recent study by Krause *et al.*,[119] who concluded that the attachment of strongly electron-withdrawing ligands (*e.g.*, the trifluoroacetate groups in complex **79**) enhances the stability *and* activity of Grubbs-Hoveyda type catalysts.

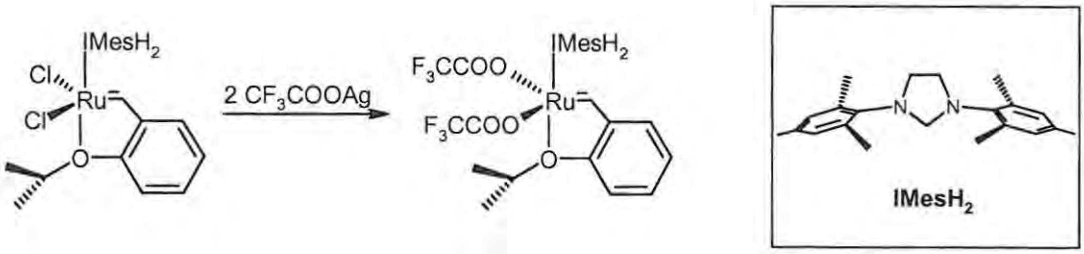

78 **79**

Scheme 48

This finding appears to contradict previous work reported on 1st-generation Grubbs-type systems,[122] which has shown that, in general, an increase in the electron-*donating* character of the ligands leads to enhanced metathesis activity, due to greater lability of the phosphine leaving group.

Furthermore, it was reported that the observed ^{1}H NMR chemical shifts[119] for the complexes **79** – **81** (Figure 52) did not appear to fit the trends reported by Hoveyda and co-workers[120] who, in comparing the ^{1}H NMR spectra of complex **78** with the parent system **20** (Figure 51), noted that the stronger electron donation by the heterocyclic ligand (IMesH$_2$) in complex **78** (relative to the PCy$_3$ ligand in complex **20**), resulted in increased electron density at the ruthenium centre, manifested by:-

i) greater shielding of the carbene proton H_α; and

ii) an upfield shift of the isopropyl methine proton H_β, reflecting weaker electron donation by the axial phenoxy ligand to the ruthenium centre.

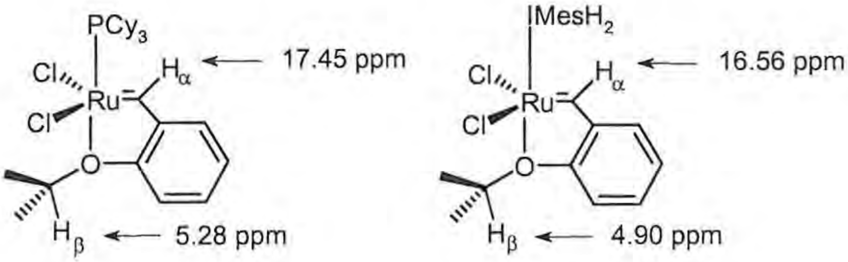

20 **78**

Figure 51. Selected ^{1}H NMR chemical shifts for complexes **20** and **78**.[120]

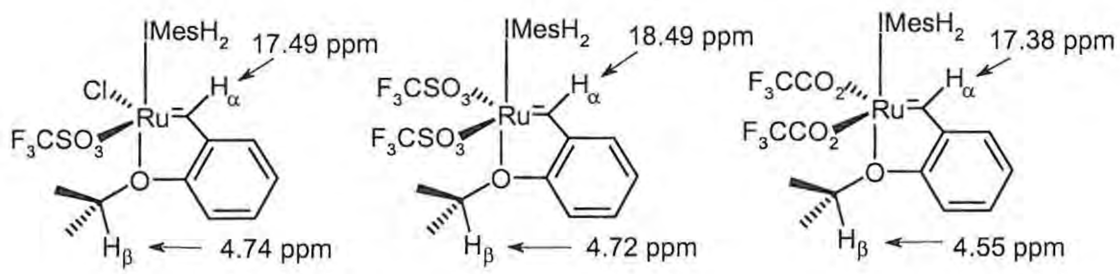

80 **81** **79**

Figure 52. Selected ^{1}H NMR chemical shifts for complexes **79** - **81**.[119]

Table 15. Hammett parameters (σ_m) and field/inductive parameters (F) of electron-withdrawing ligands in complexes **78-81**.[123]

Substituent	σ_m	**F**
-Cl	0.37	0.42
$-OSO_2CF_3$	0.56	0.56
$-OCOCF_3$	0.56	0.58

The observations made by Krause *et al.*[119] would appear to suggest that their assessment of ligand electron-withdrawing ability was based purely on σ-electron-withdrawing effects. Table 15 shows the relative σ-electron-withdrawing effects of the ligands employed in the series of complexes **78-81** (Figures 51 and 52) as described by the Hammett parameters (σ_m) and field/inductive parameters (F).[123] Both of these empirical descriptors are considered to be relatively accurate indicators of the electron-withdrawing effect of substituents (the higher the value the greater the electron-withdrawing ability), the F parameter being a refinement of the Hammet parameter in which resonance or polarization effects are omitted.[123]

The mono- and disubstituted complexes **80** and **81** (Figure 52) show the expected trend in the progressive deshielding of the carbene proton H_α with the addition of one, and then two, electron-withdrawing CF_3SO_3 ligands. However, based on the parameters in Table 15, the presence of the two CF_3CO_2 ligands in complex **79** should result in deshielding of H_α, which is greater than, or at least equivalent to, that observed in complex **81**. This is clearly not the case, as the H_α nucleus in complex **79** resonates upfield of H_α in both complexes **80** and **81**.

Moreover, the upfield shift of the isopropyl methine proton H_β (by *ca.* 0.2 ppm) in the series **80**→**81**→**79** would appear to indicate a weakening of the bond between the ruthenium and the chelating phenoxy ligand and thus an increase in the electron density at the ruthenium centre. These anomalous observations led Krause *et al.*[119] to conclude that the correlation noted by Hoveyda between ^1H NMR chemical shifts and electron density at the ruthenium centre did not hold true for complexes **79-81**. However, they did not consider the possibility of a π-donor interaction between the ligand and the ruthenium. In view of the apparent contradictions, it was decided to investigate the nature of the metal-ligand electronic interactions more closely.

While α-halogenation typically weakens the electron-donor ability of acids (or, more accurately, their conjugate bases),[124] the trifluoroacetate system appears to be a special case. In a detailed study of the valence orbitals of the trifluoroacetate ligand, Lichtenberger *et al.*[125] describe how the *p*-orbital electrons of each of the three fluorine atoms have a "filled-filled" interaction with the carbon-carbon σ-bond which, in turn, has a "filled-filled" interaction with the in-plane symmetric combination of the oxygen *p*-orbital electrons. The HOMO of the ligand is the anti-bonding combination of all three, which can form bonding and antibonding interactions with metal orbitals of the appropriate symmetry. In short, the nett effect of these "filled-filled" interactions is the countering of the inductive electron withdrawal by the fluorine atoms, and the potential for unanticipated ligand-metal π-interaction.

This possibility of π-donor interaction prompted a search for a better descriptor of overall ligand donor potential, *i.e.* a measure of the nett transfer of electron density from ligand to metal, including both σ- and π-effects. Perhaps the best known such parameter is Tolman's electronic parameter (TEP).[126] Originally developed for phosphines (R_3P), the TEP is based on the position of the A_1 ν(CO) infrared vibration of the nickel complex $(R_3P)Ni(CO)_3$. The observed trend is that increasing the donor power of the phosphine ligand lowers the ν(CO) vibrational frequency due to back-donation from the metal into the CO π* orbitals. Although originally an empirical measure with limited applicability, the TEP was revisited from a computational perspective by Perrin *et al.*,[126] who used DFT techniques to generate a computed electronic parameter (CEP) for a wide range of ligands using Tolman's nickel probe complex. These CEP's correlated impressively with available TEP's, thus extending the scope of the TEP concept to an apparently unlimited range of ligands.

Following the method developed by Perrin *et al.*,[126] we carried out DFT geometry optimisations and frequency calculations on the complexes $ClNi(CO)_3$ **82**, $(F_3CCO_2)Ni(CO)_3$ **83** and $(F_3CSO_3)Ni(CO)_3$ **84** (Figure 53). Carboxylate and sulfonate ligands were modelled in the unidentate binding mode (*i.e.* bonding through only one oxygen atom) to match the binding modes in complexes **79-81**, as determined by single-crystal X-ray analysis.[112] The calculated A_1 $\nu(CO)$ values for complexes **82-84** suggest the trend in nett donor potential: **82** > **83** > **84**. This observation supports the π-bonding theory, and reverses the electron-withdrawing order of the $OCOCF_3$ and OSO_2CF_3 ligands suggested by the field/inductive parameter (F) data in Table 15.

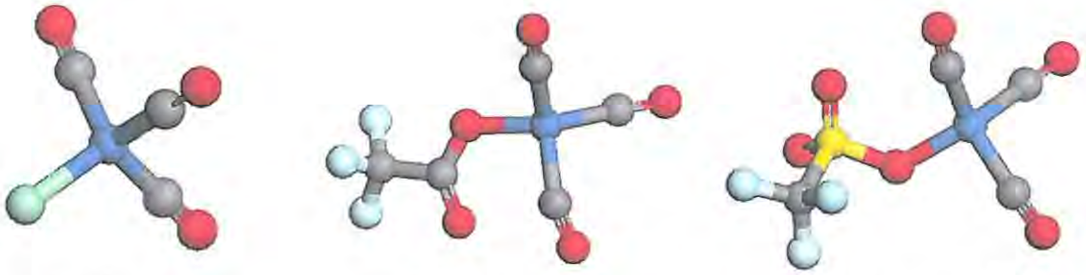

2094.93 cm^{-1} 2098.19 cm^{-1} 2113.75 cm^{-1}

82 **83** **84**

Figure 53. DFT geometry-optimised Nickel complexes for CEP calculations and the corresponding A_1 $\nu(CO)$ IR vibrational frequencies.

This reassessment of the relative electron-withdrawing ability of the ligands has two important implications for the interpretation of the results reported by Krause *et al.*[119]

1) The ^1H NMR chemical shifts shown in Figure 52 are *not* inconsistent with Hoveyda's observations.[120] The π-donor ability of the $OCOCF_3$ ligand increases the

electron density at the ruthenium centre, which causes shielding of the benzylidene proton H_α, weakening of the chelating phenoxy bond to ruthenium and, hence, further shielding of the isopropyl methine proton H_β.

2) Krause *et al.*[119] reported that, compared to the parent system **78**, complexes **80** and **81** exhibit lower catalytic activity, while complex **79** exhibits enhanced activity. They attributed this to the supposed greater electron-withdrawing ability of the $OCOCF_3$ ligand. On the contrary, however, it seems that it is the electron-*donating* ability of this ligand that enhances catalytic activity by weakening the ruthenium-oxygen bond, which must break if the catalyst is to bind to the substrate!

In order to further explore the correlation between CEP's and the shielding of the benzylidene proton H_α, the Grubbs-Hoveyda parent complex **78** was reacted with silver acetate to afford the putative di-acetate complex **85** (Scheme 49). Although not stable enough to isolate, the presence of complex **85** was inferred by the appearance of a signal in the benzylidene region of the ^1H NMR spectrum, resonating significantly upfield (δ = 14.40 ppm) of the corresponding signal from the parent complex **78** (δ = 16.56 ppm). Integration of the relative carbene signals in the ^1H NMR spectrum showed a 40% conversion to complex **85** after 3 hours of reaction time. The CEP for the acetate ligand was calculated, by geometry optimisation and frequency analysis of the nickel complex $(F_3CCO_2)Ni(CO)_3$, to be 2079.85 cm^{-1}.

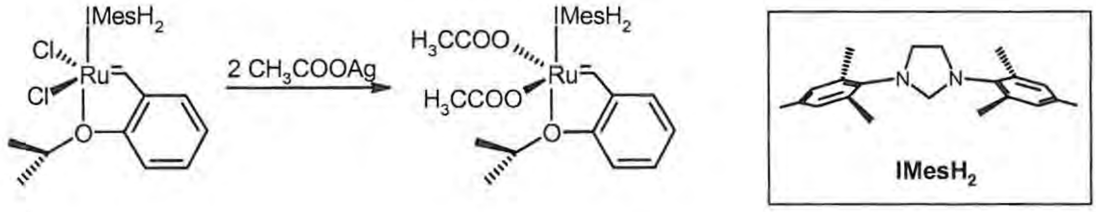

78 **85**

Scheme 49

A graphical representation (Figure 54) of the above-mentioned data shows a reasonably good linear relationship (r^2=0.9557) between ligand CEP's as measured by the A_1 ν(CO) values, and the corresponding ^1H NMR chemical shifts of the benzylidene protons H_α for the variously substituted Grubbs-Hoveyda analogues. This approach, which has not been previously applied to transition metal catalysts, promises to be a useful tool both for ligand design and for the characterisation of ruthenium complex species in solution. The latter is of particular importance as many of the catalytic species of interest are not isolable, and therefore difficult to characterise.

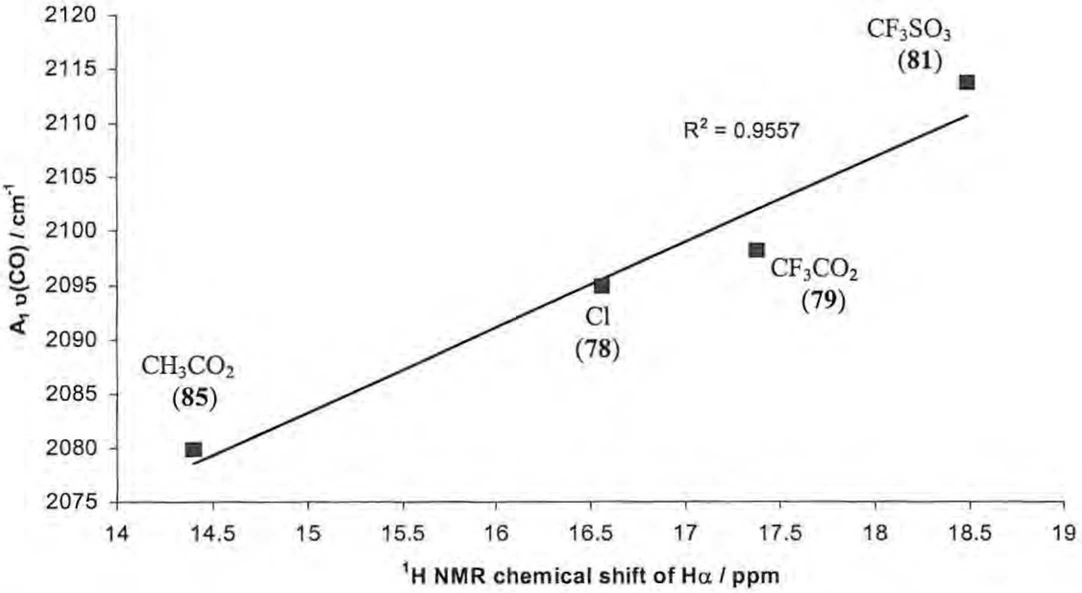

Figure 54. Plot of DFT-calculated A_1 ν(CO) frequencies of ligands *vs.* the ^1H NMR chemical shift of the benzylidene proton H_α in the corresponding disubstituted Grubbs-Hoveyda complex (in parentheses).

This study serves to highlight the significance of ligand electronic parameters in fine-tuning catalyst stability and activity. The importance of electron-withdrawing capacity, particularly with respect to complex stability, is reflected by the instability of the electron-donating acetate system **85**, and the failure of our attempted preparation of the *t*-butoxy analogue **86** (Scheme 50). The consequence of *excessive* electron-withdrawing ability, however, is reflected by the decreased activity of the trifluorosulfonate system **83**, as observed by Krause *et al.*[119]

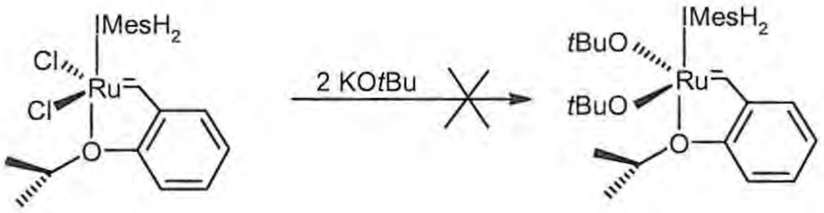

78 **86**

Scheme 50.

2.3.2.2 Malonate-derived ligands

The malonate system was an appealing option as a ligand, due to its potential for metal chelation and structural elaboration. It is known to form metal complexes in a unidentate (a) and bidentate (b) fashion (Figure 55);[127] a third mode of complexation, the bis-chelating mode (c), is unlikely in the square pyramidal ruthenium complexes under investigation, due to the preferred *trans-* arrangement of the anionic ligands.[90, 119, 121]

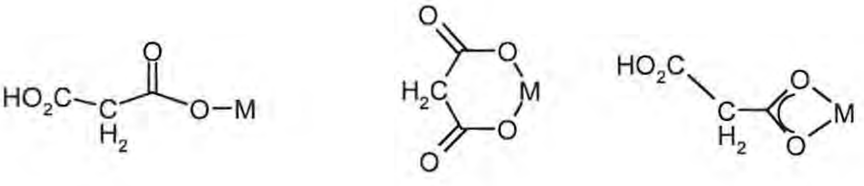

a b c

Figure 55. Binding modes of the malonate anion.[127]

An initial attempt at malonate-chloride exchange with the Grubbs-Hoveyda complex **80** was made *via* the *tert*-butyldimethylsilyl ester **87**, prepared in quantitative yield from malonic acid **86** following a textbook procedure (Scheme 51).[128] However, no reaction was observed upon stirring a solution of the silyl ester **87** and the Grubbs-Hoveyda complex **78** in THF for three hours. Upon addition of two molar equivalents of tetrabutylammonium fluoride (TBAF), to facilitate cleavage of the silyl ester groups, a sudden colour change from green to yellow was noted. ^{1}H NMR analysis of the residue, following workup, showed no signals in the carbene region, indicating decomposition of the ruthenium benzylidene functionality; in fact, no identifiable products were detected (Scheme 51).

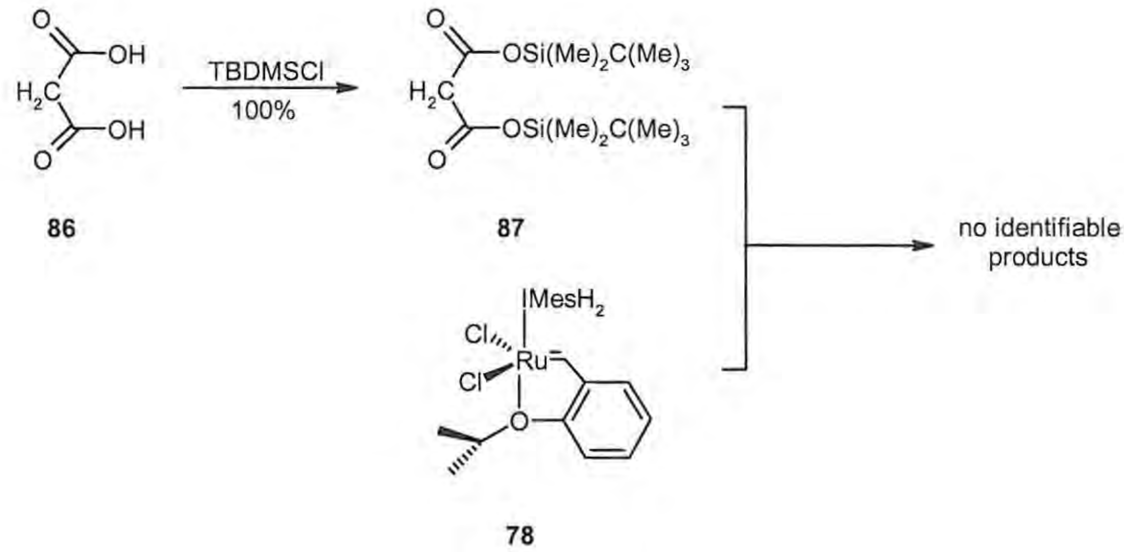

Scheme 51.

A second attempt at malonic acid complexation was made using a method developed by Hoveyda and co-workers (Scheme 52).[121] A mixture of complex **78**, silver carbonate and malonic acid **86** was refluxed in benzene-THF (1:1) and monitored hourly by ^{1}H NMR analysis. Examination of the benzylidene proton region (δ = *ca.* 17ppm) indicated formation of two new ruthenium benzylidene complexes, at maximum concentration after 3 hours of refluxing (Figures 56 and 57). Both of these complexes exhibited limited stability in solution, undergoing complete decomposition in 6-12 hours. The stability of the complexes was also assessed in benzene-d_6, in order to eliminate the possibility of interference from any acid present in the chloroform. No increase in stability was observed under these conditions. Chromatographic isolation of the products was thus impossible, as was more detailed spectroscopic analysis of the mixture. The major product, which was also the first to appear in the reaction mixture, was tentatively assigned the monosubstituted structure **88** (Scheme 52, Figure 57), based on the ^{1}H NMR data (Figure 56). While there is an equal likelihood of either chlorine atom being substituted, only one isomeric product is shown. The assignment of structure **88** is supported by the splitting of the H_γ signal, which is typically a singlet in symmetrically disubstituted species. The H_α, H_β and H_γ

signals were assigned to the respective products by matching of the relative peak integral ratios. For H$_\beta$ and H$_\gamma$, where peak overlap and multiplicity are problematic, peak integrals were assigned using the deconvolution and peak fitting functions available as part of the MestreC software package.[129]

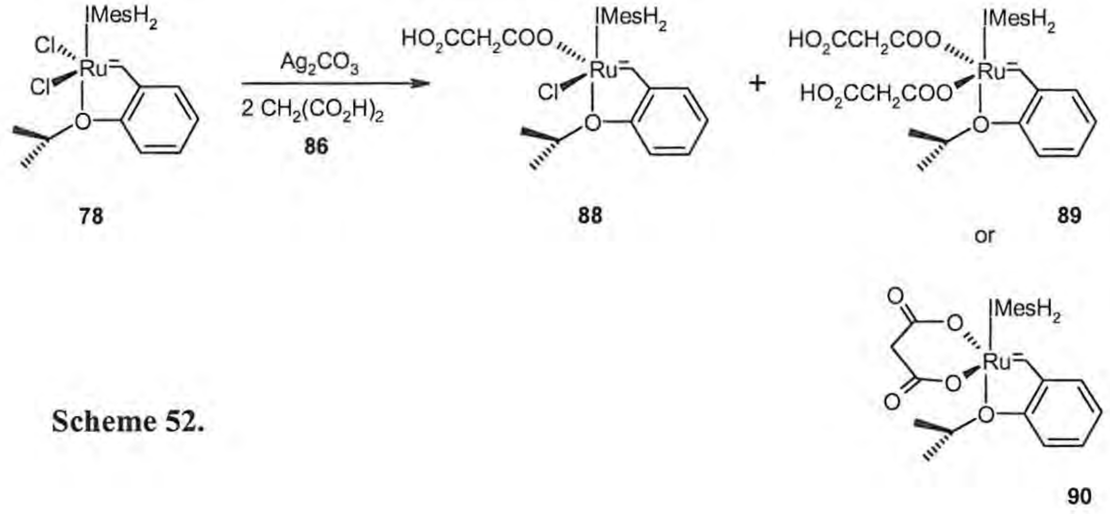

Scheme 52.

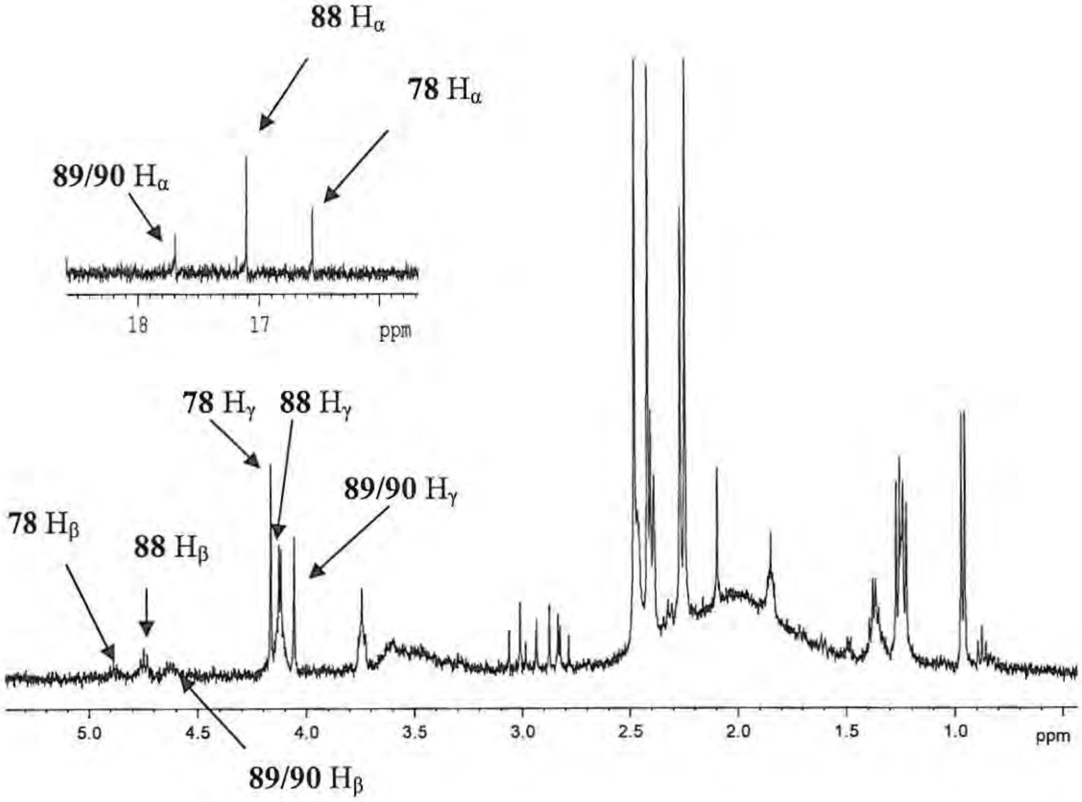

Figure 56. 400MHz ^{1}H NMR spectrum of the mixture of products depicted in Scheme 52 (inset, illustrating carbene signals, not to scale), in CDCl$_3$.

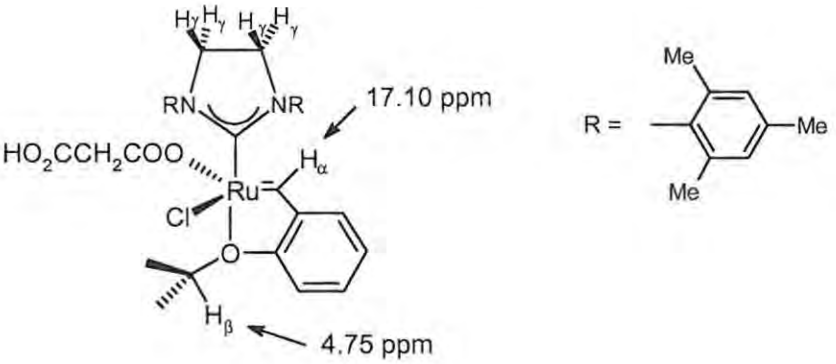

Figure 57. Selected ^{1}H NMR chemical shifts for complex **88**.

Two structures seemed possible for the remaining, minor product, *viz.* the expected bidentate system **90** or the dimalonate species **89** (Scheme 52). However, unambiguous assignment could not be made with the available data, due to the complexity of the ^{1}H NMR spectrum (Figure 56) and the transient nature of the species. Moreover, attempts to drive the reaction to completion by increasing the malonic acid concentration, led to a progressive *decrease* in the yield of both products, with no conversion at all with a 100-fold molar excess of malonic acid! This observation led us to suspect some form of unanticipated interaction between the malonic acid and the silver species in solution.

The key to understanding this behaviour, we believe, lies in a description of the crystal structure of silver malonate by Charbonnier *et al.*,[130] who determined that, in a given sample of silver malonate, half of the silver atoms are mono-coordinated as Ag-$OCOCH_2CO_2H$ **91** (Scheme 53), and half are five-coordinated by four oxygen atoms and one silver atom, forming centrosymmetrical 8-membered rings bridged by silver-silver bonds to form the bimetallic silver complex **92** (Figure 58). This arrangement is fairly common in silver carboxylate complexes.[131] Formation of the silver complex **92** provides an explanation for the decreasing yield of complex **88** (Scheme 52) with increasing malonic acid concentration, since a large excess of malonic acid is likely to sequester the available silver ions in solution, thus preventing abstraction of chloride ions from complex **78** and subsequent substitution of the malonate ligands.

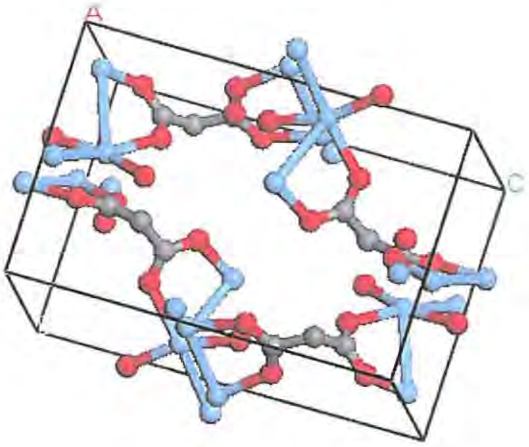

Figure 58. Ball-and-stick model (protons omitted) of the unit cell of bimetallic silver species **92**.[130]

If silver malonate takes the form of species **91** and **92** in solution, then its reactivity profile should differ from that of the free malonic acid **86** and silver carbonate used in Scheme 52. The mono-coordinated species **91** can be expected to react with the Grubbs-Hoveyda complex **78** as before, with initial formation of the monosubstituted complex **88**. While the bimetallic silver complex **92** is not expected to participate in the reaction, due to the relative inaccessibility of the silver atoms, its formation effectively reduces the concentration of the active species **91**. Therefore, addition of a stoichiometric equivalent of silver malonate (**91** and **92**) to complex **78** should result in only a small percentage conversion to the monosubstituted species **88** (and possibly the disubstited species **89**). This hypothesis was tested by synthesis of silver malonate *via* a literature procedure,[132] and subsequent reaction with the Grubbs-Hoveyda complex **78** (Scheme 53). This reaction afforded *only* the monosubstituted product **88** in poor yield, as determined by ^{1}H NMR analysis (Figure 59), and none of the minor products **89** or **90** detected in the previous reaction (Scheme 52). This result supports the previous assignment of the H_α, H_β and H_γ signals to product **88** (Figure 56). Furthermore, on the basis of this result, it was suspected that the minor product was the desired bidentate malonate system **90**, which would not be expected to form in the silver malonate synthesis outlined in Scheme 53, since in this reaction the 'active' species would be the mono-silver salt **91** rather than 'di-silver' malonate.

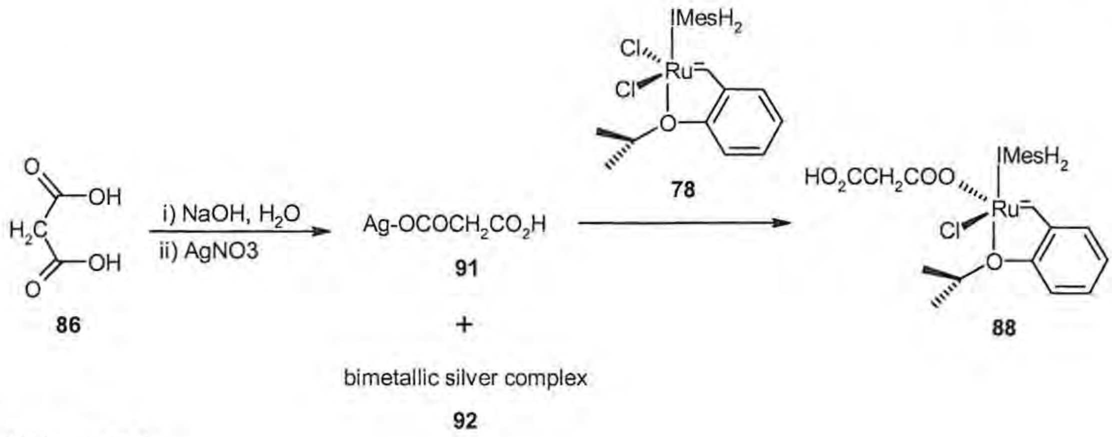

Scheme 53.

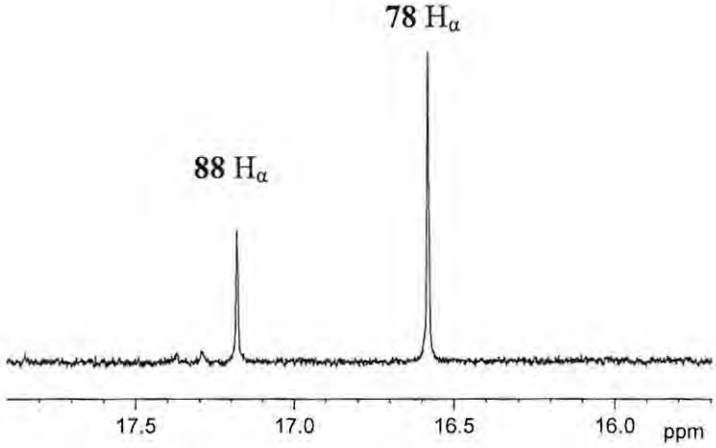

Figure 59. Partial 400MHz ^1H NMR spectrum (showing the carbene region only) of the mixture of product **88** and starting material **78** depicted in Scheme 53, in C_6D_6.

This assumption is further supported by a comparison of the DFT geometry-optimised structures for complexes **88** – **90** with that of parent complex **78** (Figure 60). Substitution of the single malonate ligand in complex **88** does not appear to involve significant steric interference with the rest of the complex. This is evident from the apparent lack of disturbance in the geometry of the $IMesH_2$ ligand, and the indicated ruthenium-phenoxy chelating distance whereas, in the case of the disubstituted complex **89**, the geometry of the $IMesH_2$ moiety is significantly distorted, and the ruthenium-phenoxy bond substantially elongated. The bidentate system **90** appears to be an intermediate case, in which the $IMesH_2$ geometry appears undisturbed, while the ruthenium-phenoxy bond is slightly elongated – an arrangement that could be favourable for catalyst initiation!

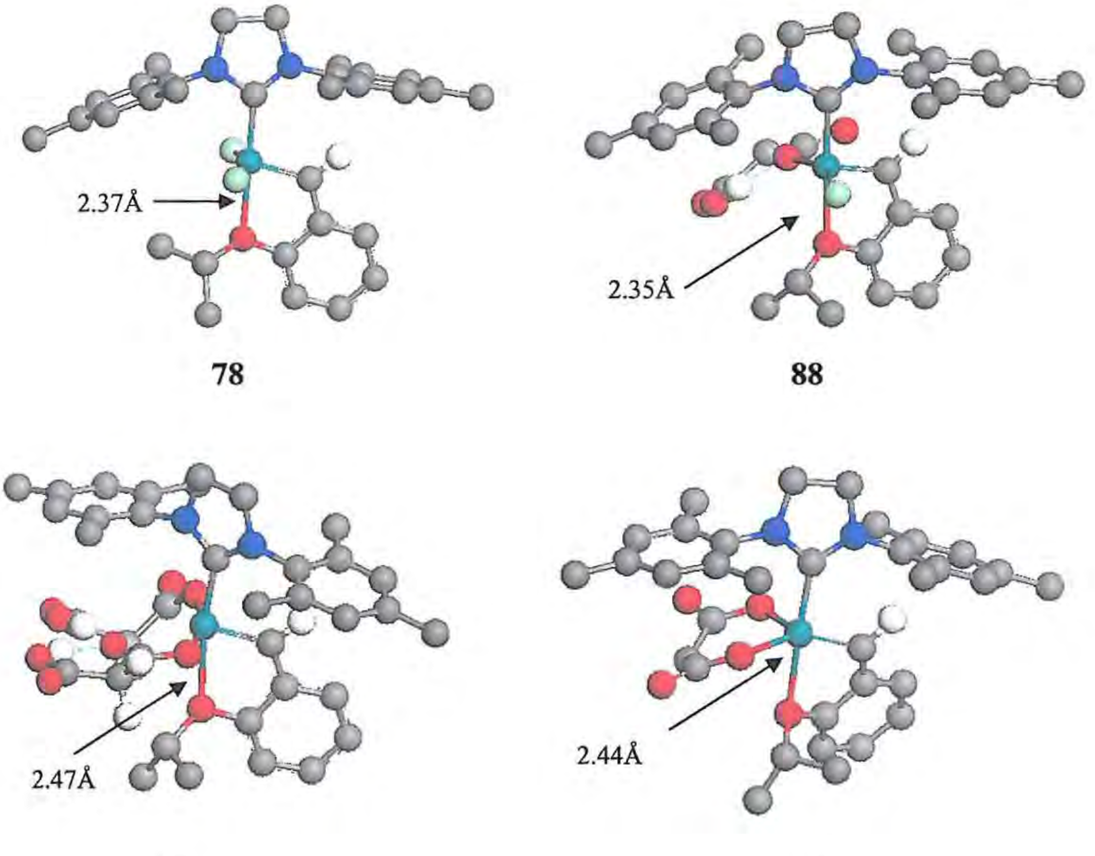

78 **88**

89 **90**

Figure 60. DFT geometry-optimised structures of the complexes **78, 88, 89** and **90** (peripheral protons omitted for clarity).

Several useful observations can be made based on these preliminary complexation studies.

i) A fine balance exists between catalyst activity and stability, which is highly sensitive to ligand electronic effects.

ii) Calculation of ligand electronic parameters is a potentially useful technique for the identification of coordination complexes in solution. This technique may prove particularly useful in systems employing catalysts generated *in-situ*, which are often transient in nature.[41]

iii) The potential of the malonate di-anion to bind to ruthenium in a bidentate fashion appears to have been demonstrated, and this may have useful implications from a ligand design perspective.

iv) The use of silver salts to facilitate ligand substitution reactions may introduce additional complexity through the formation of competing complexes, *e.g.*, the bimetallic silver malonate species **92**.

2.4 TRIDENTATE MALONATE- AND SUCCINATE-DERIVED LIGAND SYSTEMS

The results of the preliminary complexation studies highlight the potential advantages of a tridentate ligand system, in which the bidentate malonate moiety is tethered to the NHC moiety, as in the putative catalyst **93** (Figure 61). Attachment of the pre-formed tridentate ligand to the parent ruthenium complex could presumably be mediated by a silver salt, as the presence of the bulky NHC moiety should disfavour formation of competing silver carboxylate complexes such as species **92**. Moreover, tethering the malonate moiety to the NHC would alleviate steric crowding around the substrate coordination site, and impart additional stability to the complex through formation of a stable six-membered chelate ring. The structural elaboration of simple succinate-derived systems to form longer-chain diacids also offers a potential route to multidentate Schiff-base-type ligands (such as the pyrrole derivative **97**, Scheme 54), the utility of which has been demonstrated by Verpoort and co-workers.[66]

With these ideas in mind, the putative catalysts **93** and **94** were geometry-optimised at the DFT level (Figure 61), and some basic assessments made regarding their potential as metathesis catalysts. In structure **93**, the ruthenium-phenoxy bonding distance is 2.36Å, which is comparable to the 2.37Å calculated for the known catalyst **78** (Figure 60). The fact that this distance is significantly shorter than the 2.44Å calculated for the untethered bidentate system **90** (Figure 60) would appear to suggest that the tethering of the malonate moiety to the NHC moiety would, in fact, alleviate the steric interference with the phenoxy group. The equatorial O-Ru-O angle of 89° formed by chelation of the malonate moiety to the ruthenium centre, however, deviates significantly from the generally preferred *trans*-arrangement of the anionic ligands, the relative importance of which has not, to our knowledge, been addressed in the literature. In contrast, the equatorial O-Ru-O angle in structure **94**, at 150°, is closer to the typically observed *trans*-arrangement. The ruthenium-phenoxy distance of 2.24 Å is significantly shorter than in previously calculated systems, which may disfavour dissociation of the phenoxy ligand. Should this be the case, addition of electron-withdrawing substituents to the benzylidene ligand may be explored in order to weaken the ruthenium-phenoxy bond. This approach has been applied with some success to existing catalyst systems.[120]

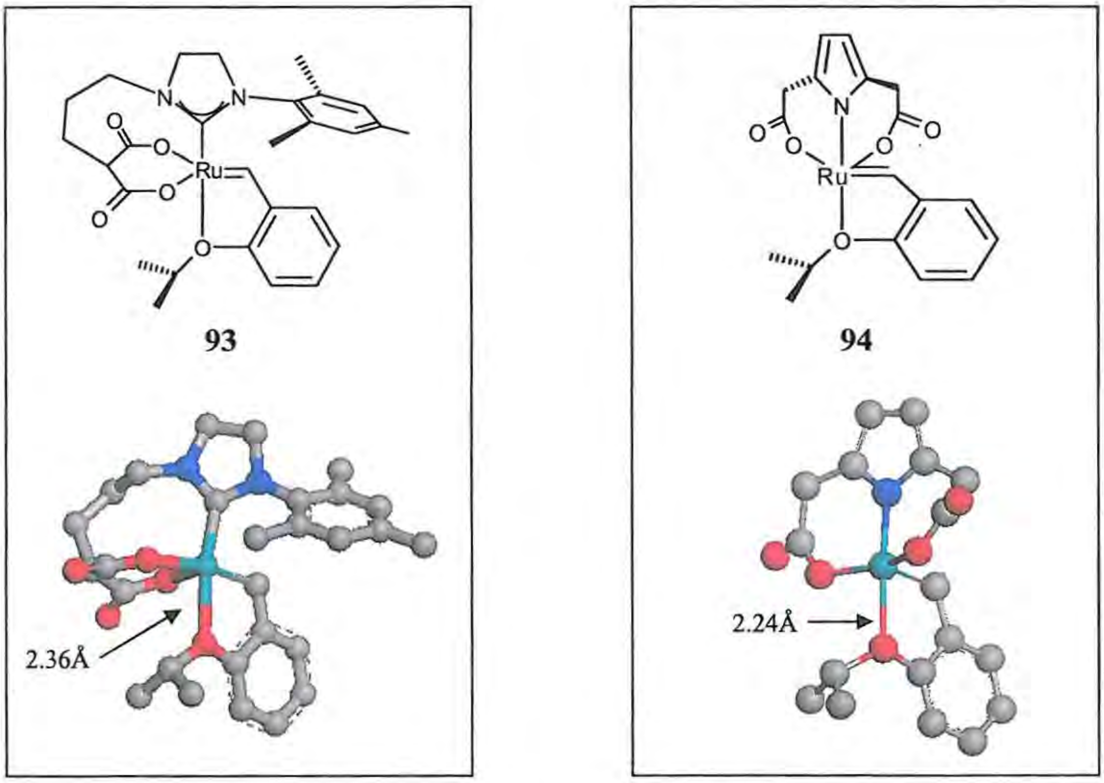

93

94

Figure 61. Wire-frame drawings and ball-and-stick DFT models of putative catalysts **93** and **94** (protons omitted for clarity).

Synthesis of the tridentate ligand system in the putative catalyst **94** may be approached using the succinate derivative **95** as a scaffold, as is illustrated by the work of Li *et al.*[133] (Scheme 54). Compound **95** may be converted, in a two-step process, to pyrrole-2,5-diacetic acid, represented as the tautomeric system **97**.

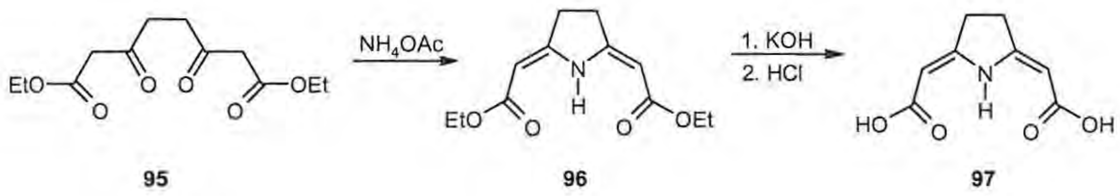

Scheme 54

The diester **95** has been previously synthesised by several different means, as illustrated in Scheme 55. These include the cuprous chloride-catalysed dimerisation of ethyl acetoacetate (Pathway I),[134] a Grignard-type approach (Pathway II)[135] and *via* electrolysis of a potassium salt derivative (Pathway III),[136] All of these approaches involve multiple steps and numerous reagents and afford generally low yields. A simple, one-pot procedure for the synthesis of compound **95** would clearly constitute a marked improvement on these methods.

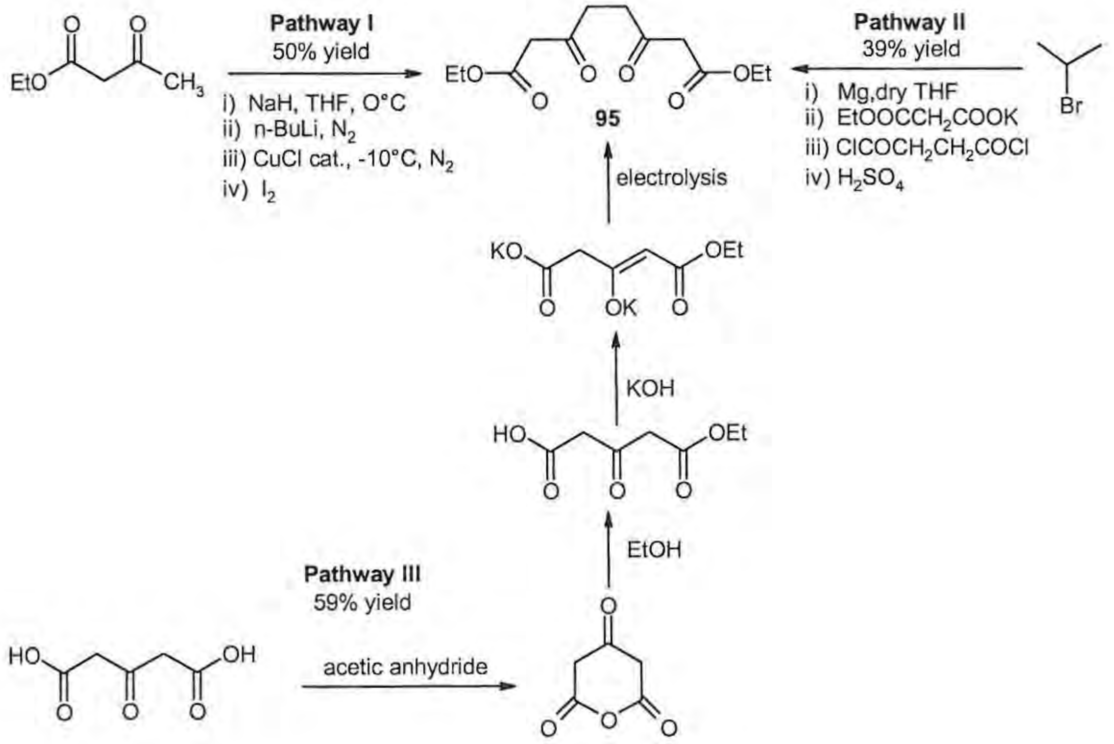

Scheme 55

2.4.1 Applications of Reformatsky-type methodology to diethyl succinate and diethyl malonate.

The Reformatsky reaction is a well-known and widely used method for the synthesis of β-hydroxy esters from ketones and aldehydes (Scheme 56).[137] Its lesser-known but equally useful variant, the Blaise reaction,[138] involves the analogous transformation of esters and nitriles. Because these methods can be extended to mono- and difluorinated bromoesters, they appeared to offer an elegant means of derivatizing simple dicarboxylic esters to generate longer-chain diesters and diacids, with the option of controlled introduction of fluorine atoms to vary the electron-withdrawing ability of the carboxylate moieties.

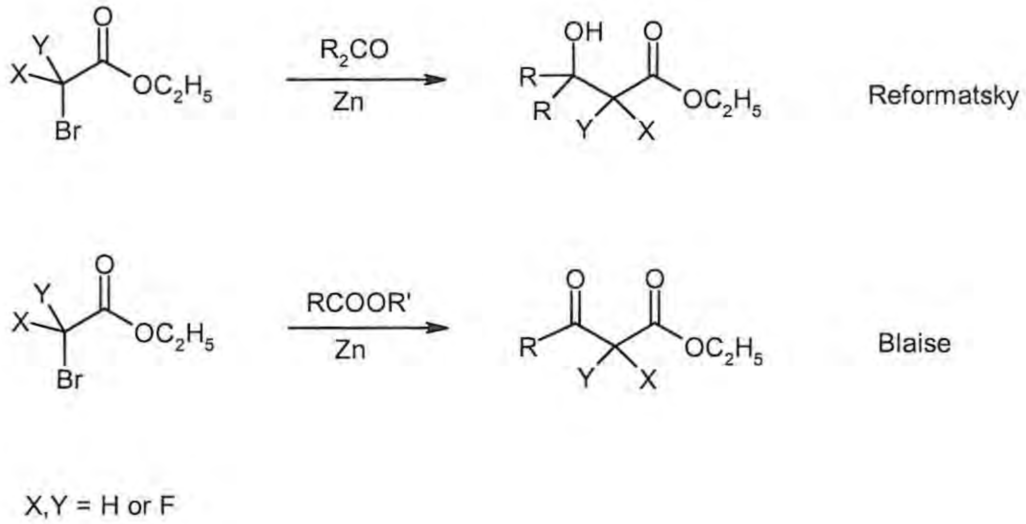

Scheme 56

It was anticipated that the zinc-catalysed Blaise condensation of diethyl succinate **98** with two equivalents of ethyl bromoacetate **99** would afford diethyl 3,6-dioxooctane-1,8-dioate **95** (Scheme 57). Unfortunately, this reaction failed repeatedly to produce the diester **95** in a yield greater than 3%, the starting material being isolated in 70-75% yield regardless of the reaction time. However, the reaction did afford, as the major product, diethyl 3-oxohexane-1,6-dioate **100** - the Blaise single-condensation product. Compound **100**, which was first described by Kato *et al.* in 1979,[139] has subsequently been synthesised in yields of up to 80% by the $NbCl_5$-mediated homologation of α-trialkylstannylmethyl-β-keto esters.[140] While the Blaise condensation approach outlined in Scheme 57 is nowhere near as efficient as this, it does present a simpler and more economical approach to compound **100**. Although the reaction outlined in Scheme 57 did not prove to be a viable route to compound **95**, recent advancements in Reformatsky-type methodology - particularly catalytic activation of the intermediate zinc complex[141] - continue to broaden the scope of this reaction, and the approach may be worth pursuing at a later stage.

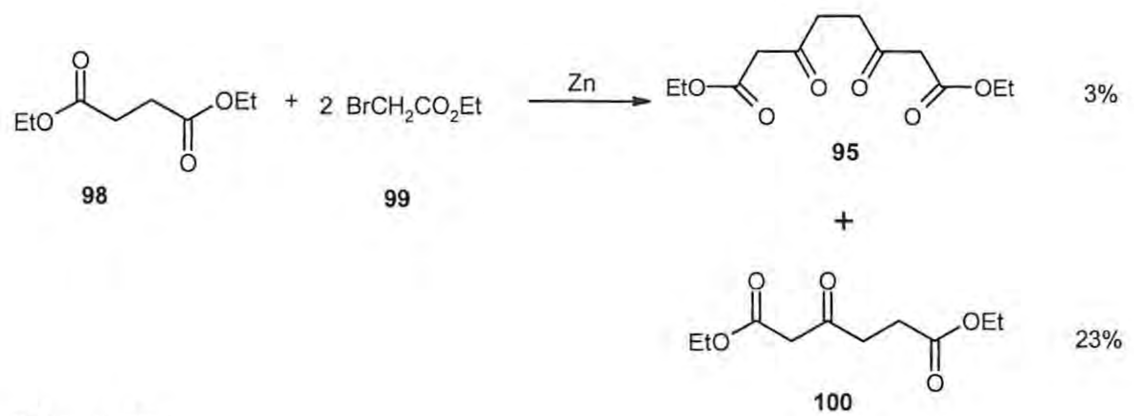

Scheme 57

The analogous double-Blaise condensation was attempted on diethyl malonate **101** but, instead of the desired product **103**, afforded the triester **104** in 50% yield (Scheme 58). The formation of compound **104** suggests that, rather than undergoing a second Blaise substitution, the intermediate **102** undergoes an α-substitution reaction with the second equivalent of ethyl bromoacetate. Reaction of compounds **99** and **102**, in basic medium, has been previously reported to produce the triester **104** in 40% yield.[142] In view of these disappointing results, it was decided to focus our efforts on developing a route to the ruthenium complex **93**.

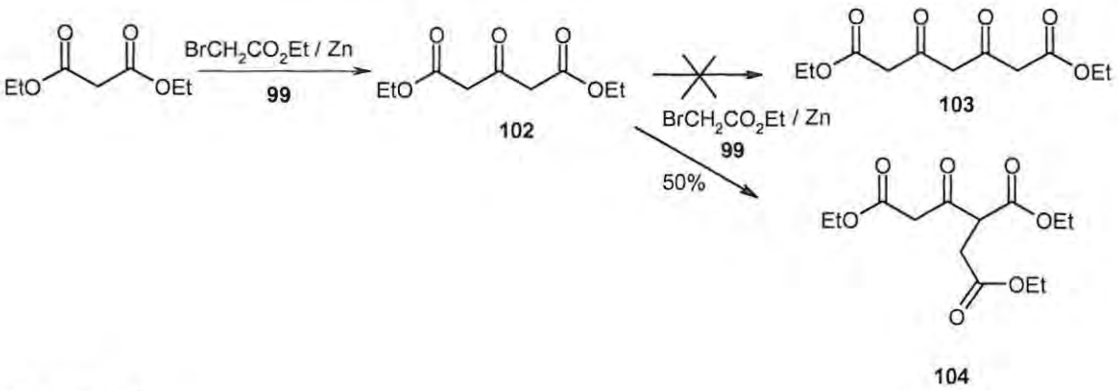

Scheme 58

2.4.2 Synthetic approach to the tridentate malonate-derived complex (93)

It was decided to approach the putative catalyst **93** *via* the retrosynthetic strategy outlined in Scheme 59, using appropriate protecting groups where necessary. This required construction of the synthon **107**, which had previously been prepared by Hoveyda and co-workers, as outlined in Scheme 60.[59]

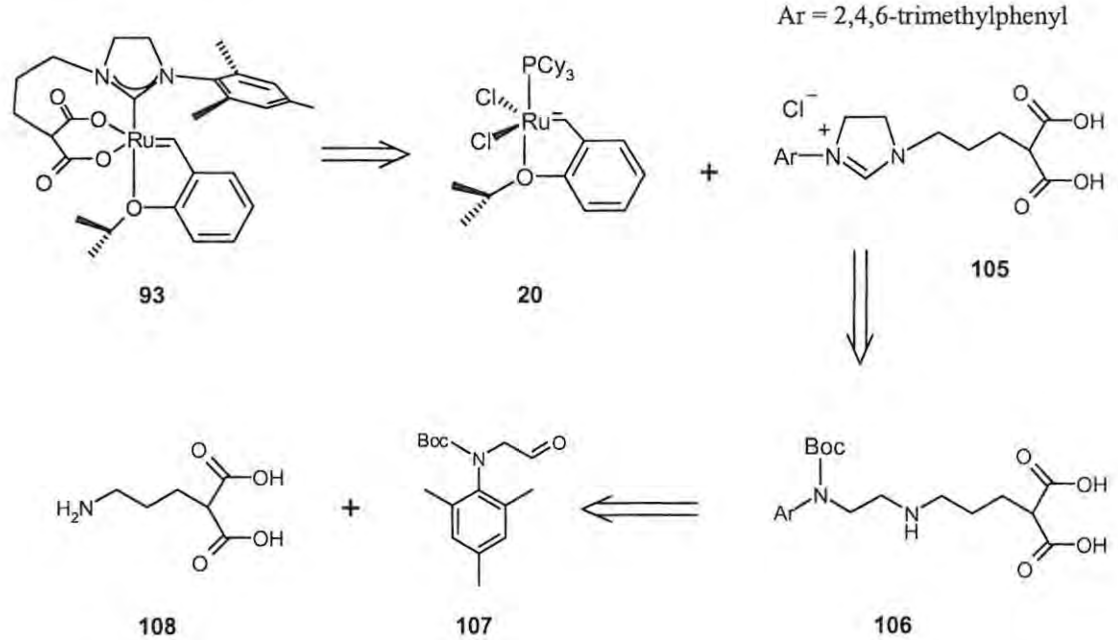

Scheme 59

The aldehyde **107** was prepared according to the literature procedure of Hoveyda and co-workers.[59] Thus, Boc-protected species **110**, prepared in quantitative yield from 2,4,6-trimethylaniline **109**, was reductively alkylated using potassium hydride and 4-bromo-2-methyl-2-butene to afford compound **111**, again in quantitative yield. Ozonolysis of this compound afforded the aldehyde **107** in approximately 80% yield. intermediates **110** and **111**, and synthon **107** were all isolated and characterised by ^1H and ^{13}C NMR, and MS analysis.

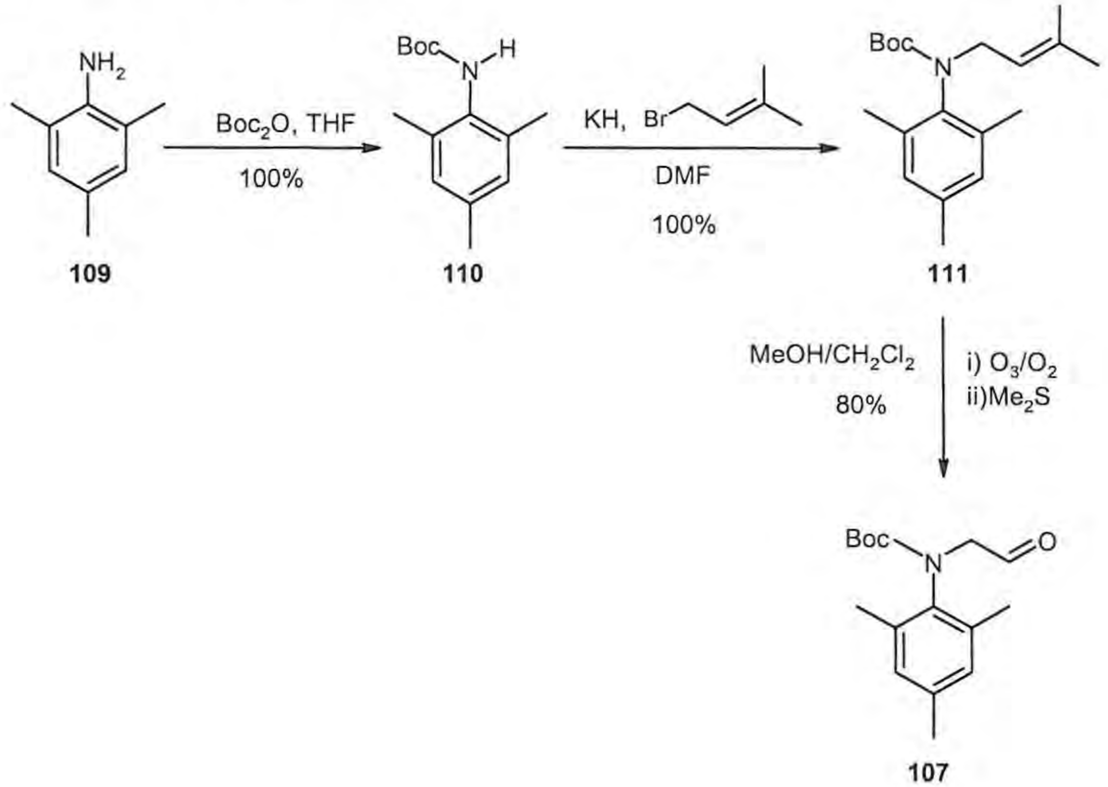

Scheme 60

Synthon **108** (Scheme 59) was approached *via* the procedure outlined in Scheme 61. α-Alkylation of diethyl malonate **101** with allyl bromide **112**, following a literature procedure,[143] afforded both the desired diethyl allylmalonate **113** in 78% yield and the dialkylated compound **114** in 22% yield; separation of these products was achieved by semi-preparative HPLC. Attempted radical addition of HBr (using a 30% solution of HBr in acetic acid) to compound **113** failed to produce the anti-Markovnikov product **115**. Instead the carboxy lactone **117** was formed - presumably *via* Markovnikov addition of HBr (to form intermediate **116**) followed by hydrolysis of an ester moiety, and cyclisation involving nucleophilic displacement of bromide. Compound **117** has been previously prepared by Kochikyan and co-workers.[144] The use of HBr gas, rather than the acetic acid solution, however, afforded (in 68% yield) the desired anti-Markovnikov product **115**, which was purified by HPLC. Conversion of the alkyl bromide **115** to the ammonium tosylate **118** was attempted using the Staudinger reaction,[145] with a view to subsequent conversion to the free amine **108** (Scheme 59). This well-known procedure has been modified by Koziara and Zwierzak[146] to operate selectively for primary or secondary alkyl halides. It was envisaged that this method, if sufficiently selective, could be applied to a mixture of primary and secondary alkyl halides (*i.e.* a mixture of the Markovnikov and anti-Markovnikov products **116** and **115**) to afford the primary or secondary amine as desired. In this way, the lengthy HPLC separation of the desired alkyl halide **115** could be avoided. However, under the specified conditions for conversion of primary alkyl halides, we were unable to isolate the expected product **118** by means of chromatography (normal- or reverse-phase), distillation or recrystallisation, and instead recovered *ca.* 30% of the starting material.

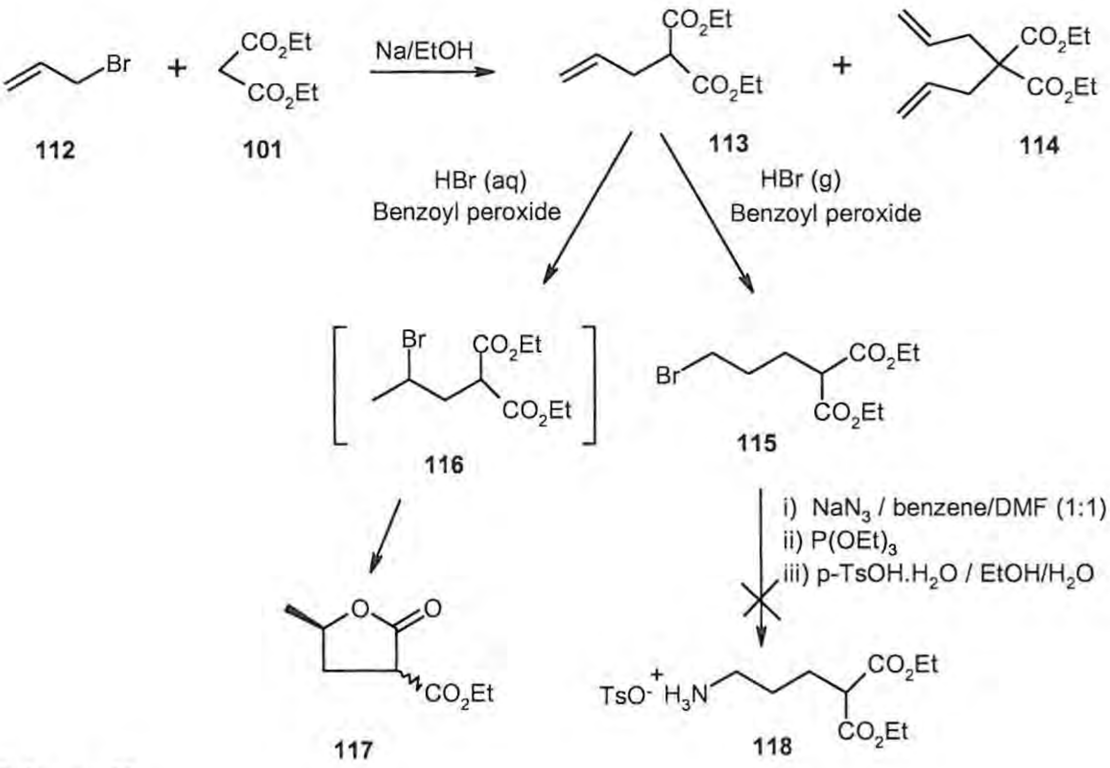

Scheme 61

The Staudinger reaction was also attempted on the secondary alkyl bromide **121**, which was prepared by α-alkylation of diethyl malonate **101** with the alkyl bromide **119**,[143] followed by Markovnikov addition of aqueous HBr.[147] Formation of the expected ammonium chloride product **122** proved equally troublesome.

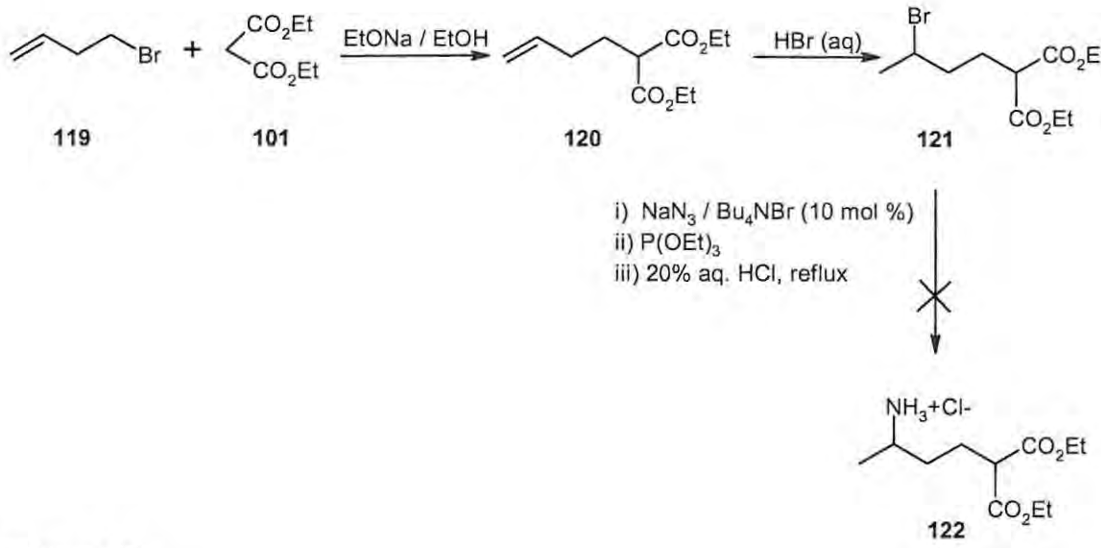

Scheme 62

In view of these difficulties, and given that HPLC was required to isolate compounds **113**, **115**, **120** and **121**, it was decided to abandon the synthesis of synthon **108** and approach species **105** (Scheme 59) directly from the existing synthon **107**, as outlined in Scheme 63.

It was envisaged that preparation of the terminal alcohol **125** (Scheme 63), subsequent closing of the NHC ring system, and replacement of the OH functionality with a malonate group, would afford relatively easy access to synthon **107**. Various attempts were made at the reductive amination of synthon **107** with 3-amino-1-propanol **123**. An initial attempt was made to carry out a one-pot synthesis of compound **125** following a procedure employed by Hoveyda and co-workers,[59] by direct reaction of compounds **107** and **123** with sodium triacetoxyborohydride **124**, which was prepared according to a literature procedure.[148] However, it was found that reduction of the aldehyde competed with the reductive amination process, affording the alcohol **126** in *ca.* 60% yield. This novel compound was identified by NMR spectroscopy (Figure 62) and high-resolution MS analysis.

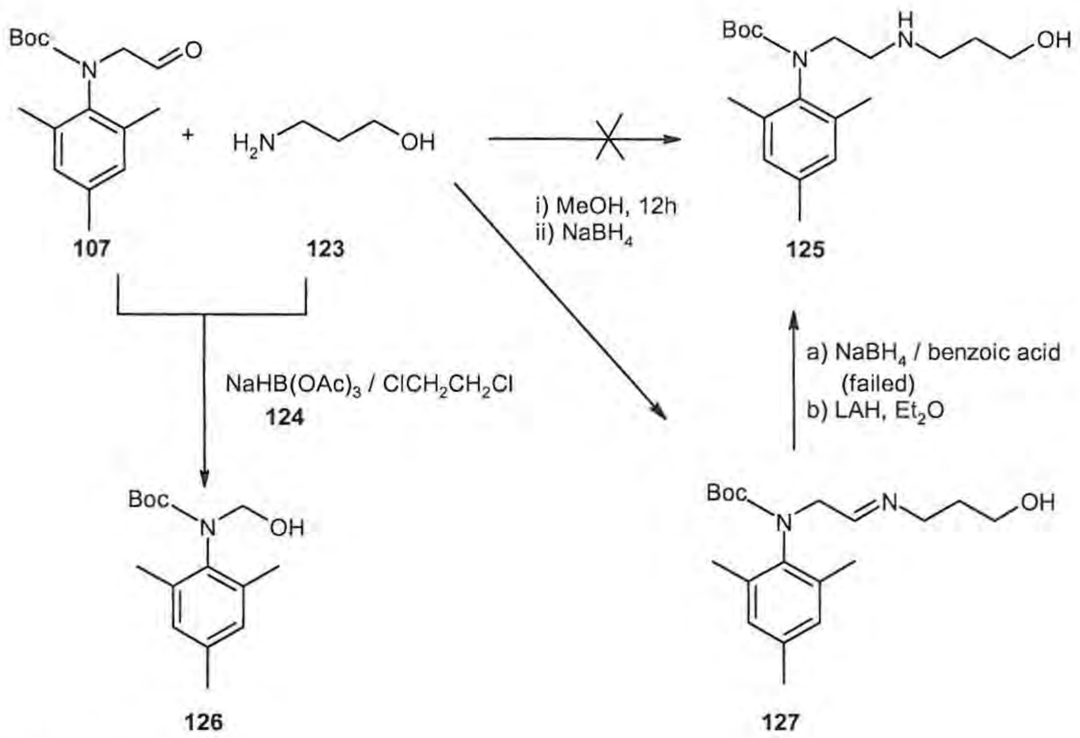

Scheme 63

Given the susceptibility of the aldehyde **107** to reduction by sodium triacetoxyborohydride **124**, it was decided to approach formation of the amine **125** in a stepwise manner, with initial formation of the imine **127**, and subsequent sodium borohydride reduction to the amine **125**, following a method developed by Abdel-Magid *et al.*[149] Under these condition, the novel imine **127** was prepared and isolated, and characterised by NMR spectroscopy (Figure 63) and high-resolution MS analysis. However, addition of sodium borohydride to a methanolic solution of the imine **127** failed to afford the amine **125**. In a recent report by Cho and Kang,[150] imines structurally similar to compound **127** were observed to be resistant to reduction by sodium borohydride alone, but were readily reduced when the sodium borohydride was activated under solvent-free conditions by boric acid, *p*-toluenesulphonic acid or benzoic acid. This approach was applied to the imine **127**, but returned only unconverted starting material. In a final attempt to reduce the imine **127**, a textbook LAH method was applied.[151] The presence of the amine product **125** was confirmed by ^1H NMR analysis (Figure 64), which showed the disappearance of the imine proton signal at *ca.* 4 ppm, and verified by high-resolution MS analysis.

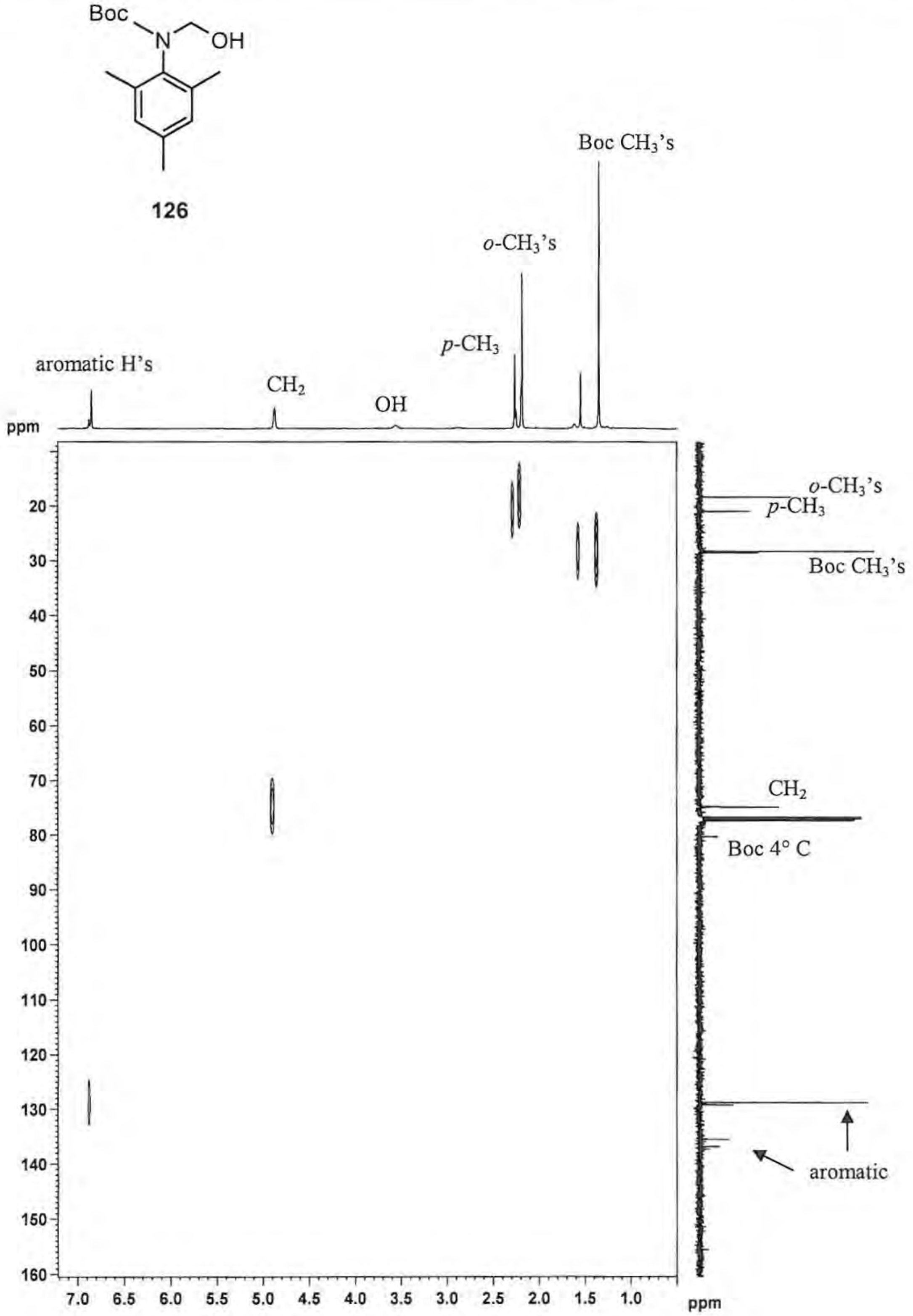

126

Figure 62. 400MHz HMQC NMR spectrum of compound **126** in $CDCl_3$. At 303K the compound exists as a pair of amide rotamers. Only signals from the major rotamer are labelled.

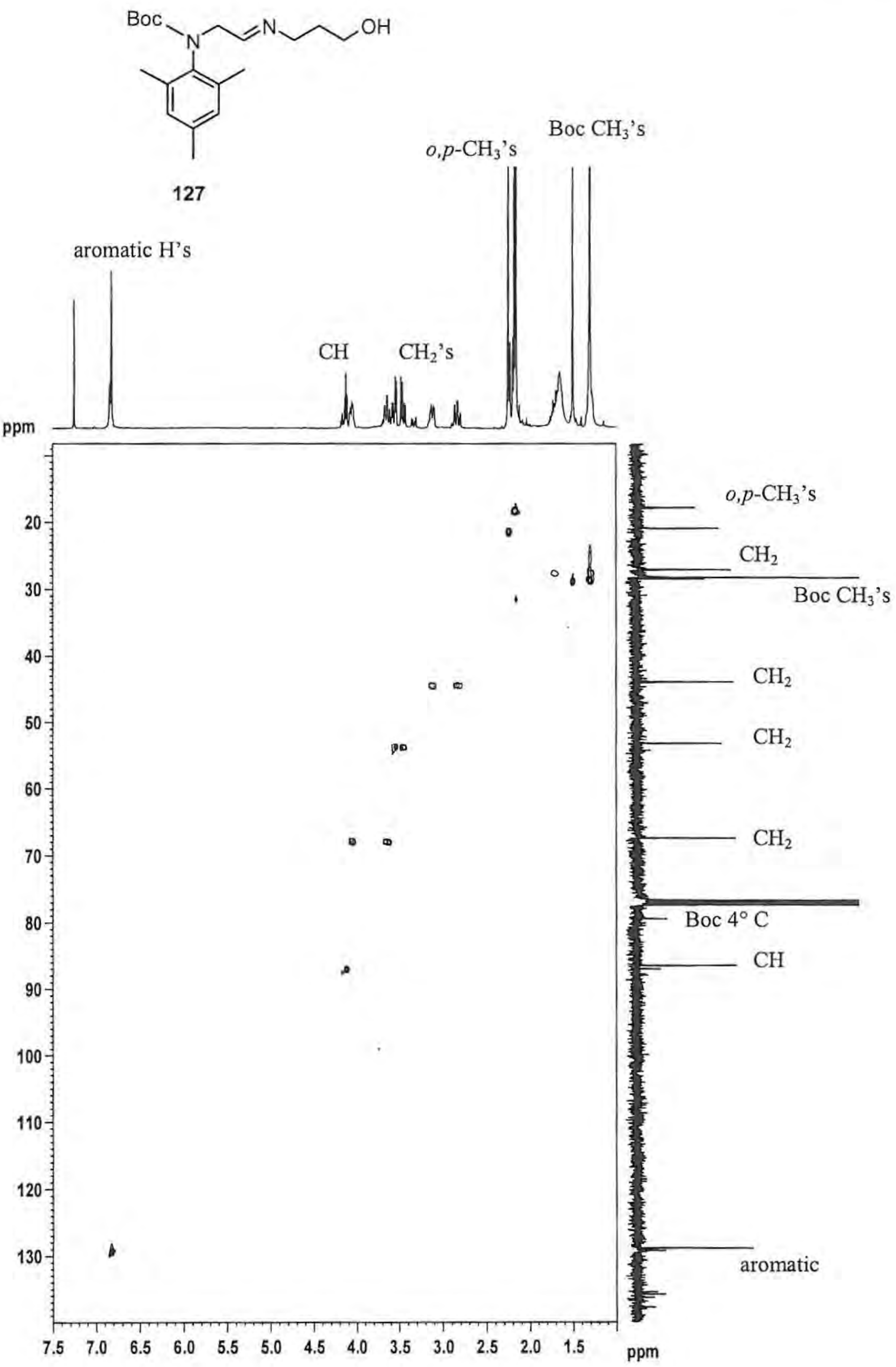

Figure 63. 400MHz HMQC NMR spectrum of compound **127** in $CDCl_3$. At 303K the compound exists as a pair of amide rotamers. Only signals from the major rotamer are labelled.

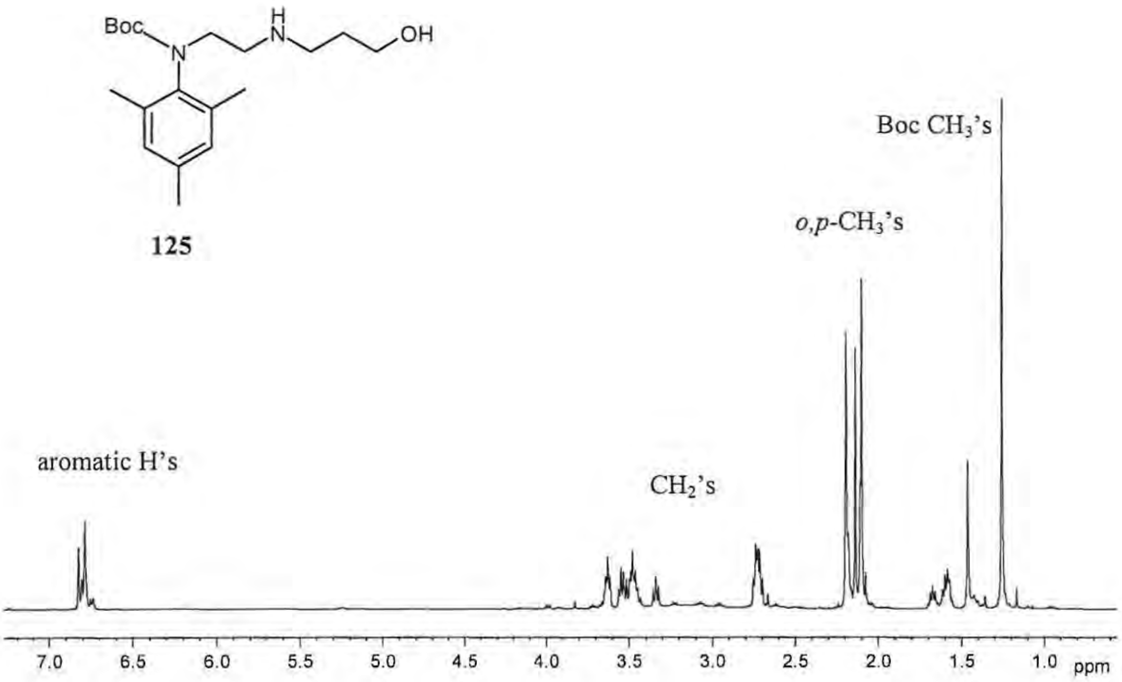

Figure 64. 400MHz ^{1}H NMR spectrum of the amine **125** in $CDCl_3$.

Having thus demonstrated the accessibility of the amine **125** it was decided that, given the limitations of time, the synthesis and evaluation of the putative catalyst **93** would be pursued further by other workers within the group. It is anticipated that the approach outlined above (*i.e.* formation of the amine **125**, and subsequent ring closure and attachment of the malonate moiety) will provide relatively easy access to the tridentate ligand **105**. The synthesis and evaluation of the tridentate ligand system **97** (Scheme 54) will also be undertaken in a future study.

2.5 KINETICS OF 1-OCTENE SELF-METATHESIS

2.5.1 Background

The cross- or self-metathesis of linear, terminal alkenes to form longer-chain, internal alkenes is a useful industrial process. However, relatively little is understood about the kinetic and mechanistic factors involved in these reactions, which are rarely discussed in the academic literature. Only a few significant kinetic studies have been reported in the past decade,[45,46, 74,122] and all of these were conducted by Grubbs and co-workers. Several important conclusions were reached in these studies.

i) Metathesis with 1st-generation Grubbs-type catalysts follows a predominantly dissociative pathway, except in the presence of an added excess of free phosphine, in which case the associative pathway becomes significant (see Scheme 21, Section 1.3.3).[46]

ii) The rate of initiation of metathesis of a series of terminal alkenes with the Grubbs 1st-generation catalyst **14** varies with the steric bulk and geometry of the substrate (with bulkier substrates reacting more slowly), while substrate electronic effects on reaction rate are small and non-linear.[122]

iii) Changing the solvent has a significant effect on catalyst initiation rates, with the rate increasing roughly in proportion to the solvent's dielectric constant.[74]

These studies have contributed a great deal to the mechanistic understanding of metathesis reactions. However, several questions remain unanswered. Of primary importance from a computational perspective, is the exact nature of the solvent effect. This is significant not only for the purpose of optimising reaction conditions, but is necessary in order to establish whether gas-phase computational data can be reasonably interpreted, or whether solvent effects need to be included. Experimental identification of the rate-determining-step (RDS), which has been reported to vary from substrate to substrate, and with substrate concentration,[74] would also be useful in assessing the applicability and limitations of computational data. A kinetic - mechanistic study was therefore undertaken, focussing on the effect of variations in solvent and substrate concentration on the self-metathesis of 1-octene **128** catalysed by the Grubbs' 1st-generation ruthenium catalyst **14** (Scheme 64).

The main objectives of this study were:-

i) to establish the effect of solvent, temperature and catalyst loading on various aspects of the reaction; and

ii) to provide experimental data with which to assess the predictive validity of a computational analysis of this particular reaction.

In common with earlier approaches, the kinetic study focussed mainly on the initiation phase of the metathesis cycle (Scheme 64), by monitoring the decreasing concentration of the benzylidene species **14**, and increasing concentrations of the heptylidene **131**, and methylidene species **132** by means of ^{1}H NMR spectroscopy. Kinetic experiments were carried out at specified temperatures, with known starting concentrations of the benzylidene **14** and 1-octene **128**. Concentrations of the carbene species **14**, **131** and **132**, at different times during the course of the reaction, were calculated on the assumption that the sum of the 3 species' concentrations were equal to the starting concentration of the benzylidene **14**, *i.e.* assuming negligible decomposition of the carbene species at the temperatures, and within the timeframes, of the experiments.

According to the currently accepted dissociative mechanism,[46] the benzylidene species **14** enters the catalytic cycle by loss of a tricyclohexylphosphine (PCy_3) ligand, and subsequent binding of the 1-octene substrate **128** (Scheme 64). Depending on the orientation of substrate binding (*i.e.* **129a** or **129b**), pathway I or II may be followed, which leads to the formation of the heptylidene **131** or the methylidene **132**, respectively. The heptylidene intermediate **131** may also bind to a substrate molecule in either one of two orientations (*i.e.* **133a** or **133b**). Formation of species **133a** (pathway III) leads to a productive metathesis event, affording the 1-octene self-metathesis product **135**, and leading to the formation of the methylidene intermediate **132**. Whether the *E*- or *Z*- isomer of the product **135** is formed depends upon the position of the alkyl group (R) of the substrate molecule in intermediate **133a**, and the resultant stereochemistry of the metallacycle intermediate **134a**. The issue of stereochemistry will be revisited in Section 2.6.

Should pathway IV be preferred, the heptylidene species binds and releases the 1-octene substrate, regenerating the same intermediate **131** in an unproductive cycle. The methylidene intermediate **132** may re-enter the catalytic cycle in a similar manner to carbenes **14** and **131**, following a productive pathway to afford intermediate **131**, or an unproductive pathway to regenerate itself. This phase of the catalytic cycle is not encountered in the kinetic study, and is therefore omitted from Scheme 64.

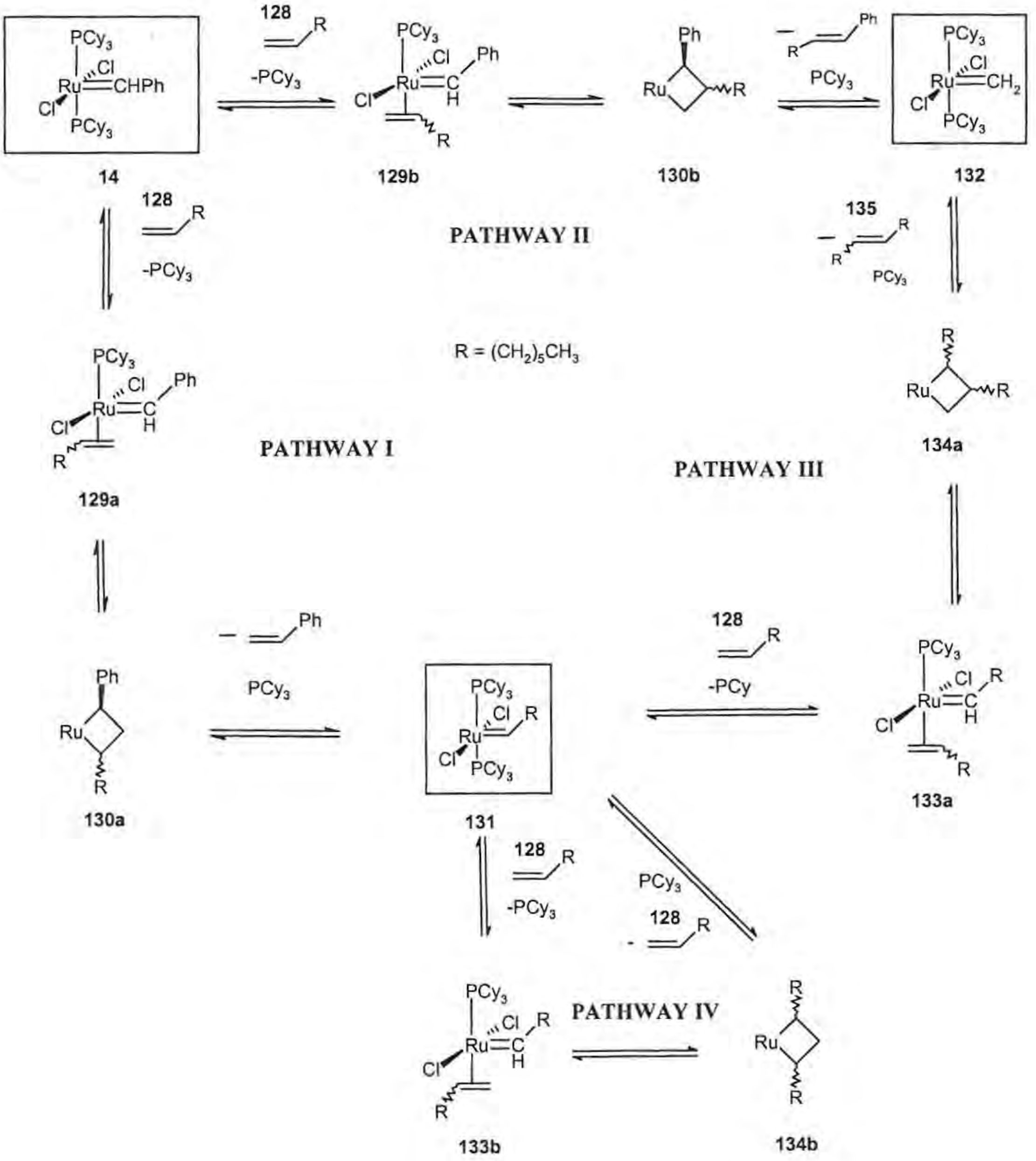

Scheme 64. Summary of the various pathways involved in the self-metathesis of 1-octene **128** with the Grubbs 1st-generation catalyst **14** (PCy_3 ligands omitted from metallacycle intermediates for clarity)

All experiments were conducted at temperatures between 0°C and 10°C, in order to reduce the possibility of competing side-reactions and catalyst degradation, and to slow the reaction down sufficiently to be observable on the NMR time-scale. The experimental procedure involved preparation of a solution of catalyst **14** under nitrogen at -40°C, in a septum-sealed screw-cap NMR tube. The 1-octene substrate **128** was added by syringe immediately prior to the start of the experiment, and a short period of time allowed for the temperature of the solution to rise to the probe temperature. Data were acquired at appropriate time intervals, depending on the reaction rate.

The general trend observed under these conditions was the complete conversion of species **14** to species **131** presumably *via* pathway I only (Scheme 64), followed by conversion of species **131** to species **132** (Pathway III) and complete disappearance of species **14**, leaving species **132** as the only remaining carbene species in solution (Figure 65). The build-up of species **132** in this manner has, in a previous study, been attributed to the fact that these experiments were conducted in a closed system, without purging of the gaseous ethylene byproduct.[22]

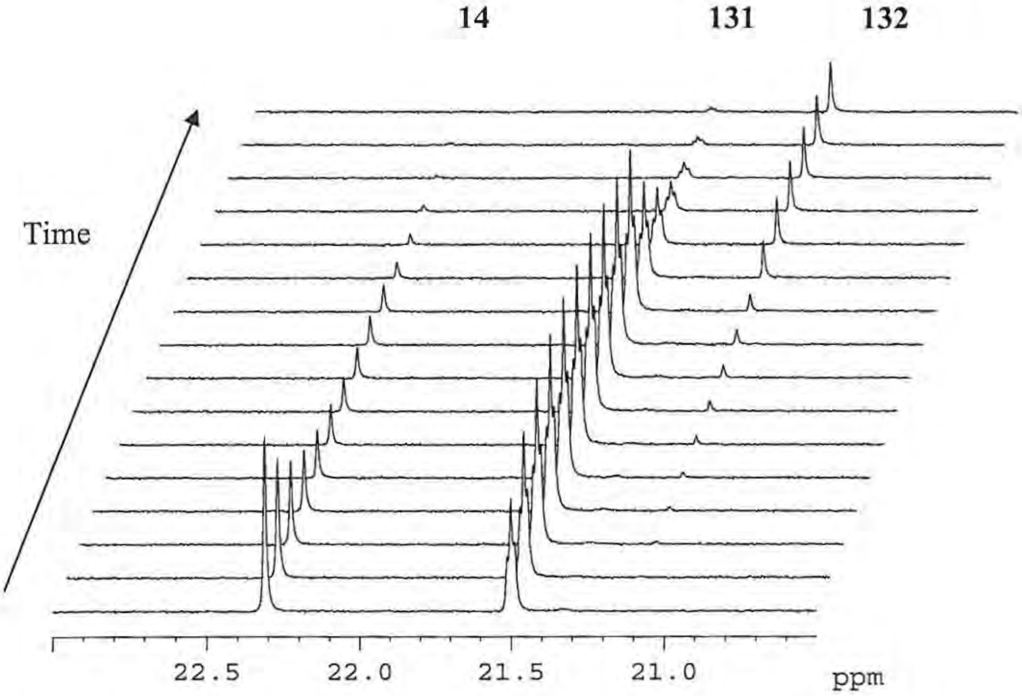

Figure 65. Representative stacked plot of the carbene region of the ^{1}H NMR spectra for a kinetic experiment in toluene-d_8 at 10°C, showing the observed transformation **14**→**131**→**132**.

These observations were consistent with those of Grubbs and co-workers[122] who, in a similar low-temperature kinetic study, noted that the selectivity of metallacycle formation (*i.e.* pathway I *vs.* pathway II, and pathway III *vs.* pathway IV; Scheme 64) is temperature-dependent. Under the low-temperature conditions of these experiments, pathway II does not appear to be followed at all. Furthermore, the formation of species **132** appears to occur solely *via* intermediate **131** and pathway III, and there is no evidence to suggest that pathway IV is followed to any significant extent. These assumptions are borne out by the subsequent kinetic analysis detailed in Section 2.5.2.

The NMR data represented in Figure 65 may be treated more quantitatively upon conversion of the peak integrals to actual concentrations. Figure 66 is a typical concentration *vs.* time curve obtained at 10°C for the three observable ruthenium carbene species (**14**, **131** and **132**), with an initial concentration of 0.02 mol.L^{-1} of the starting species **14**, and a thirty-fold excess of the substrate, 1-octene **128**.

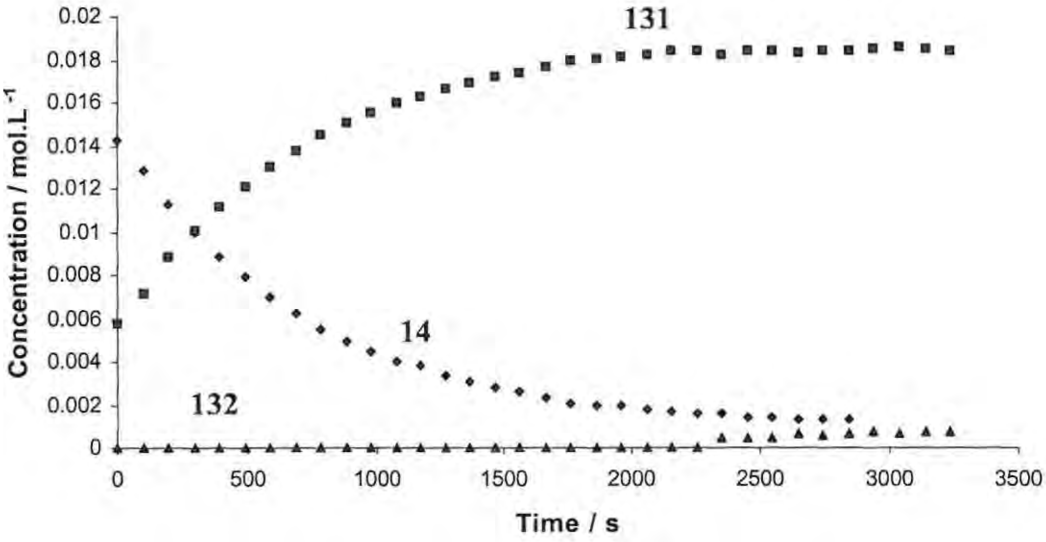

Figure 66. Plot of concentration *vs.* time for species **14**, **131** and **132** in the metathesis of 1-octene **128** in toluene-d_8 at 10°C, with an initial catalyst concentration of $[\mathbf{14}]_0 = 0.02M$, and 30 equivalents of the substrate, 1-octene **128**.

The shape of the above concentration *vs.* time curve (Figure 66) serves to support the assumptions made regarding the dominance of pathways I and III (Scheme 64). Moreover, it prompts a further assumption regarding the reversibility of the processes. In theory, each step of the pathways outlined in Scheme 64 is reversible. However, analysis of figures 65 and 66 suggest that, under the conditions of these experiments, the equilibria strongly favour product formation; hence the processes can be considered essentially irreversible.

Therefore under these conditions, the complex catalytic cycles detailed in Scheme 64 can be represented by the simple uni-directional, two-step consecutive reaction depicted in Scheme 65. Because the 1-octene substrate **128** is present in excess, each of the depicted reaction steps may be treated as pseudo-first-order with respect to reactants **14** and **131** respectively, and the concentration of 1-octene **128** will not feature in the corresponding rate equations.

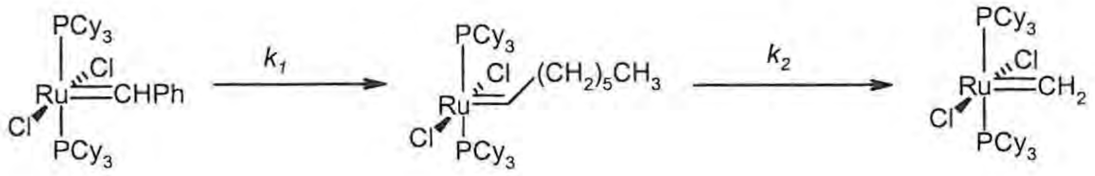

14 **131** **132**

Scheme 65

This simplification of the catalytic cycle is necessary in order to extract meaningful information from the kinetic data. However, it also necessitates the careful comparison of calculated with experimental data, in order to validate the assumptions on which the simplifications are based. These concerns are addressed in Section 2.5.2.

The rate equations for the simplified transformations outlined in Scheme 65 (where **14**=A; **131**=B; **132**=C) are:

$$-d[\mathrm{A}]/dt = k_1[\mathrm{A}] \tag{1}$$

$$d[\mathrm{B}]/dt = k_1[\mathrm{A}] - k_2[\mathrm{B}] \tag{2}$$

$$d[\mathrm{C}]/dt = k_2[\mathrm{B}] \tag{3}$$

Assuming that at t=0, [A] = $[\mathrm{A}]_0$ and [B] = [C] = 0, these equation can be integrated to give:[152]

$$[A] = [A]_0 \exp(-k_1 t) \tag{4}$$

$$[B] = \frac{[A]_0 k_1}{k_2 - k_1}\left[\exp(-k_1 t) - \exp(-k_2 t)\right] \tag{5}$$

$$[C] = [A]_0\left[1 - \frac{k_2}{k_2 - k_1}\exp(-k_1 t) + \frac{k_1}{k_2 - k_1}\exp(-k_2 t)\right] \tag{6}$$

A useful feature of this simplified system is that, at $[\mathrm{B}]_{\mathrm{max}}$,[152]

$$\mathrm{d}[\mathrm{B}]/\mathrm{dt} = 0 \tag{7}$$

and, hence, from equation (2):

$$k_1[\mathrm{A}] = k_2[\mathrm{B}] \tag{8}$$

Therefore, both rate constants are accessible from the concentration *vs.* time data. While determination of k_1 has provided the basis for all of the above-mentioned kinetic studies,[45,46, 74,122] k_2 has not, to the best of our knowledge, been reported for any metathesis reaction. A comparison of both rate constants under various conditions should provide useful insight into the effects of varying conditions on catalyst activity.

2.5.2 Determination of k_1 and k_2

For all of the k_1 determinations, 0.02M stock solutions of catalyst **14** were prepared at -40°C in the appropriate solvent and transferred under nitrogen to septum-sealed, screw-cap NMR tubes. The required volume of 1-octene **128** was added by syringe, and data acquisition started immediately at the required temperature. Data were collected at 1, 2 or 5 minute intervals as appropriate, and experiments performed in triplicate where possible. A representative plot of concentration *vs.* time (Figure 67) and the negative log thereof (Figure 68) illustrate the pseudo-first-order behaviour of the system.

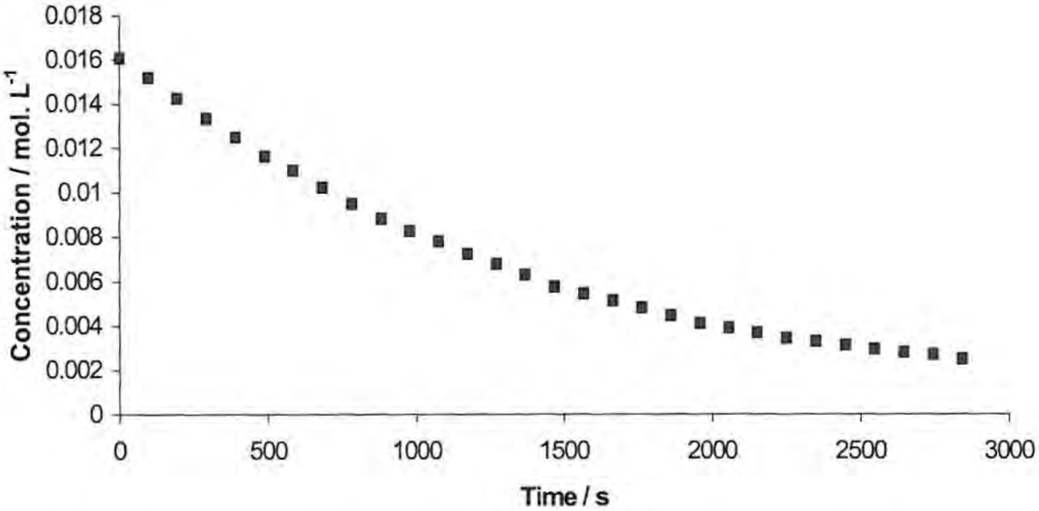

Figure 67. Representative plot of the concentration of benzylidene **14** *vs.* time for the metathesis of 1-octene **128** in toluene-d_8 at 10°C.

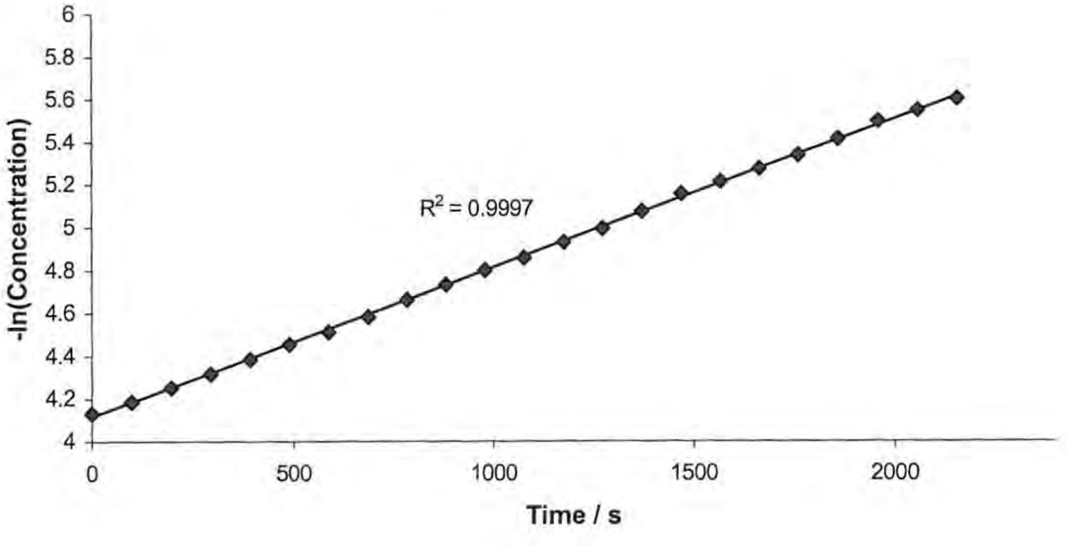

Figure 68. Representative plot of the negative logarithm of the benzylidene **14** concentration *vs.* time for the metathesis of 1-octene **128** in toluene-d_8 at 10°C.

Because the reactions occurred too rapidly for data to be recorded from time zero, the Guggenheim method of regression analysis[153] was used to obtain the pseudo-first-order rate constants. This involves plotting the concentration data as pairs of points separated by a constant time interval, thus reducing errors arising from erroneous or inconsistent time-scales. Using this approach, a standard method for the calculation of k_1 was employed for all of the kinetic data. This involved generating a Guggenheim plot (Figure 69) over the first two half-lives of species **14** - the gradient of which, under the prevalent pseudo-first-order conditions, corresponds to k_1.

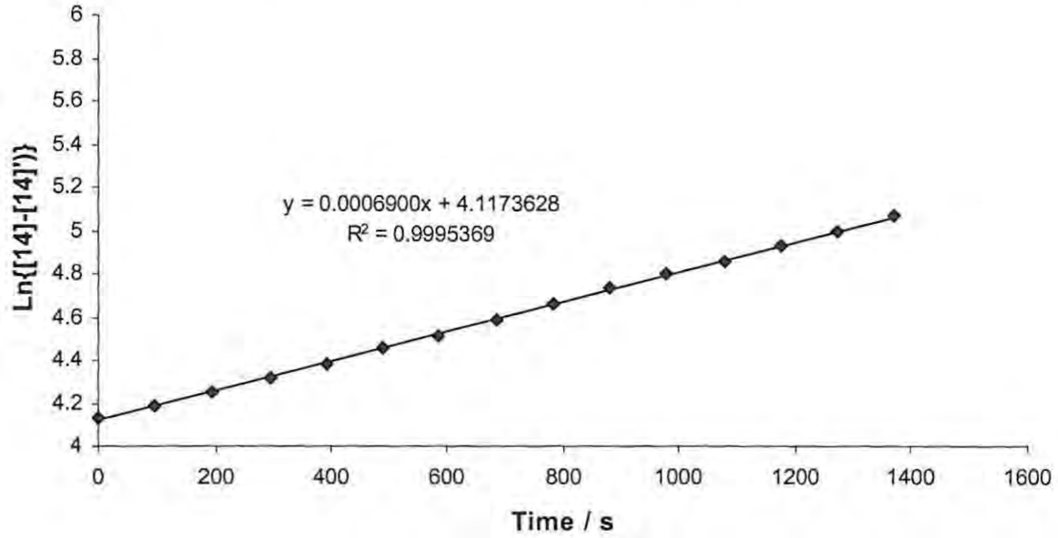

Figure 69. Representative Guggenheim plot for the metathesis of 1-octene **128** with catalyst **14** in toluene-d_8 at 10°C (notional time scale set arbitrarily to t_0).

Having thus established k_1, the full plots of concentration-time data were examined and $[\mathbf{B}]_{max}$ located for each data set {$[\mathbf{B}]_{max}$ being defined as the point at which the local gradient, *i.e.* the rate of change from a given [**B**] value to the subsequent value, had reached a minimum}. Using equation 8, k_2 could then be calculated from the determined k_1 value and the concentrations [**A**] and [**B**] at the time corresponding to $[\mathbf{B}]_{max}$ (with **A**=**14** and **B**=**131**). Equations 4-6 were used to generate complete plots of concentration *vs.* time using the calculated rate constants (Figure 70), which were then compared to the actual concentration *vs.* time data, extrapolated to time zero, as illustrated in Figure 71. Remarkably good correlations between calculated and experimental data were obtained in all cases over the first two to three half-lives of the starting species **14**, thus supporting the approach used, and the mechanistic assumptions made. Scattering of the experimental data towards the end of the data acquisition period can be ascribed to a build-up of ethylene in the NMR tube, resulting in a deviation from constant pressure conditions.[22]

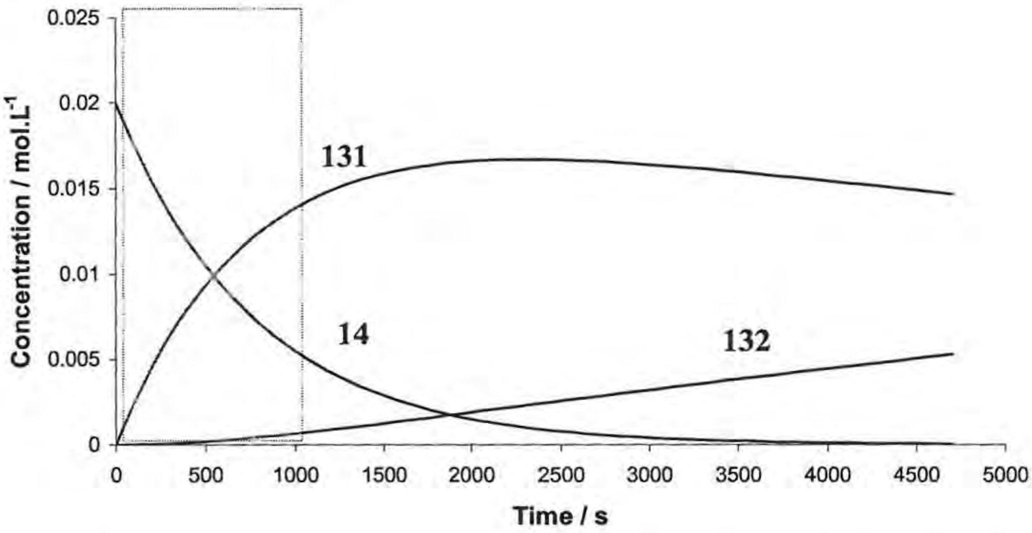

Figure 70. Representative concentration *vs.* time curve for species **14, 131** and **132** (Scheme 68), as calculated using equations 4-6, based on the determined k_1 and k_2 values for the metathesis of 1-octene **128** with catalyst **14** in toluene-d_8 at 10°C.

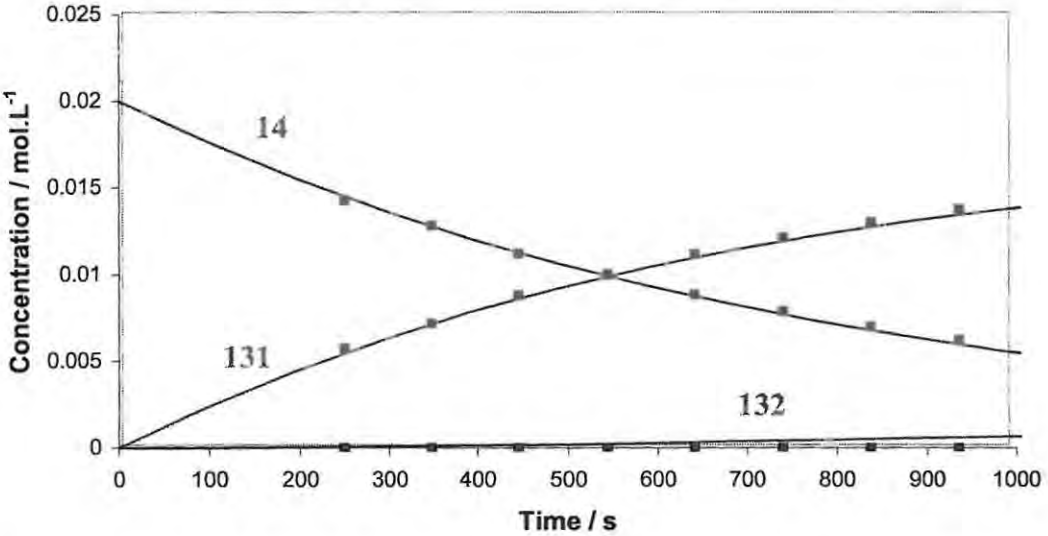

Figure 71. Representative plot of calculated (lines) and experimental (markers) concentration *vs.* time data for species **14, 131** and **132** in the reaction depicted in Figure 70, over the first two half-lives of species **14** (shaded region, Figure 70)

Table 16 contains the k_1 values for all of the kinetic experiments conducted in this study, as calculated by the method described above. These results show excellent reproducibility, with the k_1 values for duplicate data sets falling well within the experimental uncertainties (except in the case where the solvent is chloroform, which will be discussed in section 2.5.3).

Table 16. Pseudo-first-order rate constants (k_1) for a series of kinetic experiments, as calculated by the Guggenheim method described above.

Solvent	**$[14]_0$ / M**	**$[128]_0$ / M**	**T / °C**	**k_1 [a] / s^{-1}**
benzene-d_6	0.0201	0.602	10	$61.9 \pm 3.8 \times 10^{-5}$
benzene-d_6	0.0200	0.600	10	$66.6 \pm 4.1 \times 10^{-5}$
toluene-d_8	0.0200	0.300	10	$65.8 \pm 1.6 \times 10^{-5}$
toluene-d_8	0.0200	0.300	10	$65.3 \pm 2.1 \times 10^{-5}$
toluene-d_8	0.0200	0.600	10	$697.7 \pm 4.0 \times 10^{-6}$
toluene-d_8	0.0200	1.200	10	$763.5 \pm 8.1 \times 10^{-6}$
toluene-d_8	0.0200	1.200	10	$766.4 \pm 7.3 \times 10^{-6}$
toluene-d_8	0.0200	1.800	10	$804.5 \pm 7.1 \times 10^{-6}$
chlorobenzene-d_5	0.0200	0.600	10	$129.4 \pm 4.9 \times 10^{-5}$
chloroform-d	0.0200	0.600	0	$333.2 \pm 3.0 \times 10^{-7}$
chloroform-d	0.0199	0.599	0	$381.3 \pm 2.5 \times 10^{-7}$
chloroform-d	0.0441	1.340	0	$1145.0 \pm 9.1 \times 10^{-7}$
chloroform-d	0.0313	0.142	0	$172.4 \pm 8.5 \times 10^{-7}$
chloroform-d	0.0200	0.600	10	$552.9 \pm 7.3 \times 10^{-6}$
chloroform-d	0.0200	0.600	10	$521.0 \pm 5.8 \times 10^{-6}$

[a] Standard deviations were obtained from the pseudo-first-order regression analyses.

The two sections that follow will deal with the effects of varying solvents and substrate concentrations on the catalyst initiation and propagation rate constants (k_1 and k_2, respectively). Kinetic data were gathered at two different temperatures for the reactions in chloroform, but the competing radical process in this solvent (dealt with in section 2.5.3) renders interpretation of the rate data for the metathesis reaction problematic.

2.5.3 Determination of solvent effects

The data presented in Table 17 for benzene-d_6, toluene-d_8 and chlorobenzene-d_5 appear to support the observation made by Grubbs and coworkers[74] that the catalyst initiation rate (represented by rate constant k_1) is proportional to the dielectric constant of the solvent. This effect has been ascribed to the stabilising effect of polar solvents on the monophosphine intermediate **35** and free PCy_3, which are assumed to be more polar than the starting material **14**. This assumption is borne out by comparison of the relative Mulliken and Hirshfeld charge densities at the ruthenium centres, which clearly shows the increased polarity of the monophosphine species (Figure 72). The stabilising effect of the polar solvents thus enhances the rate of phosphine dissociation (and thus catalyst initiation) in these systems.

Table 17. Rate constants for the metathesis of 1-octene **128** with Grubbs catalyst **14** in various solvents, at 10°C. $[\mathbf{14}]_0 = 0.02M$, thirty-fold substrate excess. Rate constants were determined over 2 half-lives.

Solvent	**Dielectric constant ε**[154]	$k_1{}^a / s^{-1}$	k_2 / s^{-1}	k_1/k_2
benzene-d_6	2.3	$64.5 \pm 4.1 \times 10^{-5}$	6.1×10^{-5}	10.6
toluene-d_8	2.4	$697.7 \pm 4.0 \times 10^{-6}$	5.7×10^{-5}	12.2
chlorobenzene-d_5	5.6	$129.4 \pm 4.9 \times 10^{-5}$	7.8×10^{-5}	16.5
chloroform-d	4.8	$536.9 \pm 7.3 \times 10^{-6}$	3.6×10^{-5}	14.9

[a] Where multiple data sets were available, the tabulated k_1 values represent the mean. In these cases, the quoted standard deviations are the largest observed in the set.

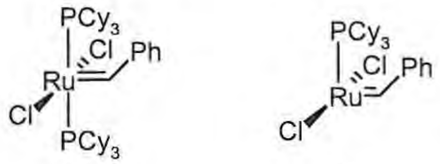

	14	**35**
Mulliken :	0.183	0.288
Hirshfeld :	0.199	0.265

Figure 72. Catalytic species **14** and **35** and the Mulliken and Hirshfeld atomic charge densities at their respective ruthenium centres, as calculated at the DFT level.

Grubbs' suggestion is further supported by our observation that the k_1/k_2 ratio increases with increasing solvent polarity (Table 17). This observation can be tentatively explained by comparing the relative steric and electronic effects of the carbene substituents in species **14** and **131**, and their effect on phosphine dissociation. In the benzylidene species **14**, the electronic effect of the phenyl substituent [as reflected by the Hammett parameter (σ_m=0.06) and the field/inductive parameter (F=0.12)][123] is essentially electron-withdrawing[122] and, consequently, its contribution to the dissociation of the phosphine ligand is likely to be primarily steric in nature rather than electronic. The ruthenium centre of the resulting monophosphine derivative **35** will be somewhat electron-deficient and subject to stabilisation by a polar solvent – an expectation evidenced by the marked increase of k_1 with increasing solvent polarity. In contrast, the alkylidene substituent in species **131** is both sterically bulky *and* electron-*donating* in nature (σ_m= -0.06, F=0.01).[123] The rate of phosphine dissociation is therefore enhanced by both of these factors, and the resultant monophosphine derivative **136** is stabilised by electron-donation to the ruthenium centre, making it less electron-deficient than in the case of species **14**. The electronic stabilising influence of the solvent is thus less pronounced, which explains the smaller impact of solvent polarity on k_2.

The relative electron densities at the ruthenium centres in the monophosphine species may also explain why k_1 is substantially greater than k_2 under all conditions studied. Because the benzylidene monophosphine **35**, generated by dissociation of species **14**, is more electron-deficient than the alkylidene species **136**, generated by species **131**, it is also more reactive, hence the larger k_1 value. This observation highlights the correlation between polarization within the ruthenium alkylidene complex and metathesis activity, which has been alluded to in a study by Paquette and co-workers (who reported that electron-donating carbene substituents tend to retard metathesis activity).[155] This correlation is clearly demonstrated in the present study. Furthermore, the results presented here are unique in that they reflect the interplay between the electronic characteristics of the substrate and the solvent, the judicious selection of which may provide a means of tuning catalyst activity and selectivity under various conditions.

As is evident from Table 17, the rate of metathesis initiation in chloroform is lower than expected based on the relative solvent polarities. We believe that the explanation for this behaviour lies in the existence of a competing radical mechanism under these conditions. Evidence for such a mechanism was observed by Amir-Ebrahimi *et al.*[156] who used EPR analysis to detect the generation of radical anions upon treatment of a range of π-acceptors with the Grubbs catalyst **14** in dichloromethane. In the same year, Snapper and co-workers reported that the Grubbs catalyst **14** facilitates the radical Kharasch addition of $CHCl_3$ to alkenes (Scheme 66).[157]

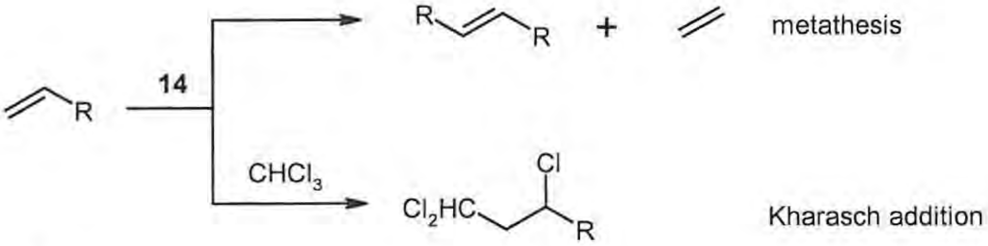

Scheme 66

A more recent and general publication by Opstal and Verpoort[158] illustrates, with supporting experimental evidence and mechanistic proposals, the catalytic potential of a family of ruthenium complexes similar to Grubbs catalyst **14** in the atom transfer radical addition (ATRA) of halogenated alkanes to alkenes. Since the discovery of this dual activity of Grubbs-type catalysts, some attention has been given to the tuning of reaction conditions to promote either ATRA or metathesis.[159] The Kharasch addition of chloroform to 1-octene **128** therefore provides an explanation for the decreased metathesis activity of catalyst **14** in this solvent. A similar rate decrease was observed for metathesis reactions conducted in dichloromethane by Grubbs and co-workers,[74] for which no explanation was offered at the time. We believe that this observation may perhaps have been due to the same competing process.

2.5.4 Determination of substrate concentration effects

In an attempt to obtain real rate constants from the pseudo-rate-constants, the initial concentration of the 1-octene substrate **128** was varied, in order to obtain the rate constant with respect to the 1-octene **128** concentration. However, a plot of k_1 *vs.* 1-octene **128** concentration shows a distinct deviation from linearity, which becomes more pronounced at higher concentration (Table 18, Figure 73).

Table 18. Rate constants for metathesis of 1-octene **128** with Grubbs catalyst **14** in toluene-d_8, at 10°C. $[\mathbf{14}]_0 = 0.02$M, k_1 values determined over 2 half-lives.

$[\mathbf{128}]_0$/ mol.L^{-1}	k_1 ^{a} /s^{-1}	k_2 / s^{-1}	k_1/k_2
0.30	$65.5 \pm 2.1 \times 10^{-5}$	12.9×10^{-5}	5.1
0.60	$697.7 \pm 4.0 \times 10^{-6}$	5.7×10^{-5}	12.2
1.20	$765.0 \pm 8.1 \times 10^{-6}$	4.4×10^{-5}	17.4
1.80	$804.5 \pm 7.1 \times 10^{-6}$	4.5×10^{-5}	17.6

[a] Where multiple data sets were available, the tabulated k_1 values represent the mean. In these cases, the quoted standard deviations are the largest observed in the set.

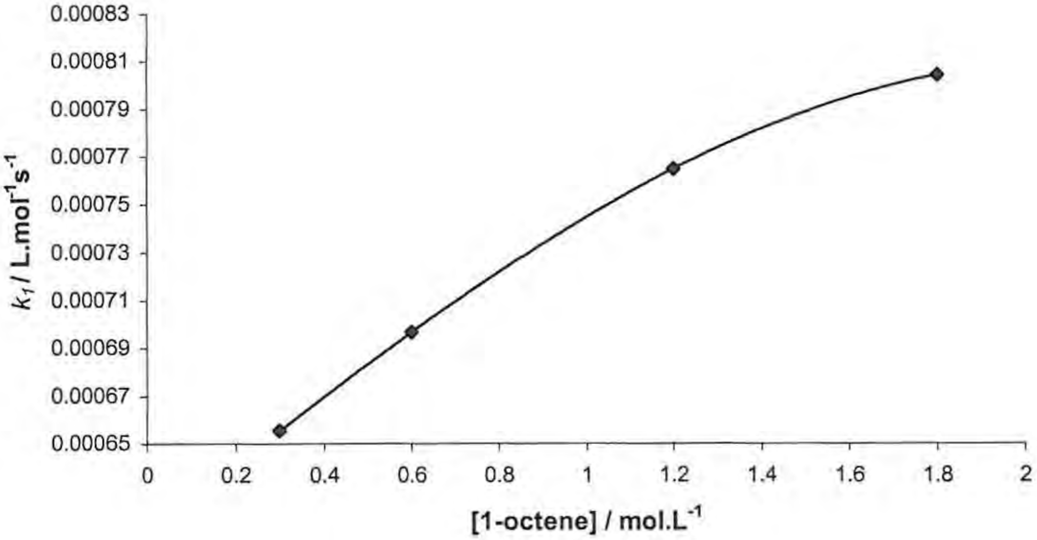

Figure 73. Plot of initiation rate constants k_1 vs. initial concentration of 1-octene **128** for the metathesis reaction catalysed by Grubbs catalyst **14** in toluene-d_8, at 10°C. $[\mathbf{14}]_0 = 0.02$M,

This behaviour can be explained by analysing the catalyst initiation in terms of phosphine dissociation (equation 9) and substrate coordination (equation 10) steps (see Scheme 64, p126):-

$$\mathrm{RuCl_2(PCy_3)_2{=}CHPh}\ \mathbf{14} \underset{k'_{-1}}{\overset{k'_1}{\rightleftharpoons}} \mathrm{RuCl_2(PCy_3){=}CHPh}\ \mathbf{35} + \mathrm{PCy_3} \ldots\ldots\ldots(9)$$

$$\mathrm{RuCl_2(PCy_3){=}CHPh}\ \mathbf{35} + \mathrm{C_8H_{16}}\ \mathbf{128} \underset{k'_{-2}}{\overset{k'_2}{\rightleftharpoons}} \mathrm{RuCl_2(PCy_3)(C_8H_{16}){=}CHPh}\ \mathbf{129a} \ldots\ldots\ldots(10)$$

(Note: k'_1 and k'_2 should not be confused with the observed rate constants k_1 and k_2.) Since the concentration of monophosphine **35** is very low, a steady-state assumption may be applied (*i.e.* $\pm d[\mathbf{35}]/dt \approx 0$), and pseudo-first-order behaviour is observed with respect to the starting species **14**, with $d[\mathbf{129a}]/dt = -d[\mathbf{14}]/dt$, thus:-[160]

$$k_1 = \frac{k'_1\, k'_2\, [\mathbf{128}] + k'_{-1}\, k'_{-2}\, [\mathrm{PCy_3}]}{k'_2\, [\mathbf{128}] + k'_{-1}\, [\mathrm{PCy_3}]} \ldots\ldots\ldots\ldots\ldots\ldots\ldots\ldots\ldots\ldots(11)$$

This analysis is consistent with the behaviour of the systems reported in Section 2.5.2. A linear k_1 *vs.* [**128**] relationship would be expected if both [**128**] and [$\mathrm{PCy_3}$] were much greater than the starting concentration of species **14** and, hence, effectively constant.[160] While this is the case for 1-octene **128**, which is in vast excess, it is not so for unbound $\mathrm{PCy_3}$, the concentration of which has been shown to vary in proportion to the square root of the concentration of catalyst **14** (equation 12).[46]

$$[\mathrm{PCy_3}] = \sqrt{{}^{k'_1}\!/\!{}_{k'_{-1}}\, [\mathbf{14}]_0 [\mathbf{128}]} \ldots\ldots\ldots\ldots\ldots\ldots\ldots\ldots\ldots\ldots(12)$$

This assessment is supported by the observations of Grubbs and co-workers,[46] who achieved linearity of k_1 *vs.* substrate concentration by the addition of excess $\mathrm{PCy_3}$ to the reaction mixture, thereby facilitating the calculation of real rate constants from observed pseudo-first-order constants, and establishing the dominance of the abovementioned dissociative pathway (equations 9 and 10). For the purposes of this study, however, the pseudo-first-order constants reported in Table 18 provide a sufficient measure of comparative solvent and substrate effects.

Thus it is evident that, while the k_1 values increase as expected with increasing substrate concentration, there is a somewhat surprising decrease in the corresponding k_2 values! The rate constant k_2 is, effectively, an indicator of the efficiency of the propagation phase (pathway III, Scheme 64) of the catalytic cycle, whereas k_1 is simply an initiation rate constant, therefore valid only for the first catalyst turnover (pathway I) and of little significance in terms of catalyst efficiency. An analysis of this type may therefore be of great value in determining optimum catalyst loading for an industrial metathesis process, by monitoring the impact of catalyst loading on the k_1/k_2 ratio. This study also serves to highlight the fact that the initiation rate constant k_1 is not a particularly useful measure of catalyst efficiency when considered in isolation.

2.6 COMPUTATIONAL ANALYSIS OF 1-OCTENE SELF-METATHESIS

From the results obtained in the kinetic study, it is apparent that variations in solvent polarity, temperature and catalyst loading have a pronounced effect on catalyst activity. While the incorporation of these effects into DFT calculations is complicated at best, the analysis of temperature effects may be approached more simply by molecular dynamics techniques.

In Section 2.5 it was noted that the selectivity of metallacycle formation (*i.e.* pathway I *vs.* pathway II; Scheme 67) is determined by temperature[122] and that pathway I is followed exclusively at low temperature, with pathway II competing at higher temperature. It is therefore reasonable to assume that pathway I is kinetically favoured (*i.e.* involves lower activation energies) while pathway II is thermo-dynamically favoured (*i.e.* the ground state energy of intermediate **132** is lower than that of intermediate **131**). Both pathways were explored at the semi-empirical and DFT levels. However, the semi-empirical technique failed to adequately represent the ruthenium-alkene π-interaction in intermediates **129** or the metallacycle geometries in intermediates **130**.

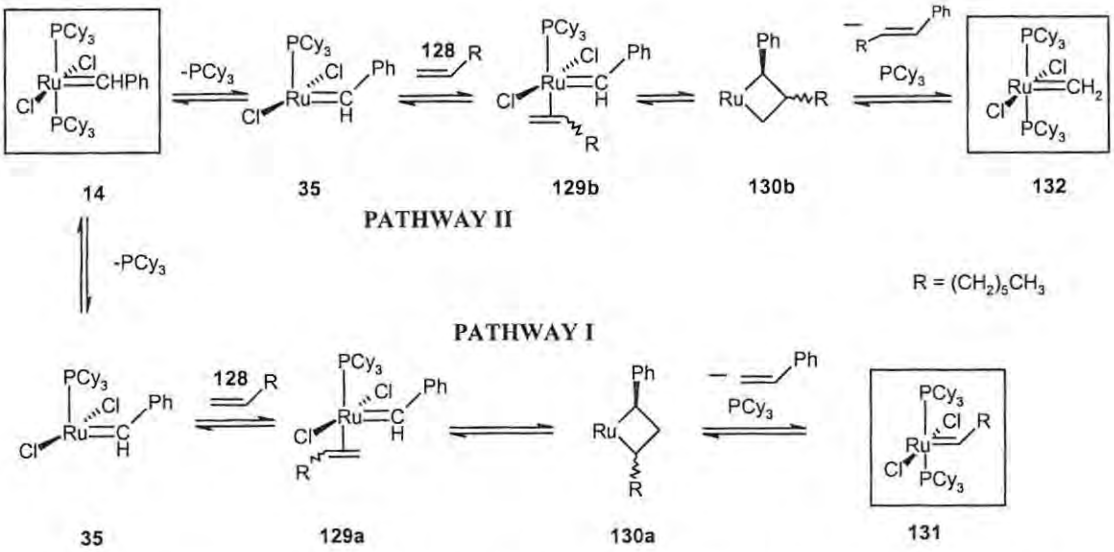

Scheme 67. Initiation phase of the self-metathesis reaction of 1-octene **128** with the Grubbs 1st-generation catalyst **14** (extracted from Scheme 64), showing the two possible pathways to intermediates **131** and **132**. Phosphine ligands are omitted from the metallacycles **130** for clarity.

Figure 74 illustrates the DFT-level electronic energies of the intermediates represented in Scheme 67, relative to that of the precatalyst **14**. The *cis*- and *trans*-designations refer to the position of the alkyl group (R) with respect to the phenyl moiety attached to the carbene carbon (see Figure 75). Only ground state energies are included, as these systems proved to be prohibitively large for transition state calculations at this level. A comparison of the relative energies of intermediates **131** and **132** (4.14 and 3.13 kcal.mol^{-1} respectively) supports the assumption that pathway II is thermodynamically favoured.

While the absence of transition state data prohibits the determination of the kinetically favoured pathway, some aspects of the pathway dependence on temperature may be explored relatively simply, at the molecular mechanics level. It has been noted that at high temperatures pathway II becomes operational,[122] which may occur *via* either of the two pathways **14→35→129b→130b→132** depicted in Figure 74. An alternative but as-yet unexplored rotation of the bound substrate in either of the *cis*- or *trans*-forms of the species **129a** (Figure 75) could also offer access to intermediate **132** at sufficiently high temperatures to overcome the rotational barrier for this process.

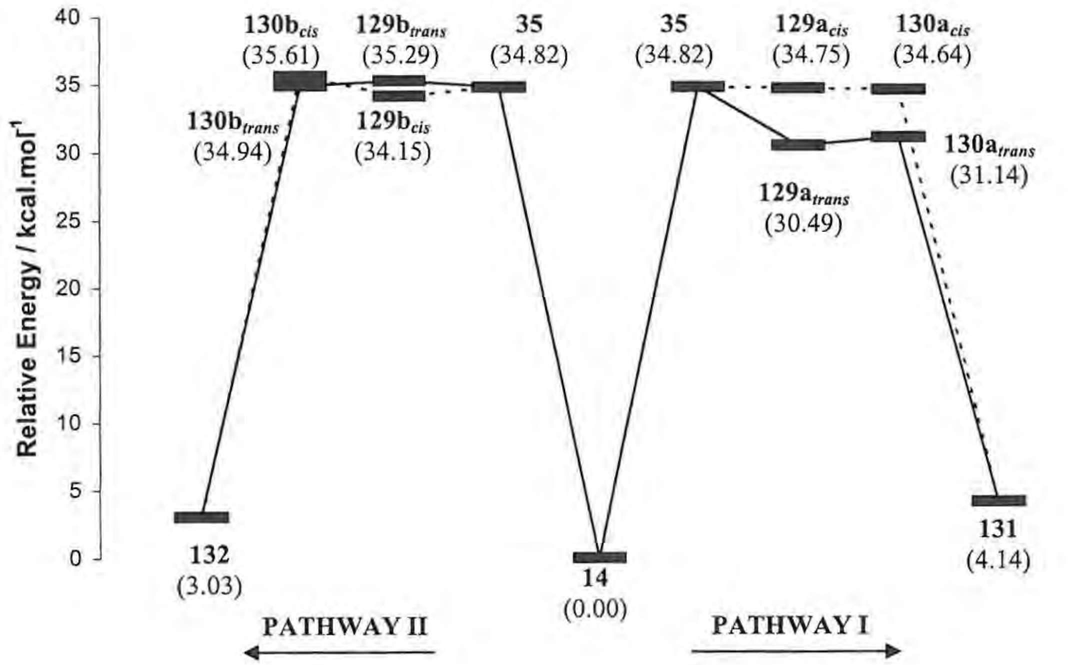

Figure 74. DFT-level relative electronic energy profile for the formation of intermediates depicted in Scheme 67 (energies quoted for monophosphine species include that of unbound PCy_3)

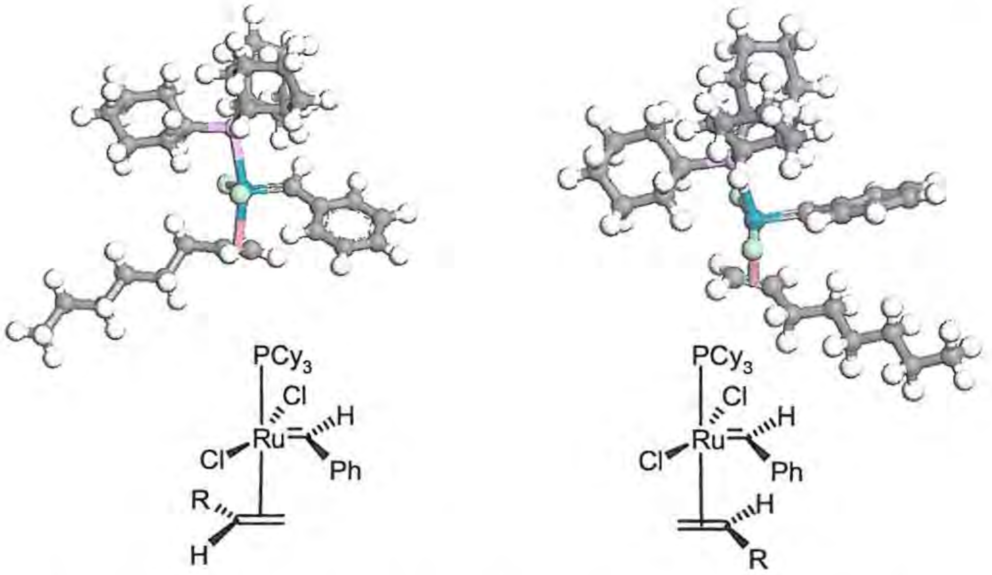

Figure 75. Intermediates **129a**$_{trans}$ (left) and **129b**$_{cis}$ (right) optimised at the DFT level, with line drawings showing the stereochemical designations [R=$(CH_2)_5CH_3$].

Molecular dynamics techniques were therefore revisited in order to explore the likelihood of internal rotation of the coordinated substrate in the π-complex intermediates **129a** and **129b** at different temperatures. To this end, intermediate **129a**$_{trans}$ was geometry-optimised at the molecular mechanics level, and subjected to three annealed dynamics simulations with mid-cycle temperatures of 800K, 1000K, and 2000K. This temperature range was determined by Meier *et al.*,[76] by analysis of the Maxwell-Boltzmann distribution of molecular speeds for organometallic species of this type, to be reflective of molecules at the higher end of the energy spectrum. These temperatures are not, therefore, to be confused with the actual temperatures at which the reactions are conducted.

Results of the dynamics simulation at 800K showed no deviation from the binding orientation in intermediate **129a**$_{trans}$. However, when the mid-cycle temperature was raised to 1000K, the rotational barrier was overcome, and the intermediate took the form of the higher-energy rotamer **129b**$_{cis}$ for approximately 7% of the duration of the simulation (Figure 76). The grouping of the **129b**$_{cis}$ isomers (circled) would appear to suggest that the temperature conditions of the simulation closely approximate the actual rotational barrier for this species, which is exceeded only twice in the simulation period.

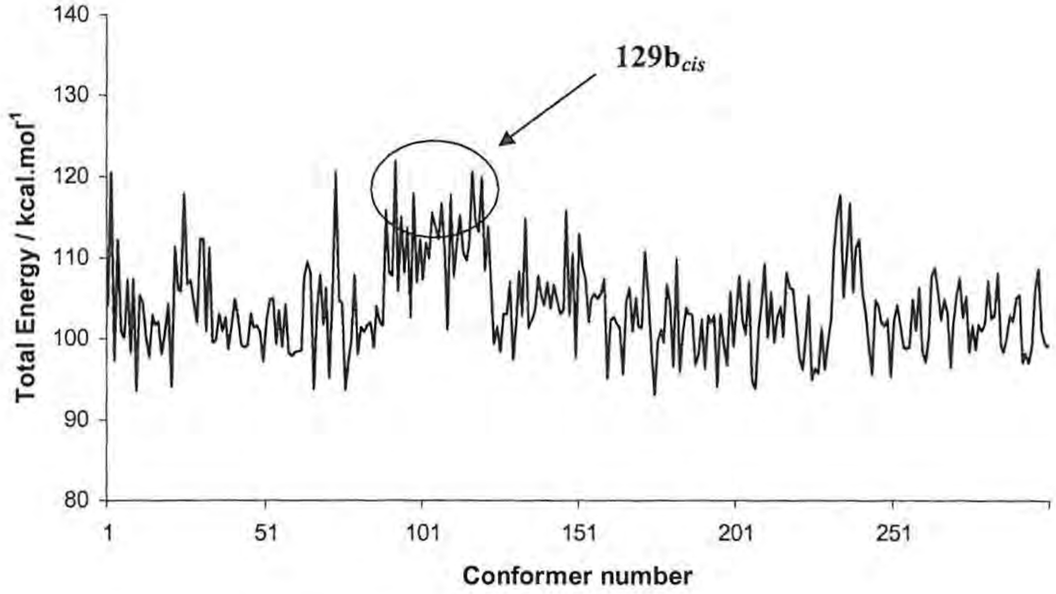

Figure 76. Total energy profile for the molecular dynamics simulation of the substrate-bound intermediate **129** (Scheme 67), with a mid-cycle temperature of 1000K. The intermediate takes the form of rotamer $\mathbf{129a}_{trans}$, except in the region indicated, where it adopts the form of rotamer $\mathbf{129b}_{cis}$.

Results of the dynamics simulation performed with a mid-cycle temperature of 2000K are depicted in Figure 77. At these higher temperatures, the energy of the molecules is generally much higher than the rotational barrier. The molecule thus changes orientation from rotamer $\mathbf{129a}_{trans}$ to $\mathbf{129b}_{cis}$ at random intervals (*i.e.* instances of the $\mathbf{129b}_{cis}$ orientation are scattered randomly throughout the energy profile in Figure 77), with the $\mathbf{129b}_{cis}$ orientation existing for approximately 12% of the simulation period. From these results, it seems that at high temperature, the rotation $\mathbf{129a}_{trans} \rightarrow \mathbf{129b}_{cis}$ occurs readily, permitting pathway II (Scheme 67) to be followed.

The propagation phase of the metathesis cycle (Scheme 68) was also explored at the DFT level. Data obtained in the kinetic analysis (Figure 65, p127) suggests that, at low temperature (10°C), the productive pathway III is preferred. Although the unproductive pathway IV is theoretically feasible, there is no experimental evidence to suggest that it plays a significant role.

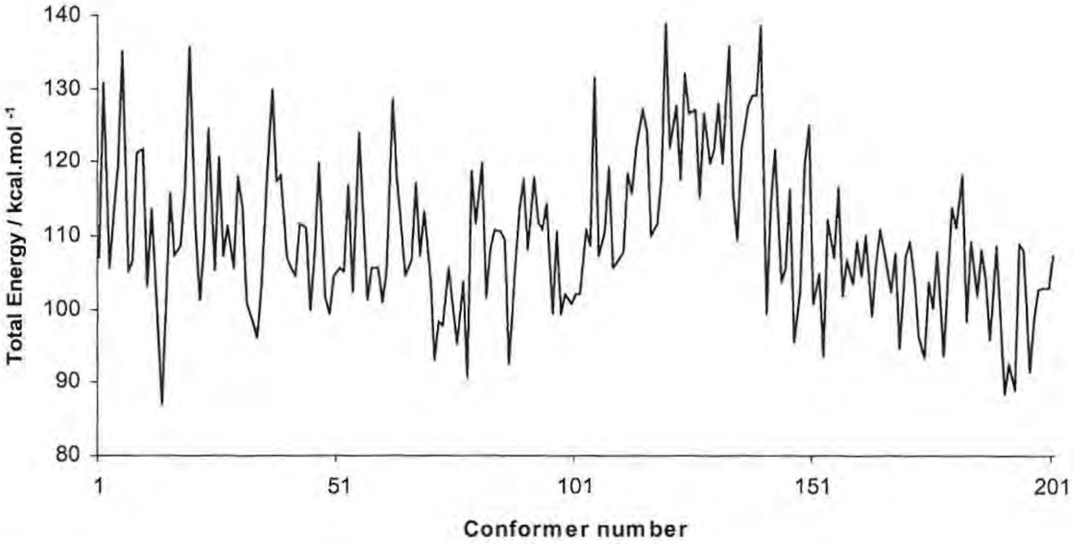

Figure 77. Total energy profile for the molecular dynamics simulation of the substrate-bound intermediate **129** (Scheme 67), with a mid-cycle temperature of 2000K.

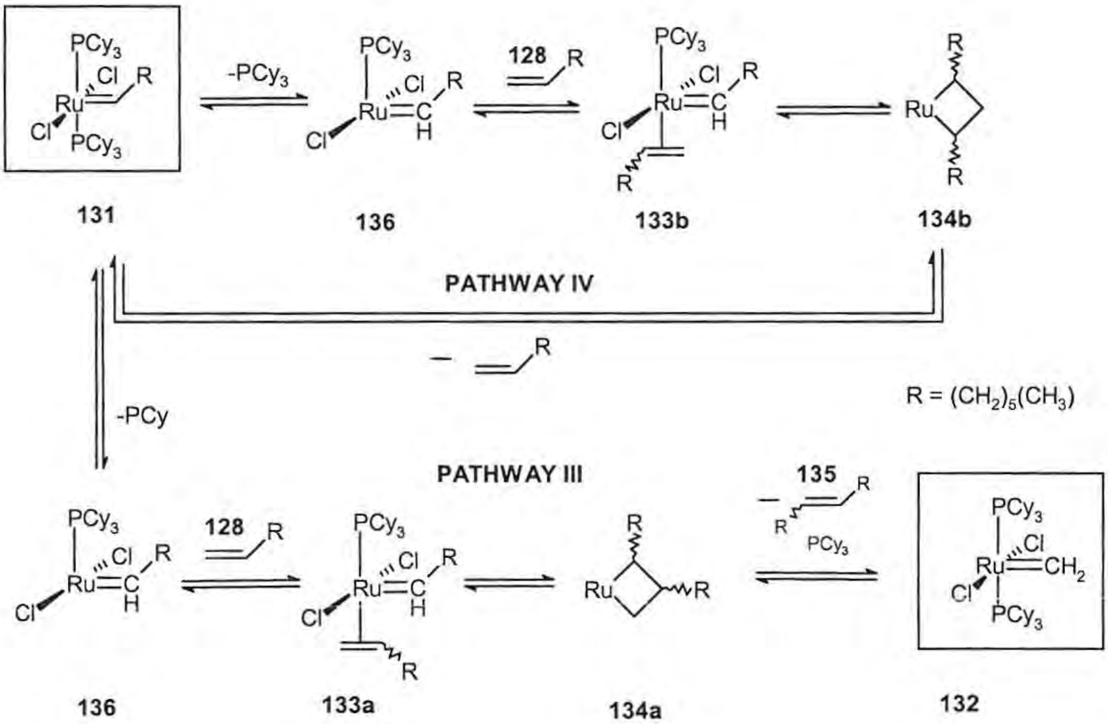

Scheme 68. Productive (III) and unproductive (IV) metathesis pathways for species **131** (extracted from Scheme 64), showing productive formation of the self-metathesis product **135**.

The DFT-level energy profile (Figure 78) would appear to suggest that, in addition to being the kinetically favoured pathway (as determined experimentally in the kinetic study), the productive pathway III is also thermodynamically favoured. Thus, it is expected that a rise in the reaction temperature should not result in competition from the unproductive pathway IV. It is also reasonable to assume that a rotational barrier exists between intermediates **133a** and **133b** similar to that explored above. However, attempts to explore this rotational barrier at the molecular dynamics level proved unsuccessful, as the square pyramidal geometry of the species became unreasonably distorted at the simulation temperatures. Whether this is a failure of the force-field to represent the system correctly, or an indication that the rotation does not take place, has yet to be established.

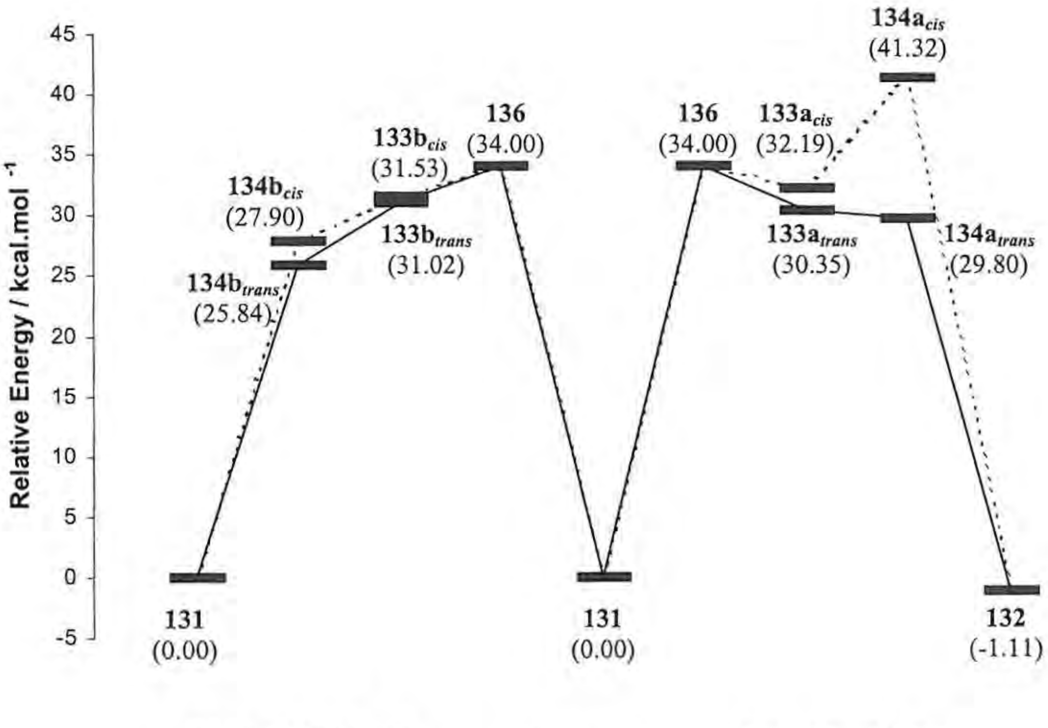

Figure 78. DFT-level relative electronic energy profile for the formation of intermediates depicted in Scheme 68 (energies attributed to monophosphine species include that of unbound PCy_3)

Computational analyses of this type show considerable promise in predicting the metathesis activity of a given catalyst towards a given substrate under various reaction conditions. A comparison of the energies of intermediates at the DFT level provides a means of predicting the pathway preference for reactions under conditions of thermodynamic control. This type of assessment may prove useful in pre-determining the effects of varying temperature conditions on a given metathesis reaction. However, in order to provide a more thorough analysis of the energetics of the reaction, it is necessary to consider the relevant transition state energies. Thus, future work will involve extending the DFT calculations, perhaps at a non-gradient-corrected level, to include the transition states.

2.7 CONCLUSIONS

The use of metathesis reactions in synthesis has expanded significantly in the past decade with the development of state-of-the-art, structurally defined catalyst systems.[13] The design of such systems requires an intimate understanding of the catalytic processes, for which a growing number of tools have become available. Foremost among these are a number of rapidly-developing computational techniques. In the present study, the integration of some of these techniques in the rational design and development of novel metathesis catalysts has been explored.

Several computational methods encompassing the use of molecular mechanics, semi-empirical techniques and density functional theory (DFT) were assessed in terms of their ability to generate reliable structural and energy data for a known metathesis catalyst. These techniques were benchmarked against experimental and computational data reported by other groups, and found to compare remarkably well. Not surprisingly, the DFT approach proved to be the most reliable, and was employed for the bulk of the computational work.

The DFT approach developed in the benchmarking study was employed in the design of a putative camphor-derived tridentate ligand for Grubbs-type ruthenium catalysts. The synthetic approach to this ligand provided the context for several interesting computational studies. Through energy-profiling of the various mechanistic pathways and analysis of the intermediate and transition state geometries, some useful insight was gained into the driving force behind the C-8 functionalisation of camphor. In addition, a coset analysis approach was combined with conventional DFT techniques to resolve some confusion in the literature regarding the origin of the major by-product in this process. Although ring-opening of the C-8-brominated system failed to proceed as expected, the novel compounds **62**, **63**, **69** and **71** were isolated and characterised. Computational approaches, including the use of *ab initio* NMR prediction techniques, were employed to assist in the characterisation of these compounds. Single-crystal X-ray analysis of the novel camphoric acid derivative **69** revealed a chiral, H-bonded polymeric array that may render this compound an interesting candidate for chiral inclusion studies. The formation of compounds **63** and

69 present some new challenges to our mechanistic understanding of rearrangements in camphor-derived systems, and these will be addressed in a future study.

Attempts to replace the anionic ligands in known ruthenium catalyst systems led to a detailed computational analysis of the electronic effect of these ligands on the metal centre and their resultant impact on catalyst activity. The evaluation of computed electronic parameters (CEP's) for the anionic ligands of catalysts **79**, **80** and **81** provided a useful measure of the nett electron donor potential of the ligands, in terms of which we were able to clarify some misconceptions in the literature regarding their relative electronic effects. In addition to their potential usefulness as a ligand design tool, the correlation of ligand CEP's with ^1H NMR data was demonstrated to be a promising means of characterising transient catalytic species in solution. Preliminary complexation studies demonstrated the potential of the malonate di-anion to bind to ruthenium in a bidentate manner. This observation led to the use of the malonate system as a scaffold for the design of potential tridentate ligand systems. Results of these studies also suggested the formation of competing complexes when silver salts are used to facilitate ligand substitution.

Based on the results of the complexation studies, putative catalysts **93** and **94** were proposed, and a broad assessment of their prospective geometries and catalyst activities was made, based on DFT-level calculations. A novel synthetic route to the ligand system for catalyst **94** was proposed, based on Reformatsky-type methods. Although this approach proved to be largely unsuccessful, some promising progress was made towards the synthesis of the ligand system required for catalyst **93**.

A detailed kinetic study of the catalysed self-metathesis of 1-octene **128** was undertaken, focussing on the effect of varying solvents and substrate concentrations. The approach used to analyse the kinetic data allowed unprecedented access to rate constants (k_2) for the propagation phase of the catalytic cycle, as opposed to the standard approach of assessing only the initiation phase (k_1). This new information confirmed previous assessments of solvent effects on catalyst activity, and provided new evidence to support the correlation between polarization within the catalytically active species, and metathesis activity. Analysis of the effect of varying substrate concentrations on metathesis activity highlighted the distinction between initiation and propagation rates, and the approach employed in this analysis shows promise as a means of determining optimum catalyst loadings for metathesis reactions.

A preliminary computational analysis of the catalysed 1-octene self-metathesis reaction showed a generally pleasing correlation with the kinetic results, indicating the potential of DFT techniques to predict the pathway selectivity for a given catalyst/substrate combination. Furthermore, molecular dynamics calculations have been demonstrated to be a useful means of exploring general mechanistic issues such as the feasibility of ligand rotation.

Future research is expected to focus on:-

(i) a mechanistic analysis of the camphor rearrangements reported in Section 2.2.2.2 and an assessment of the chiral host potential of compound **69**;

(ii) an alternative synthetic approach to the tridentate camphor-derived ligand **38**;

(iii) completion of the synthetic approach to putative catalyst **93**;

(iv) further exploration of the utility of ligand CEP calculations in the catalyst design process; and

(v) application of the kinetic approach to a range of metathesis substrates.

3. EXPERIMENTAL

3.1 COMPUTATIONAL

3.1.1 Computational methods

3.1.1.1 Molecular mechanics calculations

All molecular mechanics calculations were performed using the Cerius^2 software package, developed by BIOSYMM/Molecular Simulations, running on an SGI O^2 unix-based platform. The default Universal Force Field was used,[161] which is a general-purpose force-field parameterized for the full periodic table, and validated for numerous structure types including metal complexes. Charges were included *via* the charge-equilibration method,[162] applying the Qeq_charged 1.0 parameter set supplied with the programme. All structures were minimized to convergence using the conjugate gradient method.[163]

After initial minimization of the system, isothermal molecular dynamics methods were employed to locate lowest energy conformers. Annealed dynamics simulations were performed with a mid-cycle temperature of 1000K (unless otherwise stated) and the lowest energy structure from each cycle was saved and minimized. In all cases, the global minimum was selected from a total of 300 anneal cycles.

3.1.1.2 Semi-empirical calculations

All semi-empirical calculations were carried out using the Spartan '02 programme developed by Wavefunction Inc.[88] Geometry optimisations were performed using the semi-empirical PM3 model, which is parameterised for transition metals.

3.1.1.3 Density functional calculations

All density functional theory (DFT) calculations were performed using the DMol^3 DFT code[89] provided in the MaterialsStudio (version 2.2) package of Accelrys Inc, on LINUX-based Pentium IV PC's. All calculations made use of the non-local generalized gradient approximation (GGA) functional by Perdew and Wang (PW91).[164] The basis set employed was a 'double numerical plus polarization' (DNP) basis set: - a polarized split valence basis set of numeric atomic functions which are exact solutions to the Kohn-Sham equations for the atoms.[165]

Geometry optimizations were subjected to convergence criteria of threshold values 2 x 10^{-5} Ha, 0.004 Ha/Å, 0.005 Å and 1 x 10^{-5} Ha for energy, force, displacement and self-consistent field (SCF) density, respectively, unless otherwise stated. All calculations employed a method based on the direct inversion of iterative subspace (DIIS) technique developed by Pulay,[166] in order to speed up SCF convergence. Where necessary, a small electron thermal smearing value of 0.005 Ha was specified to facilitate SCF convergence.

Preliminary transition state geometries were obtained using the integrated linear synchronous transit/quadratic synchronous transit (LST/QST) method,[167] and then subjected to full TS optimizations using an eigenvector-following algorithm. Where necessary, these geometries were confirmed using intrinsic reaction path (IRP) calculations, based on the nudged elastic band (NEB) algorithm,[168] to map the pathways connecting the relevant reactant, TS and product geometries.

All the structures identified as stationary points were subjected to full frequency analysis in order to verify their classification as equilibrium geometries (zero imaginary frequencies) or transition states (one imaginary frequency).

All reported energies refer to Gibbs free energy corrections to the total electronic energies at 298.15 K, including zero-point energy (ZPE) corrections, unless stated otherwise.

3.1.2 Computational data

Tables 19 and 20 contain energy data for the molecules and transformations represented in Schemes 24 (Section 2.1.2) and 25 (Section 2.2.1) of the discussion. Tables 21 and 22 contain energy data for the molecules and transformations represented in Scheme 28 (Section 2.2.2.1) of the discussion, with X=H, Y=Br (Table 21), and X=Y=Br (Table 22). Table 23 contains data depicted in Scheme 34 of the same section.

Table 19. Total electronic and free energies, gas phase enthalpies and entropies for molecules depicted in Scheme 24, calculated at the DFT level. Geometry optimizations were subjected to convergence criteria of threshold values 1 x 10^{-5} Ha, 0.002 Ha/Å, 0.005 Å and 1 x 10^{-6} Ha for energy, force, displacement and self-consistent field (SCF) density, respectively.

Molecule	E (Hartrees)	G (Hartrees)	H (Hartrees)	S (cal/mol.K)
31	-6090.2674820	-6090.2259048	-6090.5652984	105.917
TS I	-6090.2356734	-6090.2031925	-6090.1434116	125.820
i	-5747.0858356	-5747.066728	-5747.0227766	92.504
TS II	-5825.6690081	-5825.6057579	-5825.5512135	114.798
ii	-5825.6882998	-5825.6208042	-5825.5681786	110.758
TS III	-5825.6717389	-5825.6051746	-5825.5523157	111.250
iii	-5825.6830224	-5825.6130313	-5825.5612598	108.960
PH_3	-343.1464752	-343.1441294	-343.1192166	52.435
C_2H_4	-78.5788536	-78.5509017	-78.5246838	55.180

Table 20. Total electronic and free energies, gas phase enthalpies and entropies for molecules depicted in Scheme 25, calculated at the DFT level.

Molecule	E (Hartrees)	G (Hartrees)	H (Hartrees)	S (cal/mol.K)
41	-5702.9795682	-5702.8263351	-5702.7639327	131.338
TS I	-5702.9451109	-5702.7977741	-5702.7320507	138.326
i	-5359.7972370	-5359.6685135	-5359.6116664	119.647
TS II	-5438.3854734	-5438.2119250	-5438.1445139	141.878
ii	-5438.4123247	-5438.2323222	-5438.1703963	130.333
TS III	-5438.3909869	-5438.2109637	-5438.1490489	130.311
iii	-5438.4005453	-5438.2217890	-5438.1582249	133.780
PH_3	-343.1466147	-343.1441860	-343.1192748	52.430
C_2H_4	-78.5783454	-78.5499059	-78.5237246	55.102

Table 21. Total electronic and free energies, gas phase enthalpies and entropies for molecules depicted in Scheme 28, X=H, Y=Br, calculated at DFT level.

molecule	E (Hartrees)	G (Hartrees)	H (Hartrees)	S (cal/mol.K)
48a	-5613.7293877	-5613.544223	-5613.486877	120.692
48a → 50' TS	-5613.7250396	-5613.537614	-5613.484457	111.878
50'	-5613.7598643	-5613.571946	-5613.515719	118.337

Table 22. Total electronic and free energies, gas phase enthalpies and entropies for molecules depicted in Scheme 28, X=Y=Br, calculated at the DFT level.

molecule	E (Hartrees)	G (Hartrees)	H (Hartrees)	S (cal/mol.K)
48b	-8187.4741898	-8187.301516	-8187.240652	128.103
48b → 49b TS	-8187.4497827	-8187.277147	-8187.217948	124.595
49b	-8187.4757682	-8187.303681	-8187.243397	126.881
48b → 52ii TS	-8187.4561275	-8187.283124	-8187.224115	124.198
52ii	-8187.4784476	-8187.306949	-8187.246345	127.551
52ii→ 52i TS	-8187.4707330	-8187.299644	-8187.239829	125.889
48b → 52i TS	-8187.4519901	-8187.280126	-8187.220691	125.089
52i	-8187.4768999	-8187.307208	-8187.245013	130.902
52i→ 45 TS	-8187.4700738	-8187.298551	-8187.238619	126.138
45'	-8187.4949724	-8187.321963	-8187.260873	128.571

Table 23. Total electronic and free energies, gas phase enthalpies and entropies for molecules depicted in Scheme 34, calculated at the DFT level.

molecule	E (Hartrees)	G (Hartrees)	H (Hartrees)	S (cal/mol.K)
47b	-5613.7332885	-5613.548481	-5613.491728	119.445
57	-10761.2189698	-10761.058466	-10760.993758	136.191
57→ 59 TS	-10761.2055904	-10761.04637	-10760.98255	134.329
59	-10761.2253823	-10761.06653	-10761.00101	137.904
59 →60 TS	-10761.2209575	-10761.06260	-10761.99800	136.000
60	-10761.2664150	-10761.10597	-10761.04099	136.776

Table 24. Total electronic and free energies, gas phase enthalpies and entropies for brominated camphoric acid derivatives **43**, **66** and **69**, calculated at the DFT level and subjected to convergence criteria of threshold values 1.0 x 10^{-5} Ha, 0.002 Ha/Å, 0.005 Å and 1 x 10^{-6} Ha for energy, force, displacement and self-consistent field (SCF) density, respectively.

molecule	E (Hartrees)	G (Hartrees)	H (Hartrees)	S (cal/mol.K)
43	-3265.4217690	-3265.2235070	-3265.1647950	123.567
66	-3265.4258937	-3265.2286277	-3265.1695288	124.382
69	-3265.4343748	-3265.2355534	-3265.1770251	123.183

Tables 25 - 29 contain comparisons of experimental and computed ^{13}C NMR shifts for selected camphor derivatives, as discussed on page 88. Chemical shifts were calculated using the GAUSSIAN GIAO NMR prediction technique,[114] at the HF/6-311+G(2d,p) level of theory, and referenced to TMS (the geometry optimization and chemical shift of which were calculated at the same level of theory).

Table 25. Calculated *vs.* experimental ^{13}C chemical shifts for lactone **63**.

Carbon number	$\delta_{calculated}$ (ppm)	$\delta_{experimental}$ (ppm)	absolute error (ppm)
9	18.7	16.4	2.3
10	21.4	21.1	0.3
7	26.7	27.0	0.3
8	37.6	34.5	3.1
5	51.1	44.7	6.4
1	52.5	49.9	2.6
6	54.1	54.5	0.4
4	74.1	69.2	4.9
11	176.7	181.0	4.3
2	181.9	192.5	10.6

Table 26. Calculated *vs.* experimental ^{13}C chemical shifts for camphoric acid **68**.

Carbon number	$\delta_{calculated}$ (ppm)	$\delta_{experimental}$ (ppm)	absolute error (ppm)
9	17.4	21.3	3.9
10	19.7	21.8	2.1
8	25.3	22.5	2.8
5	29.9	23	6.9
6	35.9	32.5	3.5
7	43.2	45.9	2.7
4	52.2	52.4	0.2
1	54.8	53.8	1.0
3	183.1	175.5	7.6
2	192.6	177.4	15.2

Table 27. Calculated *vs.* experimental ^{13}C chemical shifts for 8-bromocamphoric anhydride **62**.

Carbon number	$\delta_{calculated}$ (ppm)	$\delta_{experimental}$ (ppm)	absolute error (ppm)
10	15.2	14.2	1.0
9	17.6	17.1	0.5
6	22.6	23.6	1.0
5	31.9	34.8	2.9
8	43.3	38	5.3
1	48.1	48.1	0.0
4	48.6	52.1	3.5
7	49.6	53.3	3.7
3	178.0	169.0	9.0
2	182.3	172.1	10.2

Table 28. Calculated *vs.* experimental ^{13}C chemical shifts for bromocamphoric acid **69**.

Carbon number	$\delta_{calculated}$ (ppm)	$\delta_{experimental}$ (ppm)	absolute error (ppm)
8	20.7	22.1	1.4
7	25.1	22.2	2.9
4	30.9	22.4	8.5
5	33.5	28.4	5.1
6	45.8	40.3	5.5
2	52.6	47.3	5.3
3	56.1	52.2	3.9
1	56.3	61.7	5.4
9	182.3	173.5	8.8
10	190.6	174.3	16.3

Table 29. Calculated *vs*. experimental ^{13}C chemical shifts for 9-bromocamphoric acid **66**.

Carbon number	$\delta_{calculated}$ **(ppm)**	$\delta_{experimental}$ **(ppm)**	**absolute error (ppm)**
8	16.0	18.7	2.7
10	19.2	21.2	1.9
5	25.6	23.5	2.1
6	36.2	33.6	2.6
9	46.5	41.5	5.0
7	50.8	48.6	2.2
4	52.7	49.9	2.8
1	56.4	55.7	0.7
3	182.7	174.5	8.2
2	192.0	176.2	15.8

Table 30. ^{1}H NMR chemical shifts of the benzylidene protons H_{α}, and ligand computed electronic parameters (CEP's) for complexes depicted in Figure 54 (page 103).

Complex	**δ (ppm)**	**CEP (cm^{-1})**
85	14.40	2079.85
78	16.56	2094.93
79	17.38	2098.19
81	18.49	2113.75

Table 31. Mulliken and Hirshfeld atomic charge densities on the ruthenium metal centres of selected catalytic intermediates depicted in Figure 72 (page 135)

Intermediate	**Mulliken charge**	**Hirshfeld charge**
14	0.183	0.199
35	0.288	0.265

Table 32. Electronic energies, calculated at the DFT level, for the intermediates depicted in Figure 74 (Section 2.6).

Intermediate	**E (hartrees)**
14	-7729.2792975
35	-6682.1337956
129a$_{\text{cis}}$	-6996.5728017
129a$_{trans}$	-6996.5795862
129b$_{cis}$	-6996.5737478
129b$_{trans}$	-6996.5719390
130a$_{cis}$	-6996.5729671
130a$_{trans}$	-6996.5785514
130b$_{cis}$	-6996.5714270
130b$_{trans}$	-6996.5724958
131	-7734.0827120

Table 33. Electronic energies, calculated at the DFT level, for the intermediates depicted in Figure 78 (Section 2.6).

Intermediate	**E (hartrees)**
131	-7734.0827120
136	-6686.9385195
133a$_{\text{cis}}$	-7001.3802932
133a$_{trans}$	-7001.3832246
133b$_{cis}$	-7001.3813360
133b$_{trans}$	-7001.3821511
134a$_{cis}$	-7001.3657341
134a$_{trans}$	-7001.3840989
134b$_{cis}$	-7001.3871320
134b$_{trans}$	-7001.3904138
132	-7498.2242794

SYNTHESIS

3.2.1 General

All melting points were determined using a Kofler hot-stage apparatus and are uncorrected. NMR spectra were recorded on a Bruker AMX400 spectrometer at 303 K (unless stated otherwise) in the specified deuterated solvents. Spectra recorded in $CDCl_3$ were calibrated on the solvent signals at 7.25ppm for ^1H and 77.0ppm for ^{13}C. Spectra recorded in DMSO-d_6 were calibrated using the solvent signals at 2.50ppm for ^1H and 39.5ppm for ^{13}C. Infra-red spectra were recorded on a Perkin Elmer FT-IR Spectrum 2000 spectrometer, the samples being analysed as KBr discs, or as thin films on CsI discs. Low-resolution mass spectrometry was carried out on a Finnigan MAT GCQ mass spectrometer, using the electron ionization (EI) mode unless stated otherwise. Optical rotations were measured using a Perkin-Elmer 141 polarimeter; concentrations are quoted in grams per 100ml.

Normal phase HPLC was effected on a Whatman Partisil 10 Magnum 6 normal phase column using a Spectra-Physics P100 isocratic pump and a Waters R1410 differential refractometer detector. Flash chromatography was carried out using Merck silica gel 60 (particle size 0.040 – 0.063mm) and vacuum chromatography with Merck TLC grade silica gel (particle size 10 – 40 μ). Chromatotron plates were made with silica gel 60 PF_{254} containing $CaSO_4$.

All dry solvents were prepared by conventional methods as described by Perrin and Armarego.[169] Thus, Et_2O, C_6H_6, THF and toluene were distilled from Na wire and bezophenone under N_2, while CH_2Cl_2 was pre-dried over CaH_2 and then distilled from $CaCl_2$ under N_2.

3.2.2 Approaches to tridentate camphor ligands

3.2.2.1 C-8 Functionalisation of camphor

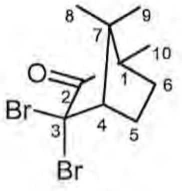

44b

(+)-3,3,-Dibromocamphor[95] **44b**

A mixture of (+)-3-bromocamphor **44a** (55g, 0.24mol) and Br_2 (18ml, 0.35mol) was heated in a round-bottomed flask at 50°C for 24 hours in the dark. The cooled reaction mixture was diluted with Et_2O (200ml) and water (200ml), and the excess Br_2 removed by the addition of solid sodium metabisulphite. The aqueous layer was extracted with Et_2O (2 x 50ml) and the combined organic extracts were dried over anhydrous $MgSO_4$. The solvent was evaporated *in vacuo* to afford (+)-3,3-dibromocamphor **44b** (58g, 78%), m.p. 61°C (lit.,[95] 60°C); $[\alpha]_D^{21}$= +32.7° (*c* 1.06, $CHCl_3$) {lit.,[170] $[\alpha]_D^{25}$ = +37.1° (*c* 1.67, EtOH)}; δ_H (400MHz; $CDCl_3$) 1.00 (3H, s, 9-CH_3), 1.10 (3H, s, 8-CH_3), 1.23 (3H, s, 10-CH_3), 1.63 (2H, m, 6-CH_2), 2.06 (1H, m, 5-H), 2.30 (1H, m, 5-H) and 2.80 (1H, d, *J* 4.0 Hz, 4-H); δ_C (100MHz; $CDCl_3$) 10.3 (C-10), 22.5 (C-9), 24.0 (C-8), 29.0 (C-6), 29.1 (C-5), 46.1 (C-1), 57.7 (C-7), 59.5 (C-4), 63.4 (C-3) and 206.5 (C-2).

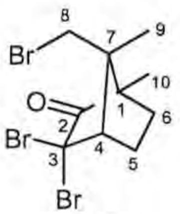

45

(+)-3,3,8-Tribromocamphor[96] **45**

(+)-3,3-Dibromocamphor **44b** (30g, 97mmol) was added to a cooled solution of Br_2 (8.0ml, 0.15mol) in chlorosulphonic acid (45ml). The resulting solution was stirred at room temperature for 4 hours, then added, dropwise, to ice-water (*ca.* 300ml). The excess acid was neutralized with solid sodium hydrogen carbonate and the excess Br_2 destroyed with sodium disulphite. The resulting aqueous mixture was extracted with Et_2O (4 x 100ml) and the combined organic extracts were dried over anhydrous $MgSO_4$. The solvent was evaporated *in vacuo*, and the residual oil distilled at 175°C under reduced pressure to afford crude 3,3,8-tribromocamphor **45** [(19g, 51%); δ_C (100MHz; $CDCl_3$) 9.7, 16.5, 21.7, 32.4, 38.1, 47.9, 52.2, 52.3, 57.7 and 211.1], which was used without further purification.

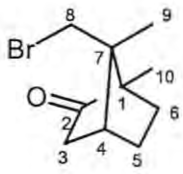

42

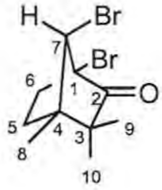

54

(+)-8-Bromocamphor[96] **42** *and (-)-3,3,4-trimethyl-1,7-dibromonorbornan-2-one* **54**

(+)-3,3,8-Tribromocamphor **45** (8.0g, 20mmol) was dissolved in glacial acetic acid (40ml) in a round-bottomed flask. Zinc dust (4.4g) was added, and the reaction mixture stirred vigorously while being cooled with ice-water. Stirring was continued for 1 hour, during which time the exothermic reaction subsided. The solution was then decanted from the zinc salt into Et_2O (*ca.* 300ml), and the resulting mixture was washed with water (10 x 50ml) and dried over anhydrous $MgSO_4$. Removal of the solvent *in vacuo* afforded a brown oil (9.7g) which was chromatographed [flash chromatography on silica gel; elution with hexane-EtOAc (9:1)] to afford two fractions.

i) (+)-8-Bromocamphor **42** (44%). An analytical sample was prepared by further chromatography [HPLC on Partisil 10; elution with hexane-EtOAc (9:1)], affording white crystals of (+)-8-bromocamphor **42**, m.p. 82-84°C (lit.,[95] 83-85°C); $[\alpha]_D^{22}=+72.5°$ (*c* 0.80, $CHCl_3$), {lit.,[95] $[\alpha]_D^{25} = +76.7°$ (*c* 1.24, $CHCl_3$)}; δ_H (400MHz; $CDCl_3$) 0.92 (3H, s, 9-CH_3), 1.14 (3H, s, 10-CH_3), 1.38 (1H, m, 5-H), 1.56 (1H, m, 6-H), 1.81 (1H, m, 6-H), 1.91 (1H, m, 5-H), 1.95 (1H, d, *J* 18.4 Hz, 3-H), 2.39 (1H, m, 3-H), 2.44 (1H, t, *J* 4.4Hz, 4-H), 3.10 (1H, d, *J* 11.0 Hz, 8-H) and 3.17 (1H, d, *J* 11.0 Hz, 8-H); δ_C (100MHz; $CDCl_3$) 9.4 (C-10), 15.6 (C-9), 26.3 (C-5), 31.8 (C-6), 39.5 (C-8), 41.4 (C-4), 42.4 (C-3), 51.5 (C-1), 58.2 (C-7) and 217.8 (C-2); *m/z* 231/233 (M^+, 57% / 55%) and 107 (100).

ii) (-)-3,3,4-Trimethyl-1,7-dibromonorbornan-2-one **54** 10%, m.p. 117-119°C (lit.,[95] 123-124°C); ν_{max}(thin film)/cm^{-1} 1761 (C=O); $[\alpha]_D^{23}$=-53.3° (c 1.05, $CHCl_3$) {lit.,[95] $[\alpha]_D^{23}$ = -51.5° (*c* 1.57, $CHCl_3$)}; δ_H (400MHz; $CDCl_3$) 1.08 (3H, s, 9-CH_3), 1.23 (3H, s, 8-CH_3), 1.39 (3H, s, 10-CH_3), 1.68-1.74 (1H, m, 5-H), 2.09-2.12 (1H, m, 6-H), 2.12-2.15 (1H, m, 5-H), 2.29-2.32 (1H, m, 6-H) and 4.22 (1H, s, 7-H); δ_C (100MHz; $CDCl_3$) 15.8 (C-8), 23.4 (C-10), 24.6 (C-9), 31.9 (C-5), 33.5 (C-6), 47.5 (C-4), 47.9 (C-3), 65.2 (C-7), 71.6 (C-1) and 210.7 (C-2); *m/z* 309 (M+, 4%) and 159 (100).

3.2.2.2 Attempted approach to 8-bromocamphoric acid (43)

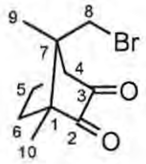

61

(+)-8-Bromocamphorquinone[105] **61**

A solution of (+)-8-Bromocamphor **42** (10g, 43mmol) and SeO_2 (14g, 120mmol) in glacial acetic acid (150ml) was heated under reflux in a round-bottomed flask fitted with a reflux condenser, for 12 hours with stirring. After cooling to room temperature, the solid residue was filtered off and washed with methanol. The volatiles products were removed from the filtrate and washings *in vacuo* at *ca.* 50°C. The residue was dissolved in ethyl acetate, washed with water, saturated $NaHCO_3$ solution and again with water. The aqueous phase was rendered slightly alkaline and extracted repeatedly with ethyl acetate. The combined organic solutions were dried over Na_2SO_4, the solvents removed *in vacuo*, and the residue chromatographed [flash chromatograpy on silica gel; elution with hexane-EtOAc (3:1)] to afford (+)-8-bromocamphorquinone **61** as a yellow powder (75%), m.p. 108-110°C (lit.,[99] 95-96°C); (Found: **M**$^+$ 244.00989. $C_{10}H_{13}O_2Br$ requires *M*, 244.00989); ν_{max}(thin film)/cm^{-1} 1773 and 1755 (C=O); $[\alpha]_D^{20}$= –73.6° (*c* 1.07, $CHCl_3$) {lit.,[99] $[\alpha]_D^{23}$ = -79.3° (*c* 1.00 $CHCl_3$)}; δ_H (400MHz; $CDCl_3$) 1.14 (3H, s, 10-CH_3), 1.25 (3H, s, 9-CH_3), 1.67 (1H, m, 5-H), 1.78 (1H, m, 6-H), 2.04 (1H, m, 6-H), 2.16 (1H, m, 5-H), 2.97 (1H, d, J 5.2 Hz, 4-H), 2.99 (1H, d, *J* 8.8 Hz, 8-H) and 3.31 (1H, d, *J* 8.8 Hz , 8-H); δ_C (100MHz; $CDCl_3$) 9.2 (C-10), 14.4 (C-9), 21.9 (C-5), 31.7 (C-6), 38.0 (C-8), 47.7 (C-7), 56.3 (C-4), 59.3 (C-1), 201.2 (C-3) and 203.3 (C-2); *m/z* 245/247 (M$^+$, 12% / 11%) and 109 (100).

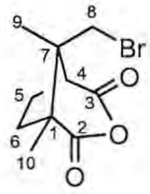

62

(+)-8-bromocamphoric anhydride **62**

H_2O_2 (10ml of a 30% solution) was added to a solution of (+)-8-bromocamphorquinone **61** (1g) in glacial acetic acid (25ml) in a round-bottomed flask. The resulting solution was stirred for 24 hours at room temperature, and then added to water. The oily residue was extracted into Et_2O, and the solvent removed *in vacuo*. The residue was added again to water, and *(+)-8-bromocamphoric anhydride* **62** was filtered off as a white solid (0.65g, 61%), m.p. 132-136°C; ν_{max}(thin film)/cm^{-1} 1810 and 1764 (C=O), 983 (C-O-C); $[\alpha]_D^{23}$= +34.2° (*c* 0.190, $CHCl_3$); δ_H (400MHz; $CDCl_3$) 1.20 (3H, s, 9-CH_3), 1.29 (3H, s, 10-CH_3), 1.98 (1H, m, 6-H), 2.14 (1H, m, 5-H), 2.25 (1H, m, 5-H), 2.28 (1H, m, 6-H), 3.15 (1H, d, *J* 6.8 Hz, 4-H), 3.29 (1H, d, *J* 20 Hz, 8-CH_2) and 3.32 (1H, d, *J* 20 Hz, 8-CH_2); δ_C (100MHz; $CDCl_3$) 14.2 (C-10), 17.1 (C-9), 23.6 (C-6), 34.8 (C-5), 38.0 (C-8), 48.1 (C-1), 52.1 (C-4), 53.3 (C-7), 169.0 (C-3) and 172.1 (C-2); *m/z* 261/263 (MH^+, 32% / 31%) and 109 (100).

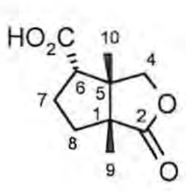

63

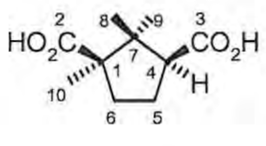

68

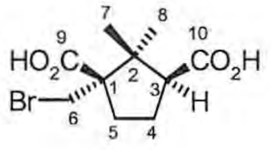

69

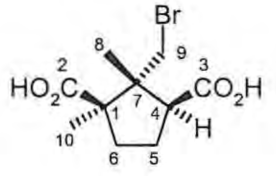

66

(1R, 5S, 6S)-1,5-Dimethyl-2-oxo-3-oxabicyclo[3.3.0]octane-6-carboxylic acid **63**, *1,4-camphoric acid* **68,** *(1S,3S)-1-bromomethyl-2,2-dimethylcyclopentane-1,3-dicarboxylic acid* **69** and *(+)-9-bromocamphoric acid* **66**

A mixture of (+)-8-bromocamphoric anhydride **62** (200mg) was boiled under reflux for 5 hours in 5M-HCl. The cooled crude mixture was extracted several times with Et_2O, the combined organic extracts were dried over anhydrous $MgSO_4$, and the solvent was removed *in vacuo*. Chromatography [HPLC on Partisil 10; elution with hexane-EtOAc (3:1)] of the resultant mixture afforded

i) *(1R, 5S, 6S)-1,5-Dimethyl-2-oxo-3-oxabicyclo[3.3.0]octane-6-carboxylic acid* **63** as a white crystalline solid (*ca.* 30%), m.p. 98-100°C (Found: **M**$^+$ 198.08921. $C_{10}H_{14}O_4$ requires *M*, 198.08921); ν_{max}(thin film)/cm^{-1} 3276 (COOH), 1743 and 1728 (lactone C=O), 1181 and 1162 (lactone C-O); δ_H (400MHz; $CDCl_3$) 1.21 (3H, s, 9-CH_3), 1.29 (3H, s, 10-CH_3), 1.65 (1H, ddd, *J* 13.6, 10.8 and 7.7 Hz, 8-H), 1.91 (1H, m, 7-H), 2.05 (1H, dddd, J 13.4, 7.6, 7.6 and 2.5 Hz, 7-H), 2.28 (1H, ddd, *J* 13.6, 8.3 and 2.5 Hz, 8-H), 2.78 (1H, dd, *J* 11.6 and 7.5 Hz, 6-H), 3.95 (1H, d, *J* 10.3 Hz, 4-H) and 4.29 (1H, d, *J* 10.0 Hz, 4-H); δ_C (100MHz; $CDCl_3$) 18.7 (C-9), 21.4 (C-10), 26.7 (C-7), 37.6 (C-8), 51.1 (C-5), 52.5 (C-1), 54.1 (C-6), 74.1 (C-4), 176.7 (CO_2H) and 181.9 (C-2); *m/z* (APCI-MS) 197 (M-1, 100%).

Further chromatography of the residual material [HPLC on Partisil 10; elution with hexane-EtOAc (3:1)] afforded, as white crystalline solids:-

ii) 1,4-camphoric acid **68**, m.p. 168-170°C; ν_{max} (thin film)/cm^{-1} 3437 cm^{-1} (COOH) and 1651 (C=O); δ_H (400MHz; DMSO-d_6) 0.75 (3H, s, 9-CH_3), 1.11 (3H, s, 10-CH_3), 1.18 (3H, s, 8-CH_3), 1.36 (1H, m, 6-H), 1.72 (1H, m, 5-H), 1.93 (1H, m, 5-H), 2.34 (1H, m, 6-H) and 2.72 (1H, t, *J* 9.6 Hz , 4-H); δ_C (100MHz; DMSO-d_6) 21.3 (C-9), 21.8 (C-10), 22.5 (C-8), 23.0 (C-5), 32.5 (C-6), 45.9 (C-7), 52.4 (C-4), 53.8 (C-1), 175.5 (C-3) and 177.4 (C-2); *m/z* 201 (MH$^+$, 1.7%) and 136 (100);

iii) *(1S,3S)-1-bromomethyl-2,2-dimethylcyclopentane-1,3-dicarboxylic acid* **69**,† m.p. 192-196°C; δ_H (400MHz; DMSO-d_6) 0.81 (3H, s, 8-CH_3), 1.20 (3H, s, 7-CH_3), 1.70-1.78 (1H, m, 4-CH_2), 1.78-1.87 (1H, m, 5-CH_2), 1.92-2.04 (1H, m, 4-CH_2), 2.29-2.40 (1H, m, 5-CH_2), 2.82 (1H, t, *J* 9.2 Hz , 3-H) and 3.81 (2H, dd, *J* 9.6 and 10.7 Hz, 6-CH_2); δ_C (100MHz; DMSO-d_6) 22.1 (C-8), 22.2 (C-7), 22.4 (C-4), 28.4 (C-5), 40.3 (C-6), 47.3 (C-2), 52.2 (C-3), 61.7 (C-1), 175.5 (C-9) and 177.4 (C-10); *m/z* 279/281 (M$^+$, 7% / 7%) and 181 (100); and

iv) (+)-9-Bromocamphoric acid **66**

See synthesis below for analytical data.

---

† Since elemental analytical data was not accessible for this compound, single crystal X-ray analysis was used to unambiguously assign the structure.

3.2.2.3 Synthesis and lactonisation of 9-bromocamphoric acid (66)

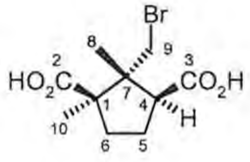

66

(+)-9-Bromocamphoric acid[112] **66**

A mixture of (+)-3,9,-dibromocamphor **65** (2g) in 55% nitric acid (20ml) and glacial acetic acid (5ml) was boiled under reflux for 4 hours, then cooled to room temperature. The acidic mixture was neutralized with aqueous sodium hydroxide, and extracted with Et_2O. The combined organic extracts were dried over anhydrous magnesium sulphate, and the solvent was removed *in vacuo*. The resultant yellow residue was recrystallised from chloroform to afford 9-bromocamphoric acid **66** as a white solid (700mg, 39%), m.p. 217-219°C (lit.,[112] 228°C), $[\alpha]_D^{24}$=5.3° (*c* 0.105, EtOH) {lit.,[112] $[\alpha]_D^{22}$ = +8.5° (*c* 1.3, EtOH)}; δ_H (400MHz; DMSO-d_6) 1.01 (3H, s, 8-CH_3), 1.24 (3H, s, 10-CH_3), 1.46 (1H, m, 6-H), 1.91 (2H, m, 5-H), 2.38 (1H, m, 6-H), 3.01 (1H, t, *J* 9.6 Hz, 4-H), 3.81 (1H, d, *J* 10.8 Hz, 9-CH_2), 3.91 (1H, d, *J* 10.8 Hz, 9-CH_2) and 11.5-13 (2H, br s, 2 x CO_2H); δ_C (100MHz; DMSO-d_6) 18.6 (C-8), 21.2 (C-10), 23.5 (C-5), 33.6 (C-6), 41.5 (C-9), 48.6 (C-7), 49.9 (C-4), 55.7 (C-1), 174.5 (C-3) and 176.2 (C-2).

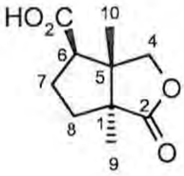

67

(1R,5R,6R)-Dimethyl-2-oxo-3-oxabicyclo[3.3.0]octane-6-carboxylic acid[112] **67**

(+)-9-Bromocamphoric acid **66** (355mg) in water (3ml) was neutralized in the presence of phenolphthalein by dropwise addition of *ca.* 6M aq. $NaHCO_3$. The solution was heated under reflux for 25min, and then cooled to room temperature. The solution was acidified with concentrated HCl to *ca.* pH 5, and extracted with ethyl acetate. The crude product was purified by chromatography [chromatotron; elution with hexane-EtOAc (1:1)], m.p. 166-170°C (lit.,[112] 167°C); δ_H (400MHz; $CDCl_3$) 1.23 (3H, s, 10-

CH_3), 1.36 (3H, s, 9-CH_3), 1.44 (1H, ddd, *J* 12.4 Hz, 8.6 Hz and 2.1 Hz, 8-H), 1.96 (1H, m, 8-H), 2.43 (1H, m, 7-H), 2.60 (1H, dddd, *J* 12.9 Hz, 10.2 Hz, 7.6 Hz and 2.2 Hz, 7-H), 3.07 (1H, dd, *J* 9.5Hz and 8.7 Hz, 6-H), 4.04 (2H, d, *J* 8.6 Hz, 4-H_b) and 4.48 (2H, d, *J* 8.6 Hz, 4-H_b); δ_C (100MHz; $CDCl_3$) 19.7 (C-10), 20.0 (C-9), 25.3 (C-8), 28.9 (C-7), 43.1 (C-6), 53.4 (C-5), 57.7 (C-1), 75.1 (C-4), 175.4 (C-2) and 177.7 (CO_2H).

3.2.2.4 Attempted alternative ring-opening approaches

LAH reduction of (+)-8-bromocamphoric anhydride[106] **62**

(+)-8-Bromocamphoric anhydride **62** (53mg) was suspended in diethyl ether (4ml). LAH (47mg) was added, and the mixture refluxed under nitrogen for 5 hours with stirring. On cooling, THF (5ml) was added, and the solution quenched with H_2O (*ca.* 5ml). The resulting solution was filtered and extracted with ethyl acetate, and the solvent was removed *in vacuo.* NMR showed no identifiable products.

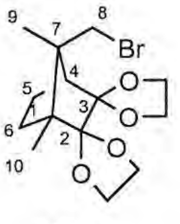

71

8-Bromocamphorquinone ethylene diketal **71**

p-Toluenesulphonic acid (0.2g, 1mmol) and ethylene glycol (0.75ml, 13mmol) were added to a solution of 8-bromocamphorquinone (250mg, 1mmol) in benzene (20ml). The mixture was refluxed with vigorous stirring in a Dean-Stark apparatus for 38 hours. Upon cooling, the resultant solution was filtered through a silica plug, which was washed with ethyl acetate. The filtrate and washings were dried over anhydrous $MgSO_4$, and the solvent was removed *in vacuo.* The residue was chromatographed [chromatotron; elution with hexane-EtOAc (3:1)] to afford a mixture of white crystalline products. Further chromatography [HPLC on Partisil 10; elution with hexane-EtOAc (3:1)] afforded *8-bromocamphorquinone ethylene diketal* **71** (4.7%) as a white crystalline solid (Found: **M**$^+$, 332.06088. $C_{14}H_{21}O_4Br$ requires *M*, 332.06232); δ_H

(400MHz; $CDCl_3$) 0.83 (3H, s, 10-CH_3), 1.37 (3H, s, 9-CH_3), 1.41 (1H, m, 5-H), 1.52 (1H, m, 6-H), 1.86 (1H, m, 6-H), 2.01 (1H, d, *J* 4.4 Hz, 4-H), 2.10 (1H, m, 5-H), 3.14 (1H, d, *J* 10 Hz, 8-CH_2), 3.60 (1H, d, *J* 10 Hz, 8-CH_2) and 3.88 (8H, m, 4 x CH_2O); δ_C (100MHz; $CDCl_3$) 10.2 (C-10), 17.1 (C-9), 20.4 (C-6), 29.1 (C-5), 42.1 (C-8), 49.3 (C-7), 51.6 (C-4), 53.7 (C-1), 64.5, 64.6, 65.0 and 66.1 (4 x CH_2O); *m/z* 99 (100%).

An inseparable mixture of products presumed to be the monoketals **72** and **73** was also isolated as a white crystalline material (43%).

Attempted phosphine addition to 8-bromocamphoric anhydride[117] **62**

Freshly distilled $ClPPh_2$ (1ml) was added, under anhydrous conditions, at 0°C, to a round-bottomed flask containing freshly prepared lithium ribbon (200mg) in dry THF (10ml). The solution was stirred under nitrogen for 30 minutes at 0°C, and for a further 12 hours at room temperature. It was then added, dropwise, to a stirred solution of 8-bromocamphoric anhydride **62** (100mg, 0.38mmol) until a white precipitate formed and the solution became clear. The resulting mixture was then stirred, under nitrogen, for a further 2 days. H_2O (10ml) was added, and the crude product extracted into Et_2O. Chromatography [HPLC on Partisil 10; elution with hexane-EtOAc (3:1)] afforded the unconverted starting material in 50% yield, and camphoric anhydride **74** in 40% yield as a white crystalline solid, m.p. 108-112°C (no literature melting point located); δ_H (400MHz; $CDCl_3$) 0.99 (3H, s, 9-CH_3), 1.09 (3H, s, 8-CH_3), 1.26 (3H, s, 10-CH_3), 1.95 (2H, m, 6-H), 2.09 (1H, m, 5-H), 2.22 (1H, m, 5-H) and 2.82 (1H, d, *J* 7.2 Hz , 4-H); δ_C (100MHz; $CDCl_3$) 14.1 (C-10), 20.2 (C-9), 20.8 (C-8), 24.5 (C-5), 33.5 (C-6), 43.7 (C-1), 53.8 (C-7), 54.4 (C-4), 170.0 (C-3) and 172.9 (C-2).

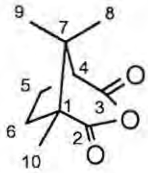

74

3.2.3 Ruthenium complexation studies

Note: All solid organometallic compounds were transferred and stored in a nitrogen-filled glovebox. In general, manipulations involving organometallic species were performed using standard Schlenk techniques.

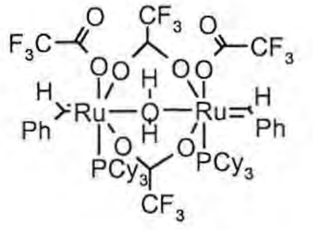

75

Attempted synthesis of the diruthenium complex $[Ru_2(=CHPh)_2(CF_3CO_2)_2(\mu\text{-}CF_3CO_2)_2(PCy_3)_2(\mu\text{-}H_2O)]$[93] **75**

A solution of CF_3CO_2Ag (55mg, 0.25mmol) in dry THF (3ml) was added dropwise by cannula to a solution of the Grubbs 1st-generation catalyst $Ru(=CHPh)Cl_2(PCy_3)_2$ **14** (102mg, 0.12mmol) in dry hexane at 0°C. After complete addition, the solution was stirred for a further 30 minutes at 0°C. The solution was filtered under nitrogen, and the filtrate evaporated to dryness. Recrystallisation from hexane at -22°C afforded the crystalline silver complex $AgClPCy_3$ **76** (70mg, 65%); δ_H (400MHz; $CDCl_3$) 1.0-2.0 (broad multiplet); δ_C (100MHz; $CDCl_3$) 25.7, 26.8, 26.9 and 31.2; δ_P (162MHz; $CDCl_3$) 38.1, 40.9, 47.5 and 57.3.

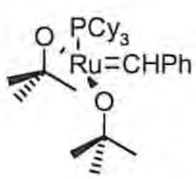

77

Attempted synthesis of the ruthenium complex $[Ru(=CHPh)PCy_3(Bu^tO)_2]$[94] **77**

The Grubbs 1st-generation catalyst $Ru(=CHPh)Cl_2(PCy_3)_2$ **14** (300mg, 0.36mmol) and $KOBu^t$ (180mg, 1.6mmol) were weighed out into a round-bottomed flask. Dry benzene (12ml) was added by syringe, and the solution was stirred under nitrogen for 24 hours. The solvent was removed by freeze-drying. The resultant grey powdery residue was suspended in dry pentane (20ml) and dry benzene (0.2ml). CuCl (350mg, 3.6mmol) was added, the suspension was stirred for 20 minutes, then cooled to -30°C for 24 hours. The supernatant solution was decanted, and the solvent removed *in vacuo*. ^{1}H NMR analysis of the crude product revealed no signals in the carbene region. ^{31}P NMR analysis showed a large signal at 11.75ppm, indicative of free PCy_3.

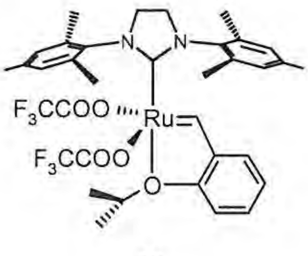

79

*The bis(trifluoroacetoxy) derivative of the Hoveyda catalyst [Ru(CF_3CO_2)$_2$(=CH-o-*i*-Pr-O-C_6H_4)($IMesH_2$)]*[119] **79**

A solution of CF_3CO_2Ag (39mg, 0.17mmol) in dry THF (5ml) was added, under argon, to a solution of $RuCl_2$(=CH-*o*-*i*-Pr-O-C_6H_4)($IMesH_2$) **78** (45mg, 7.2x10^{-5}mol) in dry THF (5ml). The resultant solution was stirred under argon for 20 minutes, the supernatant solution removed by syringe, and the solvent removed *in vacuo* to afford lilac crystals of the expected complex [Ru(CF_3CO_2)$_2$(=CH-*o*-*i*-Pr-O-C_6H_4)($IMesH_2$)] **79** (42mg, 75%); δ_H (400MHz; $CDCl_3$) 0.94 [6H, d, *J* 6.8 Hz, (CH_3)$_2$CHOAr], 2.26 (12H, s, mesityl *o*-CH_3), 2.43 (6H, s, mesityl *p*-CH_3), 4.12 [4H, s, N(CH_2)$_2$N], 4.62 [1H, septet, (CH_3)$_2$C*H*OAr], 6.63 (1H, d, *J* 7.6 Hz, ArH), 6.94 (1H, m, ArH), 7.07 (1H, m, ArH), 7.14 (4H, s, mesityl ArH), 7.34 (1H, m, ArH) and 17.45 (1H, s, Ru=CH); δ_C (100MHz; $CDCl_3$) 17.3, 21.0, 22.0, 51.8, 74.3, 114.1, 115.5, 122.2, 129.7, 130.2, 133.9, 134.7, 135.0, 141.1, 151.1, 158.1, 208.0 and 313.5.

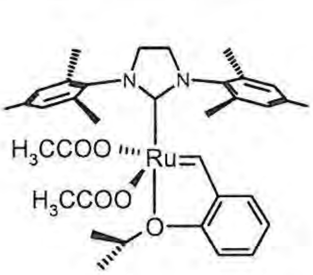

85

*The diacetoxy ruthenium complex [Ru(CH_3CO_2)$_2$(=CH-o-*i*-Pr-O-C_6H_4)($IMesH_2$)]*[119] **85**

A solution of CH_3CO_2Ag (5.6mg, 3.3 x 10^{-5} mol) in dry THF (5ml) was added, under argon, to a solution of the Hoveyda catalyst $RuCl_2$(=CH-*o*-*i*-Pr-O-C_6H_4)($IMesH_2$) **78** (10mg, 1.6x10^{-5}mol) in dry THF (5ml). The resultant solution was heated under reflux for 3 hours, the supernatant solution removed from the precipitated solid by syringe, and the solvent removed from the supernatant *in vacuo*. ^1H NMR analysis of the crude residue revealed the appearance of a new signal in the carbene region at $\delta = 14.40$ ppm.

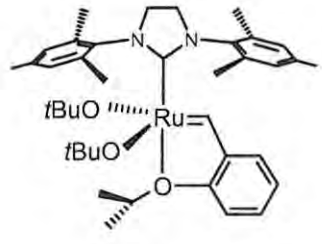

86

Attempted synthesis of $Ru(Bu^tO)_2(=CH$-*o*-i-*Pr*-*O*-$C_6H_4)(IMesH_2)$ **86**

A solution of the Hoveyda catalyst $RuCl_2(=CH$-*o*-*i*-Pr-O-$C_6H_4)(IMesH_2)$ **78** (10.5mg, 1.67×10^{-5}mol) and $KOBu^t$ (4.0mg, 3.6×10^{-5}mol) in dry benzene (10ml) was stirred under argon for 1 week. The solvent was removed *in vacuo*. ^1H NMR analysis of the residue revealed only unconverted starting material.

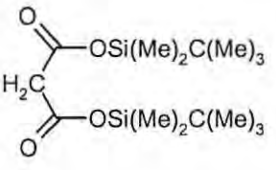

87

*Bis(*t*-butyldimethylsilyl) malonate*[128] **87**

t-Butyldimethylsilyl chloride (7.5g, 50mmol), malonic acid (2.6g, 25mmol) and a spatula tip of imidazole were stirred in dry DMF for 12 hours under nitrogen. The solution was poured into H_2O (50ml) and the resulting mixture extracted twice with petroleum ether (30-60°). The solvent was removed *in vacuo* and the resulting oil distilled under reduced pressure to afford the silyl ester **87** in quantitative yield; δ_H (400MHz; $CDCl_3$) 0.26 [12H, s, $Si(CH_3)_2$], 0.90 [18H, s, $C(CH_3)_3$] and 3.33 (2H, s, CH_2); δ_C (100MHz; $CDCl_3$) –5.0 [$Si(CH_3)$], -4.9 [$Si(CH)_3$], 25. 3 [$C(CH_3)$], 25.4 [$C(CH_3)$], 25.6 [$C(CH_3)$], 45.0 (CH_2) and 166.9 (C=O); *m/z* 333 (100%).

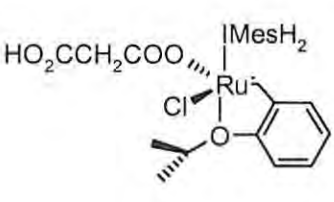

88

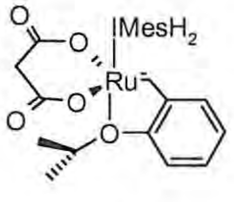

90

Grubbs-Hoveyda derivatives **88** and **90**

The Hoveyda catalyst $RuCl_2(=CH\text{-}o\text{-}i\text{-}Pr\text{-}O\text{-}C_6H_4)(IMesH_2)$ **78** (12mg, 1.9 x 10^{-5}mol), malonic acid **86** (3.8mg, 3.6 x 10^{-5}mol) and silver carbonate (5.5mg, 2.0 x 10^{-5}mol) were transferred, under argon, to a round-bottomed flask. Dry benzene (4ml) and dry THF (4ml) were added, and the solution was heated under reflux for three hours. The solvent was removed *in vacuo*. ^1H NMR analysis of the crude residue revealed two new signals in the carbene region at δ = 16.58 ppm and 17.11 pm. Complete disappearance of these signals was noted upon standing in solution for 6-12 hours, indicating decomposition of the complexes.

Silver malonate[132] (**91** and **92**)

Malonic acid **86** (1.4g, 13mmol) was dissolved in ethanol (20ml) and neutralized with 1M aqueous NaOH. The resultant solution was added, dropwise, to a solution of silver nitrate (4.5g) in H_2O (20ml). The resultant dense white precipitate was filtered off, washed with ethanol and Et_2O, and dried in a vacuum desiccator.

Grubbs-Hoveyda derivative **88** *via silver malonate route*

The Hoveyda catalyst $RuCl_2(=CH\text{-}o\text{-}i\text{-}Pr\text{-}O\text{-}C_6H_4)(IMesH_2)$ **78** (12mg, 1.9 x 10^{-5}mol) was dissolved in dry THF (5ml) under argon, and an excess of the silver malonate species **91** and **92** added. The suspension was heated under reflux for three hours, the supernatant liquid transferred to a round-bottomed flask, and the solvent removed *in vacuo*. ^1H NMR analysis of the crude residue revealed a new signal in the carbene region at 17.11 pm.

3.2.4 Blaise syntheses

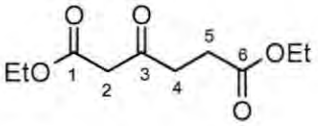

100

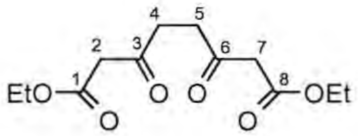

95

Diethyl 3-oxohexane-1,6-dioate **100** *and diethyl 3,6-dioxooctanedioate*[138] **95**

Activated zinc powder (3.5g, 53mmol) and dry benzene (15ml) were warmed to 50 °C in a 2-necked round-bottomed flask fitted with a reflux condenser and rubber septum. Ethyl bromoacetate **99** (5.0ml, 45mmol) was added dropwise by syringe, under nitrogen, while maintaining the temperature below 85 °C. After the exothermic reaction had subsided, diethyl succinate **98** (3.7ml, 22 mmol) was added by syringe. The solution was boiled under reflux under nitrogen for 4 hours, allowed to cool to room temperature, and then quenched with ethyl acetate (10ml), saturated aqueous ammonium chloride (10ml) and brine (10ml). The resulting mixture was filtered and the filtrate extracted several times with ethyl acetate. The combined organic extracts were dried over anhydrous magnesium sulphate, and the solvent was removed *in vacuo* to afford a yellow oil, which was chromatographed (flash chromatography; gradient elution with hexane-EtOAc (3:1), followed by hexane-EtOAc (1:1) to yield:

i) unconverted starting material **98** (2.9g, 74%);

ii) diethyl 3-oxohexane-1,6-dioate **100** as a yellow oil (1.1g, 23%); δ_H (400MHz; $CDCl_3$) 1.16 (3H, t, J 6.1 Hz, 6-$CO_2CH_2CH_3$), 1.20 (3H, t, J 6.1 Hz, 1-$CO_2CH_2CH_3$), 2.52 (2H, t, J 6.6 Hz, 5-CH_2), 2.78 (2H, t, J 6.6 Hz, 4-CH_2), 3.41 (2H, s, 2-CH_2), 4.04 (2H, q, J 7.1 Hz, 6-$CO_2CH_2CH_3$) and 4.11 (2H, q, J 7.1 Hz, 1-$CO_2CH_2CH_3$); δ_C (100MHz; $CDCl_3$) 13.89 (CH_2CH_3), 13.91 (CH_2CH_3), 27.8 (C-2), 37.2 (C-3), 49.1 (C-4), 60.5 (6-$CO_2CH_2CH_3$), 61.2 (1-$CO_2CH_2CH_3$), 166.8 (C-6), 172.4 (C-1) and 200.9 (C-3); and

iii) diethyl 3,6-dioxooctanedioate **95** as a yellow oil (180mg, 3%); δ_H (400MHz; $CDCl_3$) 1.19 (6H, t, J 7.1 Hz, 2 x CH_2CH_3), 2.77 (4H, s, 4,5-CH_2), 3.41 (4H, s, 2,7-CH_2) and 4.11 (4H, q, J 7.1 Hz, 2 x CH_2CH_3); δ_C (100MHz; $CDCl_3$) 13.9 (2 x CH_2CH_3), 36.2 (C-4,5), 49.0 (C-2,7), 61.2 (2 x CH_2CH_3), 166.8 (C-1,7) and 201.0 (C-3,6); *m/z* 217 (M+H, 100%).

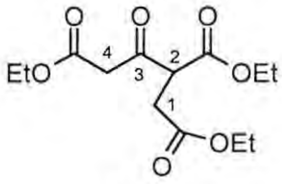

104

Triethyl 3-oxobutane-1,2,4-tricarboxylate[138] **104**

Activated zinc powder (3.5g, 53mmol) and dry benzene (15ml) were warmed to 50°C in a 2-necked round-bottomed flask fitted with a reflux condenser and rubber septum. Ethyl bromoacetate (5.0ml, 45mmol) was added dropwise by syringe, under nitrogen, while maintaining the temperature below 85°C. After the exothermic reaction had subsided, diethyl malonate (3.4ml, 22 mmol) was added by syringe. The solution was boiled under reflux under nitrogen for 4 hours, allowed to cool to room temperature, and then quenched with ethyl acetate (10ml), saturated aqueous ammonium chloride (10ml) and brine (10ml). The mixture was filtered and the filtrate extracted several times with ethyl acetate. The combined organic extracts were dried over anhydrous magnesium sulphate, and the solvent was removed *in vacuo* to afford a yellow oil, which was chromatographed (vacuum chromatography; gradient elution 100% hexane → 100% ethyl acetate) to yield triethyl 3-oxobutane-1,2,4-tricarboxylate **104** (3.2g, 50%); ν_{max}(thin film)/cm^{-1} 1636 (C=O); (δ_H (400MHz; CDCl$_3$) 1.26 (9H, m, CH$_2$C*H*$_3$), 3.15 (2H, d, *J* 7.2 Hz, CHC*H*$_2$), 3.48 (2H, s, 4-CH$_2$), 3.86 (1H, t, *J* 7.2 Hz, 2-CH) and 4.15-4.22 (6H, overlapping m, C*H*$_2$CH$_3$); δ_C (100MHz; CDCl$_3$) 13.9 (CH$_2$*C*H$_3$), 14.0 (2 x CH$_2$*C*H$_3$), 41.3 (CH*C*H$_2$), 47.0 (C-2), 49.2 (C-4), 61.5 (*C*H$_2$CH$_3$), 61.8 (2 x *C*H$_2$CH$_3$), 166.6 (CHCH$_2$*C*O), 168.5 (2 x *C*O$_2$Et) and 199.5 (C-3); *m/z* 289 (M+H, 86%) and 173 (100).

3.2.5 Approach to the tridentate malonate-derived complex (93)

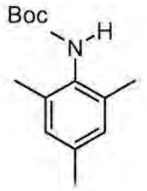

110

N-(tert-*Butyloxycarbonyl)-2,4,6-trimethylaniline*[59] **110**

2,4,6-Trimethylaniline (3.6g, 26mmol) was dissolved in dry THF (20ml) under argon, in a two-necked round-bottomed flask fitted with a septum seal and a reflux condenser. A solution of di-*tert*-butyl dicarbonate (5.8g, 26mmol) in dry THF was added by cannula. The resulting solution was refluxed under argon for 7 days. The solvent was removed *in vacuo* and the solid residue dried under high vacuum, affording orange crystals of *N*-(*tert*-butyloxycarbonyl)-2,4,6-trimethylaniline **110** in quantitative yield, m.p. 66-68°C (no literature melting point available); δ_H (400MHz; $CDCl_3$) 1.49 (9H, s, Bu^t), 2.21 (6H, s, *o*-CH_3), 2.24 (3H, s, *p*-CH_3), 5.79 (1H, br s, NH) and 6.86 (2H, s, ArH); δ_C (100MHz; $CDCl_3$) 18.3 [3 x $C(CH_3)_3$], 20.9 (2 x *o*-CH_3), 28.3 9 (*p*-CH_3), 79.7 [$C(CH_3)_3$], 128.8 (ArC), 133.7 (ArC), 135.6 (ArC), 136.5 (ArC) and 152.2 (C=O); *m/z* 235 (M^+, 19%) and 179 (100).

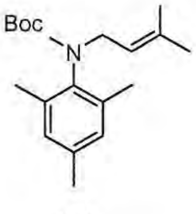

111

N-(tert-*Butyloxycarbonyl)*-N-*(3-methylbut-2-enyl)-2,4,6-trimethylaniline*[59] **111**

Potassium hydride (approx. 1.5g in a 30% mineral oil dispersion) was rinsed with dry hexane in a round-bottomed flask fitted with a septum seal, and the liquid decanted off. DMF (20ml) was added, and the suspension cooled to 0°C. *N*-(*tert*-Butyloxycarbonyl)-2,4,6-trimethylaniline (6.2g, 26mmol) was dissolved in DMF (40ml) and added dropwise by cannula while stirring. The solution was stirred for a further 2 hours at room temperature. 4-Bromo-2-methyl-2-butene (3.8 ml, 33mmol) was added dropwise by syringe, and the resultant milky white solution stirred at room temperature for 1 hour. The mixture was then transferred to a large separating funnel and diluted with saturated aq. sodium bicarbonate (100ml), H_2O (100ml) and Et_2O (200ml). The organic layer was removed, and the aqueous layer washed with Et_2O (2 x 150ml). The combined organic extracts were washed with an equal volume of saturated aq. NaCl, dried over $MgSO_4$ and the solvent removed *in vacuo*. The oily residue was chromatographed [flash chromatograpy on silica gel; elution with hexane-Et_2O (10:1)] to afford *N*-(*tert*-butyloxycarbonyl)-*N*-(3-methylbut-2-enyl)-2,4,6-trimethylaniline **111** as a bronze-coloured oil (8g, 100%). In $CDCl_3$, at 303K, this compound exists as a 2.4:1 mixture of amide rotamers. The NMR chemical shift data are for the major isomer only. δ_H (400MHz; $CDCl_3$) 1.31 (9H, s, Bu^t), 1.41 (3H, s, $CH{=}C(CH_3)_2$), 1.66 (3H, s, $CH{=}C(CH_3)_2$), 2.12 (6H, s, *o*-CH_3), 2.14 (3H, s, *p*-CH_3), 4.04 (2H, d, *J* 7.2 Hz, NCH_2), 5.31 (1H, m, $CH{=}C(CH_3)_2$) and 6.79 (2H, s, aromatic H); δ_C (100MHz; $CDCl_3$) 17.1 (*p*-CH_3), 17.2 (*o*-CH3), 20.6 [$CH{=}C(CH_3)_2$], 25.3 [$CH{=}C(CH_3)_2$], 28.0 [$OC(CH_3)_3$], 46.1 (NCH_2), 76.6 [$C(CH_3)_3$], 79.2 [$CH{=}C(CH_3)_2$], 119.8 [$CH{=}C(CH_3)_2$], 128.4 (ArC), 134.7 (ArC), 135.6 (ArC), 136.2 (ArC) and 154.6 (C=O).

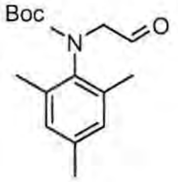

107

N-(tert-*Butyloxycarbonyl)*-N-*(formylmethyl)-2,4,6-trimethylaniline*[59] **107**

N-(*tert*-Butyloxycarbonyl)-*N*-(3-methylbut-2-enyl)-2,4,6-trimethylaniline **111** (6.0g, 20 mmol) was dissolved in dry CH_2Cl_2 (150ml) and methanol (50ml) and the solution cooled to -78°C in a round-bottomed flask connected to a wash-bottle containing an aqueous solution of potassium iodide. Ozone was bubbled through the solution until the potassium iodide solution turned brown. The reaction mixture was then warmed to room temperature and dimethyl sulfide (2.9ml, 39 mmol) was added. The solvent was removed *in vacuo*, and the crude product purified by chromatography [flash chromatograpy on silica gel; elution with hexane-ethyl acetate (5:1)] to afford *N-(tert*-butyloxycarbonyl)-*N*-(formylmethyl)-2,4,6-trimethylaniline **107** in 80% yield as a colourless oil. In $CDCl_3$, at 303K, this compound exists as a 1.6:1 mixture of amide rotamers. The NMR data refers to the major rotamer only. δ_H (400MHz; $CDCl_3$) 1.35

(9H, s, OC(CH_3)$_3$), 2.20 (6H, s, *o*-CH_3), 2.22 (3H, s, *p*-CH_3), 3.93 (2H, d, *J* 1.5 Hz, NCH_2), 6.86 (2H, d, *J* 0.4 Hz, ArH) and 9.81 (1H, m, C*H*O); δ_C (100MHz; CDCl$_3$) 18.1 (*o*-CH$_3$), 18.2 (*o*-CH$_3$), 20.9 (*p*-CH$_3$), 28.1 [3 x OC(*C*H$_3$)$_3$], 59.1 (N*C*H$_2$), 80.7 [O*C*(CH$_3$)$_3$], 129.1 (ArC), 135.5 (ArC), 137.5 (ArC), 153.5, (ArC) and 198.8 (*C*HO); *m/z* 278 (M^+, 62%) and 148 (100).

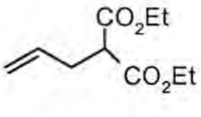

113

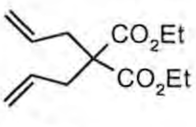

114

Diethyl allylmalonate[143] **113** *and diethyl diallylmalonate* **114**

Sodium pieces (1g) were added slowly to dry absolute ethanol (30ml), while maintaining the temperature below 35°C. After complete consumption of the sodium, freshly distilled diethyl malonate (5.8ml, 38mmol) was added dropwise with stirring. The solution was stirred at 50°C for 30 minutes, allyl bromide (3.3ml, 38mmol) was then added, and the resultant solution boiled under reflux for 13 hours. The solvent was removed *in vacuo*, and water (5ml) added. The aqueous solution was extracted with ethyl acetate (2 x 10ml), the combined organic extracts dried over MgSO$_4$, and the solvent removed *in vacuo*. Chromatography of the crude product [HPLC on Partisil 10; elution with hexane-EtOAc (6:1)] afforded:

i) diethyl allylmalonate **113**, as a colourless oil (78%); δ_H (400MHz; CDCl$_3$) 1.24 (6H, t, *J* 6.2 Hz, 2 x CH$_2$CH_3), 2.62 (2H, t, *J* 7.4 Hz, C=CHCH_2), 3.39 (1H, t, *J* 7.4 Hz, CH$_2$C*H*CO), 4.17 (4H, q, *J* 6.2 Hz, 2 x CH_2CH$_3$), 5.07 (2H, m, H_2C=C) and 5.76 (1H, m, C=C*H*); δ_C (100MHz; CDCl$_3$) 14.1 (2 x CH$_2$*C*H$_3$), 32.8 (*C*H$_2$CH), 51.7 (CH$_2$*C*H), 61.4 (2 x *C*H$_2$CH$_3$), 117.5, (H$_2$*C*=C), 134.1 (C=*C*H) and 169.0 (2 x *C*=O); and

ii) diethyl diallylmalonate **114**, as a colourless oil (22%); δ_H (400MHz; CDCl$_3$) 1.24 (6H, t, *J* 7.0 Hz, 2 x CH$_2$CH_3), 2.63 (4H, d, *J* 7.2 Hz, 2 x C=CHCH_2), 4.17 (4H, q, *J* 7.0 Hz, 2 x CH_2CH$_3$), 5.10 (4H, m, 2 x H_2C=C), 5.65 (2H, m, 2 x C=C*H*); δ_C (100MHz; CDCl$_3$) 14.1 (2 x CH$_2$*C*H$_3$), 36.8 [C(*C*H$_2$)$_2$], 57.2 [*C*(CH$_2$)$_2$], 61.2 (2 x *C*H$_2$CH$_3$), 119.1 (2 x H$_2$*C*=C), 132.3 (2 x C=*C*H) and 170.8 (2 x *C*=O).

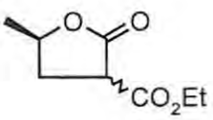

117

Ethyl-5-methyl-2-oxo-tetrahydrofuran-3-carboxylate **117**

Diethyl allylmalonate **113** (4.4g, 22mmol) and benzoyl peroxide (250mg) were dissolved in an equal volume of toluene. The resultant solution was added dropwise to a 33% solution of HBr in acetic acid (4ml), maintained at -10°C. The solution was allowed to warm to room temperature, and stirred for a further 30 minutes. H_2O (5ml) was added, and the organic layer separated, washed with a further volume of H_2O, and dried over anhydrous $MgSO_4$. The solvent was removed *in vacuo* and the residual oil purified by chromatography [chromatotron; elution with hexane-EtOAc (2:1)], to afford a racemic mixture of 5-methyl-2-oxo-tetrahydrofuran-3-carboxylate **117** (*ca.* 40%) (^{1}H and ^{13}C NMR chemical shifts refer to the major isomer only). δ_H (400MHz; $CDCl_3$) 1.29 (3H, m, CH_2CH_3), 1.46 (d, *J* 11.0 Hz, $CHCH_3$), 2.25-2.32 (1H, m, CH_2), 2.52-2.65 (1H, m, CH_2), 3.55-3.65 (1H, m, *CH*), 4.21-4.29 (2H, m, CH_2CH_3) and 4.55-4.60 (1H, m, *CH*); δ_C (100MHz; $CDCl_3$) 14.1 (CH_2CH_3), 20.8 ($CHCO_2Et$), 33.7 (CH_2), 47.2 ($CHCH_3$), 62.2 (CH_2CH_3), 75.8 ($CHCH_3$) and 168.3 (2 x *C*=O).

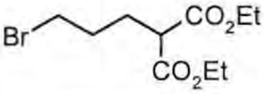

115

Diethyl 2-(3-bromopropyl)malonate **115**

A solution of diethyl allylmalonate **113** (5.0g, 25mmol) in petroleum ether (40-60°, 80ml) was stirred in a round-bottomed flask, and cooled to 0°C. Benzoyl peroxide (400mg) was added, and HBr gas passed through the solution for 15 minutes, while stirring at 0°C, and then for a further 30 minutes at room temperature. An equal volume of H_2O was added, and the organic layer separated, washed twice with H_2O and dried over anhydrous $MgSO_4$. The solvent was removed *in vacuo* and the oily residue was chromatographed [chromatotron; elution with hexane-EtOAc (2:1)] to afford a 12:1 mixture of compound **115** and starting material **113**, which were separated by further chromatography [HPLC on Partisil 10; elution with hexane-EtOAc (9:1)] to afford diethyl 2-(3-bromopropyl)malonate **115**, as a pale yellow oil, in 68% yield; δ_H (400MHz; $CDCl_3$) 1.24 (6H, t, *J* 7.2 Hz, 2 x CH_2CH_3), 1.89 (2H, m, $BrCH_2CH_2$), 2.02 (2H, m, $BrCH_2CH_2CH_2$), 3.31 (1H, t, *J* 8.0 Hz, *CH*), 3.38 (2H, t, 7.8 Hz, $BrCH_2$) and 4.17 (4H, q, *J* 7.2 Hz, 2 x CH_2CH_3); δ_C (100MHz; $CDCl_3$) 14.0 (2 x CH_2CH_3), 27.2 ($BrCH_2CH_2CH_2$), 30.2 ($BrCH_2CH_2$), 32.5 ($BrCH_2$), 51.1 (*CH*), 61.4 (2 x CH_2CH_3) and 169.0 (*C*=O); *m/z* 281/283 (M^+, 83% / 80%) and 201 (100).

Attempted amination of diethyl 2-(3-bromopropyl)malonate **115**[146]

A solution of diethyl 2-(3-bromopropyl)malonate **115** (7g, 20mmol) and NaN_3 (2.6g, 40mmol) in a 1:1 mixture of benzene : DMF (25ml) was boiled under reflux for 3 hours. After cooling to room temperature, H_2O (100ml) was added, the organic phase was separated, and the aqueous phase extracted twice with benzene. The combined organic solutions were dried over anhydrous $MgSO_4$ and filtered into a round-bottomed flask. $P(OEt)_3$ (3.3g, 20mmol) was added dropwise, and the resultant solution stirred at room temperature for 20 hours. The solvent was removed *in vacuo*, and the residue diluted with ethanol (20ml) containing *p*-toluenesulphonic acid (3.8g, 20mmol) and H_2O (0.36ml). The resultant solution was boiled under reflux for 6 hours. The solvent was removed *in vacuo* and a portion of the residue chromatographed (flash chromatography on silica gel; elution with 100% EtOAc) to afford the starting material **115** in 28% yield. Reverse-phase chromatography (C18 sep-pack; gradient elution H_2O → MeOH) failed to afford any identifiable products.

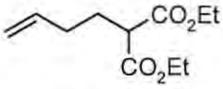

120

Diethyl 2-(3-butenyl)malonate[143] **120**

Sodium pieces (0.77g) were added slowly to dry absolute ethanol (30ml), while maintaining the temperature below 35°C. After complete consumption of the sodium, freshly distilled diethyl malonate (5.8ml, 38mmol) was added dropwise with stirring. The solution was stirred at 50°C for 30 minutes. 4-Bromo-1-butene (3.4ml, 33mmol) was added, and the resultant solution boiled under reflux for 18 hours. The solvent was removed *in vacuo*, and water (5ml) added. The aqueous solution was extracted with ethyl acetate (2 x 10ml), the combined organic extracts dried over $MgSO_4$, and the solvent removed *in vacuo* to afford the crude products (83%), chromatography of which [HPLC on Partisil 10; elution with hexane-EtOAc (6:1)] gave, as a yellow oil, an analytically pure sample of diethyl 2-(3-butenyl)malonate **120**; δ_H (400MHz; $CDCl_3$) 1.26 (6H, t, *J* 7.2 Hz, 2 x CH_2CH_3), 1.99 (2H, m, CH_2CH), 2.09 (2H, m, $CH_2=CHCH_2$), 3.34 (1H, t, *J* 7.6 Hz, *CH*), 4.19 (4H, q, *J* 7.2 Hz, 2 x CH_2CH_3), 5.01 (2H, m, $CH_2=CH$) and 5.77 (1H, m, $CH_2=CH$); δ_C (100MHz; $CDCl_3$) 14.1 (2 x CH_2CH_3), 27.8 ($CH_2=CHCH_2$), 31.3 (CH_2CH), 51.2 (*C*H), 61.3 (2 x CH_2CH_3), 115.9 ($CH_2=CH$), 136.9 ($CH_2=CH$) and 169.4 (2 x *C*=O).

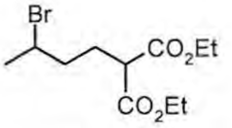

121

Diethyl 2-(3-bromobutyl)malonate[147] **121**

A 33% aqueous solution of HBr (3.2ml) was cooled to -10°C, and a spatula-tip of zinc dust added. Crude diethyl 2-(3-butenylmalonate) **120** (4.4g) was added dropwise. After complete addition, the solution was allowed to warm to room temperature, and stirred for an additional 30 minutes. An equal volume of H_2O was added, and the organic layer separated and washed with H_2O. The crude product was dried over anhydrous $MgSO_4$ and the solvent removed *in vacuo*. Chromatography [HPLC on Partisil 10; elution with hexane-EtOAc (6:1)] afforded diethyl 2-(3-bromobutyl)-malonate **121** as a yellow oil (58%), δ_H (400MHz; $CDCl_3$) 1.25 (6H, t, *J* 7.2 Hz, 2 x CH_2CH_3), 1.69 (3H, d, *J* 6.4 Hz, CH_3CHBr), 1.81 (2H, q, *J* 8.8 Hz, $BrCHCH_2$), 1.98 (1H, m, $BrCHCH_2CH_2$), 2.10 (1H, m, $BrCHCH_2CH_2$), 3.31 (1H, t, *J* 8.6 Hz, *CH*), 4.09 (1H, q, *J* 6.4 Hz, *CH*Br) and 4.18 (4H, m, 2 x CH_2CH_3); δ_C (100MHz; $CDCl_3$) 14.0 (2 x CH_2CH_3), 26.3 (CH_3CHBr), 26.9 ($BrCHCH_2CH_2$), 38.4 ($BrCHCH_2$), 50.2 (*C*HBr), 51.2 (*C*HCO), 61.4 (2 x CH_2CH_3) and 169.0 (*C*=O); *m/z* 295/297 (100%/ 92%).

Attempted amination of diethyl 2-(3-bromobutyl) malonate **121**[146]

A solution of diethyl 2-(3-bromobutyl)malonate **121** (240mg, 8.0 x 10^{-4} mol), NaN_3 (110mg, 1.6 x 10^{-4} mol) and Bu_4NBr (*ca.* 10mg) in H_20 was heated under reflux for 6 hours. After cooling to room temperature, benzene (5ml) was added, the organic phase was separated and the aqueous phase was extracted twice with benzene. The combined organic extracts were dried over anhydrous $MgSO_4$ and filtered into a round-bottomed flask. $P(OEt)_3$ (132mg, 8.0 x 10^{-4} mol) was added dropwise, and the resultant solution stirred at 30°C for 4 hours, and then for a further 12 hours at room temperature. The solvent was removed *in vacuo*, and a 20% solution of HCl (20ml) added. The resultant solution was heated under reflux for 2 hours. After cooling, an equal volume of Et_2O was added, and the aqueous phase was separated and washed twice with Et_2O. Reverse-phase chromatography (C18 sep-pack; gradient elution $H_2O \rightarrow MeOH$) failed to afford any identifiable products.

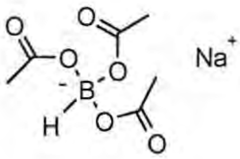

124

Sodium triacetoxyborohydride[148] **124**

A solution of sodium borohydride (370mg, 9.9mmol) in dry benzene (50ml) was prepared under argon, and cooled to 10°C. Anhydrous acetic acid (1.7ml, 30mmol) was added, dropwise, with stirring. The mixture was allowed to warm to room temperature and stirred, under argon, overnight. The slurry was filtered, and the white powder washed with dry Et_2O and dried in a vacuum desiccator to afford analytically pure sodium triacetoxyborohydride **124** (960mg, 46%); δ_H (400MHz; DMSO-d_6) 1.88 (9H, s, CH_3CO); δ_C (100MHz; DMSO-d_6) 23.0 (CH_3CO) and 173.9 (C=O).

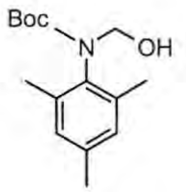

126

N-*(*tert*-Butyloxycarbonyl)-*N-*(hydroxymethyl)-2,4,6-trimethylaniline* **126**

3-Amino-1-propanol (173mg, 2.3mmol) and sodium triacetoxyborohydride (975mg, 4.6mmol) were suspended in 1,2-dichloroethane (20ml) in a round-bottomed flask. A solution of *N*-(*tert*-butyloxycarbonyl)-*N*-(formylmethyl)-2,4,6-trimethylaniline **107** (640mg, 2.3mmol) in 1,2-dichloroethane (6ml) was added, dropwise, over a period of 30 minutes. The solution was stirred at room temperature for 4 hours, and then diluted with saturated aq. $NaHCO_3$ (60ml) and dichloromethane (30ml). The organic phase was separated, and the aqueous phase extracted with dichloromethane (2 x 50ml). The combined organic extracts were dried over anhydrous $MgSO_4$, and the solvent removed *in vacuo*. The residue was chromatographed [HPLC on Partisil 10; elution with hexane-EtOAc (1:1)] to afford N-*(*tert*-butyloxycarbonyl)-*N-*(hydroxymethyl)-2,4,6-trimethylaniline* **126** as a colourless oil in *ca.* 60% yield (Found: **M**$^+$ 265.16764. $C_{15}H_{23}O_3N$ requires M, 265.16779). In $CDCl_3$, at 303K, this compound exists as a 3.8:1 mixture of amide rotamers. The NMR data refers to the major rotamer only. δ_H (400MHz; $CDCl_3$) 1.33 [9H, s, (OC(CH_3)$_3$], 2.18 (6H, s, 2 x *o*-CH_3), 2.26 (3H, s, *p*-CH_3), 3.55 (1H , br s, OH), 4.87 (2H, s, CH_2) and 6.85 (2H, s, ArH); δ_C (100MHz; $CDCl_3$) 18.2 (*o*-CH_3), 21.0 (*p*-CH_3), 28.2 [OC(CH_3)$_3$], 74.8 (CH_2), 80.3 [O*C*(CH_3)$_3$], 128.8 (ArC), 129.0 (ArC), 135.5 (ArC) and 155.8 (ArC); *m/z* 265 (M$^+$, 3%) and 191 (100).

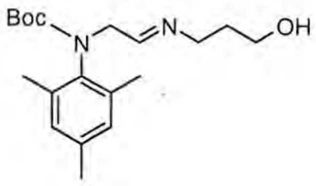

127

N-*(*tert-*Butyloxycarbonyl)-*N-*[2-(3-hydroxypropylimino)-ethyl]-2,4,6-trimethylaniline* **127**

A solution of *N*-(*tert*-Butyloxycarbonyl)-*N*-(formylmethyl)-2,4,6-trimethylphenylamine **107** (1.0g, 3.6mmol) and 3-amino-1-propanol **123** (270μL, 3.5mmol) in dry methanol was stirred for 12 hours under argon. $NaBH_4$ (0.35g, 9.2mmol) was added, and the solution stirred at room temperature for a further 15 minutes. The reaction mixture was quenched with 1M aq. NaOH, and extracted twice with Et_2O. The combined organic extracts were washed with saturated aq. NaCl, and dried over anhydrous $MgSO_4$. The solution was filtered, and the solvent removed *in vacuo*. The residue was recrystallised from hexane, to afford N-*(*tert-*butyloxycarbonyl)-*N-*[2-(3-hydroxy-propylimino)-ethyl]-2,4,6-trimethylaniline* **127** (0.93g, 78%) as a white crystalline solid m.p. 106-108°C (Found: **M**$^+$ 334.22485. $C_{19}H_{30}O_3N_2$ requires M, 334.22564). In $CDCl_3$, at 303K, this compound exists as a 3.8:1 mixture of amide rotamers. The NMR data refers to the major rotamer only. δ_H (400MHz; $CDCl_3$) 1.28 (1H, m, CH_2), 1.30 (9H, s, Bu^t), 1.71 (1H, m, CH_2), 2.15 (3H, s, *o*-CH_3), 2.18 (3H, s, *o*-CH_3), 2.24 (3H, s, *p*-CH_3), 2.83 (1H, m, CH_2), 3.11 (1H, m, CH_2), 3.50 (2H, m, CH_2), 3.64 (1H, m, CH_2), 4.11 (1H, t, *J* 6.7 Hz, CH) and 6.82 (2H, s, ArH); δ_C (100MHz; $CDCl_3$) 17.7 (*o*-CH_3), 17.8 (*o*-CH_3), 20.9 (*p*-CH_3), 27.1 (CH_2), 28.2 [$OC(CH_3)_3$], 44.0 (CH_2), 53.2 (CH_2), 67.4 (CH_2), 79.4 [$OC(CH_3)_3$], 86.5 (CH), 128.8 (ArC), 129.2 (ArC), 135.5 (ArC), 135.8 (ArC), 136.3 (ArC) and 137.7 (ArC).

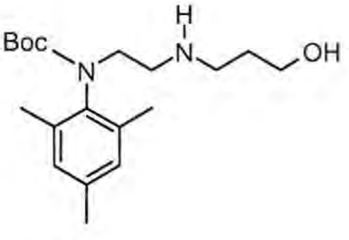

125

N-(tert-*Butyloxycarbonyl)*-N-*[2-(3-hydroxy-propylamino)-ethyl]-2,4,6-trimethylaniline* **125**

Method a. [150]

N-(*tert*-Butyloxycarbonyl)-*N*-[2-(3-hydroxy-propylimino)-ethyl]-2,4,6-trimethylaniline **127** (100mg, 3.0×10^{-4} mol), $NaBH_4$ (20mg, 5.2×10^{-4} mol) and benzoic acid (37mg, 3.0×10^{-4} mol) were ground in a mortar and pestle for 1 hour. The solid residue was dissolved in Et_2O, and a saturated solution of $NaHCO_3$ was added dropwise. The resultant solution was extracted three times with Et_2O, and the combined organic extract dried over anhydrous $MgSO_4$. The solvent was removed *in vacuo*, but ^1H NMR analysis of the crude residue revealed only unconverted starting material.

Method b.[151]

N-(*tert*-Butyloxycarbonyl)-*N*-[2-(3-hydroxy-propylimino)-ethyl]-2,4,6-trimethylaniline **127** (540mg, 1.6 mmol) was dissolved in dry Et_2O in a round-bottomed flask, and LAH (120mg, 3.1 mmol) added slowly with stirring. The solution was stirred for 12 hours, after which the LAH was quenched by the dropwise addition of H_2O. 10M aq. NaOH (5 ml) was added, and the solution extracted three times with Et_2O. The combined organic extracts were dried over anhydrous $MgSO_4$, and the solvent was removed *in vacuo* to afford crude N-(tert-*butyloxycarbonyl)*-N-*[2-(3-hydroxy-propylamino)-ethyl]-2,4,6-trimethylaniline* **125** as a colourless oil (Found: M^+ 336.24190. $C_{19}H_{32}O_3N_2$ requires M, 336.24129). ^1H NMR analysis of the crude mixture showed retention of the functionalities present in the precursor **127**, with the exception of the triplet at 4.11 ppm corresponding to the imine proton.

3.2.6 Kinetic Data

Tables 34 through 48 contain the concentration *vs.* time data for the kinetic experiments summarised in Table 16, section 2.5.2 of the discussion (see Scheme 64, p.126). Solutions of catalyst **14** were prepared under nitrogen at -40°C, in a septum-sealed screw-cap NMR tube. The 1-octene substrate **128** was added by syringe immediately prior to the start of the experiment, and a short period of time allowed for the temperature of the solution to rise to the probe temperature. Data were acquired at appropriate time intervals, depending on the reaction rate. The times referred to are uncorrected (i.e. the starting time refers to the start of the data acquisition period) and concentrations are relative to the total initial carbene concentration.

Table 34. Concentration *vs.* time data for the self-metathesis of 1-octene **128** {[**128**]$_0$ = 0.602 M} with Grubbs catalyst **14** {[14]$_0$ = 0.0201 M} in benzene-d_6 at T = 10°C.

Time / s	**[14] / M**	**[131] / M**	**[132] / M**
0	0.005988	0.014077	0
338	0.00496	0.015106	0
676	0.003937	0.016128	0
1014	0.003262	0.016803	0
1352	0.002354	0.017712	0
1690	0.00227	0.017674	0.000243
2028	0.002032	0.017882	0.000304
2366	0.001617	0.018274	0.000349
2704	0.001522	0.018273	0.00054
3042	0.001473	0.018283	0.000618
3380	0.001367	0.018317	0.000763
3718	0.001052	0.018583	0.000859
4056	0.001224	0.018315	0.001051
4394	0.001241	0.018206	0.001236
4732	0.001119	0.018275	0.001342
5070	0.001233	0.018156	0.001352
5408	0.000911	0.01835	0.001608
5746	0.001264	0.018096	0.00141
6084	0.000914	0.018073	0.002158
6422	0.001191	0.017768	0.002211
6760	0.001037	0.017909	0.002238
7098	0.001149	0.017591	0.00265
7436	0.001019	0.017652	0.002788

7774	0.001333	0.017189	0.003087
8112	0.001419	0.01698	0.003332
8450	0.001059	0.017126	0.003762
8788	0.000936	0.017269	0.003721
9126	0.00098	0.017017	0.004138
9464	0.000905	0.017165	0.003992
9802	0.001297	0.016489	0.00456
10140	0.001075	0.016263	0.005454
10478	0.000893	0.016488	0.005369
10816	0.000708	0.016461	0.005793
11154	0.000947	0.016106	0.006025
11492	0.001093	0.015675	0.006593
11830	0.000843	0.016153	0.006139
12168	0.001058	0.015592	0.006829
12506	0.000788	0.015458	0.007639
12844	0.001044	0.015033	0.007977
13182	0.000779	0.014866	0.008842
13520	0.000453	0.015469	0.008286
13858	0.000999	0.014777	0.008577
14196	0.000944	0.014711	0.008821
14534	0	0.014995	0.010141
14872	0	0.01472	0.010691
15210	0	0.014441	0.011248
15548	0	0.014805	0.01052
15886	0	0.014242	0.011646
16224	0	0.014152	0.011826
16562	0	0.013353	0.013424
16900	0	0.014012	0.012107
17238	0	0.013094	0.013943
17576	0	0.012899	0.014332
17914	0	0.013084	0.013962
18252	0	0.013362	0.013407
18590	0	0.012542	0.015046
18928	0	0.011569	0.016992
19266	0	0.011592	0.016946
19604	0	0.011533	0.017064
19942	0	0.011334	0.017463
20280	0	0.011208	0.017714
20618	0	0.010358	0.019414
20956	0	0.00977	0.02059
21294	0	0.009114	0.021903
21632	0	0.010287	0.019556
21970	0	0.009173	0.021785
22308	0	0.009834	0.020462

Table 35. Concentration *vs.* time data for the self-metathesis of 1-octene **128** {[**128**]$_0$ = 0.600 M} with Grubbs catalyst **14** {[**14**]$_0$ = 0.0200 M} in benzene-d_6 at T = 10°C.

Time / s	**[14] / M**	**[131] / M**	**[132] / M**
0	0.004754	0.01522	0
98	0.004344	0.01563	0
196	0.004065	0.015909	0
294	0.003658	0.016316	0
392	0.003454	0.01652	0
490	0.00314	0.016834	0
588	0.002947	0.017028	0
686	0.0028	0.017174	0
784	0.002564	0.01741	0
882	0.002451	0.017396	0.000255
980	0.002285	0.017527	0.000324
1078	0.002114	0.017678	0.000365
1176	0.002094	0.017684	0.000392
1274	0.001973	0.017795	0.000411
1372	0.001848	0.017914	0.000423
1470	0.00186	0.017845	0.000537
1568	0.001765	0.01792	0.000578
1666	0.001768	0.017912	0.000588
1764	0.001647	0.018021	0.000613
1862	0.001614	0.017953	0.000815
1960	0.00162	0.017947	0.000815
2058	0.001604	0.017934	0.000872
2156	0.001538	0.018013	0.000845
2254	0.001538	0.018009	0.000854
2352	0.001539	0.017933	0.001004
2450	0.001383	0.018095	0.000992
2548	0.001533	0.017909	0.001063
2646	0.001425	0.017974	0.001151
2744	0.001438	0.017969	0.001135
2842	0.001475	0.017887	0.001225

Table 36. Concentration *vs.* time data for the self-metathesis of 1-octene **128** $\{[x]_0 = 0.300\ M\}$ with Grubbs catalyst **14** $\{[\mathbf{14}]_0 = 0.0200\ M\}$ in toluene-d_8 at T = 10°C.

Time / s	**[14] / M**	**[131] / M**	**[132] / M**
0	0.017666	0.002334	0
175	0.015398	0.004602	0
350	0.013419	0.006581	0
525	0.011823	0.008177	0
700	0.010382	0.009618	0
875	0.009202	0.010798	0
1050	0.008314	0.011686	0
1225	0.007487	0.012513	0
1400	0.006737	0.013263	0
1575	0.006029	0.013971	0
1750	0.005638	0.014362	0
1925	0.005177	0.014823	0
2100	0.004763	0.015237	0
2275	0.00459	0.01541	0
2450	0.004203	0.0157	0.000194
2625	0.004073	0.015829	0.000196
2800	0.003923	0.015909	0.000335
2975	0.003823	0.015983	0.000388
3150	0.003666	0.016127	0.000415
3325	0.003603	0.016152	0.00049
3500	0.003594	0.016129	0.000554
3675	0.003539	0.016161	0.000599
3850	0.003466	0.016226	0.000616
4025	0.003478	0.01621	0.000624
4200	0.003423	0.016179	0.000797
4375	0.003341	0.016314	0.00069
4550	0.003221	0.016405	0.000748
4725	0.003229	0.016323	0.000896

Table 37. Concentration *vs.* time data for the self-metathesis of 1-octene **128** {[**128**]$_0$ = 0.300 M} with Grubbs catalyst **14** {[**14**]$_0$ = 0.0200 M} in toluene-d_8 at T = 10°C.

Time / s	**[14] / M**	**[131] / M**	**[132] / M**
0	0.01629	0.00371	0
180	0.014125	0.005875	0
360	0.012334	0.007666	0
540	0.011629	0.008371	0
720	0.009747	0.010253	0
900	0.008707	0.011293	0
1080	0.00791	0.01209	0
1260	0.007161	0.012839	0
1440	0.006666	0.013334	0
1620	0.006057	0.013943	0
1800	0.005648	0.014352	0
1980	0.005319	0.014681	0
2160	0.004916	0.015084	0
2340	0.004809	0.01504	0.000302
2520	0.004562	0.015307	0.00026
2700	0.004467	0.015404	0.000257
2880	0.004317	0.015523	0.00032
3060	0.004192	0.015575	0.000467
3240	0.004093	0.01568	0.000455
3420	0.00401	0.015754	0.000471
3600	0.004034	0.01571	0.000511
3780	0.003905	0.015813	0.000565
3960	0.003883	0.015769	0.000696
4140	0.003891	0.015764	0.000689
4320	0.003783	0.01582	0.000794
4500	0.003867	0.015742	0.000783
4680	0.003747	0.015866	0.000775
4860	0.003703	0.015826	0.000943

Table 38. Concentration *vs*. time data for the self-metathesis of 1-octene **128** {[**128**]$_0$ = 0.600 M} with Grubbs catalyst **14** {[**14**]$_0$ = 0.0200 M} in toluene-d_8 at T = 10°C.

Time / s	[14] / M	[131] / M	[132] / M
0	0.01607	0.003898	0
98	0.015196	0.004772	0
196	0.014244	0.005724	0
294	0.013335	0.006633	0
392	0.012497	0.007471	0
490	0.011617	0.008351	0
588	0.010985	0.008983	0
686	0.010226	0.009743	0
784	0.009467	0.010501	0
882	0.008823	0.011145	0
980	0.008234	0.011734	0
1078	0.007776	0.012192	0
1176	0.007223	0.012745	0
1274	0.006786	0.013182	0
1372	0.006266	0.013702	0
1470	0.00576	0.014208	0
1568	0.005446	0.014522	0
1666	0.005121	0.014847	0
1764	0.0048	0.015168	0
1862	0.004448	0.01552	0
1960	0.004099	0.015869	0
2058	0.003889	0.016079	0
2156	0.003683	0.016285	0
2254	0.003426	0.016542	0
2352	0.003304	0.016664	0
2450	0.003131	0.016837	0
2548	0.002932	0.017036	0
2646	0.002795	0.017173	0
2744	0.002705	0.017263	0
2842	0.002488	0.01748	0

Table 39. Concentration *vs.* time data for the self-metathesis of 1-octene **128** {[**128**]$_0$ = 1.200 M} with Grubbs catalyst **14** {[**14**]$_0$ = 0.0200 M} in toluene-d_8 at T = 10°C.

Time / s	**[14] / M**	**[131] / M**	**[132] / M**
0	0.01639	0.00361	0
98	0.014949	0.005051	0
196	0.013576	0.006424	0
294	0.012309	0.007691	0
392	0.011275	0.008725	0
490	0.010464	0.009536	0
588	0.009621	0.010379	0
686	0.008835	0.011165	0
784	0.008294	0.011706	0
882	0.007719	0.012281	0
980	0.007018	0.012982	0
1078	0.006531	0.013469	0
1176	0.006243	0.013757	0
1274	0.005569	0.014431	0
1372	0.005333	0.014667	0
1470	0.004892	0.015108	0
1568	0.004486	0.015514	0
1666	0.004232	0.015768	0
1764	0.004076	0.015924	0
1862	0.00374	0.01626	0
1960	0.00352	0.01648	0
2058	0.003265	0.016735	0
2156	0.002976	0.017024	0
2254	0.002955	0.017045	0
2352	0.002507	0.017493	0
2450	0.002384	0.017616	0
2548	0.002379	0.017621	0
2646	0.002167	0.017833	0
2744	0.001994	0.018006	0
2842	0.002009	0.017795	0.000392
2940	0.001808	0.018013	0.000357
3038	0.001805	0.01798	0.00043
3136	0.001736	0.018066	0.000396
3234	0.001703	0.018073	0.000448
3332	0.001715	0.018108	0.000353
3430	0.001528	0.018241	0.000461
3528	0.001548	0.018228	0.000447
3626	0.001516	0.018251	0.000465
3724	0.001327	0.018396	0.000553

Table 40. Concentration *vs*. time data for the self-metathesis of 1-octene **128** {[**128**]$_0$ = 1.200 M} with Grubbs catalyst **14** {[**14**]$_0$ = 0.0200 M} in toluene-d_8 at T = 10°C.

Time / s	**[14] / M**	**[131] / M**	**[132] / M**
0	0.014753	0.005064	0
98	0.01364	0.006177	0
196	0.012534	0.007283	0
294	0.011716	0.008101	0
392	0.010878	0.008939	0
490	0.010125	0.009692	0
588	0.009413	0.010404	0
686	0.008725	0.011092	0
784	0.008025	0.011792	0
882	0.007512	0.012305	0
980	0.006815	0.013002	0
1078	0.006434	0.013383	0
1176	0.006039	0.013778	0
1274	0.005474	0.014343	0
1372	0.005065	0.014752	0
1470	0.004631	0.015186	0
1568	0.004124	0.015693	0
1666	0.003845	0.015972	0
1764	0.003753	0.016064	0
1862	0.003319	0.016498	0
1960	0.003227	0.01659	0
2058	0.002768	0.017049	0
2156	0.002788	0.017029	0
2254	0.002556	0.017261	0
2352	0.002425	0.017393	0
2450	0.002236	0.017581	0
2548	0.002151	0.017666	0
2646	0.002073	0.017744	0
2744	0.001856	0.017961	0
2842	0.001992	0.017825	0
2940	0.001617	0.017967	0.000467
3038	0.001519	0.018019	0.000558
3136	0.001563	0.018103	0.000303
3234	0.001259	0.01837	0.000376
3332	0.001376	0.018184	0.000514
3430	0.001133	0.018394	0.00058
3528	0.001411	0.018156	0.000501

Table 41. Concentration *vs.* time data for the self-metathesis of 1-octene **128** {[**128**]$_0$ = 1.800 M} with Grubbs catalyst **14** {[**14**]$_0$ = 0.0200 M} in toluene-d_8 at T = 10°C.

Time / s	**[14] / M**	**[131] / M**	**[132] / M**
0	0.015515	0.00445	0
98	0.014247	0.005718	0
196	0.013093	0.006872	0
294	0.011942	0.008023	0
392	0.010962	0.009003	0
490	0.010048	0.009917	0
588	0.009224	0.010741	0
686	0.008551	0.011414	0
784	0.007903	0.012062	0
882	0.007315	0.01265	0
980	0.006692	0.013273	0
1078	0.006172	0.013793	0
1176	0.005572	0.014393	0
1274	0.005209	0.014756	0
1372	0.004892	0.015073	0
1470	0.004427	0.015538	0
1568	0.004172	0.015793	0
1666	0.003793	0.016172	0
1764	0.003503	0.016462	0
1862	0.003288	0.016677	0
1960	0.003248	0.016717	0
2058	0.002818	0.017147	0
2156	0.002706	0.017259	0
2254	0.002547	0.017418	0
2352	0.002336	0.017629	0
2450	0.002115	0.01785	0
2548	0.002012	0.017819	0.00027
2646	0.001772	0.018111	0.000165
2744	0.001499	0.018398	0.000137
2842	0.001656	0.018161	0.000295
2940	0.001541	0.018231	0.000386
3038	0.001126	0.018742	0.000194
3136	0.001246	0.018553	0.000332
3234	0.001235	0.018523	0.000413
3332	0.001038	0.018663	0.000529
3430	0.001201	0.018546	0.000436
3528	0.001058	0.018679	0.000456
3626	0.001242	0.018406	0.000635
3724	0.000973	0.018624	0.000736

Table 42. Concentration *vs.* time data for the self-metathesis of 1-octene **128** $\{[\mathbf{128}]_0 = 0.600$ M$\}$ with Grubbs catalyst **14** $\{[\mathbf{14}]_0 = 0.0200$ M$\}$ in chlorobenzene-d_5 at T = 10°C.

Time / s	**[14] / M**	**[131] / M**	**[132] / M**
0	0.014269	0.005748	0
98	0.012824	0.007192	0
196	0.01121	0.008807	0
294	0.009983	0.010033	0
392	0.008844	0.011173	0
490	0.007884	0.012133	0
588	0.007002	0.013015	0
686	0.006216	0.0138	0
784	0.005468	0.014548	0
882	0.004949	0.015067	0
980	0.004449	0.015567	0
1078	0.004013	0.016004	0
1176	0.003771	0.016246	0
1274	0.003327	0.01669	0
1372	0.003069	0.016948	0
1470	0.002833	0.017183	0
1568	0.002578	0.017438	0
1666	0.002332	0.017685	0
1764	0.002089	0.017927	0
1862	0.001997	0.01802	0
1960	0.001914	0.018102	0
2058	0.001759	0.018258	0
2156	0.001633	0.018384	0
2254	0.001595	0.018422	0
2352	0.001555	0.018238	0.000448
2450	0.001408	0.018378	0.000461
2548	0.001353	0.018432	0.000463
2646	0.001318	0.018369	0.000658
2744	0.001289	0.018449	0.000558
2842	0.001317	0.018375	0.000649
2940	0.00113	0.018503	0.000768
3038	0.001123	0.018567	0.000652
3136	0.001118	0.018517	0.000764
3234	0.001206	0.018417	0.000787

Table 43. Concentration *vs.* time data for the self-metathesis of 1-octene **128** {[**128**]$_0$ = 0.600 M} with Grubbs catalyst **14** {[**14**]$_0$ = 0.0200 M} in chloroform-*d* at T = 0°C.

Time / s	**[14] / M**	**[131] / M**	**[132] / M**
0	0.017891	0.002109	0
638	0.017869	0.002131	0
1276	0.017534	0.002466	0
1914	0.01724	0.00276	0
2552	0.017168	0.002832	0
3190	0.016653	0.003347	0
3828	0.016431	0.003569	0
4466	0.016135	0.003865	0
5104	0.015776	0.004224	0
5742	0.015562	0.004438	0
6380	0.015061	0.004939	0
7018	0.014877	0.005123	0
7656	0.014568	0.005432	0
8294	0.01431	0.00569	0
8932	0.013977	0.006023	0
9570	0.013761	0.006239	0
10208	0.013441	0.006559	0
10846	0.013169	0.006831	0
11484	0.01293	0.00707	0
12122	0.012634	0.007366	0
12760	0.01246	0.00754	0
13398	0.01202	0.00798	0
14036	0.011934	0.008066	0
14674	0.011765	0.008235	0
15312	0.011325	0.008675	0
15950	0.01122	0.00878	0
16588	0.011009	0.008991	0
17226	0.010865	0.009135	0
17864	0.010417	0.009583	0
18502	0.010265	0.009735	0
19140	0.009932	0.010068	0
19778	0.009907	0.010093	0
20416	0.009559	0.010441	0

Table 44. Concentration *vs.* time data for the self-metathesis of 1-octene **128** {[**128**]$_0$ = 0.599 M} with Grubbs catalyst **14** {[**14**]$_0$ = 0.0200 M} in chloroform-*d* at T = 0°C.

Time / s	**[A] / M**	**[B] / M**	**[C] / M**
0	0.017205	0.002767	0
600	0.016906	0.003066	0
1200	0.016474	0.003498	0
1800	0.016157	0.003815	0
2400	0.01582	0.004151	0
3000	0.015495	0.004477	0
3600	0.01517	0.004802	0
4200	0.014879	0.005093	0
4800	0.014471	0.005501	0
5400	0.01424	0.005732	0
6000	0.013944	0.006028	0
6600	0.013691	0.006281	0
7200	0.01341	0.006562	0
7800	0.012998	0.006974	0
8400	0.012643	0.007328	0
9000	0.012526	0.007446	0
9600	0.012246	0.007726	0
10200	0.012013	0.007959	0
10800	0.011652	0.00832	0
11400	0.011485	0.008486	0
12000	0.011187	0.008785	0
12600	0.010945	0.009027	0
13200	0.010528	0.009444	0
13800	0.01031	0.009662	0
14400	0.01013	0.009841	0
15000	0.009967	0.010004	0
15600	0.0096	0.010372	0
16200	0.009411	0.010561	0
16800	0.009094	0.010878	0
17400	0.008901	0.011071	0
18000	0.008825	0.011146	0
18600	0.008546	0.011426	0
19200	0.008275	0.011697	0
19800	0.008205	0.011767	0
20400	0.00794	0.012031	0
21000	0.007712	0.01226	0

Table 45. Concentration *vs.* time data for the self-metathesis of 1-octene **128** {[**128**]$_0$ = 1.34 M} with Grubbs catalyst **14** {[**14**]$_0$ = 0.0441 M} in chloroform-*d* at T = 0°C.

Time / s	**[14] / M**	**[131] / M**	**[132] / M**
0	0.038519	0.005647	0
600	0.036955	0.007212	0
1200	0.035154	0.009013	0
1800	0.032911	0.011054	0.000402
2400	0.030991	0.012855	0.00064
3000	0.02907	0.014647	0.000898
3600	0.027221	0.01644	0.001013
4200	0.025627	0.017951	0.001176
4800	0.024001	0.019542	0.001246
5400	0.02222	0.021195	0.001504
6000	0.020654	0.022655	0.001715
6600	0.019486	0.023785	0.001791
7200	0.018221	0.024853	0.002186
7800	0.016926	0.026069	0.002342
8400	0.015763	0.027155	0.002497
9000	0.014643	0.028178	0.002691
9600	0.013508	0.029226	0.002865
10200	0.012487	0.030087	0.003185
10800	0.011812	0.030728	0.003253
11400	0.010843	0.03156	0.003526
12000	0.009915	0.032359	0.003786
12600	0.009633	0.032534	0.003999
13200	0.008861	0.033207	0.004197
13800	0.008219	0.033727	0.00444
14400	0.007805	0.034172	0.004379

Table 46. Concentration *vs.* time data for the self-metathesis of 1-octene **128** {[**128**]$_0$ = 0.142 M} with Grubbs catalyst **14** {[**14**]$_0$ = 0.0313 M} in chloroform-*d* at T = 0°C.

Time / s	**[14] / M**	**[131] / M**	**[132] / M**
0	0.027337	0.003996	0
600	0.027093	0.00424	0
1200	0.026901	0.004433	0
1800	0.026592	0.004742	0
2400	0.026291	0.005043	0
3000	0.025951	0.005382	0
3600	0.025487	0.005684	0.000326
4200	0.025205	0.005993	0.000271
4800	0.024839	0.006341	0.000308
5400	0.024572	0.006605	0.000313
6000	0.02437	0.006963	0
6600	0.023991	0.007181	0.000322
7200	0.023577	0.00761	0.000293
7800	0.023261	0.007907	0.000329
8400	0.022939	0.008211	0.000366
9000	0.022645	0.008488	0.000403
9600	0.022308	0.008821	0.000409
10200	0.022047	0.009046	0.000482
10800	0.02175	0.009356	0.000454
11400	0.021502	0.009549	0.000566
12000	0.020983	0.010031	0.000638
12600	0.020746	0.010284	0.000607
13200	0.0205	0.01056	0.000546
13800	0.020242	0.010798	0.000586
14400	0.019776	0.011205	0.000705
15000	0.019506	0.011545	0.000566
15600	0.019305	0.011629	0.000798
16200	0.018971	0.012	0.000724

Table 47. Concentration *vs.* time data for the self-metathesis of 1-octene **128** {[**128**]$_0$ = 0.600 M} with Grubbs catalyst **14** {[**14**]$_0$ = 0.0200 M} in chloroform-*d* at T = 10°C.

Time / s	**[14] / M**	**[131] / M**	**[132] / M**
0	0.016583	0.003417	0
98	0.015457	0.004543	0
196	0.015329	0.004671	0
294	0.014585	0.005415	0
392	0.013793	0.006207	0
490	0.013048	0.006952	0
588	0.01249	0.00751	0
686	0.011648	0.008352	0
784	0.011112	0.008888	0
882	0.010471	0.009529	0
980	0.009928	0.010072	0
1078	0.009313	0.010687	0
1176	0.009034	0.010966	0
1274	0.008436	0.011564	0
1372	0.007906	0.012094	0
1470	0.007474	0.012526	0
1568	0.007006	0.012994	0
1666	0.006643	0.013357	0
1764	0.006247	0.013753	0
1862	0.005842	0.01398	0.000355
1960	0.005596	0.014189	0.00043
2058	0.005306	0.014484	0.00042
2156	0.004933	0.014834	0.000466
2254	0.004626	0.0151	0.000549
2352	0.004436	0.015301	0.000524
2450	0.003958	0.015776	0.000532
2548	0.003957	0.015729	0.000628
2646	0.003689	0.016044	0.000534
2744	0.003713	0.016074	0.000426
2842	0.003404	0.016337	0.000517
2940	0.003107	0.01664	0.000506
3038	0.003055	0.01661	0.00067
3136	0.00267	0.016875	0.000909
3234	0.002698	0.016971	0.000662
3332	0.002625	0.017	0.00075

Table 48. Concentration *vs*. time data for the self-metathesis of 1-octene **128** {[**128**]$_0$ = 0.600 M} with Grubbs catalyst **14** {[**14**]$_0$ = 0.0200 M} in chloroform-*d* at T = 10°C.

Time / s	**[14] / M**	**[131] / M**	**[132] / M**
0	0.017795	0.002205	0
158	0.016633	0.003367	0
316	0.015455	0.004545	0
474	0.014333	0.005667	0
632	0.013308	0.006692	0
790	0.012281	0.007719	0
948	0.011333	0.008667	0
1106	0.010504	0.009496	0
1264	0.009646	0.010354	0
1422	0.008877	0.011123	0
1580	0.008204	0.011796	0
1738	0.007346	0.012473	0.000363
1896	0.006815	0.01301	0.000349
2054	0.006277	0.013515	0.000416
2212	0.005744	0.014058	0.000397
2370	0.005163	0.014622	0.000431
2528	0.004621	0.015128	0.000504
2686	0.004426	0.015336	0.000475
2844	0.003916	0.015754	0.000659
3002	0.003634	0.01607	0.000592
3160	0.003337	0.016356	0.000614
3318	0.003027	0.016644	0.000658
3476	0.002871	0.016776	0.000707
3634	0.002555	0.0171	0.00069
3792	0.002277	0.017358	0.00073
3950	0.00238	0.017199	0.000841
4108	0.002059	0.017501	0.000881
4266	0.00189	0.017665	0.00089
4424	0.001646	0.017882	0.000945
4582	0.001692	0.017757	0.001102
4740	0.00137	0.018108	0.001044
4898	0.001386	0.018127	0.000974
5056	0.00119	0.01829	0.001041
5214	0.001246	0.018192	0.001124
5372	0.001161	0.018199	0.001281

4. REFERENCES

1. B. Cornils and W.A. Herrmann, *J. Catal.*, 2003, **216**, 23.
2. F. Cavani and F. Trifirò, *Catalysis Today,* 1997, **34**, 269.
3. R.V. Chaudhari, A. Seayad and S. Jayasree, *Catalysis Today,* 2001, **66**, 371.
4. R.H. Crabtree, *J. Chem Soc., Chem. Commun.*, 1999, 1611.
5. K. Grela, M. Tryznowski and M. Bieniek, *Tetrahedron Lett.*, 2002, **43**, 9055.
6. H. Olivier, *J. Mol. Catal. A: Chemical*, 1999, **146**, 285.
7. E.L.V. Goetheer, A.W. Verker, L.J.P. van den Broeke, E. de Wolf, B-J. Deelman, G. van Koten and J.T.F. Keurentjes, *J. Catal.,* 2003, **219**, 126.
8. M. Wende and J. A. Gladysz, *J. Am. Chem. Soc.*, 2003, **125**, 5861.
9. C. Marcilly, *J. Catal.*, 2003, **216**, 47.
10. G. M. Bond, J. Stringer, D.K. Brandvold, F. A. Simsek, M-G Medina and G. Egeland, *Energy & Fuels,* 2001, **15**, 309.
11. J.N. Armor, *Applied Catalysis A: General,* 2000, **194-195**, 3.
12. M. Asadullah, T. Miyazawa, S. Ito, K. Kunimori and K. Tomishige, *Energy & Fuels*, 2003, **17**, 842.
13. T.M. Trnka and R.H. Grubbs, *Acc. Chem. Res.*, 2001, **34**, 18.
14. S.K. Armstrong, *J. Chem. Soc., Perkin Trans. 1*, 1998, 371.
15. R.H. Grubbs and S. Chang, *Tetrahedron*, 1998, **54**, 4413.
16. R. Grigg, W. Martin, J. Morris and V. Sridharan, *Tetrahedron Lett.*, 2003, **44**, 4899.
17. L. Banfi, A. Basso, G. Guanit and R. Riva, *Tetrahedron Lett.*, 2003, **44**, 7655.
18. O. Fujimura and R.H. Grubbs, *J. Am. Chem. Soc.*, 1996, **118**, 2499.
19. A. Furstner, *Angew. Chem., Int. Ed. Engl.,* 2000, **39**, 3012.
20. D. J. Wallace, *Tetrahedron Lett.*, 2003, **44**, 2145.

21. P. Van de Weghe, D. Aoun, J-G. Boiteau and J. Eustache, *Org. Lett.*, 2002, **4**, 4105.

22. H.E. Blackwell, D.J. O'Leary, A.K. Chaterjee, R.A. Washenfelder, D.A. Bussmann and R.H. Grubbs, *J. Am. Chem. Soc.*, 2000, **122**, 58.

23. W.E. Crowe and Z. J. Zhang, *J. Am. Chem. Soc.*, 1993, **115**, 10998.

24. W.E. Crowe and D.R. Goldberg, *J. Am. Chem. Soc.*, 1995, **117**, 5162.

25. A.K. Chatterjee, T. Choi, D.P. Sanders and R.H. Grubbs, *J. Am. Chem. Soc, 2003,* **125**, 11360.

26. M.L. Randall and M.L. Snapper, *J. Mol. Catal.,*1998, **133**, 29.

27. S. Randl, S. J. Connon and S. Blechert, *J. Chem. Soc., Chem. Commun.*, 2001, 1796.

28. W.J. Feast and E. Khosravi, *J. Fluor. Chem.*, 1999, **100**, 117.

29. D.M. Lynn, S. Kanaoka and R.H. Grubbs, *J. Am. Chem. Soc.*, 1996, **118**, 784.

30. C. Bolm, C.L. Dinter, A. Seger, H. Hocker and J. Brozio, *J. Org.Chem.*, 1999, **64**, 5730.

31. S. Mukherjee, K.W.C. Poon, D.L. Flynn and P. Hanson, *Tetrahedron Lett.*, 2003, **44**, 7187.

32. K.C. Caster, E.F. Tokas, C.G. Keck and M.E. Hontz, *J. Mol. Catal. A: Chemical.*, 2002, **190**, 65.

33. S. Joo, Y. Yun, J. Jin, D. Kim and W. Zin, *Macromolecules*, 2000, **33**, 6704.

34. J. Zaminer, C. Stapper and S. Blechert, *Tetrahedron Lett.,* 2002, **43**, 6739.

35. H. Hagiwara, T. Kasumi, S. Endou, T. Hoshi and T. Suzuki, *Tetrahedron*, 2002, **58**, 6651.

36. D. Banti and M. North, *Tetrahedron Lett.,* 2002, **43**, 1561.

37. D.S. La, E.S. Sattely, J.G. Ford, R.R. Schrock and A.H. Hoveyda, *J. Am. Chem. Soc.*, 2001, **123**, 7767.

38. R.A.J. Wybrow, L.A. Johnson, B. Auffray, W.J. Moran, H. Adams and J.P. Harrity, *Tetrahedron Lett.*, 2002, **43**, 7851.

39. J.A.K. du Plessis and P. Heenop, *S. Afr. J. Chem.*, 1979, **32**, 1.

40. J.A.K. du Plessis and P. Heenop, *S. Afr. J. Chem.*, 1980, **33**, 51.

41. P.O. Nubel and C.L. Hunt, *J. Mol. Catal. A: Chemical,* 1999, **145**, 323.

42. S.T. Nguyen, L.K. Johnson, R.H Grubbs and J.W. Ziller, *J. Am. Chem. Soc.,* 1992, **114**, 3974.

43. S.T. Nguyen, R.H. Grubbs and J.W. Ziller, *J. Am. Chem. Soc.,* 1993, **115**, 9858.

44. G.C. Fu, S.T. Nguyen and R.H. Grubbs, *J. Am. Chem. Soc.,* 1993, **115**, 9856.

45. P. Schwab, R.H. Grubbs and J.W. Ziller, *J. Am. Chem. Soc.,* 1996, **118**, 100.

46. E.L. Dias, S.T. Nguyen and R.H. Grubbs, *J. Am. Chem. Soc.*, 1997, **119**, 3887.

47. Z. Whu, S.T. Nguyen, R.H. Grubbs and J.W. Ziller, *J. Am. Chem. Soc.,* 1995, **117**, 5503.

48. L. Jafarpour and S.P. Nolan, *J. Organomet. Chem.,* 2001, **617**, 17.

49. T. Weskamp, W.C. Schattenmann, M. Spiegler and W.A. Herrmann, *Angew. Chem., Int. Ed. Engl.,* 1998, **37**, 2490.

50. T. Weskamp, F.J. Kohl, W. Hieringer, D. Gleich and W.A. Herrmann, *Angew. Chem., Int. Ed. Engl.,* 1999, **38**, 2416.

51. M. Scholl, T.M. Trnka, J.P. Morgan and R.H. Grubbs, *Tetrahedron Lett.,* 1999, **40**, 2247.

52. J. Huang, E.D. Stevens, S.P. Nolan and J.L Petersen, *J. Am. Chem. Soc.,* 1999, **121**, 2674.

53. M. Scholl, S. Ding, C.W. Lee and R.H. Grubbs, *Org. Lett.*, 1999, **1**, 953.

54. A. Furstner, O.R. Thiel, L. Ackermann, H-J Schanz and S.P. Nolan, *J. Org. Chem.,* 2000, **65**, 2204.

55. D. M. Lynn, B. Mohr and R.H. Grubbs, *J. Am. Chem. Soc.,* 1998, **120**, 1627.

56. D.M. Lynn, B. Mohr, R.H. Grubbs, L.M. Henling and M.W. Day, *J. Am. Chem. Soc.,* 2000, **122**, 6601.

57. T.A. Kirkland, D.M. Lynn and R.H. Grubbs, *J. Org. Chem.*, 1998, **63**, 9904.

58. J.S. Kingsbury, J.P.A. Harrity, P.J. Bonitatebus, Jr. and A.H. Hoveyda, *J. Am. Chem. Soc.,* 1999, **121**, 791.

59. J.J. Van Veldhuizen, S.B. Garber, J.S. Kingbury and A.H. Hoveyda, *J. Am. Chem. Soc.*, 2002, **124**, 4954.

60. S.T. Nguyen and R.H. Grubbs, *J. Organomet. Chem.*, 1995, **497**, 195.

61. P. Nieczypor, W. Buchowitz, W.J.N. Meester, F.P.J.T. Rutjes and J.C. Mol, *Tetrahedron Lett.*, 2001, **42**, 7103.

62. M. Ahmed, A.G.M. Barrett, D.C. Braddock, S.M. Cramp and P.A. Procopiou, *Tetrahedron Lett.*, 1999, **40**, 8657.

63. J. Dowden and J. Savovic, *J. Chem. Soc., Chem. Commun.*, 2001, 37.

64. Q. Yao and A.R. Motta, *Tetrahedron Lett.*, 2004, **45**, 2447.

65. R. Castarlenas, C. Fischmeister, C. Bruneau and P.H. Dixneuf, *J. Mol.Catal. A: Chemical*, 2004, **213**, 31.

66. B. De Clercq and F. Verpoort, *Tetrahedron Lett.*, 2002, **43**, 9101.

67. T. Opstal and F. Verpoort, *J. Mol. Catal. A: Chemical*, 2003, **200**, 49.

68. S.F. Vyboishchikov, M. Buhl and W. Thiel, *Chem. Eur. J.*, 2002, **8** (17), 3962.

69. J.A. Tallarico, P.J. Bonitatebus and M.L. Snapper, *J. Am. Chem. Soc.*, 1997, **119**, 7157.

70. C. Adlhart and P. Chen, *Helv. Chim. Acta*, 2000, **83**, 2192.

71. C. Hinderling, C. Adlhart and P. Chen, *Angew. Chem., Int. Ed.*, 1998, **37**, (19), 2685.

72. C. Adlhart, C. Hinderling, H. Baumann and P. Chen, *J. Am. Chem. Soc.*, 2000, **122**, 8204.

73. M.S. Sanford, M. Ulman and R.H. Grubbs, *J. Am. Chem. Soc.*, 2001, **123**, 749.

74. M.S. Sanford, J.A. Love and R.H. Grubbs, *J. Am. Chem. Soc.*, 2001, **123**, 6543.

75. O.M. Aagaard, R.J. Meier and F. Buda, *J. Am. Chem. Soc.*, 1998, **120**, 7174.

76. R. J. Meier, O.M. Aagaard and F. Buda, *J. Mol. Catal. A: Chemical*, 2000, **160**, 189.

77. F. Bernardi, A. Bottoni and G.P. Miscione, *Organometallics*, 2003, **22**, 940.

78. S. Fomine, S.M Vargas and M.A. Tlenkopatchev, *Organometallics,* 2003, **22**, 93.

79. L. Cavallo, *J. Am. Chem. Soc.,* 2002, **124**, 8965.

80. C. Adlhart and P. Chen, *Angew. Chem. Int. Ed.,* 2002, **41** (23), 4484.

81. C. Adlhart and P. Chen, *J. Am. Chem. Soc.* 2004, **126**, 3496.

82. S. G. Burton, Ph.D Thesis, Rhodes University, 1993.

83. K.W. Wellington, Ph.D. Thesis, Rhodes University, 1999.

84. J.P. Hagemann, Ph.D. Thesis, Rhodes University, 1997.

85. A. Daubinet, Ph.D Thesis, Rhodes University, 2001.

86. T.R. Tshikudo, MSc Thesis, Rhodes University, 2002.

87. B. Gxoyiya, MSc Thesis, Rhodes University, 2003.

88. Wavefunction, Inc.: 18401 Von Karman Avenue, Suite 370, Irvine, CA 92612.

89. (a) B. Delley, *J. Chem. Phys.,* 1990, **92**. 508.
(b) B. Delley, *J. Phys. Chem.,* 1996, **100**, 6107.
(c) B. Delley, *J. Chem. Phys.,* 2000, **113**, 7756.

90. P. Schwab, M.B. France, J.W. Ziller and R.H. Grubbs, *Angew. Chem., Int. Ed. Engl.,* 1995, **34**, 2039.

91. T. Money, *Nat. Prod. Rep.,* 1985, **2**, 253.

92. D. Amoroso, G.P.A. Yap and D.E. Fogg, *Organometallics*, 2002, **21**, 3335.

93. (a) W. Buchowicz, J.C. Mol, M. Lutz and A.L. Spek, *J. Organomet. Chem.*, 1999, **588**, 205.
(b) W. Buchowitz, F. Ingold, J.C. Mol, M. Lutz and A.L. Spek, *Chem. Eur. J.*, 2001, **7**, 2842.

94. M.S. Sanford, L.M. Henling, M.W. Day and R.H. Grubbs, *Angew. Chem., Int. Ed.*, 2000, **39**, 3451.

95. (a) C.R. Eck, R.W. Mills and T. Money, *J. Chem Soc., Chem. Commun.,* 1973, 911.
(b) C.R. Eck, R.W. Mills and T. Money, *J. Chem. Soc., Perkin Trans. 1*, 1975, 251.

96. P. Cachia, N. Darby, C.R. Eck and T. Money, *J. Chem. Soc., Perkin Trans. 1*, 1976, 359.

97. J.H. Hutchinson. T. Money and S.E. Piper, *Can. J. Chem.*,1986, **64**, 854.

98. W.M. Dadson and T. Money, *J. Chem. Soc., Chem. Commun.*, 1982, 112.

99. R. Antkowiak and W.Z. Antkowiak, *Polish J. Chem*, 1994, **68**, 2297.

100. A. Bondi, *J. Phys. Chem.*, 1964, **68**, 441.

101. P.C. Moews, J.R. Knox and W.R. Vaughan, *J. Am. Chem. Soc.*, 1978, **100**, 260.

102. W.M. Dadson, J.H. Hutchinson and T. Money, *Can. J. Chem.*,1990, **68**, 1821.

103. (a) C.J. Collins and C.K. Johnson, *J. Am. Chem. Soc.*, 1973, **95**, 4766.
(b) C.J. Collins and C.K. Johnson, *J. Am. Chem. Soc.*, 1974, **96**, 2514.

104. K.A. Lobb, unpublished work.

105. C.A. Bear and J. Trotter, *Acta Cryst.*, 1975, **B31**, 904.

106. I.V. Komarov, A. Monsees, R. Kadyrov, C. Fischer, U. Schmidt and A. Börner, *Tetrahedron: Assymetry*, 2002, **13**, 1615.

107 E. Pretsch, T. Clerc, J. Seibl and W. Simon, *Tables of Spectral Data for Structure Determination of Organic Compounds*, Springer-Verlag, Berlin, 1989.

108. K.M. Baker and B.R. Davis, *Tetrahedron*, 1968, **24**, 1655.

109. C.G. Ferguson, T. Money, J. Pontillo, P.D.M. Whitelaw and M.K.C. Wong, *Tetrahedron*, 1996, **52**, 14661.

110. K.A. Lobb and P.T. Kaye, *S. Afr. J. Chem.*, 2003, **56**, 60.

111. W.B. Smith, *J. Org. Chem.*, 1999, **64**, 60.

112. M-J Brienne and J. Jacques, *Tetrahedron,* 1970, **26**, 5087.

113. P.P. Korkas, E. Weber, M. Czugler and G. Náray-Szabó, *J. Chem Soc., Chem. Commun.*, 1995, 2229.

114. Gaussian 03, Revision B.05, M.J. Frisch, G.W. Trucks, H.B. Schlegel, G.E. Scuseria, M.A. Robb, J.R. Cheesema, J.A. Montgomery, Jr., T. Vreven, K.N. Kudin, J.C. Burant, J.M. Millam, S.S. Iyengar, J. Tomasi, V. Barone, B. Mennucci, M. Cossi, G. Scalmani, N. Rega, G.A. Petersson, H. Nakatsuji, M. Hada, M. Ehara,

K. Toyota, R. Fukuda, J. Hasegawa, M. Ishida, T. Nakajima, Y. Honda, O. Kitao, H. Nakai, M. Klene, X. Li, J.E. Knox, H.P. Hratchian, J.B. Cross, V. Bakken, C. Adamo, J. Jaramillo, R. Gomperts, R.E. Stratmann, O. Yazyev, A.J. Austin, R. Cammi, C. Pomelli, J.W. Ochterski, P.Y. Ayala, K. Morokuma, G.A. Voth, P. Salvador, J. J. Dannenberg, V.G. Zakrzewski, S. Dapprich, A.D. Daniels, M.C. Strain, O. Farkas, D.K. Malick, A.D. Rabuck, K. Raghavachari, J.B. Foresman, J.V. Ortiz, Q. Cui, A.G. Baboul, S. Clifford, J. Cioslowski, B.B. Stefanov, G. Liu, A. Liashenko, P. Piskorz, I. Komaromi, R.L. Martin, D.J. Fox, T. Keith, M.A. Al-Laham, C.Y. Peng, A. Nanayakkara, M. Challacombe, P.M.W. Gill, B. Johnson, W. Chen, M.W. Wong, C. Gonzalez, and J.A. Pople, Gaussian, Inc., Wallingford CT, 2004.

115. a) W.L. Meyer, A.P. Lobo and R.N. McCarthy, *J. Org. Chem.*, 1967, **32**, 1754.
b) W.L. Meyer, C.E. Capshaw, J.H.Johnson, A.R. Klusener, A.P.Lobo and R.N.McCarthy, *J. Org. Chem.*, 1977, **42**, 527.

116. R. Klein, MSc Thesis, Rhodes University, 1999.

117. I.V. Komarov, M.V. Gorichko and M.Y. Kornilov, *Tetrahedron: Asymmetry*, 1997, **8**, 435.

118. W. Buchowicz, personal communication.

119. J.O. Krause, O. Nuyken, K. Wurst and M.R. Buchmeiser, *Chem. Eur. J.*, 2004, **10**, 777.

120. A.H. Hoveyda, D.G. Gillingham, J.J. Van Veldhuizen, O. Kataoka, S.B. Garber, J.S. Kingsbury and J.P.A. Harrity, *Org. Biomol. Chem.*, 2004, **2**, 8.

121. J.S. Kingsbury, S.B. Garber, J.M. Giftos, B.L. Gray, M.M. Okamoto, R.A. Farrer, J.T. Fourkas and A.H. Hoveyda, *Angew. Chem., Int. Ed. Engl.*, 2001, **40**, 4251.

122. M. Ulman and R.H. Grubbs, *Organometallics*, 1998, **17**, 2484.

123. C. Hansch, A. Leo and R.W. Taft, *Chem. Rev.*, 1991, **91**, 165.

124. N.S. Panina, A.N. Belyaev and S.A. Simanova, *Russian Journal of General Chemistry*, 2002, **72**, 91.

125. D.L. Lichtenberger, J.R. Pollard, M.A. Lynn, F.A. Cotton and X. Feng, *J. Am. Chem. Soc.*, 2000, **122**, 3182.

126. L. Perrin, E. Clot, O. Eisenstein, J. Loch and R.H. Crabtree, *Inorg. Chem.*, 2001, **40**, 5806.

127. G. Wilkinson (Ed), *Comprehensive Coordination Chemistry*, Pergamon Press, Oxford, 1987, vol. 2, p. 443.

128. B.S. Furniss, A.J. Hannaford, P.W.G. Smith and A.R. Tatchell, *Vogel's Textbook of Practical Organic Chemistry,* Longman, Singapore, 1996, p. 461.

129. http://www.Mestre-C.com

130. F. Charbonnier, R. Faure, H. Loiseleur, *Revue de Chimie Minerale,* 1981, **18**, 245.

131. H-L Zhu, X-M Zhang, X-Y Liu, X-J Wang, G-F- Liu, A. Usman and H-K Fun, *Inorg. Chem. Commun.,* 2003, **6**, 1113.

132. G. Wulff, G. Röhle and W. Krüger, *Chem. Ber.*, 1972, **105**, 1079.

133. R. Li, D.S. Larsen and S. Brooker, *New J. Chem.,* 2003, **27**, 1353.

134. K.G. Hampton and J.J. Christie, *J. Org. Chem.,* 1975, **40**, 3887.

135. W. Flitsch and F-J. Lüttig, *Liebigs Ann. Chem.,* 1987, 893.

136. R. Willstätter and A. Pfannenstiel, *Justus Liebigs Ann. Chem.*, 1920, **422**, 1.

137. R. Ocampo, W.R. Dolbier, Jr., K.A. Abboud and F. Zuluaga, *J. Org. Chem.,* 2002, **67**, 72.

138. H.M. Deutsch, X. Ye, Q. Shi, Z. Liu and M.M. Schweri, *Eur. J. Med. Chem.,* 2001, **36**, 303.

139. T. Kato, N. Katagiri and R. Sato, *J. Chem. Soc., Perkin Trans. I,* 1979, 525.

140. M. Yamamoto, M. Nakazawa, K. Kishikawa and S. Kohmoto, J. Chem. Soc., *Chem. Commun.,*1996, 2353.

141. L. Chen, G. Zhao and Y. Ding, *Tetrahedron Lett.,* 2003, **44**, 2611.

142. N.J. Leonard and W.E. Goode, *J. Am. Chem. Soc.,* 1950, **72**, 5404.

143. G. Deleris, J. Dunogues and A. Gadras, *Tetrahedron*, 1988, **44**, 4243.

144. V.S. Arutyunyan, T.V. Kochikyan, E.V. Arutyunyan and A.A. Avetisyan, *Khim. Zh. Armenii,* 2000, **53**, 121.

145. A. Koziara, K. Osowska-Pacewicka, S. Zawadzki and A. Zwierzak, *Synthesis*, 1985, 202.

146. A. Koziara and A. Zwierzak, *Synthesis*, 1992, 1063.

147. H.M. Weiss, *J. Chem. Ed.*, 1995, **72**, 848.

148. D.A. Evans, K.T. Chapman and E.M. Carreira, *J. Am. Chem. Soc.*, 1988, **110**, 3567.

149. A.F. Abdel-Magid, K.G. Carson, B.D. Harris, C.A. Maryanoff and R.D. Shah, *J. Org. Chem.*, 1996, **61**, 3849.

150. B.T. Cho and S.K. Kang, *Tetrahedron*, 2005, **61**, 5725.

151. B.S. Furniss, A.J. Hannaford, P.W.G. Smith and A.R. Tatchell, *Vogel's Textbook of Practical Organic Chemistry*, Longman, Singapore, 1996, p.447.

152. R.G. Wilkins, *Kinetics and Mechanism of Reactions of Transition Metal Complexes*, VCH, Weinheim, 1991, p.18.

153. J.W. Moore and R.G. Pearson, *Kinetics and Mechanism*, John Wiley and Son, New York, 1981, p.70.

154. B.S. Furniss, A.J. Hannaford, P.W.G. Smith and A.R. Tatchell, *Vogel's Textbook of Practical Organic Chemistry*, Longman, Singapore, 1996, p.1442.

155. K. Basu, J.A. Cabral and L.A. Paquette, *Tetrahedron Lett.*, 2002, **43**, 5453.

156. V. Amir-Ebrahimi, J.G. Hamilton, J. Nelson, J.J. Rooney, J.M. Thompson, A.J. Beaumont, A.D. Rooney and C.J. Harding, J. Chem. Soc., *Chem. Commun.*, 1999, 1621.

157. J.A. Tallarico, L.M. Malnick and M.L. Snapper, *J. Org. Chem.*, 1999, **64**, 344.

158. T. Opstal and F. Verpoort, *Tetrahedron Lett.*, 2002, **43**, 9259.

159. J. Faulkner, C.D. Edlin, D. Fengas, I. Preece, P. Quayle and S.N. Richards, *Tetrahedron Lett.*, 2005, **46**, 2381.

160. R.G. Wilkins, *Kinetics and Mechanism of Reactions of Transition Metal Complexes*, VCH, Weinheim, 1991, p.30.

161. A.K. Rappé, C.J. Casewit, K.S. Colwell, W.A. Goddard and W.M. Skiff, *J. Am. Chem. Soc.*, 1992, **114**, 10024.

162. A.K. Rappé and W.A. Goddard, *J. Phys. Chem.*, 1991, **95**, 3358.

163. R. Fletcher and C.M. Reeves, *Comput. J.*, 1964, **7**, 149.

164. J.P. Perdew and Y Wang, *Phys. Rev.,* 1992, **B45**, 13244.

165. W. Kohn and L.J. Sham, *Phys. Rev. A.,* 1963,**140**, 1133.

166. P. Pulay, *J. Comp. Chem.,* 1982, **3**, 556.

167. T.A. Halgren and W.N. Lipscomb, *Chem. Phys. Lett.,* 1977, **49**, 225.

168. G. Henkelman and H. Jonsson, *J. Chem. Phys.*, 2000, **113**, 9978.

169. D.D. Perrin and W.L.F. Armarego, *Purification of Laboratory Chemicals,* Pergamon Press, Oxford, 1988.

170. D.L. Kuo, *Can. J. Chem.*, 1988, **66**, 1794.

5. APPENDIX

5.1 CRYSTALLOGRAPHIC DATA FOR (-)-3,3,4-TRIMETHYL-1,7-DIBROMONORBORNANE-2-ONE (54)

Table 49. Crystal data and structural refinement for compound **54**.

Empirical formula	$C_{10}H_{14}Br_2O$	
Formula weight	310.03	
Temperature	173(2) K	
Wavelength	0.71073 Å	
Crystal system	Orthorhombic	
Space group	P2(1)2(1)2(1)	
Unit cell dimensions	a = 6.5795(9) Å	α= 90°.
	b = 10.9019(15) Å	β= 90°.
	c = 15.862(2) Å	γ = 90°.
Volume	1137.8(3) $Å^3$	
Z	4	
Density (calculated)	1.810 Mg/m^3	
Absorption coefficient	7.086 mm^{-1}	
F(000)	608	
Crystal size	0.48 x 0.36 x 0.02 mm^3	
Theta range for data collection	2.27 to 28.00°.	
Index ranges	-8<=h<=8, -14<=k<=14, -20<=l<=16	
Reflections collected	7771	
Independent reflections	2717 [R(int) = 0.0401]	
Completeness to theta = 28.00°	99.4 %	
Absorption correction	Integration	
Max. and min. transmission	0.8713 and 0.1321	
Refinement method	Full-matrix least-squares on F^2	
Data / restraints / parameters	2717 / 0 / 121	
Goodness-of-fit on F^2	1.037	
Final R indices [I>2sigma(I)]	R1 = 0.0297, wR2 = 0.0725	
R indices (all data)	R1 = 0.0355, wR2 = 0.0752	
Absolute structure parameter	0.002(17)	
Largest diff. peak and hole	1.422 and -0.351 e.$Å^{-3}$	

Table 50. Atomic coordinates (x 10^4) and equivalent isotropic displacement parameters (Å^2x 10^3) for compound **54**. U(eq) is defined as one third of the trace of the orthogonalized U^{ij} tensor.

	x	y	z	U(eq)
C(1)	4501(6)	136(3)	5022(2)	25(1)
C(2)	5434(6)	-845(4)	5581(3)	29(1)
C(3)	4239(6)	-825(4)	6406(2)	34(1)
C(4)	2775(6)	280(4)	6263(3)	34(1)
C(5)	1150(7)	-114(4)	5606(3)	43(1)
C(6)	2347(6)	-338(4)	4791(3)	33(1)
C(7)	3972(6)	1136(3)	5654(2)	26(1)
C(8)	5695(8)	-655(5)	7159(3)	51(1)
C(9)	3168(8)	-2073(4)	6527(3)	57(1)
C(10)	1884(8)	899(5)	7040(3)	52(1)
O(1)	6809(5)	-1538(3)	5401(2)	47(1)
Br(1)	6166(1)	582(1)	4073(1)	46(1)
Br(2)	6292(1)	2038(1)	6093(1)	31(1)

Table 51. Bond lengths [Å] and angles [°] for compound **54**.

C(1)-C(2)	1.518(5)
C(1)-C(7)	1.521(5)
C(1)-C(6)	1.552(5)
C(1)-Br(1)	1.925(4)
C(2)-O(1)	1.213(5)
C(2)-C(3)	1.526(6)
C(3)-C(8)	1.542(5)
C(3)-C(9)	1.545(6)
C(3)-C(4)	1.559(6)
C(4)-C(10)	1.522(6)
C(4)-C(5)	1.554(6)
C(4)-C(7)	1.556(5)

C(5)-C(6)	1.532(6)
C(5)-H(5A)	0.9900
C(5)-H(5B)	0.9900
C(6)-H(6A)	0.9900
C(6)-H(6B)	0.9900
C(7)-Br(2)	1.945(4)
C(7)-H(7)	1.0000
C(8)-H(8A)	0.9800
C(8)-H(8B)	0.9800
C(8)-H(8C)	0.9800
C(9)-H(9A)	0.9800
C(9)-H(9B)	0.9800
C(9)-H(9C)	0.9800
C(10)-H(10A)	0.9800
C(10)-H(10B)	0.9800
C(10)-H(10C)	0.9800

C(2)-C(1)-C(7)	102.3(3)
C(2)-C(1)-C(6)	105.8(3)
C(7)-C(1)-C(6)	100.6(3)
C(2)-C(1)-Br(1)	113.9(3)
C(7)-C(1)-Br(1)	117.7(2)
C(6)-C(1)-Br(1)	114.8(3)
O(1)-C(2)-C(1)	127.1(4)
O(1)-C(2)-C(3)	126.5(4)
C(1)-C(2)-C(3)	106.4(3)
C(2)-C(3)-C(8)	110.2(3)
C(2)-C(3)-C(9)	109.2(4)
C(8)-C(3)-C(9)	107.0(3)
C(2)-C(3)-C(4)	101.8(3)
C(8)-C(3)-C(4)	113.8(4)
C(9)-C(3)-C(4)	114.6(4)
C(10)-C(4)-C(5)	113.6(4)
C(10)-C(4)-C(7)	115.6(4)
C(5)-C(4)-C(7)	95.6(3)

C(10)-C(4)-C(3)	117.6(4)
C(5)-C(4)-C(3)	108.0(3)
C(7)-C(4)-C(3)	103.9(3)
C(6)-C(5)-C(4)	104.8(3)
C(6)-C(5)-H(5A)	110.8
C(4)-C(5)-H(5A)	110.8
C(6)-C(5)-H(5B)	110.8
C(4)-C(5)-H(5B)	110.8
H(5A)-C(5)-H(5B)	108.9
C(5)-C(6)-C(1)	102.6(3)
C(5)-C(6)-H(6A)	111.3
C(1)-C(6)-H(6A)	111.3
C(5)-C(6)-H(6B)	111.3
C(1)-C(6)-H(6B)	111.3
H(6A)-C(6)-H(6B)	109.2
C(1)-C(7)-C(4)	95.5(3)
C(1)-C(7)-Br(2)	114.7(3)
C(4)-C(7)-Br(2)	118.5(2)
C(1)-C(7)-H(7)	109.1
C(4)-C(7)-H(7)	109.1
Br(2)-C(7)-H(7)	109.1
C(3)-C(8)-H(8A)	109.5
C(3)-C(8)-H(8B)	109.5
H(8A)-C(8)-H(8B)	109.5
C(3)-C(8)-H(8C)	109.5
H(8A)-C(8)-H(8C)	109.5
H(8B)-C(8)-H(8C)	109.5
C(3)-C(9)-H(9A)	109.5
C(3)-C(9)-H(9B)	109.5
H(9A)-C(9)-H(9B)	109.5
C(3)-C(9)-H(9C)	109.5
H(9A)-C(9)-H(9C)	109.5
H(9B)-C(9)-H(9C)	109.5
C(4)-C(10)-H(10A)	109.5
C(4)-C(10)-H(10B)	109.5

H(10A)-C(10)-H(10B)	109.5
C(4)-C(10)-H(10C)	109.5
H(10A)-C(10)-H(10C)	109.5
H(10B)-C(10)-H(10C)	109.5

Table 52. Anisotropic displacement parameters ($Å^2 \times 10^3$) for compound **54**. The anisotropic displacement factor exponent takes the form: $-2p^2[h^2a^{*2}U^{11} + ... + 2 h k a^* b^* U^{12}]$

	U^{11}	U^{22}	U^{33}	U^{23}	U^{13}	U^{12}
C(1)	31(2)	23(2)	21(2)	0(1)	-1(1)	-1(1)
C(2)	31(2)	21(2)	36(2)	-2(2)	-11(2)	-2(2)
C(3)	44(2)	30(2)	29(2)	8(2)	-12(2)	-14(2)
C(4)	29(2)	43(2)	29(2)	-4(2)	4(2)	-8(2)
C(5)	29(2)	50(2)	50(2)	-3(2)	-9(2)	-5(2)
C(6)	38(2)	29(2)	33(2)	1(2)	-14(2)	-5(2)
C(7)	29(2)	25(2)	25(2)	-3(1)	-3(2)	1(2)
C(8)	69(3)	48(3)	37(2)	15(2)	-26(2)	-19(2)
C(9)	82(4)	42(2)	46(3)	17(2)	-17(3)	-30(3)
C(10)	51(3)	68(3)	38(2)	-10(2)	18(2)	-14(2)
O(1)	40(2)	29(1)	71(2)	-8(2)	-14(2)	7(1)
Br(1)	66(1)	47(1)	26(1)	-6(1)	14(1)	-15(1)
Br(2)	38(1)	26(1)	28(1)	-4(1)	1(1)	-8(1)

Table 53. Hydrogen coordinates (x 10^4) and isotropic displacement parameters ($Å^2$x 10^3) for compound **54**.

	x	y	z	U(eq)
H(5A)	447	-871	5789	52
H(5B)	127	542	5525	52
H(6A)	1764	131	4315	40
H(6B)	2374	-1220	4644	40
H(7)	3003	1726	5386	31
H(8A)	6670	-1334	7173	77
H(8B)	4911	-645	7684	77
H(8C)	6428	122	7098	77
H(9A)	2400	-2278	6016	85
H(9B)	2237	-2024	7008	85
H(9C)	4188	-2710	6633	85
H(10A)	1000	1577	6865	79
H(10B)	2987	1218	7392	79
H(10C)	1089	301	7362	79

Table 54. Torsion angles [°] for compound **54**.

C(7)-C(1)-C(2)-O(1)	-145.8(4)
C(6)-C(1)-C(2)-O(1)	109.3(4)
Br(1)-C(1)-C(2)-O(1)	-17.7(5)
C(7)-C(1)-C(2)-C(3)	36.6(4)
C(6)-C(1)-C(2)-C(3)	-68.4(4)
Br(1)-C(1)-C(2)-C(3)	164.6(2)
O(1)-C(2)-C(3)-C(8)	57.0(5)
C(1)-C(2)-C(3)-C(8)	-125.4(4)
O(1)-C(2)-C(3)-C(9)	-60.4(5)
C(1)-C(2)-C(3)-C(9)	117.3(4)
O(1)-C(2)-C(3)-C(4)	178.0(4)
C(1)-C(2)-C(3)-C(4)	-4.3(4)
C(2)-C(3)-C(4)-C(10)	-157.9(3)
C(8)-C(3)-C(4)-C(10)	-39.3(5)
C(9)-C(3)-C(4)-C(10)	84.4(5)
C(2)-C(3)-C(4)-C(5)	72.0(4)
C(8)-C(3)-C(4)-C(5)	-169.4(3)
C(9)-C(3)-C(4)-C(5)	-45.8(5)
C(2)-C(3)-C(4)-C(7)	-28.7(3)
C(8)-C(3)-C(4)-C(7)	89.9(4)
C(9)-C(3)-C(4)-C(7)	-146.5(4)
C(10)-C(4)-C(5)-C(6)	163.3(4)
C(7)-C(4)-C(5)-C(6)	42.2(4)
C(3)-C(4)-C(5)-C(6)	-64.4(4)
C(4)-C(5)-C(6)-C(1)	-8.1(4)
C(2)-C(1)-C(6)-C(5)	75.7(4)
C(7)-C(1)-C(6)-C(5)	-30.4(4)
Br(1)-C(1)-C(6)-C(5)	-157.8(3)
C(2)-C(1)-C(7)-C(4)	-51.9(3)
C(6)-C(1)-C(7)-C(4)	57.0(3)
Br(1)-C(1)-C(7)-C(4)	-177.5(3)
C(2)-C(1)-C(7)-Br(2)	73.0(3)
C(6)-C(1)-C(7)-Br(2)	-178.0(2)

Br(1)-C(1)-C(7)-Br(2)	-52.6(3)
C(10)-C(4)-C(7)-C(1)	-179.8(4)
C(5)-C(4)-C(7)-C(1)	-60.2(3)
C(3)-C(4)-C(7)-C(1)	49.9(3)
C(10)-C(4)-C(7)-Br(2)	58.2(5)
C(5)-C(4)-C(7)-Br(2)	177.7(3)
C(3)-C(4)-C(7)-Br(2)	-72.2(3)

5.2 CRYSTALLOGRAPHIC DATA FOR (1*R*, 5*S*, 6*S*)-1,5-DIMETHYL-2-OXO-3-OXABICYCLO[3.3.0]OCTANE-6-CARBOXYLIC ACID (63)

Table 55. Crystal data and structure refinement for the lactone **63**.

Empirical formula	$C_{10}H_{14}O_4$	
Formula weight	198.21	
Temperature	173(2) K	
Wavelength	0.71073 Å	
Crystal system	Orthorhombic	
Space group	$P\,2_1\,2_1\,2_1$	
Unit cell dimensions	a = 9.3979(18) Å	α= 90°.
	b = 10.030(2) Å	β= 90°.
	c = 10.499(2) Å	γ = 90°.
Volume	989.7(3) $Å^3$	
Z	4	
Density (calculated)	1.330 Mg/m^3	
Absorption coefficient	0.103 mm^{-1}	
F(000)	424	
Crystal size	0.38 x 0.36 x 0.20 mm^3	
Theta range for data collection	2.81 to 28.00°.	
Index ranges	-12<=h<=12, -13<=k<=6, -13<=l<=13	
Reflections collected	6737	
Independent reflections	1388 [R(int) = 0.0285]	
Completeness to theta = 28.00°	99.9 %	
Absorption correction	None	
Max. and min. transmission	0.9798 and 0.9621	
Refinement method	Full-matrix least-squares on F^2	
Data / restraints / parameters	1388 / 0 / 133	
Goodness-of-fit on F^2	1.072	
Final R indices [I>2sigma(I)]	R1 = 0.0320, wR2 = 0.0862	
R indices (all data)	R1 = 0.0355, wR2 = 0.0881	
Absolute structure parameter	-10(10)	
Largest diff. peak and hole	0.233 and -0.164 e.$Å^{-3}$	

Table 56. Atomic coordinates (x 10^4) and equivalent isotropic displacement parameters ($Å^2$x 10^3) for the lactone **63**. U(eq) is defined as one third of the trace of the orthogonalized U^{ij} tensor.

	x	y	z	U(eq)
C(1)	3778(2)	-67(2)	453(2)	26(1)
C(2)	2733(2)	777(2)	-293(2)	29(1)
C(4)	4923(2)	1275(2)	-1134(2)	26(1)
C(5)	5117(2)	-57(1)	-419(1)	22(1)
C(6)	6360(2)	-37(2)	527(2)	26(1)
C(7)	5859(2)	913(2)	1595(2)	32(1)
C(8)	4250(2)	678(2)	1692(2)	34(1)
C(9)	3141(2)	-1426(2)	757(2)	44(1)
C(10)	5185(2)	-1212(2)	-1370(2)	31(1)
C(11)	7778(2)	372(2)	-25(2)	28(1)
O(1)	8869(1)	-126(2)	629(1)	42(1)
O(2)	7925(1)	1085(2)	-947(1)	41(1)
O(3)	3383(1)	1498(1)	-1185(1)	32(1)
O(4)	1449(1)	834(2)	-166(2)	44(1)

Table 57. Bond lengths [Å] and angles [°] for the lactone **63**.

C(1)-C(2)	1.514(2)
C(1)-C(9)	1.522(2)
C(1)-C(5)	1.556(2)
C(1)-C(8)	1.564(2)
C(2)-O(4)	1.216(2)
C(2)-O(3)	1.331(2)
C(4)-O(3)	1.4659(18)
C(4)-C(5)	1.543(2)
C(4)-H(4A)	0.9900
C(4)-H(4B)	0.9900
C(5)-C(10)	1.532(2)
C(5)-C(6)	1.534(2)
C(6)-C(11)	1.510(2)
C(6)-C(7)	1.545(2)
C(6)-H(6)	1.0000
C(7)-C(8)	1.534(2)
C(7)-H(7A)	0.9900
C(7)-H(7B)	0.9900
C(8)-H(8A)	0.9900
C(8)-H(8B)	0.9900
C(9)-H(9A)	0.9800
C(9)-H(9B)	0.9800
C(9)-H(9C)	0.9800
C(10)-H(10A)	0.9800
C(10)-H(10B)	0.9800
C(10)-H(10C)	0.9800
C(11)-O(2)	1.211(2)
C(11)-O(1)	1.331(2)
O(1)-H(1)	0.82(3)

C(2)-C(1)-C(9)	110.76(15)
C(2)-C(1)-C(5)	102.49(13)
C(9)-C(1)-C(5)	116.55(14)
C(2)-C(1)-C(8)	110.30(14)
C(9)-C(1)-C(8)	111.39(15)
C(5)-C(1)-C(8)	104.84(12)
O(4)-C(2)-O(3)	120.42(17)
O(4)-C(2)-C(1)	127.83(17)
O(3)-C(2)-C(1)	111.74(14)
O(3)-C(4)-C(5)	105.45(12)
O(3)-C(4)-H(4A)	110.7
C(5)-C(4)-H(4A)	110.7
O(3)-C(4)-H(4B)	110.7
C(5)-C(4)-H(4B)	110.7
H(4A)-C(4)-H(4B)	108.8
C(10)-C(5)-C(6)	113.56(13)
C(10)-C(5)-C(4)	110.04(12)
C(6)-C(5)-C(4)	113.20(12)
C(10)-C(5)-C(1)	114.38(12)
C(6)-C(5)-C(1)	103.63(11)
C(4)-C(5)-C(1)	101.34(12)
C(11)-C(6)-C(5)	115.27(13)
C(11)-C(6)-C(7)	112.33(13)
C(5)-C(6)-C(7)	104.19(12)
C(11)-C(6)-H(6)	108.3
C(5)-C(6)-H(6)	108.3
C(7)-C(6)-H(6)	108.3
C(8)-C(7)-C(6)	104.73(14)
C(8)-C(7)-H(7A)	110.8
C(6)-C(7)-H(7A)	110.8
C(8)-C(7)-H(7B)	110.8
C(6)-C(7)-H(7B)	110.8
H(7A)-C(7)-H(7B)	108.9
C(7)-C(8)-C(1)	107.34(13)
C(7)-C(8)-H(8A)	110.2

C(1)-C(8)-H(8A)	110.2
C(7)-C(8)-H(8B)	110.2
C(1)-C(8)-H(8B)	110.2
H(8A)-C(8)-H(8B)	108.5
C(1)-C(9)-H(9A)	109.5
C(1)-C(9)-H(9B)	109.5
H(9A)-C(9)-H(9B)	109.5
C(1)-C(9)-H(9C)	109.5
H(9A)-C(9)-H(9C)	109.5
H(9B)-C(9)-H(9C)	109.5
C(5)-C(10)-H(10A)	109.5
C(5)-C(10)-H(10B)	109.5
H(10A)-C(10)-H(10B)	109.5
C(5)-C(10)-H(10C)	109.5
H(10A)-C(10)-H(10C)	109.5
H(10B)-C(10)-H(10C)	109.5
O(2)-C(11)-O(1)	123.07(16)
O(2)-C(11)-C(6)	124.65(15)
O(1)-C(11)-C(6)	112.27(14)
C(11)-O(1)-H(1)	113.7(18)
C(2)-O(3)-C(4)	110.11(12)

Table 58. Anisotropic displacement parameters ($Å^2$x 10^3)for the lactone **63**. The anisotropic displacement factor exponent takes the form: $-2\pi^2[h^2a^{*2}U^{11} + ... + 2 h k a^* b^* U^{12}]$

	U^{11}	U^{22}	U^{33}	U^{23}	U^{13}	U^{12}
C(1)	21(1)	28(1)	29(1)	-1(1)	5(1)	-3(1)
C(2)	23(1)	31(1)	34(1)	-9(1)	-1(1)	1(1)
C(4)	21(1)	29(1)	29(1)	5(1)	0(1)	0(1)
C(5)	18(1)	23(1)	25(1)	0(1)	1(1)	0(1)
C(6)	20(1)	29(1)	29(1)	3(1)	-2(1)	-1(1)
C(7)	29(1)	42(1)	26(1)	-3(1)	-1(1)	-4(1)
C(8)	29(1)	49(1)	26(1)	-5(1)	4(1)	1(1)

C(9)	43(1)	34(1)	56(1)	4(1)	17(1)	-10(1)
C(10)	28(1)	30(1)	35(1)	-7(1)	4(1)	0(1)
C(11)	20(1)	31(1)	33(1)	-4(1)	0(1)	-1(1)
O(1)	20(1)	53(1)	51(1)	9(1)	-5(1)	0(1)
O(2)	25(1)	52(1)	46(1)	13(1)	5(1)	-3(1)
O(3)	24(1)	37(1)	35(1)	4(1)	-4(1)	6(1)
O(4)	19(1)	53(1)	59(1)	-9(1)	2(1)	2(1)

Table 59. Hydrogen coordinates (x 10^4) and isotropic displacement parameters ($Å^2$x 10^3) for the lactone **63**.

	x	**y**	**z**	**U(eq)**
H(4A)	5401	2010	-672	31
H(4B)	5326	1217	-2003	31
H(6)	6463	-951	897	31
H(7A)	6336	698	2410	39
H(7B)	6066	1852	1371	39
H(8A)	3743	1539	1766	41
H(8B)	4028	132	2452	41
H(9A)	2311	-1312	1312	66
H(9B)	3854	-1976	1191	66
H(9C)	2849	-1864	-35	66
H(10A)	6058	-1140	-1877	47
H(10B)	4357	-1176	-1936	47
H(10C)	5185	-2061	-907	47
H(1)	9640(30)	170(30)	400(20)	53(7)

Table 60. Torsion angles [°] for the lactone **63**.

C(9)-C(1)-C(2)-O(4)	37.3(2)
C(5)-C(1)-C(2)-O(4)	162.27(17)
C(8)-C(1)-C(2)-O(4)	-86.5(2)
C(9)-C(1)-C(2)-O(3)	-141.81(15)
C(5)-C(1)-C(2)-O(3)	-16.80(17)
C(8)-C(1)-C(2)-O(3)	94.40(16)
O(3)-C(4)-C(5)-C(10)	92.65(14)
O(3)-C(4)-C(5)-C(6)	-139.10(13)
O(3)-C(4)-C(5)-C(1)	-28.77(14)
C(2)-C(1)-C(5)-C(10)	-91.53(15)
C(9)-C(1)-C(5)-C(10)	29.6(2)
C(8)-C(1)-C(5)-C(10)	153.24(14)
C(2)-C(1)-C(5)-C(6)	144.32(13)
C(9)-C(1)-C(5)-C(6)	-94.58(17)
C(8)-C(1)-C(5)-C(6)	29.08(15)
C(2)-C(1)-C(5)-C(4)	26.80(14)
C(9)-C(1)-C(5)-C(4)	147.91(15)
C(8)-C(1)-C(5)-C(4)	-88.44(14)
C(10)-C(5)-C(6)-C(11)	72.26(18)
C(4)-C(5)-C(6)-C(11)	-54.15(18)
C(1)-C(5)-C(6)-C(11)	-163.06(14)
C(10)-C(5)-C(6)-C(7)	-164.19(13)
C(4)-C(5)-C(6)-C(7)	69.40(15)
C(1)-C(5)-C(6)-C(7)	-39.50(15)
C(11)-C(6)-C(7)-C(8)	159.95(14)
C(5)-C(6)-C(7)-C(8)	34.52(17)
C(6)-C(7)-C(8)-C(1)	-16.1(2)
C(2)-C(1)-C(8)-C(7)	-117.65(16)
C(9)-C(1)-C(8)-C(7)	118.92(17)

C(5)-C(1)-C(8)-C(7)	-7.98(19)
C(5)-C(6)-C(11)-O(2)	26.6(2)
C(7)-C(6)-C(11)-O(2)	-92.6(2)
C(5)-C(6)-C(11)-O(1)	-154.34(14)
C(7)-C(6)-C(11)-O(1)	86.53(18)
O(4)-C(2)-O(3)-C(4)	179.03(16)
C(1)-C(2)-O(3)-C(4)	-1.82(18)
C(5)-C(4)-O(3)-C(2)	20.09(16)

Table 61. Hydrogen bonds for the lactone **63**

D-H...A	d(D-H)	d(H...A)	d(D...A)	<(DHA)
O(1)-H(1)...O(4)#1	0.82(3)	1.92(3)	2.7394(19)	179(2)

5.3 CRYSTALLOGRAPHIC DATA FOR (1*S*, 3*S*)-1-BROMOMETHYL-2,2-DIMETHYLCYCLOPENTANE-1,3-DICARBOXYLIC ACID (69)

Table 62. Crystal data and structure refinement for the bromocamphoric acid **69**.

Empirical Formula	$C_{10}H_{15}BrO_4$
Formula Weight	279.13
Crystal System	Orthorhombic
Space group	P212121 (No. 19)
a, b, c [Angstrom]	6.9540(2) 10.2232(3) 16.7186(4)
alpha, beta, gamma [deg]	90 90 90
V [Ang**3]	1188.56(6)
Z	4
D(calc) [g/cm**3]	1.560
F(000)	568
Mu(MoKa) [/cm]	34.5
Crystal Size [mm]	0.10 x 0.10 x 0.15
Data Collection	
Temperature (K)	113
Radiation [Angstrom]	MoKa 0.71073
Theta Min-Max [Deg]	2.3, 27.9
Scan,(Type & Range) [Deg]	phi- and omega-scans of 1.0-1.5 deg.
Dataset	-9: 9 ; -13: 13 ; -21: 21
Tot., Uniq. Data, R(int)	20515, 2836, 0.047
Observed data [I > 2.0 sigma(I)]	2186
Refinement	
Nref, Npar	2836, 138
R, wR, S	0.0368, 0.0802, 1.05
w = 1/[\s^2^(Fo^2^)+(0.0194P)^2^+1.6436P] where P=(Fo^2^+2Fc^2^)/3	
Max. and Av. Shift/Error	0.00, 0.00
Min. and Max. resd. dens. [e/Ang^3]	-0.95, 0.71

Table 63. Atomic coordinates (x 10^4) and equivalent isotropic displacement parameters ($Å^2$x 10^3) for the bromocamphoric acid **69**. U(eq) is defined as one third of the trace of the orthogonalized U^{ij} tensor.

Atom	x	y	z	U(eq) [Ang^2]
Br15	0.20137(6)	0.46010(6)	0.23125(2)	0.0520(2)
O7	0.6534(3)	0.5997(2)	0.59764(12)	0.0234(7)
O8	0.6186(4)	0.3828(2)	0.59969(12)	0.0245(7)
O10	0.6926(4)	0.6029(2)	0.23642(13)	0.0245(6)
O11	0.6872(4)	0.3841(2)	0.24139(12)	0.0213(7)
C1	0.6309(4)	0.4459(3)	0.41771(16)	0.0169(8)
C2	0.4970(4)	0.4933(3)	0.48647(16)	0.0156(9)
C3	0.4153(5)	0.6260(3)	0.45894(18)	0.0220(10)
C4	0.4456(6)	0.6327(4)	0.36800(19)	0.0250(11)
C5	0.5147(5)	0.4961(3)	0.34228(16)	0.0154(9)
C6	0.5974(4)	0.4983(3)	0.56680(16)	0.0168(9)
C9	0.6411(4)	0.5016(3)	0.26787(18)	0.0181(9)
C12	0.8278(5)	0.5152(4)	0.42129(19)	0.0297(10)
C13	0.6618(6)	0.2968(3)	0.41997(19)	0.0280(10)
C14	0.3470(5)	0.4034(4)	0.32444(18)	0.0247(10)

Table 64. Anisotropic displacement parameters (Å^{2}x 10^3)for the lactone **63**. The anisotropic displacement factor exponent takes the form: $-2\pi^2[\, h^2a^{*2}U^{11} + ... + 2\, h\, k\, a^*\, b^*\, U^{12}\,]$

Atom	**U(1,1) or U**	**U(2,2)**	**U(3,3)**	**U(2,3)**	**U(1,3)**	**U(1,2)**
Br15	0.0265(2)	0.1084(4)	0.0210(2)	0.0001(2)	-0.0105(2)	0.0066(3)
O7	0.0349(15)	0.0222(13)	0.0132(10)	0.0000(10)	-0.0050(10)	-0.0031(11)
O8	0.0383(14)	0.0239(14)	0.0113(10)	0.0017(10)	-0.0104(10)	-0.0014(12)
O10	0.0400(13)	0.0175(11)	0.0159(9)	0.0028(10)	0.0106(13)	-0.0007(12)
O11	0.0297(12)	0.0197(12)	0.0144(10)	-0.0025(9)	0.0089(11)	-0.0019(11)
C1	0.0171(14)	0.0246(16)	0.0090(12)	0.0010(14)	0.0002(11)	0.0011(15)
C2	0.0157(14)	0.020(2)	0.0110(13)	0.0008(12)	0.0001(11)	0.0000(13)
C3	0.0262(18)	0.026(2)	0.0137(14)	-0.0018(14)	0.0018(13)	0.0095(17)
C4	0.038(2)	0.023(2)	0.0141(15)	0.0045(14)	0.0047(14)	0.0104(17)
C5	0.0187(15)	0.0197(19)	0.0079(12)	0.0007(12)	0.0004(11)	0.0023(14)
C6	0.0172(15)	0.0238(19)	0.0093(12)	0.0026(13)	-0.0001(11)	0.0022(14)
C9	0.0224(15)	0.0202(18)	0.0118(11)	-0.0077(15)	-0.0024(13)	0.0019(12)
C12	0.0152(16)	0.055(2)	0.0190(14)	-0.0071(16)	0.0028(12)	-0.0049(17)
C13	0.039(2)	0.0277(19)	0.0173(15)	-0.0005(14)	-0.0011(15)	0.0160(17)
C14	0.0188(18)	0.042(2)	0.0134(14)	0.0002(14)	-0.0032(12)	-0.0025(16)

Table 65. Hydrogen coordinates (x 10^4) and isotropic displacement parameters (Å^{2}x 10^3) for the bromocamphoric acid **69**.

Atom	x	y	z	U(iso) [Ang^2]
H2	0.38760	0.43030	0.49080	0.0190
H3A	0.27680	0.63210	0.47200	0.0270
H3B	0.48370	0.69870	0.48580	0.0270
H4A	0.54320	0.69970	0.35450	0.0300
H4B	0.32370	0.65530	0.34070	0.0300
H8	0.67460	0.39080	0.64390	0.0290
H11	0.75650	0.39120	0.20050	0.0260
H12A	0.89140	0.49410	0.47200	0.0440
H12B	0.80900	0.61000	0.41750	0.0440
H12C	0.90800	0.48550	0.37670	0.0440
H13A	0.73190	0.26930	0.37200	0.0420
H13B	0.53690	0.25260	0.42180	0.0420
H13C	0.73650	0.27360	0.46760	0.0420
H14A	0.26050	0.39980	0.37140	0.0300
H14B	0.39750	0.31420	0.31500	0.0300

Table 66. Bond lengths [Å] and angles [°] for the bromocamphoric acid **69**.

Br15 -C14	1.947(3)
C5 -C14	1.532(5)
O7-C6	1.222(4)
C5 -C9	1.524(4)
O8-C6	1.311(4)
C2 -H2	0.9994
O10-C9	1.215(4)
C3 -H3A	0.9895
O11-C9	1.320(4)
C3-H3B	0.9901
O8-H8	0.8394
C4-H4A	0.9903
O11-H11	0.8396
C4-H4B	0.9901
C1-C12	1.543(5)
C12 -H12A	0.9803
C1 -C2	1.557(4)
C12 -H12B	0.9800
C1 -C5	1.583(4)
C12-H12C	0.9793
C1 -C13	1.540(4)
C13 -H13A	0.9797
C2 -C6	1.515(4)
C13 -H13B	0.9795
C2 -C3	1.541(4)
C13 -H13C	0.9799
C3 -C4	1.536(4)
C14 -H14A	0.9897

C4 -C5	1.538(5)
C14 -H14B	0.9899
C6 -O8 -H8	109.50
C6 -C2 -H2	107.97
C9 -O11-H11	109.51
C2 -C3-H3A	110.39
C2 -C1 -C12	111.1(2)
C2 -C3 -H3B	110.38
C2 -C1 -C5	100.5(2)
C4 -C3 -H3A	110.43
C5 -C1-C13	114.3(2)
C4-C3-H3B	110.45
C12 -C1-C13	109.3(3)
H3A-C3-H3B	108.68
C2 -C1-C13	111.9(2)
C3-C4-H4A	110.51
C5 -C1 -C12	109.6(2)
C3-C4-H4B	110.44
C3 -C2 -C6	113.9(2)
C5-C4-H4A	110.49
C1 -C2 -C3	105.9(2)
C5-C4-H4B	110.52
C1-C2-C6	112.9(2)
H4A-C4 -H4B	108.68
C2 -C3 -C4	106.5(3)
C1 -C12 -H12A	109.45
C3 -C4 -C5	106.2(3)
C1-C12 -H12B	109.46
C1 -C5 -C9	111.6(3)
C1-C12-H12C	109.48

C1 -C5 -C14	110.1(2)
H12A -C12-H12B	109.50
C4 -C5 -C14	112.2(3)
H12A -C12-H12C	109.46
C9 -C5 -C14	107.6(2)
H12B-C12-H12C	109.47
C4 -C5 -C9	112.0(3)
C1-C13 -H13A	109.48
C1 -C5 -C4	103.4(2)
C1-C13 -H13B	109.49
O8 -C6 -C2	113.2(3)
C1-C13-H13C	109.48
O7 -C6 -O8	123.5(3)
H13A-C13-H13B	109.53
O7 -C6 -C2	123.4(3)
H13A-C13 -H13C	109.39
O10-C9 -O11	124.0(3)
H13B-C13-H13C	109.45
O10-C9 -C5	123.7(3)
Br15-C14-H14A	109.26
O11-C9 -C5	112.4(3)
Br15-C14-H14B	109.35
Br15-C14-C5	111.6(2)
C5-C14-H14A	109.34
C1 -C2 -H2	107.95
C5-C14-H14B	109.32
C3 -C2 -H2	107.96

Table 67. Torsion angles [°] for the bromocamphoric acid **69**.

H14A-C14-H14B	107.93
C13 -C1-C2-C3	-158.1(3)
C13-C1-C2-C6	76.6(3)
C12-C1-C2-C6	-45.8(3)
C5-C1-C2-C3	-36.4(3)
C5-C1-C2-C6	-161.7(2)
C12-C1-C2-C3	79.5(3)
C12-C1-C5-C9	44.9(3)
C12-C1-C5-C14	164.4(3)
C13-C1-C5 -C4	161.4(3)
C13-C1-C5-C9	-78.1(3)
C13-C1-C5-C14	41.4(4)
C2-C1-C5-C9	161.9(2)
C2 -C1-C5-C14	-78.7(3)
C12-C1-C5-C4	-75.6(3)
C2-C1-C5-C4	41.4(3)
C3-C2-C6-O7	-18.0(4)
C3-C2-C6-O8	162.2(3)
C1-C2-C6-O8	-77.0(3)
C1-C2-C3 -C4	18.0(3)
C6-C2-C3-C4	142.7(3)
C1-C2-C6-O7	102.8(3)
C2-C3-C4-C5	8.7(4)
C3-C4-C5-C9	-151.7(3)
C3-C4-C5-C14	87.1(3)
C3-C4-C5-C1	-31.4(3)
C4-C5-C9-O10	5.2(4)
C14-C5-C9-O11	-50.7(3)

C4-C5-C9-O11	-174.5(3)
C14-C5-C9-O10	129.0(3)
C1-C5-C9-O11	70.2(3)
C1-C5-C9 -O10	-110.1(3)
C1-C5 -C14 -Br15	-179.3(2)
C4-C5-C14-Br15	66.1(3)
C9-C5-C14-Br15	-57.5(3)

Table 68. Hydrogen bonds for the bromocamphoric acid **69** (bond lengths in Å, bond angles in degrees)

D-H...A	**d(D-H)**	**d(H...A)**	**d(D...A)**	**<(DHA)**
O8-- H8.. O10	0.839(2)	1.803(2)	2.640(3)	175.33(18)
O11-- H11.. O7	0.840(2)	1.833(2)	2.652(3)	164.74(19)
C3 -- H3B.. O7	0.990(3)	2.432(2)	2.862(4)	105.63(19)
C4-- H4A..O10	0.990(4)	2.440(2)	2.808(4)	101.3(2)
C4-- H4B..Br15	0.990(4)	2.8380(5)	3.350(4)	112.9(2)
C13-- H13A..O11	0.980(3)	2.498(2)	3.121(4)	121.2(2)
C14-- H14B..O10	0.990(4)	2.408(2)	3.248(5)	142.3(2)

5.4 ACCOMPANYING COMPUTATIONAL DATA

Table 69. Calculated structures, in PDB format, supplied on the accompanying CD.

Structures	**Chapter reference**	**Page reference**
14, 35	2.1.1	37
17, 36	2.1.2	38
31, i-iii, TS I-III	2.1.2	39
39, 40	2.2.1	43
41, i-iii, TS I-III	2.2.1	44
48a, TS, 50'	2.2.2.1	48
52i, TS, 52ii	2.2.2.1	50
48b, 45', TS I-IV	2.2.2.1	51
TS I-II, 49b	2.2.2.1	53
57, 59, 60, TS I-II	2.2.2.1	65
63	2.2.2.2	72
69, 66, 43	2.2.2.2	82
68	2.2.2.2	89
62	2.2.2.2	90
82, 83, 84	2.3.2.1	101
78, 88, 89, 90	2.3.2.1	110
93, 94	2.4	112
129, 130, 131, 132	2.6	142
133, 134	2.6	145